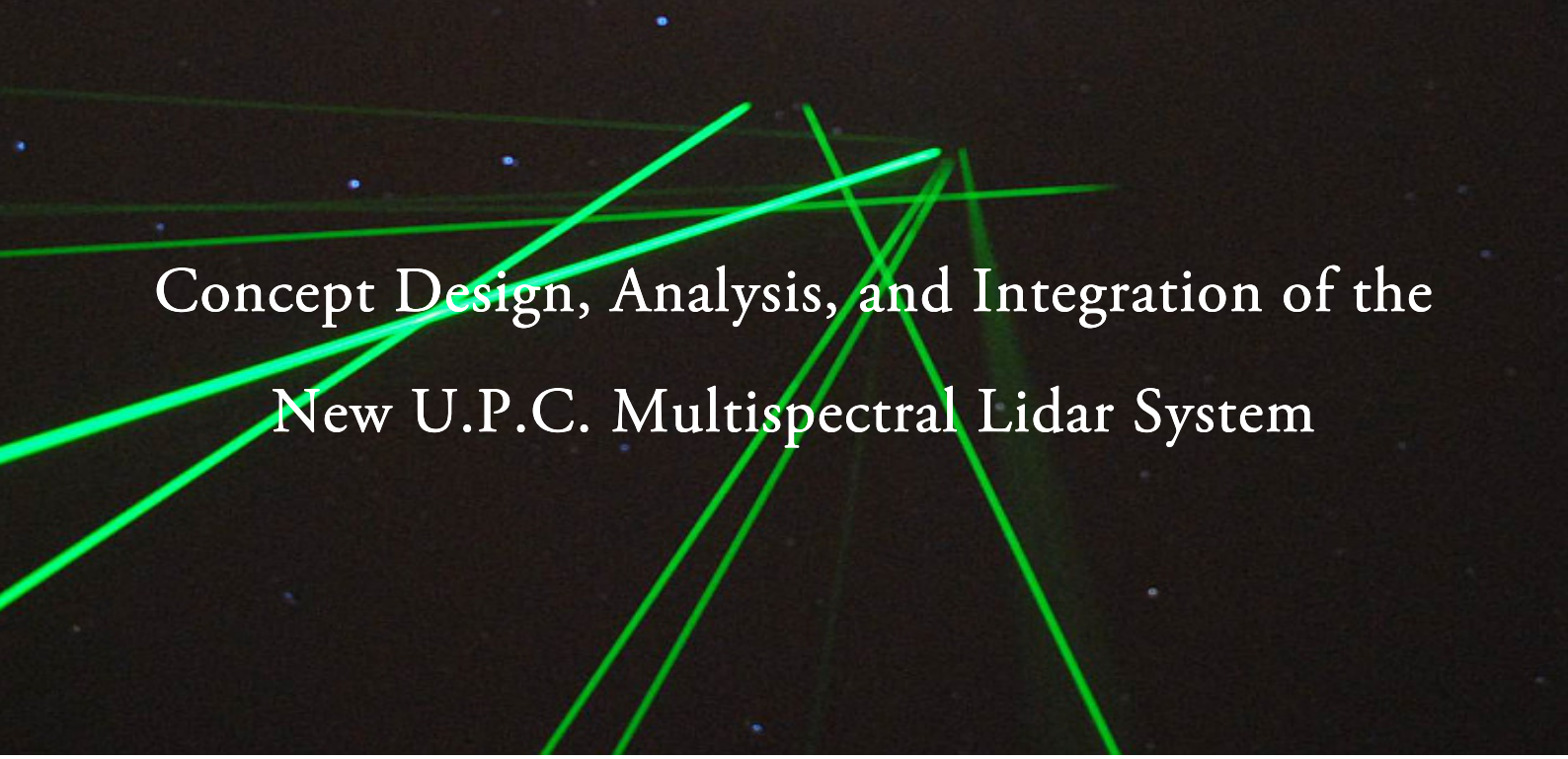

Concept Design, Analysis, and Integration of the New U.P.C. Multispectral Lidar System

(PH.D. THESIS DISSERTATION)

Submitted by

Dhiraj KUMAR

Thesis Advisor

Dr. Francesc ROCADENBOSCH

Remote Sensing Laboratory (RSLAB)

Dept. Teoria del Senyal i Comunicacions

Escola Tècnica Superior d'Enginyeria de Telecomunicació de Barcelona

UNIVERSITAT POLITÈCNICA DE CATALUNYA (SPAIN)

Barcelona, July 2012.

Oficina de Doctorat
UNIVERSITAT POLITÈCNICA DE CATALUNYA

RESUM DE TESI DOCTORAL

Dades de l'autor de la tesi

DNI / NIE / Passaport Passport: E-2.149.041

Nom i cognoms Name: DHIRAJ
Family name: KUMAR

Títol de la tesi CONCEPT DESIGN, ANALYSIS, AND INTEGRATION OF THE NEW UPC MULTISPECTRAL LIDAR SYSTEM

Unitat estructural DEP. SIGNAL THEORY AND COMMUNICATIONS (TSC), UPC

Estudis de doctorat SIGNAL THEORY AND COMMUNICATIONS (TSC)

Codis UNESCO (mínim 1 i màxim 4, els codis es poden trobar a http://doctorat.upc.edu/impresos)

250108 / **250913** / **332599** / **330707**

Resum de la tesi (màxim 4000 caràcters. Si se supera aquest límit, el resum es tallarà automàticament al caràcter 4000)

The increasing need for range-resolved aerosol and water-vapour atmospheric observation networks worldwide has given rise to multi-spectral LIDARs (Light Detection and Ranging, a synonym of laser radar) as advanced remote sensing sensors.

This Ph.D. presents the design, integration and analysis of the new 6-channel multispectral elastic/Raman LIDAR for aerosol and water-vapour content monitoring developed at the Remote Sensing Lab. (RSLAB) of the Universitat Politècnica de Catalunya (UPC). It is well known that the combination of at least three elastic and two Raman nitrogen channels are sufficient to enable retrieval of the optical and microphysical properties of aerosols with a key impact on climate change variables. The UPC lidar is part of the EARLINET (European Aerosol Research Lidar Network) -GALION (Global Atmospheric Watch Atmospheric Lidar Observation Network), a ground-based continental network including more than 28 stations. Currently, only 8 of the 28 EARLINET stations are of such advanced type. This Ph.D. specifically focuses on:

(1) Concept link-budget instrument design and overlap factor assessment. The former includes opto-atmospheric parameter modelling and assessment of backscattered power and SNR levels, and maximum system range for the different reception channels (3 elastic, and 2 aerosol and 1 water-vapour Raman channels, ultraviolet to near-infrared bands). The latter studies the laser-telescope crossover function (or overlap function) by means of a novel ray-tracing Gaussian model. The problem of overlap function computation and its near-range sensitivity for medium size aperture (f/10, f/11) bi-axial tropospheric lidar systems using both detector and fiber-optics coupling alternatives at the telescope focal-plane is analysed using this new ray-tracing approach, which provides a much simpler solution than analytical-based methods. Sensitivity to laser divergence, field-lens and detector/fiber positions, and fiber's numerical aperture is considered.

(2) Design and opto-mechanical implementation of the 6-channel polychromator (i.e., the spectrally selective unit in reception). Design trade-offs concerning light collimation, end-to-end transmissivity, net channel responsivity, and homogeneous spatial light distribution onto the detectors' active area discussed.

(3) System integration and validation. This third part is two fold: On one hand, first-order backscatter-coefficient error bounds (a level-1 data product) for the two-component elastic lidar inversion algorithm are estimated for both random (observation noise) and systematic error sources (user's uncertainty in the backscatter-coefficient calibration, and user's uncertainty in the aerosol extinction-to-backscatter lidar ratio). On the other hand, the multispectral lidar so far integrated is described at both hardware and control software level. Statistical validation results for the new UPC lidar (today in routine operation) in the framework of SPALI-2010 intercomparison campaign are presented as part of EARLINET quality assurance / optimisation of instruments' program.

The methodology developed in the first part of this Ph.D. has successfully been applied to the specification case study of the IFAE/UAB lidar system, which will be installed and operated at the Cherenkov Telescope Array (CTA) observatory. Finally, specs for automated unmanned unattended lidar operation with service times close to 365/24 are presented at the end of this Ph.D. in response to the increasing demand for larger observation times and availability periods of lidar stations.

Lloc i data Barcelona, May 16, 2012.

Signatura

Concept Design, Analysis, and Integration of the New UPC Multispectral Lidar System

Ph.D. Thesis Dissertation
submitted in partial fulfillment of the requirements for the degree of

DOCTOR OF PHILOSOPHY

Submitted by
Dhiraj KUMAR
Thesis Advisor
Dr. Francesc ROCADENBOSCH

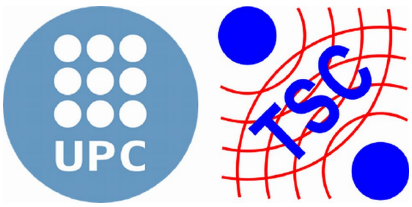

Remote Sensing Laboratory (RSLAB)
Dept. de Teoria del Senyal i Comunicacions
Escola Tècnica Superior d'Enginyeria de Telecomunicació de Barcelona
UNIVERSITAT POLITÈCNICA DE CATALUNYA
SPAIN

Barcelona, July 2012.

Concept Design, Analysis, and Integration of the New UPC Multispectral Lidar System.

[a]Remote Sensing Laboratory,
Department of Signal, Theory and Communications,
Universitat Politècnica de Catalunya (UPC),
Barcelona, SPAIN.

and

[b]Agència de Gestió d'Ajuts Universitaris i de Recerca (AGAUR),
Generalitat de Catalunya,
Barcelona, SPAIN.

Dedicated to my Mother...

ACKNOWLEDGEMENTS

The following institutions are gratefully acknowledged for their contribution to this work:

- Generalitat de Catalunya-Agency for Management of University and Research Grants (AGAUR) for the 2009/FI-DGR grant, held by the author from Jul. 9, 2009 to Jul. 8, 2012.
- Spanish Ministry of Science and Innovation (MICINN) and FEDER (European Regional Development Fund) under the R&D projects REN2003-09753-C02-C02/CLI, TEC2006-07850/TCM and TEC2009-09106 funding the RSLAB lidar and the measurement campaigns carried out in this Ph.D.
- European Commission under the ACTRIS (Aerosols, Clouds, and Trace gases Research InfraStructure Network) FP7 Grant Agreement no. 262254 and EARLINET-ASOS (European Aerosol Research Lidar Network-Advanced Sustainable Observation System) FP6 contract no. RICA-025991 funding the European Lidar Network EARLINET.
- European Space Agency (ESA) under the contract no. 21487/08/NL/HE funding the CALIPSO-satellite ground-based lidar measurements at the RSLAB.

And the participation in:

- MICINN and FEDER complementary actions CGL2006-26149-E/CLI, CGL2007-28871-E/CLI, CGL2008-01330-E funding the SPALINET (Spanish and Portuguese Lidar Network) and CGL2009-08031-E/CLI (Charmex) and CGL2006-27108-E/CLI (Damocles) initiatives.
- European Commission under the ELT (Technology development programme towards a European Extremely Large Telescope) Design Study, EU Specific Support Action, FP6 contract no. 011863 (RIDS).

(Front cover source: EARLINET consortium).

It is a pleasure to thank RSLAB members and EARLINETees who made this thesis possible.

I am indebted to my Ph.D. advisor, Dr. Francesc Rocadenbosch who consistently encouraged and guided me in preparing the present research work through all the stages and without whom it would have been impossible to continue this study.

I am also grateful to Prof. Adolfo Comerón and Dr. Michaël Sicard for their kind support and timely discussions during the various development stages of the RSLAB multispectral lidar system. I also express my sincere thanks to the other faculty and staff members of RSLAB, for their suggestions and kind co-operation during the research work. My particular thanks are due to Diego Lange, Dr. Sergio Tomás, Dr. Jordi Tiana for their kind and cheerful co-operation.

My sincere gratitude is also due to Dr. Volker Freudenthaler (Meteorological Institute, University of Munich) for his kind support on overlap factor computation.

I am also grateful to various authors, eminent scholars whose writings and publications, I have freely gone through to enhance my knowledge on the subject.

My special thanks and apologies to my wife Jharna Agrawal, Daughter Adrija for their inconvenience and sacrifice in the times of her need. I am indebted to my family for providing me a very conducive atmosphere to complete this research project.

At the end, I would like to express my sincere thanks to all those who have directly or indirectly assisted me to complete this research work.

Dhiraj Kumar

ABSTRACT

The increasing need for range-resolved aerosol and water-vapour atmospheric observation networks worldwide has given rise to multi-spectral LIDARs (Light Detection and Ranging, a synonym of laser radar) as advanced remote sensing sensors.

This Ph.D. presents the design, integration and analysis of the new 6-channel multispectral elastic/Raman LIDAR for aerosol and water-vapour content monitoring developed at the Remote Sensing Lab. (RSLAB) of the Universitat Politècnica de Catalunya (UPC). It is well known that the combination of at least three elastic and two Raman nitrogen channels are sufficient to enable retrieval of the optical and microphysical properties of aerosols with a key impact on climate change variables. The UPC lidar is part of the EARLINET (European Aerosol Research Lidar Network) -GALION (Global Atmospheric Watch Atmospheric Lidar Observation Network), a ground-based continental network including more than 28 stations. Currently, only 8 of the 28 EARLINET stations are of such advanced type. This Ph.D. specifically focuses on:

(1) Concept link-budget instrument design and overlap factor assessment. The former includes opto-atmospheric parameter modelling and assessment of backscattered power and SNR levels, and maximum system range for the different reception channels (3 elastic, and 2 aerosol and 1 water-vapour Raman channels, ultraviolet to near-infrared bands). The latter studies the laser-telescope crossover function (or overlap function) by means of a novel ray-tracing Gaussian model. The problem of overlap function computation and its near-range sensitivity for medium size aperture ($f/10$, $f/11$) bi-axial tropospheric lidar systems using both detector and fiber-optics coupling alternatives at the telescope focal-plane is analysed using this new ray-tracing approach, which provides a much simpler solution than analytical-based methods. Sensitivity to laser divergence, field-lens and detector/fiber positions, and fiber's numerical aperture is considered.

(2) Design and opto-mechanical implementation of the 6-channel polychromator (i.e., the spectrally selective unit in reception). Design trade-offs concerning light collimation, end-to-end transmissivity, net channel responsivity, and homogeneous spatial light distribution onto the detectors' active area discussed.

(3) System integration and validation. This third part is two fold: On one hand, first-order backscatter-coefficient error bounds (a level-1 data product) for the two-component elastic lidar inversion algorithm are estimated for both random (observation noise) and systematic error sources (user's uncertainty in the backscatter-coefficient calibration, and user's uncertainty in the aerosol extinction-to-backscatter lidar ratio). On the other hand, the multispectral lidar so far integrated is described at both hardware and control software level. Statistical validation results for the new UPC lidar (today in routine operation) in the framework of SPALI-2010 intercomparison campaign are presented as part of EARLINET quality

assurance / optimisation of instruments' program.

The methodology developed in the first part of this Ph.D. has successfully been applied to the specification case study of the IFAE/UAB lidar system, which will be installed and operated at the Cherenkov Telescope Array (CTA) observatory. Finally, specs for automated unmanned unattended lidar operation with service times close to 365/24 are presented at the end of this Ph.D. in response to the increasing demand for larger observation times and availability periods of lidar stations.

Contents

List of Figures

List of Tables

Chapter 1

INTRODUCTION

In the present environmental framework, remote sensing measurement of atmospheric aerosols, water vapour, clouds, winds, trace constituents and temperature have become more and more important for understanding the complex mechanisms governing Earth's atmosphere. Range-resolved atmospheric measurements, which are frequently necessary for comparison with model studies, can be most conveniently and efficiently performed by lidar (Light Detection and Ranging) systems, which are capable to provide the four-dimensional (space and time) maps of these quantities.
This chapter presents the state of the art in tropospheric lidar remote sensing, and the motivation and objectives of this Ph.D. in the context of the new RSLAB multispectral elastic/Raman lidar. The organization of the thesis is given at the end of the chapter.

1.1 INTERNATIONAL CONTEXT OVERVIEW

LIDAR (Light Detection And Ranging) remote sensing systems [*Fiocco and Smullin*, 1963] are synonyms of laser radar and represent the nearest counterpart to radiofrequency radars, with the exception that microwave radiation has now been replaced by laser radiation. Lidars are currently used on land (fixed-location or transportable) and as sensors mounted in aircraft and satellites for the observation of the terrestrial atmosphere at local and global scale, for monitoring pollutant emissions (remote spectroscopy) and as remote sensing aids at airports (Doppler measurement of wind fields) [*Measures*, 1992b; *Werner*, 2005].
In the space field, on-board lidar sensors have been incorporated since 1994 (LITE (Lidar In-space Technology Experiment) mission) [*Winker et al.*, 1996], which used an on-board lidar in the Discovery shuttle (NASA) to measure cloud structure and atmospheric aerosols at global scale). Currently we can highlight the ICESAT mission (NASA, 2006) (which incorporates the GLAS (Geoscience Laser Altimeter System) instrument [*Spinhirne et al.*, 2004] to measure the terrestrial coverage of ice, cloud/aerosol height and topographical and vegetation characteristics) and the CALIPSO (NASA-CNES, 2006) [*CALIPSO*], ADM-AEOLUS (European Space Agency (ESA), 2009) [*ESA*, 2005] and EarthCare (ESA, 2013) [*ESA*, 2004] missions.

The international purpose of this Ph.D. thesis is part of the GAW (Global Atmosphere Watch) programme of observation of aerosols[1], whose strategic goal 2008-2015 [*Bösenberg and Hoff*, 2007] is "the determination of the spatio-temporal distribution of properties of

[1]The term "aerosols" is applied to particles in suspension in the atmosphere. Aerosols affect directly the Earth's radiation balance by scattering and absorbing radiation in the atmosphere and indirectly modifying cloud formation processes, e.g. by increasing the density/size of water droplets and/or reducing the efficiency of precipitation.

atmospheric aerosols related with climate change and air quality in multi-decade time scales". More specifically, the objective of GALION (GAW Atmospheric Lidar Observation Network) is to provide the vertical component of aerosol distribution by means of advanced-specifications lidar systems organised into a network of cooperative networks (Figure 1.1). The international context of these initiatives is, ultimately, GEOSS (Global Earth Observation System of Systems), which aims to achieve global coordinated multi-sensor observation of the Earth.

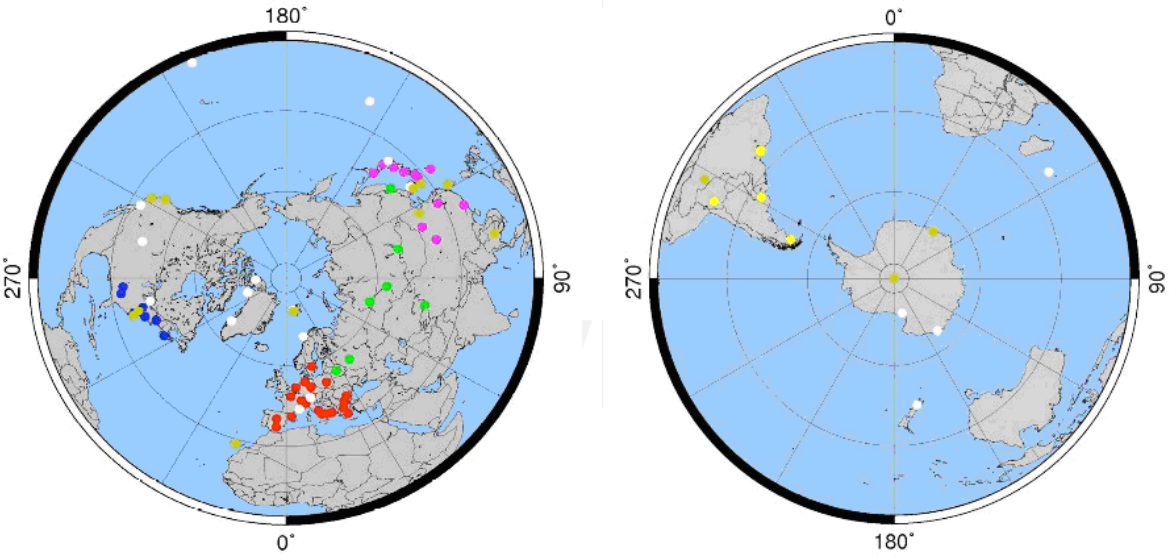

Figure 1.1: Worldwide distribution of observation networks and lidar stations (2008). The different networks are indicated in colours: EARLINET (red, 28 stations), AD-NET (violet, 23 stations), ALINE (yellow, 7 stations), CISLiNet (green, 6 stations), MPLNET (brown, 14 stations), NDACC (white, 19 stations), REALM (blue, 7 stations).

The European Lidar Observation network, EARLINET (European Aerosol Research Lidar NETwork) currently includes more than 28 lidar stations in over 15 countries, Figure 1.2, representing the most advanced coordinated effort in GALION. Contributing to the (multi-spectral) growth of the EARLINET database - which already includes more than 30000 registers, 3000 of them from the Barcelona station - has been therefore an essential goal of this thesis.

The principal areas of application of atmospheric lidar observations at continental scale are summarized in Table 1.1, and their aim is to provide end products (to environmental/ meteorological users) such as long-term trends in greenhouse gas concentration and climate change, transport of aerosols/pollution [*Ansmann et al.*, 2003], quantification of emitter sources, atmospheric chemistry, prediction of UV (ultraviolet) intensities, detection of plumes due to desert dust outbreaks, forest fires, etc.

In order to fulfil these applications, the properties of the aerosols to be observed comprise identification of aerosol layers, profiles of optical properties (extinction and backscatter coefficients, lidar ratio[2], Ångström coefficients - spectral dependence), type of aerosols (e.g. urban pollution, dust, maritime), and microphysical properties (e.g. volumetric and surface concentrations, distribution of size parameters, index of refraction).

Table 1.1 summarizes the optical parameters to be measured and the characteristics and

[2]The lidar ratio (LR) is defined as the ratio between optical extinction (α) and optical backscatter (β) due to atmospheric aerosols.

Area of application	Necessary parameters	Lidar station characteristics	Type of operation	Number of stations
1. CLIMATE				
1.a Global climatology	α, δ, (β, LR)	R	Fixed programmed (3 times/week)	20
1.b Evaluation of models	α, δ, (β, LR, MPP)	MR	Fixed programmed + diurnal cycles	50
1.c. Transport and tracers	β, (α, δ, MPP)	B	Fixed programmed + alerts	50
1.d. Radiation	α, β, (δ)	R	Random	20
2. AIR QUALITY				
2.a. Air quality determination	α, δ, β, MPP	R	Fixed programmed	50+
2.b. Air quality forecasting	B	B	Almost continuous	20
3. PLUMES due to special events	β, (α, δ, MPP)	B	Alerts	50
4. SPACE MISSION SUPPORT				
4.a. Ground calibration/validation ("ground truth")	α, δ, β, LR	MR	TBD	20
4.b. Complementary information	α, δ, β, LR	MR	Fixed programmed	20

Table 1.1: Characteristics of lidar measurements according to area of application. Initials: Raman (R), multispectral Raman (MR), elastic backscatter (B), extinction (α), backscatter (β), depolarisation (δ), lidar ratio (LR), microphysical parameters (MPP).

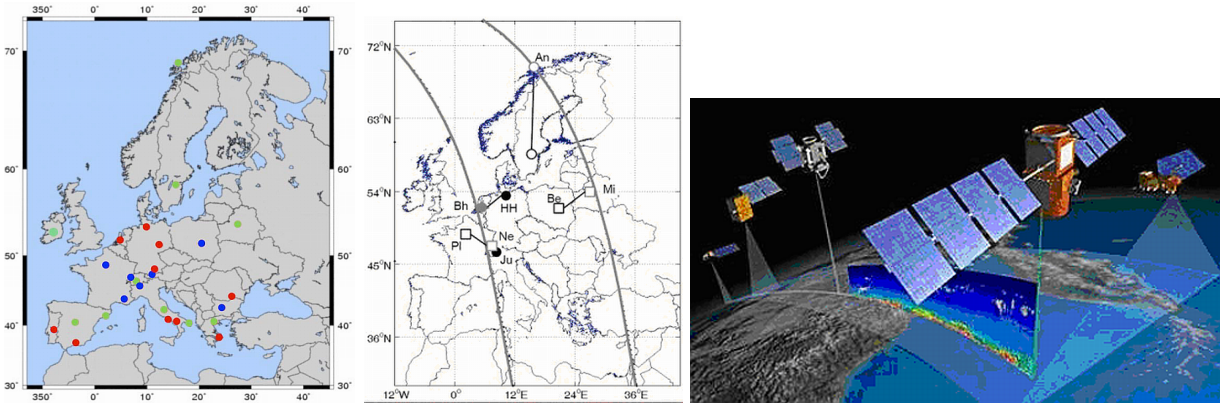

(a) **(b)** **(c)**

Figure 1.2: The RSLAB lidar station in the European Lidar Network (EARLINET) and CALIPSO mission (NASA-CNES). (a) Map of the EARLINET lidar stations: (red) multispectral elastic/Raman stations (3+2 channels or more), (blue) Raman stations (1 or more channels but without reaching the 3+2 standard), (green) elastic stations. Note: The notation "A+B" indicates "A" elastic channels and "B" Raman channels. (b) The coordinated measurements strategy considers criteria of geographical proximity (< 40 km) to the overpass trajectory ("ground track," grey lines), type of station (square icons and circles) and proximity to cooperative stations (black lines) in order to define obligatory and recommended measurements in EARLINET. (c) CALIPSO and A-train satellite constellation.

Mission	On-board lidar	Type of lidar	Data products vs. wavelength			Anticipated operation period
			355 nm	532 nm	1064 nm	
CALIPSO	CALIOP	B	-	β, δ	β	2006-2009
ADM-AEOLUS	ALADIN	HSRL	α, β, LR	-	-	2009-2011
EarthCARE	ATLID	HSRL	α, β, LR, δ	-	-	2013-2016

Table 1.2: Present and future lidar space missions. Initials: As in Table 1.1. (HSRL) High Spectral Resolution Lidar

mode of operation of the lidar stations involved [*Hoff et al.*, 2008]. The following points of the international context can be highlighted:

1. The lidar instrument must include 3+2 multispectral combined elastic/Raman channels (MR in Table 1.1). While the quantitative retrieval of the optical components of extinction (α), backscatter (β) and lidar ratio (LR) at the emission wavelength requires the combination of an elastic-type channel[3] and a Raman channel[4] [*Ansmann et al.*, 1990], the retrieval of microphysical parameters of aerosols (MPP in Table 1.1) requires a minimum of 3+2 channels [*Böckmann et al.*, 2008; *Müller et al.*, 2007]. Currently, only 8 of the 28 EARLINET stations are of this type, Figure 1.2. The upgrade of the Barcelona lidar station towards a 3+3 multispectral Raman station (which also includes a third Raman channel for the measurement of atmospheric water vapour) is a key contribution of this Ph.D. to the success of EARLINET-GALION objectives.

2. The need for "ground truth" support (calibration/validation or cal/val) -in what follows- to space missions (Table 1.2) by means of terrestrial lidar networks. Since the launch of the CALIPSO (NASA-CNES) satellite (Cloud Aerosol Lidar and Infrared Pathfinder Satellite Observation) [*CALIPSO*] in April 2006, many of the stations contributing to GALION and, specifically, most of the EARLINET stations, have carried out (in agreement with the ESA) observations coinciding with the overpasses of CALIPSO [*Winker et al.*, 2006]. ADM-AEOLUS mission (Atmospheric Dynamics Mission) [*ESA*, 2005] along with EarthCARE (Earth Clouds Aerosols and Radiation Explorer) [*ESA*, 2004] will offer the great opportunity of having available 10 years' observation of the properties of aerosols, clouds and wind at global scale [*Ansmann et al.*, 2007].
   This cal/val exercise, which at the beginning is carried out for CALIPSO and by giving support to a companion Ph.D. thesis [*Lange*, 2012], entails, on one hand, harmonising the different sets of data and, on the other hand, correcting atmospheric attenuation (aerosols/particles) in the signals received by the respective sensors (CALIOP and ALADIN). This requires, first, to have high-quality measurements of the atmospheric optical parameters by means of 3+2 multispectral elastic/Raman stations and, second, approximate error bounds for the optical parameters inverted. As a result it is possible to assess the quality or the inverted data products, which include the spectral dependence (Ångström coefficients) of the extinction and backscatter coefficients and

[3]In elastic interaction, emission and reception wavelengths coincide. The term "elastic channel" denotes "the optical and electronic elements in reception used to process the elastically backscattered lidar return power".

[4]In Raman (inelastic) interaction, the reception wavelength is red shifted in relation to the emission wavelength.

aerosol lidar ratios (LR) at the UV and VIS wavelengths (355 and 532 nm) for a wide range of types of aerosols and meteorological conditions.

3. Finally, the lidar instrument must provide observations with sufficient coverage, resolution and precision to establish climatology of aerosols at continental scale [*Matthias et al.*, 2004]. While spatially these parameters are given by the geographical structure of the network, at the temporal level they necessitate:
(i) operation that is both programmed ("weekly schedule") and coordinated (with the rest of the stations),
(ii) availability of service close to 365/24 (prompted by alerts, coincidence with overpasses of satellites of interest, etc.), and
(iii) eye-safe operation and with regard to aircraft overflights.
Concerning 3.ii above, this Ph.D. is to contribute a preliminary specification of the "unmanned unattended" eye-safe operation (i.e., by remote control [*Martucci et al.*, 2003] with minimal human supervision) of the new RSLAB multispectral elastic/Raman lidar station.

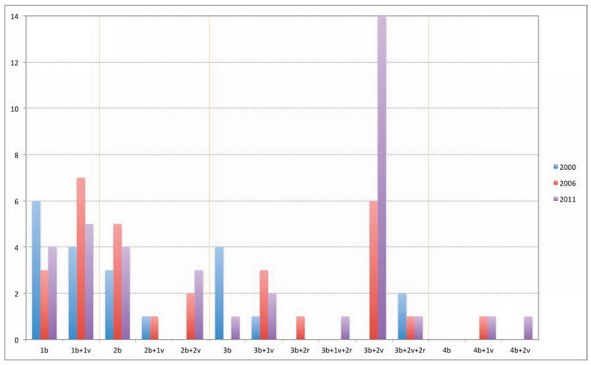

Figure 1.3: Frequency distribution of lidar system configurations of EARLINET. (Figure 6.1 in [*Apituley et al.*, 2011]).

1.2 BITS OF HISTORY: TOWARDS THE RSLAB MULTI-SPECTRAL LIDAR

The journey of lidar studies at the RSLAB started in 1993 with the first operation in Spain of a fixed backscatter lidar station in 1996 (Figure 1.4). The station consisted of a 0.5-Joule, 10-Hz repetition rate, Nd:YAG laser along with a 20-cm diameter Schmidt-Cassegrain telescope. The two elastic channels in reception at 532-nm and 1064-nm wavelengths could not be operated simultaneously and a filter had to be replaced in front of the APD-based photo-receiver to select the desired wavelength. Data acquisition was done by a 12-bit GaGe Compuscope 1012 digitizing board.
In 1997 design and construction of a 3-D scanning 2+1 elastic/Raman lidar was commenced. This instrument has been constructed in two phases: Phase I (1997-2003), where simultaneous acquisition at two elastic wavelengths (532 and 1064 nm) was incorporated, and phase II (2003-2007), where a nitrogen-Raman channel (607 nm) became the third channel of the system. A three channel polychromator (i.e., the spectrally selective unit in reception, Figure 1.4) was coupled to the telescope through an optical fiber bundle. 1064-nm and 532-nm channels used APD-based photo-receivers, while the 607-nm one used a photo-multiplier

tube (PMT). 532- and 1064-nm channels were acquired with a 12-bit Spectrum MI.3011 digitizing board, while the 607-nm channel recorded by means of a combined analog/photon-counting Licel TR20-80 transient recorder. Detection of the 532-nm channel was improved in October 2008 by substituting the APD-based photoreceiver by a PMT (see Figure 1.4). In

(a) **(b)** **(c)** **(d)**

Figure 1.4: History of U.P.C. elastic/Raman lidar system (1993-2011). (a) Nocturnal operation of the UPC's first fixed elastic lidar station (at 532 nm) (1996). (b) Emission/reception head of the transportable 2-wavelength aerosol elastic backscatter lidar (1064, 532 nm) (2002). Since 2006 this lidar system has incorporated 1 additional Raman channel at 607 nm (configuration 2+1 channels). (c) The elastic/Raman 2+1-channel lidar system in 2008 (elastic at 532 and 1064 nm and Raman at 607 nm). (d) Elastic/Raman 3+3-channel lidar system at the present (elastic channel at 355 nm and Raman at 387 and 407 nm added).

parallel, design and construction of the new RSLAB multispectral elastic/Raman lidar station was started in 2003, which began operation in Sep. 2010 and *as an output of this Ph.D. thesis*. The system is based on a Quantel Brilliant/T64 130-mJ energy, 20-Hz repetition rate, Nd:YAG source along with a 35-cm aperture, 3.91-m focal length Schmidt-Cassegrain telescope. The resulting system is a 3+2+1 system[5] (355, 532 and 1064 nm as the elastic wavelengths, 387 and 607 nm as the nitrogen Raman wavelengths, and 407 nm as the water-vapour Raman wavelength). The instrument includes a new polychromator coupled to the telescope through an optical-fiber bundle that enables to perform scanning measurements in a 90-deg elevation and 330-deg azimuth width. All channels use PMT receivers, except the 1064-nm one, which uses an APD-based photo-receiver. Acquisition is carried out by means of Licel^{TM} TR40-80 modules. Under standard clear-air conditions the sounding range goes from approximately 500 m up to 20 km. A schematic of the new system is shown in Figure 1.5 *(detailed discussion in Chapter 6)*. Measurement of the opto-atmospheric parameters of extinction and backscatter in the VIS and UV bands, which with elastic techniques is always semi-quantitative, now becomes *fully quantitative* [*Ansmann et al.*, 1992], that is, calibrated by the Raman return due to atmospheric nitrogen (the most abundant atmospheric molecular species with known stable concentration).

1.3 MOTIVATION OF THE STUDY

The motivation of this Ph.D. is derived from the requirements, mode of operation and target applications of the high-performance lidar systems being demanded in the international context (Section 1.1). The initial hypothesis of EARLINET (28 lidar stations in 15 countries) to construct a climatology of the spatio-temporal distribution of aerosols at continental scale revolves around knowing the microphysical properties of aerosols and means that, ideally,

[5]The notation 3+2+1 stands for 3 elastic, 2 nitrogen-Raman, and 1 water-vapour Raman channel in reception.

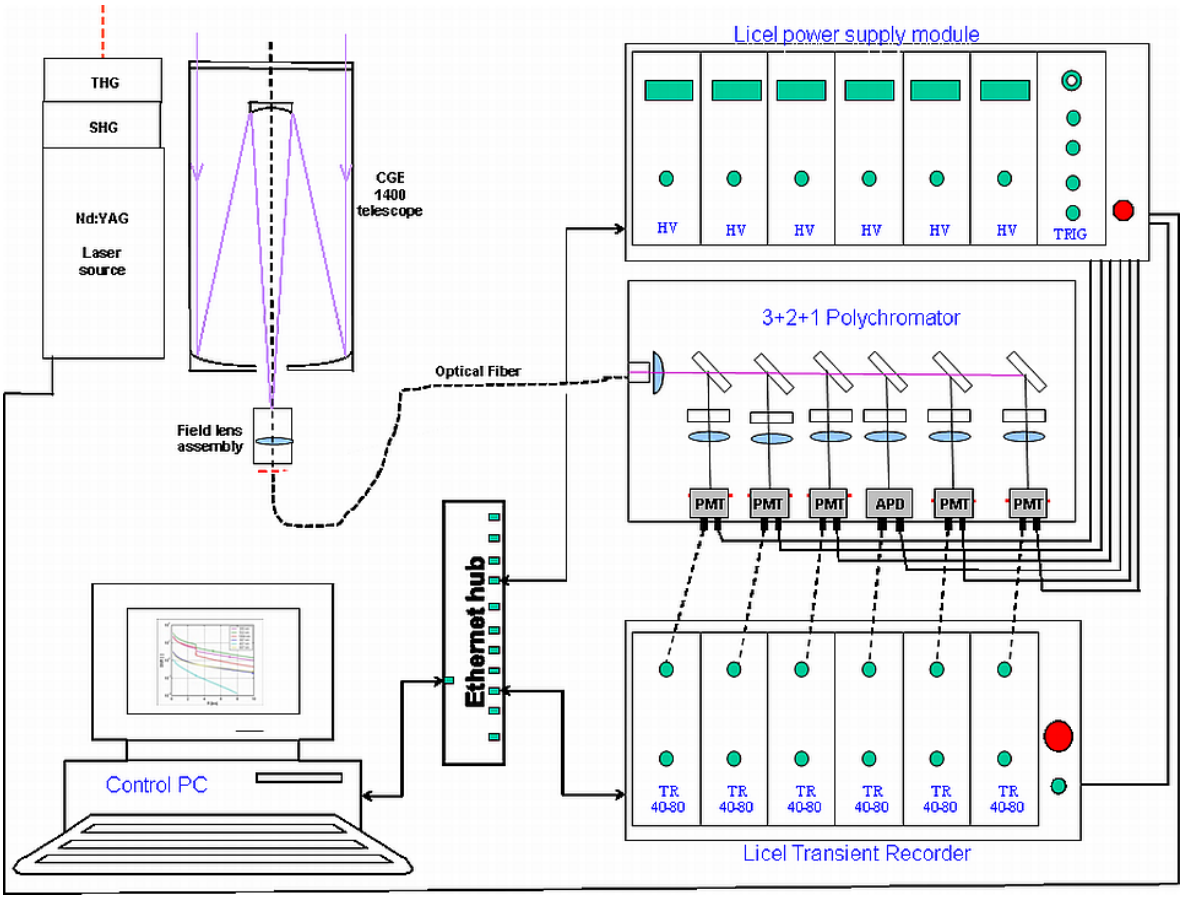

Figure 1.5: Schematic of the new RSLAB 3+2+1 multispectral elastic/Raman lidar system.

all the lidar stations of the network (to date only 8 in Europe) should have 3 elastic channels and 2 Raman channels, thus covering UV (ultraviolet), VIS (visible) and NIR (near-infrared) bands. The water-vapour channel thus being and accessory channel. Additionally, the EARLINET terrestrial lidar stations should make possible to calibrate and validate the measurements of satellite-borne lidar sensors (CALIPSO mission and incoming space missions, Table 1.2) all of which requires of finely integrated hardware, without overlooking the development of models of validation and assimilation of data. Besides, coordinated measurements within EARLINET and/or in coincidence with satellite overpasses require unmanned unattended operation supporting remote control via the Internet.
The scope of tropospheric lidar remote sensing is somehow broader because lidar measurements involve the pre-processing of lidar signals (i.e., generation of "clean data") and the inversion and categorisation of data.

1.4 MAIN OBJECTIVES

This Ph.D. is aimed at the design (both at link-budget and optical level), integration, and preliminary validation of new 3+2+1 RSLAB multi-spectral lidar system.
The main objectives are:

PART 1: On concept design of the RSLAB multi-spectral lidar system

Obj. 1. Conceptual system link-budget: Assessment of atmospheric backscattered power levels, signal-to-noise ratio (SNR) in reception, and maximum system range.

Obj. 2. Assessment of the overlap factor for detector and fiber-coupled solutions.

PART 2: On polychromator design and implementation

Obj. 3. Design and opto-mechanical implementation of the 6-channel polychromator (i.e., the spectrally selective unit in reception).

PART 3: On system integration and preliminary validation

Obj. 4. Error estimates for the two-component lidar inversion algorithm: Retrieval of the optical atmospheric aerosol backscatter coefficient.

Obj. 5. Instrument integration both at hardware and software level. Preliminary validation: SPALI-10 intercomparison campaign.

TRANSVERSAL OBJECTIVES:

T1. Participation in regular lidar measurement and ad-hoc field campaigns.

1.4.1 PART 1: Concept Design of the RSLAB multi-spectral lidar system

The new 3-D scanning 6-channel multi-spectral lidar system is the third lidar station conceptually designed at RSLAB since the birth of the lidar research activity in 1993 [*Rocadenbosch*, 1996] and has already been presented in Section 1.2. The station is a 3+2+1 elastic/Raman aerosol/water-vapour system (Figure 1.6). The RSLAB 3-D scanning multi-spectral lidar

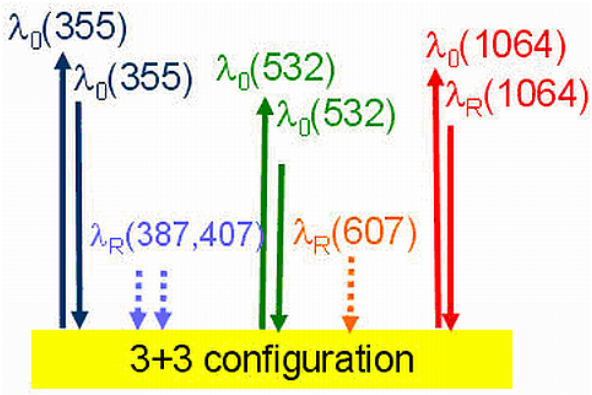

Figure 1.6: The 3+3 elastic/Raman configuration. Elastic interaction (emission and reception wavelength coincide) is depicted in solid lines. Raman interaction (reception wavelength is always longer than the emission wavelength) is depicted in dotted trace and close to the corresponding elastic wavelengths (solid-arrows). Up arrows indicate emission, down arrows indicate reception.

station simultaneously emits at 355-, 532- and 1064-nm wavelength using a Nd:YAG laser as the fundamental source. In reception, a 6-channel polychromator is used to separate three elastic return wavelengths (355-, 532- and 1064-nm wavelengths corresponding to the emitted wavelengths in the UV, VIS and NIR, respectively) and three inelastic-Raman return wavelengths (387, 607, and 407-nm). The 387- and 607-nm wavelengths are the Raman return shifts from the atmospheric nitrogen when excited at 355- and 532-nm primary wavelengths which motivates the 3+2 standard notation described above. This enables independent inversion of the optical parameters, namely, aerosol extinction and backscatter and, subsequently,

of the lidar ratio and Ångström coefficients (i.e., the aerosol wavelength dependency coefficient) as well. Besides, a 407-nm Raman channel, corresponding to the water-vapour Raman shift upon 355-nm wavelength excitation, is also included for water vapour atmospheric profiling. This "non-aerosol" sixth channel justifies the "3+2+1" channel notation used (i.e., the 3+2 notation stands for the aerosol-detection channels upon elastic and nitrogen-Raman interaction, and the "+1" notation stands for the water-vapour channel). Water-vapour atmospheric measurement is carried out in terms of the mixing ratio. The importance of the mixing ratio is that it is conserved in atmospheric processes that do not involve evaporation or condensation and that it serves well as a tracer of the movement of air parcels in the atmosphere. Moreover, when mixing ratio profiles are combined with range-resolved temperature/pressure profiles, it will also be possible to derive the relative humidity profile. All in all, and along with the 3D-angular scan capability, the system is to obtain two-dimensional quantitative maps around the lidar location of the backscatter coefficient due to atmospheric aerosols at 1064 nm, aerosol backscatter and extinction coefficients at 532 nm and 355 nm, and water-vapour mixing ratio. Under clear-air visibility conditions, the maximum range is to be tens of km for backscatter coefficients and a few km for extinction coefficients and water-vapour mixing ratio under night-time operation.

The motivation of Objs. 1-2 is two fold:

On one hand, assessment of atmospheric backscattered power levels, signal-to-noise ratio (SNR) in reception and maximum system range under standard "clear air" visibility conditions govern the "big parameters" of system design [*Kumar et al.*, 2006, 2012b]. Obj. 1 is to simulate the "big numbers" of the lidar system in a parameterized way and for all the six channels in reception. To achieve this goal a two-component (aerosol plus molecular) atmospheric model will be used. On the other hand, Raman channels have typical return levels 3-to-4 orders of magnitude lower than elastic channels, which requires medium-to-large apertures (30-cm diameter telescopes and over). However, such large telescope apertures are associated to large f-numbers, which motivates that it is not possible to have starting sounding ranges (range of full overlap) as low as required (typically some 400 m for atmospheric boundary layer monitoring) using a detector/fiber-optics directly coupled to the telescope focal plane (in the case of fiber-coupled lidar systems the fiber optics is used to convey the backscattered composite optical radiation in return to the optical polychromator) [*Kumar et al.*, 2006, 2011]. Alternatively, most EARLINET lidar stations are using two telescopes, a small one for the near range and a larger one for the far range. In obj. 2 the overlap factor (OVF) will be studied for both detector and fiber-coupled alternatives. Besides, the issue of Gaussian illumination, as is the case for laser beams, will be taken into account.

1.4.2 PART 2: Polychromator design and implementation

Once a conceptual system link-budget (obj. 1) and the intervening optical relations ruling the OVF (obj. 2) have been studied and simulated (Matlab^{TM}, ZEMAX^{TM}), obj. 3 will tackle the design of the optical polychromator to be integrated in the final lidar system (Part. 3). Obj. 3 is to present both the optical design and the mechanical implementation of the polychromator unit to be designed. Here, the RSLAB departs from an earlier design experience of a 2+1 polychromator [*Kumar et al.*, 2006]. At this point, it is acknowledged that the "mechanical implementation" should formally be located in Part. 3, but it is included here for clarity reasons.
A main design difficulty is the fact that the fiber optics (polychromator input) is not a point source and hence, cannot be perfectly collimated [*Möller*, 2007a]. Other aspects of concern

are the fact that optical filter bandwidths (e.g., interferential filters to reject background radiation) are specified for normal incidence (the filter center wavelength depends on the incident angle) and the need to cope with very different return intensities such as those corresponding to elastic and Raman channels. The literature is certainly weak in this Part. 2 for these contents are undisclosed in most commercial systems (patented).
At mechanical and opto-mechanical level, the implementation solution is not evident and requires consultancy with external technicians. Obj. 3 will resort to internal "how-to" documents within EARLINET, commercial application notes, and private communication with manufacturers.

1.4.3 PART 3: System integration and preliminary validation

Once Objs. 1-3 have specified the design parameters and optical layout of the lidar system we progress towards the final system integration and validation. As an intermediate step, obj. 4 will be devoted to approximately assess the error bounds associated to the retrieval of level-1 elastic data products, i.e., the retrieval of the optical atmospheric aerosol backscatter coefficient from the two-component lidar inversion algorithm, the so-called Fernald's or Klett-Fernald-Sasano's algorithm [*Klett*, 1985] (the error bounds on the aerosol extinction can similarly be error propagated given the backscatter-coefficient error estimates and the aerosol lidar ratio ones). More advanced error bounds such as exact forms (if any) or similar error bounds for the Raman channels form part of a companion Ph.D., specifically devoted to lidar signal processing and statistical aspects [*Lange*, 2012]. Because error estimates due to the measurement noise depend on the SNR in reception (an output from obj. 1), obj. 4 will provide a first validation of the proposed SNR ranges in obj. 1.
The core of Part. 3 will focus on obj. 5, which is to present the key aspects on instrument integration at hardware and control software level (LabView^{TM}). The overall conception of the 3+2+1 multispectral lidar is to be in accordance with the "optimization of instruments" network activity within EARLINET-ASOS (Advanced Sustainable Observation System, EC Coordination Project, March 2006-2011). Starting from the existing EARLINET infrastructure, EARLINET-ASOS is contributing to fill up the gap between the existing systems and methodologies and the required optimal performance of the network to become a leading instrument for the observation of the 4-dimensional spatio-temporal distribution of aerosols on a continental scale discussed above. [*Rocadenbosch et al.*, 2008; *Apituley et al.*, 2008].
Though not included in this Ph.D. thesis document, a subsidiary output of this obj. 5 to the RSLAB has been an "instrument master document". A major Ph.D. output is the "Instrument master document" including electronic indexing and organization of components specs, CAD simulation designs and macros, design tips, and commercial and technical support information). Obj. 5 assimilates new and existing documentation within ACTRIS knowledge database such as: (i) Specs. compilation of all lidar sub/system setups of the network into a Handbook of Instruments (HoI.) (ii) Improvement of the existing observation instrumentation (systems, sub-systems and system integration) by selecting the optimal approach from the various solutions existing at individual stations (consider e.g., transmitter/receiver topics such as the geometrical form-factor, close/far-range detector solutions, homogeneous illumination of photo-detectors, and the definition of optimal wavelength separation filters, or receiver electronics and data acquisition issues such as grounding and shielding and (iii) Instrument standardization with a view to the already discussed 3+2 aerosol elastic/Raman lidar approach.
SPALI-10 intercomparison measurement campaign (a joint campaign including key stations from EARLINET and the Spanish and Portuguese Lidar Network) is to provide a preliminary validation of the multi-spectral lidar system in terms of range-corrected lidar signals.

Finally, a transversal objective all over the Ph.D. is the participation in regular and one-off measurement campaigns, which will also serve the purpose to correct, adjust, and validate the system in a progressive manner. These measurement campaigns are (Figure 1.7):

1. Regular coordinated measurements with the European EARLINET network (3 per week, Feb. 2000-present): Contribution to the growth of the database on the distribution in 4 dimensions (spatial and temporal) of aerosols at continental scale.
   Principal products: climatology (optical parameters of extinction and backscatter of atmospheric aerosols), cloud cover (cirrus), diurnal cycle, PBL, monitoring of alerts (dust outbreaks, photochemical episodes, forest fires, volcanic eruptions).

2. CALIPSO measurements (Jun. 2006-present, also within the framework of the EARLINET network). 2-3 measurements every 16 days (diurnal and nocturnal) in coincidence with overpasses of the CALIPSO satellite (NASA-CNES).
   Results: calibration/validation from the terrestrial EARLINET network stations of the measurements taken by the elastic lidar (CALIOP) on board the CALIPSO satellite, whose mission is to provide global information on distributions of aerosols and clouds.

3. SPALINET **(SPAnish and Portuguese Lidar Network)** campaigns: "ad-hoc" measurement campaigns of intercomparison of instruments (at different points of Spain and with in-situ cooperative sensors) and intercomparison of inversion algorithms and methodologies. Geographical mobility in Spanish territory (e.g., El Arenosillo (Huelva), 28-6 to 4-7-2006 (Figure 1.7) [*Sicard et al.*, 2007]; Santa Cruz de Tenerife (Canary Islands), 20-6 to 13-7-2007; La Palma (Canary Islands), 26-5 to 15-6-2008).
   Results: Intercomparison of the lidars forming the Spanish network. Quality control on instruments and algorithms combining in-situ cooperative sensors.

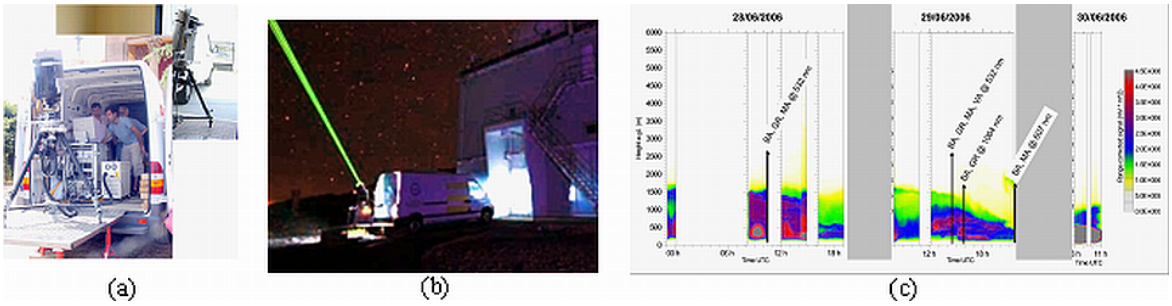

Figure 1.7: Measurement campaigns with the elastic/Raman 2+1 lidar system and Spanish lidar network (SPALINET). (a) Operation in measurement campaigns (Valencia 2003, validation GERB/CERES), (b) Campaign ORM-1: Measurement of atmospheric optical thickness (AOT) and wind fields (Observatorio Roque de los Muchachos, La Palma, Canary Islands, 20-6 to 13-7-2007 and 26-5 to 15-6-2008), (c) R2P intercomparison of the SPALINET stations of GR (Granada), MA (Madrid), Valencia (VA) and BA (Barcelona): SPALINET-1 campaign (El Arenosillo (Huelva), 28-6 to 4-7-2006).

1.5 THESIS ORGANIZATION

This Ph.D. thesis is organized as follows:
Chapter 1 focuses on the motivations and goals of this Ph.D. and in relation to the state-of-the-art of a multi-spectral elastic/Raman lidar system.

Chapter 2 describes the conceptual power link-budget (opto-atmospheric parameter modelling, power returns, signal-to-noise ratio, max. system range achieved), and a theoretical estimation of the performance of the new RSLAB 3+2+1 multispectral elastic/Raman lidar system.
Chapter 3 presents calculations and detailed analysis of overlap factor in a typical lidar system (especially in near-range) and describes the technique for its further improvement.
Chapter 4 presents complete description of the design and implementation of 6-channel polychromator in the new RSLAB 3+2+1 multispectral elastic/Raman lidar system.
Chapter 5 presents the primary analytical formulation to compute the total-backscatter range-dependent error bars from the Klett's two-component elastic-lidar inversion algorithm.
Chapter 6 is divided into two parts. Part I presents the system integration focusing on the hardware and software units involved and a scheme for the full automation of the new RSLAB 3+2+1 multispectral elastic/Raman lidar system. Part II presents pre-validation of the RSLAB lidar system by means of SPALI-10 intercomparison campaign.
Chapter 7 presents a case example based on previously described link-budget formulation (Chapter 2) needed for the establishment of an elastic/Raman lidar to incorporate astrophysical studies.
Chapter 8 finally describes the conclusion of the work carried out during the thesis and future recommendations.

Chapter 2

SYSTEM ENERGY LINK BUDGET ESTIMATION

In this chapter, energy link-budget design equations and specifications of the new 3+3 multispectral RSLAB lidar system are derived and discussed. The lidar system uses a Q-switched Nd:YAG laser emitting at 1064-, 532- and 355-nm wavelengths and the return signal is collected by a 35.6-cm aperture telescope. A spot-to-spot fiber bundle conveys the light from the telescope focal plane to a specific polychromator especially designed to minimise optical losses and physical dimensions (Chapter 4). The reception field of view, which is limited by the fiber bundle characteristics, is the same at all wavelengths. Backscattered received light is separated into the three elastic wavelengths (355, 532, 1064 nm) as well as the 386.7- and 607.4-nm N_2-Raman-shifted wavelengths, and the 407.5-nm H_2O-Raman-shifted wavelength. Signal detection is achieved by using an APD at 1064 nm and PMTs at all other wavelengths. Combined analog/photon counting acquisition is used. A customized user-friendly LabView® interface controls the receiving optoelectronic design (Ethernet-based).
An overview of the system in terms of power link-budget estimation is discussed for the channels involved and system performance assessment in terms of SNR and maximum range achieved. Concerns on the photodetector output current linearity are preliminarily addressed. The interpretation and cross-examination of the large variety of lidar parameters playing role in the overall system performance has justified implementation of a multispectral 'link-budget' software simulator.
This chapter is an adaptation of two conference papers from the author, [*Kumar et al.*, 2012b,a].

2.1 OPTO-ATMOSPHERIC PARAMETERS

In order to estimate the power link-budget and assess system performance (estimated power levels in return, SNR, and maximum system range for both the elastic and Raman channels), oversimplified opto-atmospheric profiles are preferred to complex realistic ones. The two-component atmospheric model presented next simulates an aerosol component consisting of a homogeneous load of aerosols up to the end of the boundary layer superimposed to a molecular component based on the US-standard atmosphere model [*Bodhaine et al.*, 1999].

2.1.1 Aerosol component

A wavelength-dependent aerosol component is modelled as a homogenous load of aerosols up to 3 km in height (atmospheric boundary layer (ABL)), which motivates the step-ladder profile of Figure 2.1. Beyond the ABL a purely molecular atmosphere is considered. A "clear air" atmospheric condition corresponding to a mean visibility margin (defined at 532 nm reference wavelength), $V_M = 39.12$ km, is simulated. According to Koshmieder's relationship [*Koshmieder*, 1924], this visibility translates into an aerosol extinction component, $\alpha_{532}^{aer} \simeq \alpha_{532}^{tot}$=3.912/($V_m$ [km])=0.1 km^{-1}, Section 2.1.4. A λ^{-1} aerosol wavelength dependency [*Measures*, 1992a] is used to convert the aerosol extinction computed at the 532 nm wavelength (visible band, VIS) to the rest of the elastic wavelengths (355 and 1064 nm). For the Raman channels' wavelengths, the aerosol extinction is computed as

$$\frac{\alpha_{\lambda}^{aer}}{\alpha_{\lambda_{ref}}^{aer}} = \left(\frac{\lambda_{ref}}{\lambda}\right)^{\kappa}, \tag{2.1}$$

where κ (κ=1 unless otherwise stated) is the Ångström exponent and λ_{ref} is the reference wavelength of 532 nm. Because, in contrast to the molecular component, there is not a theoretical aerosol extinction-to-backscatter ratio, a typical ratio of $S_{355}^{aer} = 25$ sr has been used by interpolation of the visibility look-up table of [*Collis and Russell*, 1976], p.88. In general, the aerosol extinction-to-backscatter ratio (the so-called "lidar ratio") is a major environmental parameter depending on the climatology and seasonal variability of the site and operational wavelength.

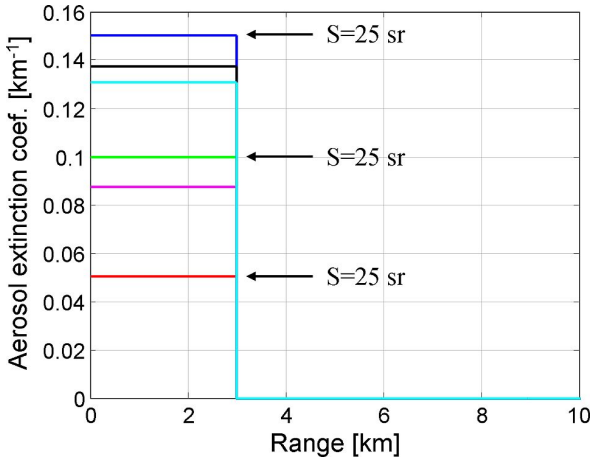

Figure 2.1: Simulated aerosol extinction profiles and related lidar ratios. (Blue) 355-nm wavelength, elastic channel, (Green) 532-nm wavelength, elastic channel, (Red) 1064-nm wavelength, elastic channel, (Magenta) 607-nm wavelength, Raman channel, (Black) 387-nm wavelength, Raman channel, and (Cyan) 407-nm wavelength, water-vapour Raman channel.

2.1.2 Molecular component

The atmospheric molecular component due to Rayleigh scattering is based on the well-known US-standard atmosphere model [*Bodhaine et al.*, 1999], in which "standard air" is defined as dry air at 1013.25 hPa, 15°C (288.15 K) and 360 ppm volume concentration of CO_2. The US-standard atmosphere model uses predetermined pressure and temperature gradients and user-input ground-level temperature/pressure boundary conditions to compute the dry-air molecular number density, $N_{DryAir}(R)$, and the height-dependent refractive index, from all of which the molecular scattering cross section is derived. In the simulations, "standard-air"

ground pressure and temperature conditions have been used. The wavelength dependency of the scattering cross section and, therefore, of the molecular extinction and backscatter parameters is assimilated by a λ^{-4} term according to classic Rayleigh's resonator theory and inclusion of King's factor (also known as F-factor) for fine modelling of the wavelength dependency. The molecular backscatter coefficient is given by

$$\beta_{\lambda}^{mol}(R) = N_{DryAir}(R)\,\frac{d\sigma_{Ray}(\pi,\lambda)}{d\Omega}, \tag{2.2}$$

where $d\sigma_{Ray}(\pi,\lambda)/d\Omega$ [$m^2 sr^{-1}$] is the differential Rayleigh's scattering cross section per solid angle unit in the backward direction and R is the range. The molecular extinction-to-backscatter ratio is the well known $8\pi/3$ Rayleigh's ratio.
Because Raman scattering is just molecular scattering in which the reception wavelength is red-shifted from the incident wavelength, the Raman backscatter profile is based on the same molecular model. Thus, the N_2-/H_2O-Raman backscatter coefficient [$m^{-1} sr^{-1}$] at the return wavelength λ_R is computed as

$$\beta_{\lambda_x}^{mol}(R) = N_X(R)\,\frac{d\sigma_{\lambda_x}(\pi)}{d\Omega}, \tag{2.3}$$

where N_X (X=N_2 for the nitrogen-Raman channel and H_2O for the water-vapour Raman channel) is the range-dependent molecule number density [molecules m^{-3}] and $d\sigma_{\lambda_R}(\pi)/d\Omega$ is the range-independent differential Raman backscatter cross section at λ_R per solid angle unit (23.15×10^{-35} m^2 $molecule^{-1}$ sr^{-1} at 387 nm, 3.71×10^{-35} m^2 $molecule^{-1}$ sr^{-1}at 607.4 nm for nitrogen (N_2), and 61.8×10^{-35} m^2 $molecule^{-1}$ sr^{-1} at 407.5 nm for water vapour) [*Inaba*, 1976]. Recalling that N_2 forms a constant fraction (≈78.084%) of dry air in the lower atmosphere, it follows that $N_{N_2}(R) \approx 0.78084 N_{DryAir}(R)$.

2.1.3 Water-vapour contribution

Water-vapour is a major active green-house gas (for it absorbs terrestrial radiation more strongly than CO_2 does) with large varying concentrations in the atmosphere. In order to assess the 407-nm channel performance a water vapour mixing-ratio profile has been simulated. The relevance of using the mixing ratio in front of the absolute water vapour concentration N_{H_2O} lies on the fact that it remains constant in atmospheric processes that do not involve condensation or evapouration.
The water vapour mixing ratio, $w(z)$ [g/kg] is defined as the ratio of the mass of water vapour to the mass of dry air contained in a certain volume [*Whiteman*, 2003]. This can be expressed as a ratio of concentrations as

$$w(R) = \frac{MW_{H_2O}}{MW_{DryAir}}\frac{N_{H_2O}(R)}{N_{DryAir}(R)} \cong \frac{MW_{H_2O}}{MW_{DryAir}}\frac{N_{H_2O}(R)}{N_{N_2}(R)/0.78} \simeq 0.485\frac{N_{H_2O}(R)}{N_{N_2}(R)}, \tag{2.4}$$

where MW is the molecular weight (MW_{H_2O}∼18 g·mol^{-1}, MW_{DryAir}∼28.94 g·mol^{-1}), N is the molecule number concentration, and we have used that N_2 forms a constant fraction (∼ 0.78) of the dry air in the lower atmosphere.
Alternatively, the water-vapour mixing ratio can be expressed as a ratio of pressures [*Rogers and Yau*, 1989] as

$$w(R) = \frac{MW_{H_2O}}{MW_{DryAir}}\frac{e(R)}{P_{DryAir}(R)} \simeq 0.622\frac{e(R)}{P_{DryAir}(R)}, \tag{2.5}$$

where P_{DryAir} is the Dry-Air pressure, $P_{DryAir} = p(R) - e(R)$, with $p(R)$ the air pressure estimated from radiosonde measurements and e(R) the water-vapour pressure. The relative humidity $RH(R)$ is related to the water vapour pressure $e(R)$ as

$$RH(R) = \frac{e(R)}{e_s(R)}, \tag{2.6}$$

where $e_s(R)$ [hPa] is the saturated water-vapour pressure. Its dependence on temperature, $T(R)$ [°C] can be modelled as ([*Buck*, 1996] modified from [*Buck*, 1981])

$$e_s(R) = 6.1121 \exp\left\{\frac{T(R)\,[18.678 - T(R)/234.5]}{257.14 + T(R)}\right\}. \tag{2.7}$$

By combining Eq.(2.5) and Eq.(2.6), the mixing ratio can be expressed as a function of the water-vapour saturation pressure (equivalently of the temperature), the relative humidity and the dry-air pressure as

$$w(R) = 0.622 \frac{e_s[T(R)]}{P_{DryAir}(R)} RH(R). \tag{2.8}$$

From Eq.(2.4) and with a view to link-budget simulations, the water-vapour molecule number concentration can be expressed as a function of the N_2 molecule number concentration and the mixing ratio as

$$N_{H_2O}(R) = \frac{MW_{DryAir}}{MW_{H_2O}} \frac{N_{N_2}(R)}{0.78} w(R; p, T, RH) \cong 2.06 N_{N_2}(R) w(R; p, T, RH), \tag{2.9}$$

where the mixing ratio dependence with pressure, temperature and relative humidity has been explicitly indicated.

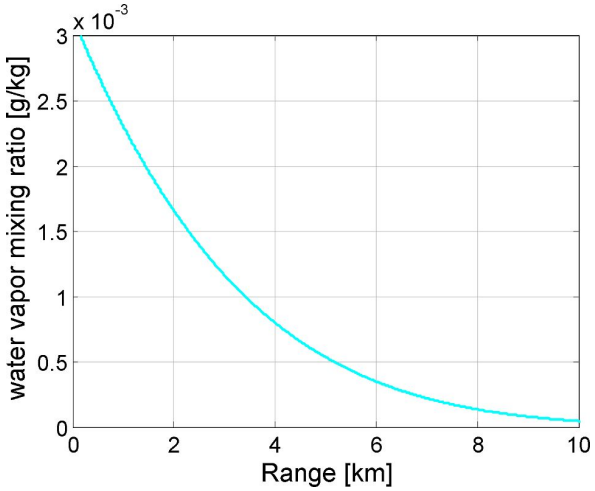

Figure 2.2: Water-vapour mixing ratio following typical values from Figure 3(b) in [*Mattis et al.*, 2002].

Figure 2.2 plots a typical mixing-ratio profile extrapolated from Figure 3(b) in [*Mattis et al.*, 2002] used in the simulations of Section 2.2 to compute the water-vapour molecule number concentration (Eq.(2.9)), $N_{H_2O}(R)$.
Following a similar derivation as in Eqs.(4-12) [*Whiteman*, 2003] the water-vapour and the N_2-Raman backscatter coefficients can also be related to each other. From the definition of

the Raman backscatter coefficient in Eq.(2.3) the water-vapour and the N_2-Raman backscatter coefficients can be related as

$$\frac{\beta_{\lambda_{H_2O}}(R)}{\beta_{\lambda_{N_2}}(R)} = \frac{N_{H_2O}(R)}{N_{N_2}(R)} \cdot \frac{[d\sigma_{H_2O}(\pi)/d\Omega]}{[d\sigma_{N_2}(\pi)/d\Omega]}, \tag{2.10}$$

where $d\sigma_X(\pi)/d\Omega$, X=H_2O, N_2 stands respectively for the water-vapour and nitrogen backscatter cross sections at the Raman return wavelength [*Measures*, 1992a].
By combining Eq.(2.4) and Eq.(2.10) it is apparent that

$$\frac{\beta_{\lambda_{H_2O}}(R)}{\beta_{\lambda_{N_2}}(R)} = \frac{w(R)}{0.485} \cdot \frac{d\sigma_{H_2O}(\pi)/d\Omega}{d\sigma_{N_2}(\pi)/d\Omega}. \tag{2.11}$$

In Eq.(2.11) it has been assumed temperature independence of the H_2O- and N_2-Raman cross sections in relation to the lidar system's optical transmission efficiency (Eq.(3) in [*Whiteman*, 2003]).
In the practical measurements, because the absolute concentration of the water-vapour species can be performed by comparing the Raman backscattered intensity with that of the nitrogen Raman return the system calibration factor is defined as

$$k^* = 0.485 \frac{OVF_{\lambda_{N_2}}(R)}{OVF_{\lambda_{H_2O}}(R)} \cdot \frac{d\sigma_{N_2}(\pi)/d\Omega}{d\sigma_{H_2O}(\pi)/d\Omega}. \tag{2.12}$$

2.1.4 Visibility Margin

The concept of total (aerosol plus molecular) atmospheric extinction and backscatter coefficients is addressed here under the assumption of oversimplified homogeneous conditions. The factors α (extinction or attenuation coefficient) and β (volume backscatter coefficient) determine the lidar signal strength in the lidar equation. The visibility margin approach

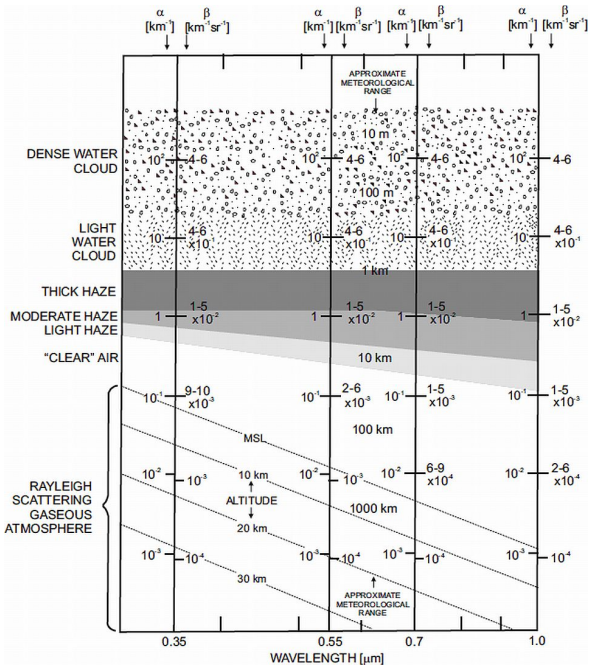

Figure 2.3: Estimated extinction, backscatter and visibility margin variation with atmospheric condition used in the link-budget study. Source: Figure 4.8 in [*Collis and Russell*, 1976].

can conveniently be used to obtain lidar performance estimates under various meteorological conditions. However, the visibility margin term is defined under non-turbid atmospheric conditions. That is, one which is free of aerosol particles. Then, the total attenuation of laser radiation is defined by its molecular extinction. The Koshmeider's relation [*Koshmieder*, 1924] connects the meteorological visibility V_M with the extinction coefficient (Section 2.1.1). It is usually given for the wavelength of 0.55μm (maximum sensitivity of the human eye). [*Kruse et al.*, 1963] gave a more general relation as a function of the wavelength λ

$$\overline{\alpha_\lambda} = \frac{3.912}{V_M}\left(\frac{550}{\lambda}\right)^q \;;\; q = \begin{cases} 0.585V_M^{1/3} & V_M \leq 6km \\ 1.3 & otherwise \end{cases} . \tag{2.13}$$

The case $q = 1.3$ represents average seeing conditions. Expected mean extinction, backscatter and visibility margins are shown decadically spaced in Figure 2.3 where Eq.(2.13) could be applied to quite turbid atmospheres such as dense water clouds.

2.2 ASSESSMENT OF SYSTEM PERFORMANCE

2.2.1 Return power levels

Elastic channels

The elastic lidar equation (single-scattering, no-absorption assumption) is defined as [*Collis and Russell*, 1976]

$$P_{\lambda_0}(R) = \frac{K}{R^2}\left[\beta_{\lambda_0}^{aer}(R) + \beta_{\lambda_0}^{mol}(R)\right]\exp\left\{-2\int_0^R\left[\alpha_{\lambda_0}^{aer}(r) + \alpha_{\lambda_0}^{mol}(r)\right]dr\right\} OVF_{\lambda_0}(R), \tag{2.14}$$

where $P(R)$ is the range-dependent power [W], $\beta(R)$ is the atmospheric volume backscatter coefficient [$m^{-1}sr^{-1}$], $\alpha(R)$ is the range-dependent extinction coefficient [m^{-1}], superindexes "aer" and "mol" stand respectively for "aerosol" and "molecular" components, λ_0 is elastic-channel wavelength, R is the range [m], and K [Wm^3] is the system constant expressed as

$$K = \frac{Ec}{2}A_r, \tag{2.15}$$

where E is the transmitted energy [J], c is the light-speed [ms^{-1}], and A_r is the telescope effective receiving area [m^2]. $OVF_{\lambda_0}(R)$ in Eq.(2.14) is the geometrical overlap function expressing the range-dependent cross-over factor between the emitted laser beam and the telescope field of view (unity for coaxial laser-telescope arrangement) discussed in Chapter 3. In Eq.(2.14) the exponential term represents the two-way path total atmospheric transmittance due to molecules and aerosols,

$$T(\lambda_0, R)^2 = \exp\left\{-2\int_0^R\left[\alpha_{\lambda_0}^{aer}(r) + \alpha_{\lambda_0}^{mol}(r)\right]dr\right\}. \tag{2.16}$$

For a vertically-pointing lidar system, as is the case, R can be assimilated to the vertical coordinate, z, however, R is retained here for completeness in the definition of the lidar equation.

Raman channels

In comparison with the elastic-backscatter lidar equation, in which both the optical emission path (i.e., from the laser source to the atmosphere) and return path (i.e., from the atmosphere back to the telescope) were operating at the same wavelength, λ_0, in the Raman case, the emission path operates at λ_0 while the return path operates at the Raman-shifted wavelength, λ_R. This translates into the two-way path Raman transmittance [*Inaba*, 1976],

$$T(\lambda_0, R)T_R(\lambda_R, R); \quad T(\lambda_i, R) = \exp\left\{-\int_0^R \left[\alpha_{\lambda_i}^{aer}(r) + \alpha_{\lambda_i}^{mol}(r)\right] dr\right\} \tag{2.17}$$

with $\lambda_i = \lambda_0, \lambda_R$ instead of the two-way path elastic transmittance of Eq.(2.16). Formally, the Raman lidar equation takes the form

$$P_{\lambda_R}(R) = \frac{K}{R^2}\beta_{\lambda_R}(R)\exp\left\{-\int_0^R \left[\alpha_{\lambda_0}^{mol}(r) + \alpha_{\lambda_0}^{aer}(r) + \alpha_{\lambda_R}^{mol}(r) + \alpha_{\lambda_R}^{aer}(r)\right] dr\right\} OVF_{\lambda_R}(R), \tag{2.18}$$

where atmospheric absorption effects have been neglected. As in Eq.(2.18), $OVF_{\lambda_R}(R)$ represents the geometrical overlap function at λ_R. The Raman backscatter coefficient, $\beta_{\lambda_R}(R)$ is computed following Section 2.1.2.

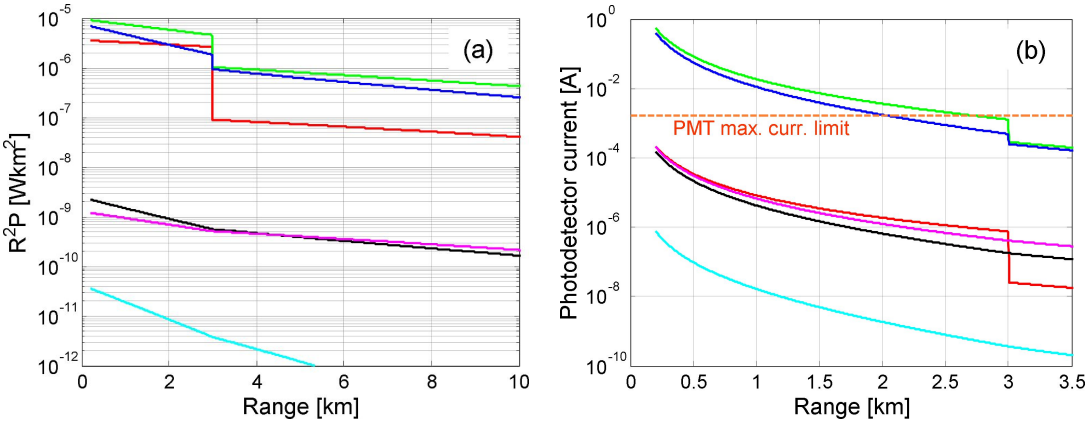

Figure 2.4: Assessed lidar signal levels in return. (a) Range-corrected return power at the telescope aperture. (b) Opto-electronic receiver output for the different channels. The horizontal line indicates the PMT maximum current limit (1.6 mA for 0.1% linearity). This made essential the use of neutral density filters in 532 and 355 nm channels to avoid saturation effects. Day-time operation assumed for the elastic channels, night-time operation assumed for the Raman ones. The step in the elastic channels corresponds to the boundary layer end (see Figure 2.1). (Traces and colors same as in Figure 2.1).

Figure 2.4a simulates the range-corrected power return signals incident on the telescope at the elastic and Raman wavelengths according to Eq.(2.14) and Eq.(2.18), respectively. The simulation range is up to 10 km. In practice, because of the large dynamic range of the lidar signals spanning some 5 orders of magnitude in both channels, simultaneous analog and photon-counting recorded data is glued according to the procedure described in [*Licel*, 2007a; *Donovan et al.*, 1993]. For the elastic channels 532 and 355 nm, it is envisaged inclusion of neutral density filters to attenuate the return power levels to levels slightly higher/comparable to those of the Raman channels (Figure 2.4a), otherwise the input light levels drive PMT detectors into deep saturation (Figure 2.4b). The 1.6-mA current rating for 0.1% photodetector linearity in the case of PMT 7400U follows [*Licel*, 2007a]. The studies of

[*Bristow*, 1998] and [*Kokhanenko et al.*, 2002] give further insight on optimum dynode chain polarisation.

Channel transmissivity

The channel transmissivity ($0 \leq \xi_{net}(\lambda) \leq 1$) is defined as the product of the individual subsystem transmission factors (i.e., the inverse of the optical losses) along the optical receiving chain. Formally,

$$\xi_{net}(\lambda) = \xi_t(\lambda) \cdot \xi_b(\lambda) \cdot \xi_{poly}(\lambda), \tag{2.19}$$

where $\xi_t(\lambda)$ is the telescope transmission, $\xi_b(\lambda)$ is the fiber-bundle transmission and $\xi_{poly}(\lambda)$ is the polychromator transmission for the channel at wavelength λ. The elastic/Raman channel transmissivities according to Eq.(2.19) are listed in Table 2.1 along with the channel voltage responsivity (or net voltage responsivity),

$$R'_v(\lambda) = R_i(\lambda)\, G_T \xi_{net}(\lambda), \tag{2.20}$$

defined as the product of the current responsivity of the detector, R_i [A/W], times the transimpedance gain G_T ($G_T = R_{in} = 50\Omega$, i.e., the input impedance of the transient recorder) and times the channel transmissivity, $\xi_{net}(\lambda)$.

Background power

The sky background radiance also contributes a power level given by

$$P_{back}(\lambda) = L_{back} \Delta\Omega \Delta\lambda \xi_{net}(\lambda), \tag{2.21}$$

where $\xi_{net}(\lambda)$ is the channel transmissivity (i.e., in the telescope-to-photodetector optical receiving path, Eq.(2.19)), L_{back} [$\mathrm{Wcm^{-2}nm^{-1}sr^{-1}}$] is the background spectral radiance, $\Delta\Omega$ [sr] is the solid angle of the telescope equal to $\pi \sin^2(FOV)$ with FOV the receiving optics field of view, and $\Delta\lambda$ [nm] is the FWHM of the optical pass-band interference filter of the receiving channel.

The power levels obtained in Eqs.(2.14) and (2.18) are transduced into voltage levels at the input of the acquisition units via the net voltage responsivities of each lidar receiving channel. Likewise, the background power, P_{back} is transduced into an offset voltage, which along with other unwanted components, must be corrected (a Rayleigh fit is usually used).

2.2.2 Signal-to-Noise Ratio

SNR formulation for the elastic and Raman channels depends upon the detection mode used in the acquisition unit (Section 2.2). Though in practice a mixed analog/photon-counting (PC) acquisition mode is used (data glued by software) in what follows the elastic channel (high return light-levels) is assumed to be acquired in analog mode and the Raman channel (low retun light-levels) in PC mode. In this oversimplification the SNR are formulated disregarding dynamic range and dead-time limitations.

SNR detection modes

I. Analog-detection mode.- The SNR under analog-detection mode can be expressed as (adapted from [*Rocadenbosch et al.*, 1998])

$$SNR_a(R) = \frac{R'_v P(R)}{\sqrt{N_{sh,s}(R) + N_{sh,b} + N_{sh,d} + N_{th}}}, \tag{2.22}$$

where R'_v [VW^{-1}] is the net voltage responsivity (Eq.(2.20)), $P\,(R)$ [W] is the range-dependent return power at the telescope input (Eqs.(2.14,2.18), Figure 2.4a), and N_x [V^2] is the noise power. Subindexes $x =$ "sh, s", "sh, b", "sh, d", "th" stand for lidar "signal-induced" shot noise, "background-induced" shot noise, "dark" shot noise, and "thermal" (Johnson) noise. For convenience, the noise power, $N_x = \sigma_x^2 B_N$ [V^2], is expressed as the product of the noise spectral density, σ_x^2 [$V^2 Hz^{-1}$] times the reception-channel noise-equivalent bandwidth, B_N [Hz]. The noise spectral densities are computed as

$$\sigma^2_{sh,s}\,(R) = 2qG_T^2 FM^2 R_{io} P(R) \xi_{net}(\lambda), \tag{2.23}$$

$$\sigma^2_{sh,b} = 2qG_T^2 FM^2 R_{io} P_{back} \xi_{net}(\lambda), \tag{2.24}$$

$$\sigma^2_{sh,d} = 2qG_T^2 \left(I_{ds} + FM^2 I_{db}\right), \tag{2.25}$$

and

$$\sigma^2_{th} = \sigma^2_{th,i} G_T^2, \tag{2.26}$$

where $P\,(R)$ and P_{back} are respectively the lidar signal (Eqs.(2.14) and (2.18)) and background-received (Eq.(2.21)) powers, q is the electron charge, F is the detector excess-noise factor, I_{ds} and I_{db} are, respectively, the surface and volume dark currents of the detector ($I_{ds} = 0$ for a PMT, $I_{db} = I_d/M$ from Table. 2.1), and $\sigma^2_{th,i}$ [V^2 Hz^{-1}] is the thermal noise of the acquisition unit, (all other variables defined in Eq.(2.20)). σ^2_{th} is directly $\sigma^2_{th} = 4kTR_{in}$ with k the Boltzmann's constant, $T = 300K$ the noise equivalent temperature, and $R_{in} = 50\Omega$ the input impedance of the transient recorder.

II. Photon-counting detection mode.- In photon-counting mode, pulse height fluctuations (photon pile-up) can be reduced by setting a discriminator level on the pulse height, therefore allowing a significant improvement in the SNR. Besides, thermal noise can be ignored by setting a PMT gain sufficiently high, so that the discriminator level source can be easily set higher than amplifier noise level [*Hamamatsu*, 1998]. In the following SNR model, the effect of the discriminator level on the SNR is neglected so that the model gives a conservative lower bound on the expected SNR. The SNR expression under photon-counting detection (Raman channel) takes the form [*Hamamatsu*, 1998]

$$SNR_{pc} = \frac{N'_s}{\sqrt{N'_s + 2(N'_b + N'_d)}}, \tag{2.27}$$

where N'_s is the (mean) number of counts per second due to the lidar return signal, N'_b is the (mean) number of counts per second due to the background light, and N'_d is the (mean) number of counts per second due to the PMT dark current. The factor 2 in the denominator accounts for the fact that N'_s is calculated by subtracting to the total number of counts per second ($N'_s + N'_b + N'_d$), the background and dark component ($N'_b + N'_d$), which results in double variance contribution from the ($N'_b + N'_d$) term. In Eq.(2.27) it is easy matter to relate the mean number of counts per second to power concept in units of [W] as introduced

in Section 2.2.2 via $N'_s = P_{\lambda_R}(R)\,\xi_{net}(\lambda_R)\,R_{io}/q$.

Noise-limited SNR modes

The approach of noise-dominant sources is well known from [*Measures*, 1992a] and is adapted here for the analog formulation of the SNR, $SNR_a(R)$. The results can easily be extrapolated to the photon-counting-mode SNR. By rewriting Eq.(2.22) and introducing Eqs.(2.23-2.26) it is straightforward to obtain

$$SNR_a(R) = \frac{P(R)}{\left\{\frac{2qI_{ds}}{R_{io}^2\xi_{net}^2(\lambda)}\frac{B_N}{M^2} + \frac{2qB_N}{R_{io}^2\xi_{net}^2(\lambda)}F\left(I_{db} + R_{io}\xi_{net}(\lambda)\left[P(R)+P_{back}\right]\right) + \frac{\sigma_{th}^2 B_N}{R_{io}^2M^2G_T^2\xi_{net}^2(\lambda)}\right\}^{\frac{1}{2}}}. \tag{2.28}$$

Eq.(2.28) above yields four limiting situations:
The first regime or signal-shot noise-limited mode occurs when noise due to the primary photocurrent becomes dominant. Then Eq.(2.28) tends to

$$SNR_a(R) \to \left[\frac{R_{io}\xi_{net}(\lambda)}{2qB_NF}\right]^{\frac{1}{2}} P(R)^{\frac{1}{2}}. \tag{2.29}$$

In this case, the highest sensitivity is achieved since detectable signal is limited only by the quantum fluctuation of the signal itself. Note that SNR depends on the optical power as $P(R)^{1/2}$ rather than as $P(R)$ and hence SNR degrades slowly. The second noise limited regime usually arises in daytime operation. On some occasions, the level of background radiation can be so high that P_{back} is much higher than the lidar return. Under these circumstances one speaks of the background noise-limited mode. Eq.(2.28) reduces to

$$SNR_a(R) \to \left[\frac{R_{io}\xi_{net}(\lambda)}{2qB_NF}\right]^{\frac{1}{2}} P_{back}^{\frac{1}{2}}, \tag{2.30}$$

and it is evident that the receiving optics transmission function, $\xi_{net}(\lambda)$ and its bandwidth $\Delta\lambda$ (Eq.(2.21)) play an important role in assessment of the minimum detectable power.
The third case corresponds to the dark-current limited mode. Assuming a photodiode gain $M \geq 10$, the surface dark current becomes less than 1% of its bulk counterpart. This leads to an asymptotic SNR given by

$$SNR_a(R) \to \left[\frac{R_{io}^2\xi_{net}^2(\lambda)}{2qB_NFI_{db}}\right]^{\frac{1}{2}} P(R), \tag{2.31}$$

Otherwise, a more complicated expression depending on both I_{ds} and I_{db} is obtained without further signifying results.
Finally, the fourth case corresponds to the thermal noise limited mode,

$$SNR_a(R) \to \left[\frac{R_i\xi_{net}(\lambda)}{\sigma_{th,i}\sqrt{B_N}}\right] P(R). \tag{2.32}$$

Figure 2.5 plots the assessed SNR versus range according to Eq.(2.22) (analog mode/elastic channels) and Eq.(2.27) (photon counting mode/Raman channels). Elastic SNRs have been computed under day-time operation (L_{back}=3.0·10^{-6} Wcm^{-2}nm^{-1}sr^{-1}) and Raman SNRs under night-time operation (L_{back}=3.0·10^{-11} Wcm^{-2}nm^{-1}sr^{-1}) in order not to blind the Raman channel. Under these conditions the elastic channels at 355-, 532-, and 1064-nm wavelengths operate in signal-induced shot-limited regime from the starting sounding range

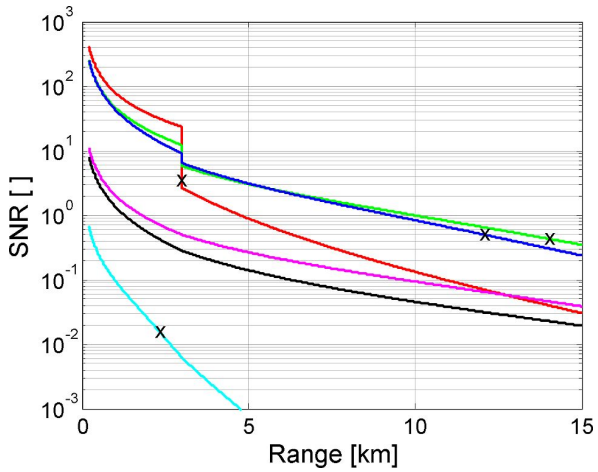

Figure 2.5: Estimated signal-to-noise ratio for the lidar channels. Crosses indicate the ending range where photo-induced signal-shot noise is no longer dominant. Day-time operation assumed for the elastic channels, night-time operation assumed for the Raman ones. (Traces and colors are same as in Figure 2.1).

until 12, 14, and 3 km respectively. From these threshold ranges onwards the 1064-nm channel operates in thermal-limited regime, and 355- and 532-nm channels in background-limited mode. This justifies why cooling the APD detector is so important for the 1064-nm channel. When analyzing the Raman channels (night-time operation), the behaviour of the 387- and 607-nm channels is signal-shot limited over the whole simulation range and until 2.4 km for the 407-nm channel from where it becomes dark-shot limited. In all cases, the threshold range is indicated with a cross in Figure 2.5. Figure 2.6 shows the noise variance components for the different channels.

Noise Equivalent Power (NEP)

The channel NEP (also called "system NEP" [W·Hz$^{-1/2}$] is defined in *analog detection mode* and departs from the well-known concept of noise expressed in power units [W] (i.e., referred to the telescope input) [*Measures*, 1992b; *Hamamatsu*, 1998] but assimilating both detector dark-noise and thermal-noise contributions in the receiving channel. Formally,

$$NEP_s = \frac{\left(\sigma^2_{sh,d} + \sigma^2_{th}\right)^{1/2}}{R'_v}, \tag{2.33}$$

where $\sigma^2_{sh,d}$ and σ^2_{th} (both in units of [V^2·Hz^{-1}]) are, respectively, the detector dark-shot noise and the thermal-noise standard deviations defined in Eqs.(2.25, 2.26), respectively. R'_v[VW^{-1}] is the net voltage responsivity defined in Eq.(2.20).
In photon-counting detection mode, the thermal-noise component can be ignored by setting a discriminator level higher than the thermal-noise level. In this mode, the detection limit is usually defined as the input light level corresponding to $SNR_{pc} = 1$. From Eq.(2.27), this limit can be approximated by $N'_s = \sqrt{2N'_d}$ [*Hamamatsu*, 1998] (assumption of negligible background noise, $N'_b << N'_d$) with an error of less than about 30%.

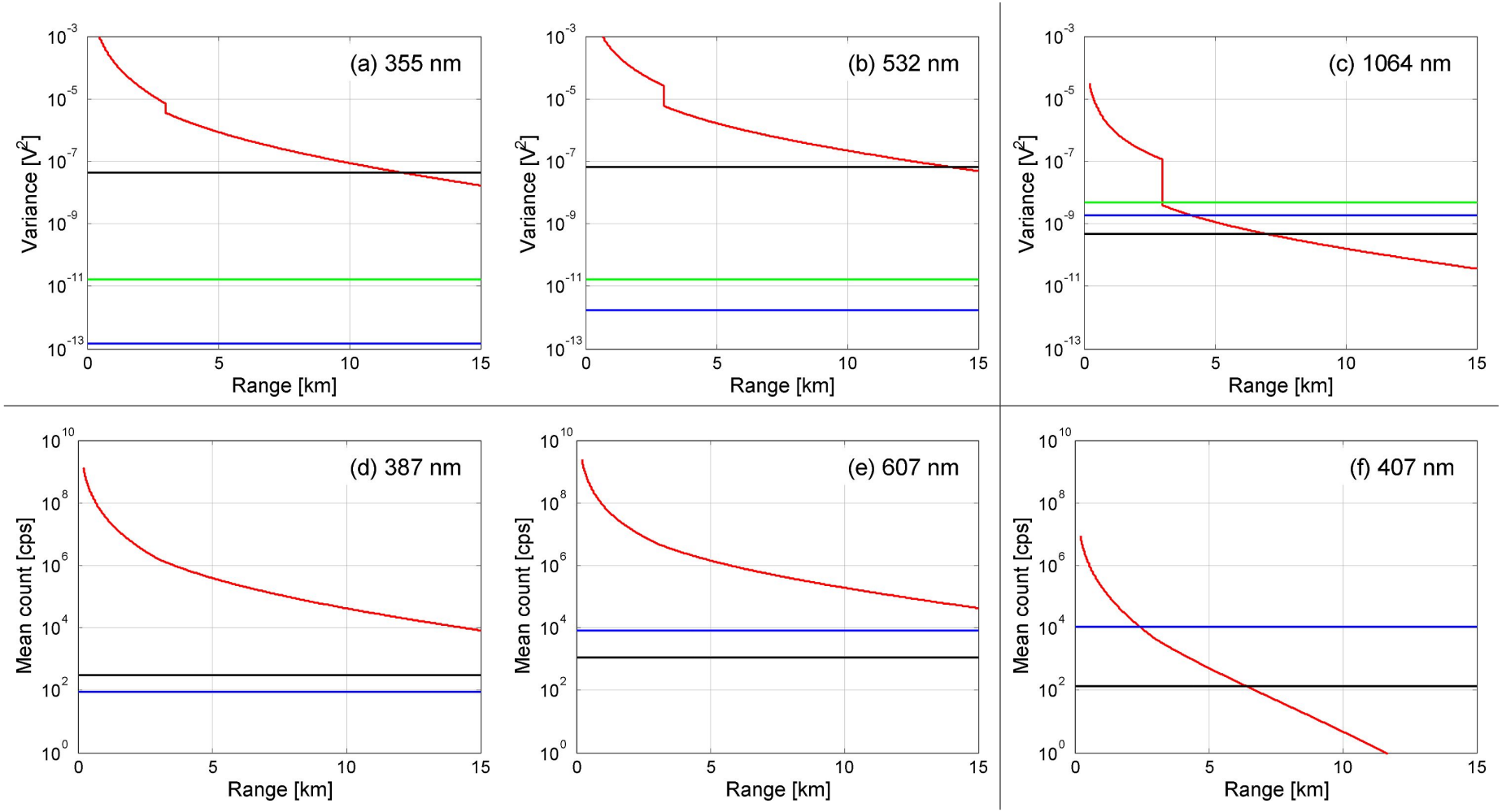

Figure 2.6: Noise variances. (a)-(c) Elastic channels, (d)-(f) Raman channels. (a) 355 nm. (b) 532 nm. (c) 1064 nm. (d) 387 nm. (e) 607 nm. (f) 407 nm. Day-time operation assumed for the elastic channels, night-time operation assumed for the Raman ones. (Red) signal-shot noise, (Black) background-shot noise, (Blue) dark-shot noise, and (Green) thermal noise.

2.2.3 Observation Time vs. Maximum System Range

A convenient way to assess system performance is to estimate the maximum lidar range (under some predefined SNR goal criterion, SNR_{goal}) at each channel wavelength as a function of the required observation time. The SNR goal criterion is not unique for it ultimately depends on the specific optical-parameter inversion algorithm chosen and on the data-product inversion uncertainties acceptable from the user's side. Following the error assessment of Figures 7-8 in [*Rocadenbosch et al.*, 1998], a SNR_{goal} in the 1-10 range is reasonable. For example, it is shown that under relatively clear atmospheric conditions (total homogeneous extinction, α_{tot}=0.1 km^{-1}) the criteria $SNR_{goal} = 1$ and $SNR_{goal} = 10$ yield, respectively, 8% and 0.2% errors in the inverted optical atmospheric extinction when using an exponential-fitting inversion method. For a very clear atmosphere (α_{tot}=0.01 km^{-1}), $SNR_{goal} = 1$ and $SNR_{goal} = 10$ yield 70% and 2% errors, respectively. A conservative figure of $SNR_{goal} = 10$ is set in what follows as in previous studies from the author [*Kumar et al.*, 2006].

The maximum system range expresses the range where the lidar return voltage signal is SNR_{goal} times the noise-voltage standard deviation at the receiver output, that is, $SNR_v\,(R_{\max}) = SNR_{goal}$ in Eq. 2.34 (analog detection), or equivalently, $SNR_{pc}\,(R_{\max}) = SNR_{goal}$ in Eq. 2.34 (photon-counting detection).

The observation time, t_{obs}, arises from the number of time-averaged lidar pulses (temporal integration) required to achieve the SNR_{goal}. Since the SNR expressions in Eqs.(2.22,2.27) are defined on a "single-pulse" basis (i.e., in response to a single laser pulse emitted) accounting for temporal pulse integration implies a SNR improvement equal to the square root of the number of integrated pulses, n_i [*Barlow*, 1989b]. Therefore, the maximum system range condition for an observation time t_{obs} (corresponding to n_i integrated pulses) is formulated as

$$SNR_X(R_{\max})\sqrt{n_i} = SNR_{goal}, \tag{2.34}$$

where subindices X = "*a*" *and* "*pc*" stand for "analog" detection (Eq.(2.22)) and "photon-counting" detection modes (Eq.(2.27)), respectively. Using that $n_i = PRF \cdot t_{obs}$ with PRF the pulse repetition frequency of the laser source,

$$SNR_X(R_{\max}) = \frac{SNR_{goal}}{\sqrt{PRF \cdot t_{obs}}}. \tag{2.35}$$

Eq.(2.35) is an implicit relationship that given an observation time, t_{obs}, and Eqs.(2.22,2.27) enable to solve the maximum range, $R_{\max}$, associated to that t_{obs}. As a result, a point $(t_{obs}, R_{\max})$ of the locus "observation time – maximum range" is obtained.

The assessed $R_{\max}$ vs. observation time for all system channels is plotted in Figure 2.7 for the "very clear" atmospheric condition defined in Section 2.1, a vertically pointing lidar (so that "range" corresponds to "height") and under both day-time and night-time conditions separately. As expected, the maximum system range for the elastic channels does not virtually degrade when changing from night-time to day-time operation. However, this is not the case for the Raman channels. Thus, with an observation time of 30 min (1800 s), the maximum range at 387 and 607 nm reduces from 9.20 and 13.24 km (night-time operation) to 2.84 and 3.47 km (day-time operation), respectively. Under night-time operation a maximum sounding range of R_{max}=10 km is reached with approximately 5 s observation time for the elastic channels at 355 and 532 nm (PMT based) and about 280 s (4.7 min) for the elastic channel at 1064 nm (APD based). In the case of the aerosol Raman channels, reaching R_{max}=10 km approximately requires 2400 s (40 min) for the 387-nm channel and 580 s (9.7 min) for the 607-nm channel. Finally, in the case of the water-vapour Raman

channel "typical" times are more difficult to be assessed because of the high variability of the water-vapour concentration in the atmosphere. However, for the simulated mixing-ratio decay profile of Figure 2.2, a 30-min to 1-h observation time yields R_{max} between 1-2 km. Henceforth, Figure 2.8 shows the performance of all the channels in the usual operating conditions (day-time for the elastic channels and night-time for the Raman channels).

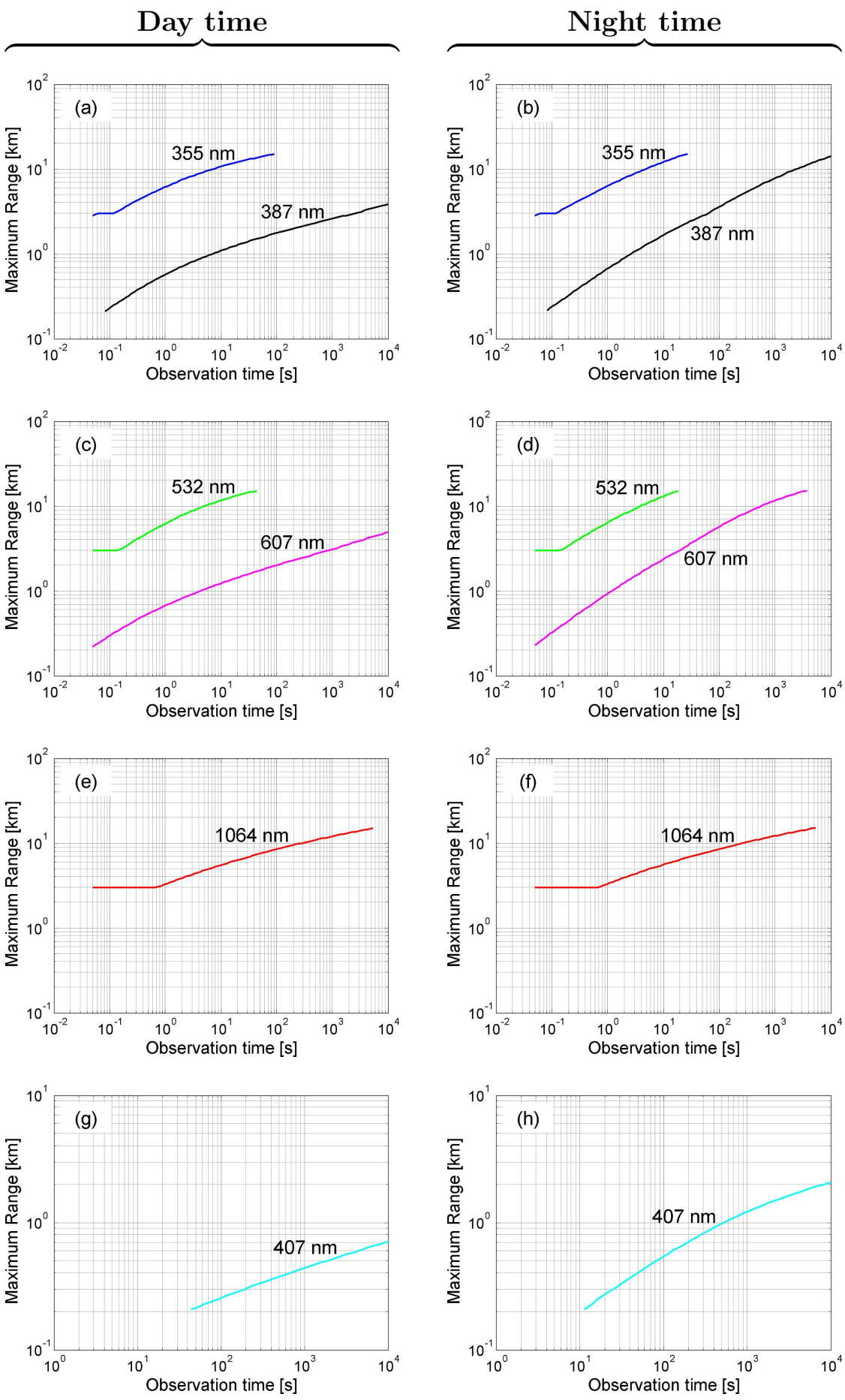

Figure 2.7: Estimated maximum system range vs. observation time. (a)-(b), (c)-(d), (e)-(f) and (g)-(h) represent (day-time)-(night-time) performance pairs for (355, 387), (532, 607), 1064 and 407nm wavelengths respectively. (Traces and colors are same as in Figure 2.1).

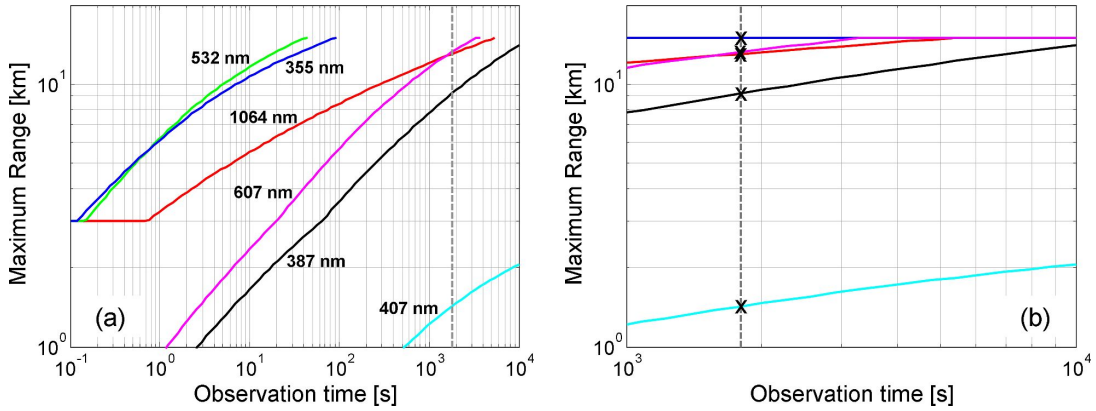

Figure 2.8: Estimated maximum system range vs. observation time. SNR_{goal}=10. (a) Estimated maximum system range versus observation time. The constant behaviour in elastic channels (e.g. 1064-nm channel (0 to 0.7 s)) is due to the step-like transient at the end of the boundary layer (3 km). (b) Detail of (a) for an observation time between 10^3-10^4 s. Crosses correspond to a typical observation time of 30 min (15 km for 532 and 355 nm, 13.24 km for 607 nm, 9.2 km for 387 nm, 13.04 km for 1064 nm and 1.4 km for 407 nm). Maximum range criterion is $SNR(R_{max})$=10. R_{max}=15 km or the maximum simulation range. Day-time operation assumed for the elastic channels, night-time operation assumed for the Raman ones. (Traces and colors are same as in Figure 2.1).

EMITTER						
Laser	Model / Type Wavelengths, λ Energy per pulse, E Repetition Rate, PRF pulse duration, τ_d	Quantel Brilliant T64 / Nd:YAG Q-Switched 1064 / 532 / 355nm 130 / 130 / 40mJ 20Hz 3.6ns				
RECEIVER						
Telescope	Model / Geometry Primary / shadow diameter Focal length, f	Celestron CGE 1400 / Schmidt-Cassegrain 0.36m / 0.12m 3.91m				
Fiber Bundle	Numerical aperture, NA Area diameter Estimated transmission, $\xi_b(\lambda)$	0.12 3mm 50 %				
Polychromator	*Ad hoc* design					
Photodetectors	Elastic channel (1064 nm) Rest of channels Active area diameter	APD (Perkin-Elmer) PMT (Hamamatsu) APD (3mm) / PMT (8mm)				
Channel Acquisition	Model Type	Licel transient recorder TR40-80 Mixed 250MHz PC + ADC 40Msps/12bit				
CHANNEL SPECIFICATIONS						
Wavelength, λ [nm]	1064	532.1	354.7	386.7	607.4	407.5
Type	Elastic			Raman 355/N_2	532/N_2	355/H_2O
Spatial resolution [m]	3.75					
Telescope transmissivity (%), $\xi_t(\lambda)$	35.6	81.3	41.6	48.6	78.6	56.5
Polychromator transmissivity (%), $\xi_{poly}(\lambda)$	42.08	20.4	29.7	27.94	46.65	20.37
End-to-end transmissivity (%), $\xi_{net}(\lambda)$	7.49	8.29	6.18	6.79	18.33	5.76
Spectral Bandwidth, $\Delta\lambda$ [nm]	1	1	1	1	1	1
Detector type	**APD**	**PMT**				
Detector model	C30956E	R7400P-03	R7400U-03	R7400U-03	R7400U-20	R7400U-20
Noise equivalent bandwidth, B_N [MHz]	10	20	20	20	20	20
Internal Gain, M	100	10^6	$7{\cdot}10^5$	$7{\cdot}10^5$	$5{\cdot}10^5$	$5{\cdot}10^5$
Noise Factor, F	4	1.3	1.3	1.3	1.3	1.3
Dark current, I_d [nA] (25ºC)	89.2	0.08 (anode)	0.01 (anode)	0.01 (anode)	0.64 (anode)	0.86 (anode)
Current Responsivity, $R_i(\lambda)$ [AW^{-1}]	34	$3.0{\cdot}10^4$	$3.8{\cdot}10^4$	$4.2{\cdot}10^4$	$3.9{\cdot}10^4$	$1.5{\cdot}10^4$
Voltage Responsivity, $R_v(\lambda)$ [VW^{-1}]	$3.7{\cdot}10^5$	$1.5{\cdot}10^6$	$1.9{\cdot}10^6$	$2.1{\cdot}10^6$	$2.0{\cdot}10^6$	$7.5{\cdot}10^5$
Net Voltage Responsivity, $R_v'(\lambda)$ [VW^{-1}]	$2.8{\cdot}10^4$	$1.2{\cdot}10^5$	$1.2{\cdot}10^5$	$1.4{\cdot}10^5$	$3.6{\cdot}10^5$	$4.3{\cdot}10^4$
Detector NEP [$fW{\cdot}Hz^{-1/2}$]	36.6	0.192	0.0444	0.0407	0.296	0.892
Channel NEP [$fW{\cdot}Hz^{-1/2}$]	925	7.7	7.7	6.4	3.0	26.2

Table 2.1: 3+3 channel RSLAB multispectral lidar system specifications.

Chapter 3

OVERLAP FACTOR AND IT'S ENHANCEMENT

The problem of overlap factor (OVF) computation and its near-range sensitivity for medium-size aperture (f/10, f/11) bi-axial tropospheric lidar systems using ray-tracing simulation software is presented. The method revisits both detector and fiber-optics coupling alternatives at the telescope focal-plane along with the insertion of a field lens. A sensitivity analysis is carried out as a function of laser divergence, field-lens and detector/fiber positions, and fiber's numerical aperture.
The ray-tracing approach presented here is straightforward and a comparatively much simpler solution than analytical-based methods. Parametric simulations are carried out to show that both approaches are coincident. Insertion of a field-lens proves to be an elegant and low sensitivity solution for OVF enhancement particularly, in the near-range of the lidar.

3.1 INTRODUCTION

Aerosols have appreciable influence on the Earth's radiation budget, air quality and visibility, clouds, precipitation, and chemical processes in the troposphere and stratosphere. In ground based tropospheric lidar remote sensing, the range at which atmospheric aerosols can be measured is determined, at the near end, by the *range of full overlap (R_{ovf})* between the laser beam and the telescope's field of view and, at the far end, by the range associated to the lowest detectable signal-to-noise ratio (SNR), usually SNR=1-10. The starting range of full overlap, R_{ovf}, is a key design parameter in an aerosol lidar system as it determines the minimum sounding range in the atmospheric boundary layer (ABL). Even though the combination of one elastic and one Raman lidar channel enables to experimentally invert the OVF function [*Wandinger and Ansmann*, 2002] below the R_{ovf}, OVF-corrected data becomes progressively noisier and noisier or must simply be disregarded.
Many experimental [*Wandinger and Ansmann*, 2002; *Sasano et al.*, 1979; *Hu et al.*, 2005] and analytical [*Stelmaszczyk et al.*, 2005; *Halldórsson and Langerholc*, 1978; *Harms*, 1979; *Sassen and Dodd*, 1982; *Jenness et al.*, 1997; *Chourdakis et al.*, 2002; *Comerón et al.*, 2011; *Measures*, 1984] approaches have been proposed in the past. Experimental methods cannot be applied at the design stage and analytical methods either suffer from large over-simplifying model assumptions, which limit their applicability to practical laser-telescope configurations, or from a complex, however, exact mathematical formulation. Thus, [*Measures*, 1984] assumes a uniform distribution for the emitted laser power and the OVF is simply computed as the intercept area between the illuminated atmospheric cross-section (i.e., the circle defined by the divergence of the laser beam at the target plane) and the telescope field-of-view circle at

the target plane. More refined approaches, particularly, that of Halldórsson and Langerholc [*Halldórsson and Langerholc*, 1978] consider a TEM_{00} Gaussian illumination in emission, inclusion of the telescope secondary obstruction, and the defocusing effects at the detector plane caused by near-range illuminated atmospheric cross sections [*Stelmaszczyk et al.*, 2005; *Halldórsson and Langerholc*, 1978; *Harms*, 1979; *Sassen and Dodd*, 1982].

The OVF in fiber-optics coupled lidar systems has been analyzed in [*Jenness et al.*, 1997; *Chourdakis et al.*, 2002; *Comerón et al.*, 2011]. Among them, the mathematical study of Comerón et. al. [*Comerón et al.*, 2011] from the RSLab extends Halldórsson and Langerholc's work [*Halldórsson and Langerholc*, 1978] to the general case of lidar systems using a fiber optics and a field lens in the telescope focal plane. With such a field-lens/fiber-optics combination the OVF is enhanced in three respects: first, the range of full overlap, R_{ovf}, becomes much lower; second, the rising edge of the overlap function is sharper; and third, the asymptotic value of the overlap function for a well-designed lidar system is also closer to unity. Yet, exact computation of the overlap function (OVF) involves a cumbersome integral computation of the area intercept among three limiting circles in the telescope focal plane: 1) the circular surface of the field lens, 2) the circle of confusion (image of a radiating point at a range R in the target plane), and 3) the numerical-aperture (NA) limiting circle of the fiber.

Alternatively to experimental and analytical OVF approaches, precise OVF determination can be carried out by using standard ray-tracing simulation tools [*Berezhnyy*, 2009]. In this approach, the laser source is modeled as a ray-emitting surface with a TEM_{00} intensity distribution. Matrix ray tracing [*Möller*, 2007b] is used to model atmospheric propagation and the receiving optical system. Since the atmosphere is assumed lossless and non-turbulent (i.e., atmospheric propagation reduces just to a pure translation) the main difficulty lies in modeling the ray distribution in the emission source and the receiving optical system. The OVF is computed as the ratio of the total number of rays reaching the detector surface (image plane) to the total number of rays entering the telescope aperture. Sensitivity analyses of the key OVF geometrical parameters and coincident results with the analytical methods are two additional advantages.

In this paper, the overlap factor has been parameterized as a function of (i) the geometry of f/10 and f/11 Schmidt-Cassegrain telescopes (i.e., f/D=10 and f/D=11, where f is the focal length and D is the diameter of the telescope aperture), (ii) distance between the laser and telescope axes, (iii) laser divergence, and (iv) detector/fiber specifications [*Freudenthaler*, 2006]. Insertion of a field lens for both detector- and fiber-optics based systems is considered. f/10 and f/11 numbers are common place in a large number of tropospheric elastic/Raman lidar sensing stations within the European Aerosol Research LIdar Network (EARLINET) [*Bösenberg and Matthias*, 2003; *EARLINET*].

This paper is organized as follows: Section 3.2 conceptually reviews the OVF from a ray-tracing perspective. Section 3.3 describes the ray-source and receiving-system optical models. Section 3.4 presents the OVF sensitivity analysis for f/10 and f/11 lidar systems (detector and fiber coupled) and cross-examines them with the analytical methods of Halldórsson and Langerholc [*Halldórsson and Langerholc*, 1978] and Comerón et. al. [*Comerón et al.*, 2011]. Emphasis is given to the case in which a field lens is inserted in the focal plane. Finally, Section 3.5 gives concluding remarks.

3.2 RAY-TRACING FUNDAMENTALS FOR OVF CALCULATION

3.2.1 Lidar return signal at the telescope focal plane

Figure 3.1 illustrates a simplified ray-tracing model for a biaxial monostatic lidar system.

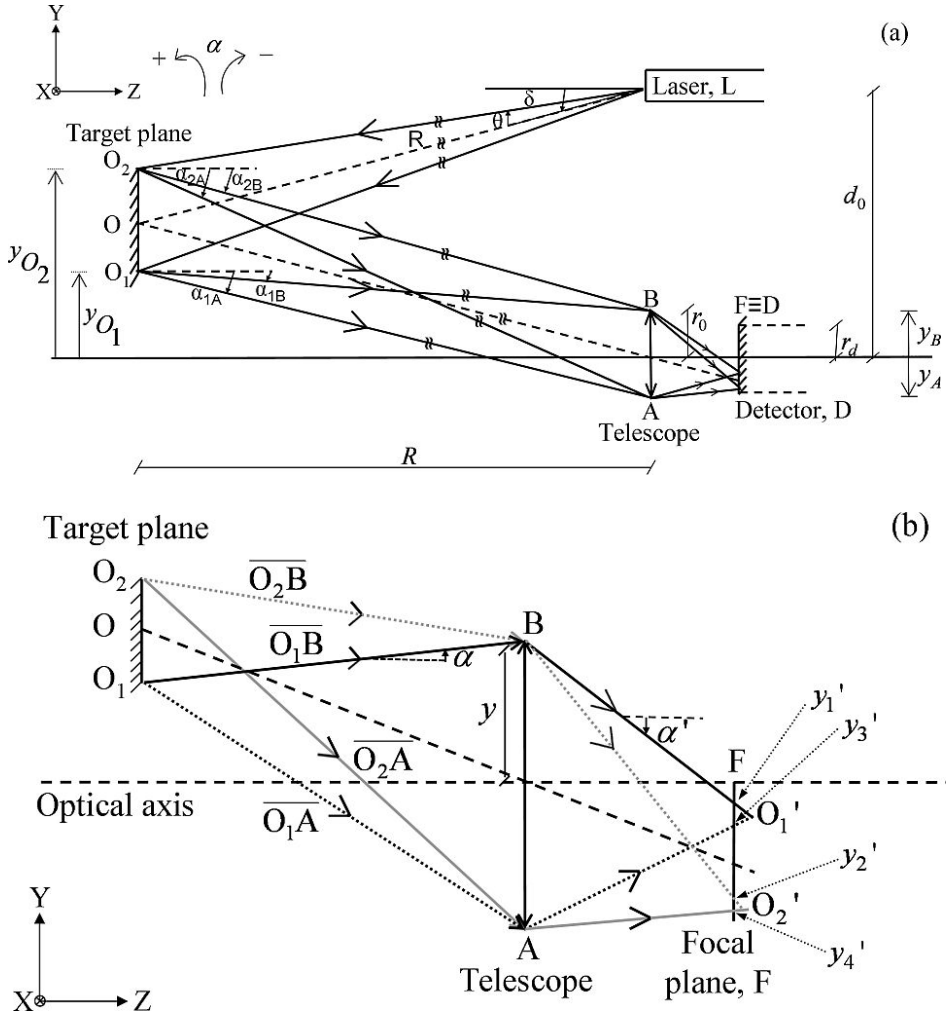

Figure 3.1: Simplified ray-tracing diagram for a biaxial monostatic lidar. (a) General view. In emission, L represents the laser, θ is the laser divergence (half angle). In reception, $\overline{\mathrm{AB}}$ represents a telescope, r_0 is the telescope radius, and F is the telescope focal plane coincident with the detector plane, D. Others: $\overline{\mathrm{O_1O_2}}$ is a fictitious mirror representing an atmospheric target plane at a distance R from the lidar, d_0 is the laser-to-telescope axial separation, and δ is the laser-to-telescope tilting angle. (b) Detail of (a). The image of the atmospheric cross section $\overline{\mathrm{O_1O_2}}$ gives rise to a confusion circle at the telescope focal plane, F. $\mathrm{O_1'}$ and $\mathrm{O_2'}$ are the image points of $\mathrm{O_1}$ and $\mathrm{O_2}$. y_1'-y_4' respectively represent the ordinates of rays $\overline{\mathrm{O_1B}}$, $\overline{\mathrm{O_2B}}$, $\overline{\mathrm{O_1A}}$ and $\overline{\mathrm{O_2A}}$ at the focal plane (primes denote 'image plane').

The image of the atmospheric cross-section $\overline{\mathrm{O_1O_2}}$ at the focal plane, F can be studied from four principal rays, $\overline{\mathrm{O_1A}}$, $\overline{\mathrm{O_1B}}$, $\overline{\mathrm{O_2A}}$, and $\overline{\mathrm{O_2B}}$ and standard matrix-ray calculus [*Möller*, 2007b]. If y is the ray ordinate from the telescope optical axis and α is the inclination angle

(positive angles counter-clock wise) we have that (Figure 3.1a)

$$\begin{cases} y_{O_1} = d_0 - (\delta + \theta)R \\ y_{O_2} = d_0 - (\delta - \theta)R \end{cases} \tag{3.1}$$

and the angles associated to principal rays $\overline{\mathrm{O_2B}}$, $\overline{\mathrm{O_2A}}$, $\overline{\mathrm{O_1B}}$ and $\overline{\mathrm{O_1A}}$ become

$$\begin{cases} \alpha_{2B} = -\frac{y_{O_2} - y_B}{R} = -\left[\frac{d_0 - r_0}{R} - (\delta - \theta)\right] \\ \alpha_{2A} = -\frac{y_{O_2} - y_A}{R} = -\left[\frac{d_0 + r_0}{R} - (\delta - \theta)\right] \\ \alpha_{1B} = -\frac{y_{O_1} - y_B}{R} = -\left[\frac{d_0 - r_0}{R} - (\delta + \theta)\right] \\ \alpha_{1A} = -\frac{y_{O_1} - y_A}{R} = -\left[\frac{d_0 + r_0}{R} - (\delta + \theta)\right] \end{cases} . \tag{3.2}$$

With reference to Figure 3.1b an incident ray from the left of telescope lens $\overline{\mathrm{AB}}$ with parameters $I = (y, \alpha)$ translates into final ray parameters, $I' = (y', \alpha')$, at the focal plane. In matrix form,

$$\begin{cases} I' = T_2 L_1 I \\ L_1 = \begin{pmatrix} 1 & 0 \\ -\frac{1}{f} & 1 \end{pmatrix}, \; T_2 = \begin{pmatrix} 1 & f \\ 0 & 1 \end{pmatrix} \end{cases} , \tag{3.3}$$

where L_1 is the thin-lens matrix and T_2 is the translation matrix for a travelling distance equal to the telescope focal length, f. From Eq.(3.3),

$$\begin{cases} y' = f\alpha \\ \alpha' = -\frac{y}{f} + \alpha \end{cases} . \tag{3.4}$$

The image of $\overline{\mathrm{O_1O_2}}$ at the focal plane, $\overline{\mathrm{O_1'O_2'}}$ is determined by outer rays, $\overline{\mathrm{O_1B}}$ and $\overline{\mathrm{O_2A}}$, which are imaged at a height $y' = f\alpha$ with $\alpha = \alpha_{1B}, \alpha_{2A}$ (Figure 3.1a,3.1b), that is, $y_1' = f\alpha_{1B}$ and $y_4' = f\alpha_{2A}$. Therefore, and by substituting Eq.(3.2) into Eq.(3.5), the size of the image spot (a circle) at the focal plane becomes

$$D_S = \left|y_1' - y_4'\right| = f\left|\alpha_{1B} - \alpha_{2A}\right| = 2f\left|\frac{r_0}{R} + \theta\right| \tag{3.5}$$

and the distance from its center to the optical axis,

$$y_1'\big|_{\theta=0, r_0=0} = y_4'\big|_{\theta=0, r_0=0} = -f\left(\frac{d_0}{R} - \delta\right). \tag{3.6}$$

In Figure 3.1 it is worth noting that the image of a point (e.g., $\mathrm{O_1}$) at a distance R from the telescope is a confusion circle at the focal plane with diameter

$$D_{CC} = f\left|\alpha_{1B} - \alpha_{1A}\right| = 2f\left|\frac{r_0}{R}\right|. \tag{3.7}$$

When Eq.(3.7) is compared with Eq.(3.5) it emerges that the incremental size, $2f\theta$ in Eq.(3.5) is due to the laser divergence. This is represented in Figure 3.2.

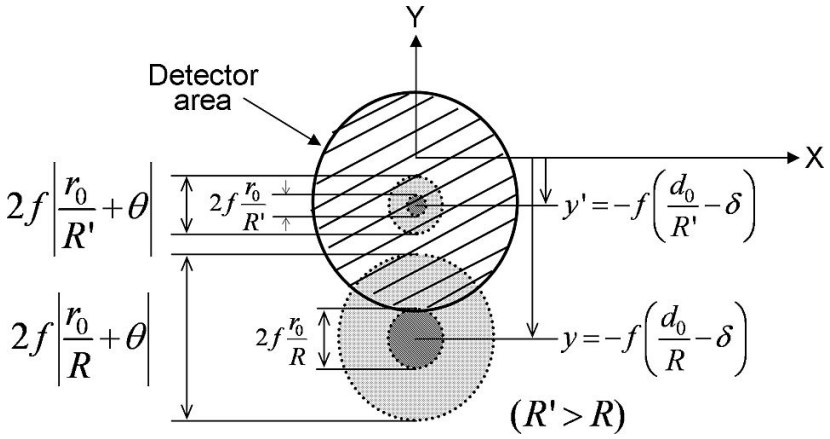

Figure 3.2: Image of the atmospheric cross section $\overline{O_1O_2}$ at the focal plane of the telescope (XY plane, label F in Figure 3.1). (Dark-grey circles) Circles of confusion associated to the atmospheric target point O (Figure 3.1a) for distances $R' > R$ and laser divergence, $\theta = 0$. (Light-grey circles) Circles of confusion associated to the atmospheric cross section $\overline{O_1O_2}$ (Figure 3.1a) for $R' > R$ and laser divergence, θ. (Circle with stripped lines) Detector area. y and y' are the ordinates of the center of the circles from the telescope optical axis.

Assuming the oversimplification of uniform energy distribution, the OVF can be determined for each range R as the *overlap area* between the detector area and that of the circle of confusion at the focal plane. Thus, in Figure 3.2, the case of an atmospheric cross section $\overline{O_1O_2}$ located at a range R from the lidar would give rise to an incomplete overlap area between the detector and the confusion circle ($OVF < 1$) and R would correspond to a range between ranges R_1 and R_2 ($R_1<R<R_2$, Figure 3.3). In contrast, for the case of an atmospheric cross section $\overline{O_1O_2}$ located at R' there is full overlap between these areas ($OVF = 1$) and R' would correspond to a range ($R_2<R'<R_3$).
In a biaxial lidar system with a misaligned laser beam crossing the telescope FOV (Figure 3.3a) the plot of the OVF versus range has four characteristic points (R_1-R_4) while for a well-aligned system two of the points (R_3 and R_4) move to infinity (Figure 3.3b). R_2 is the starting range of full overlap (i.e., $OVF(R_2) = 1$) and noted so far R_{ovf} in what follows. The condition to ensure full overlap (Figure 3.3b) is given by

$$-(\phi - \theta) \leq \delta \leq \phi - \theta, \phi > \theta. \tag{3.8}$$

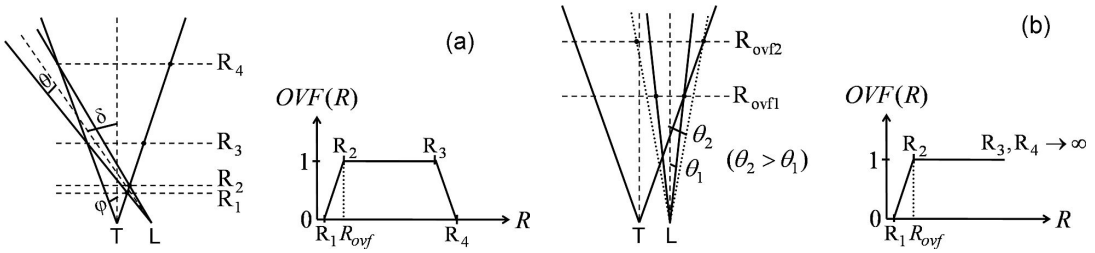

Figure 3.3: Graphical interpretation of the overlap factor for a biaxial lidar system (simplification of uniform laser irradiance at the target plane). (a) Case of a misaligned lidar system. (b) Case of a well-aligned system, Eq.(3.8).

The intercept points R_1-R_4 can be determined from the angles of arrival of the four critical rays $\overline{O_1B}$, $\overline{O_2B}$, $\overline{O_1A}$ and $\overline{O_2A}$ (Figure 3.1b), respectively, by imposing that these

angles of arrival (Eq.(3.2)) equal the FOV of the telescope, ϕ. Using that the FOV of a telescope with a detector placed in its focus is given by $\phi = \frac{r_d}{f}$, where r_d is the detector radius and f is the telescope focal length, the intercept points are computed as

$$|\alpha_{1B}(R_1)| = \phi \ ; \ |\alpha_{2B}(R_2)| = \phi \ ; \ |\alpha_{1A}(R_3)| = \phi; \ |\alpha_{2A}(R_4)| = \phi. \tag{3.9}$$

Eqs.(3.8)-(3.9) are in agreement with the classic treatment of [*Measures*, 1984].

3.2.2 Enhancement of the overlap factor: Insertion of a field-lens

In ground based tropospheric lidar systems it is important to enhance the OVF by keeping the starting range of full overlap, R_{ovf}, as close as possible to the lidar. For example, this enables monitoring of the lowest part of the atmospheric boundary layer. A classical way to achieve this is the insertion of a field lens [*Möller*, 2007b] in the telescope focal plane, F_1. The detector or fiber optics is placed at the field-lens focal plane, F_2, or very close to it (Figure 3.4).

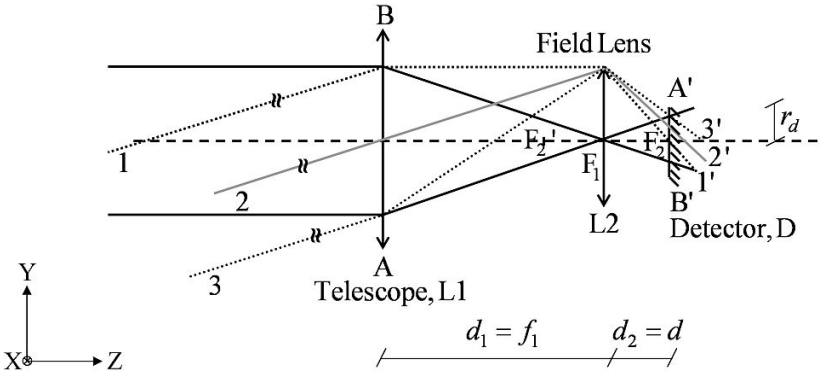

Figure 3.4: Insertion of a field lens in the telescope focal plane. L1 is the telescope objective lens, L2 is the field lens at the telescope focal plane (F_1), D is the detector/fiber end, and F_2 and F_2' respectively represent the field-lens object and image focii. $\overline{A'B'}$ represents the image of the telescope aperture $\overline{AB}$ on the detector/fiber surface.

The idea behind this approach is to have on the detector area an image of the telescope aperture smaller than the detector area itself. In other words, to ensure that the entrance pupil of the receiving optics is only limited by the telescope aperture and not by the detector area.
To formulate that, let us depart from the well-known thin-lens equation [*Möller*, 2007b],

$$-\frac{1}{x_o} + \frac{1}{x_i} = \frac{1}{f}, \tag{3.10}$$

where x_o and x_i respectively represent the object and image distances from the field lens and f is the focal length. The following conditions must hold [*Comerón et al.*, 2011]:

1. the field-lens images the telescope entrance aperture ($\overline{AB}$ in Figure 3.4) onto the detector/fiber end. Using that, $x_o = -f_1$ and $x_i = d$ in Eq.(3.10) it follows

$$\frac{1}{f_1} + \frac{1}{d} = \frac{1}{f_2}, \tag{3.11}$$

where f_1 is the telescope focal length, f_2 is the field-lens focal length, and d is the field-lens-to-detector distance. Because in practice $f_1 >> f_2$ (e.g. Table 3.1), $d \simeq f_2$ so that the detector/fiber is at the field-lens focal plane.

2. the projected image is smaller than the detector/fiber. We use the thin-lens image magnification, $m = \frac{y_i}{y_o} = \frac{x_i}{x_o}$, where y_o and y_i are the object and image heights respectively, and x_o and x_i the object and image distances to the lens, respectively. With $y_o = r_o$, $x_i = d$ and $x_o = -f_1$, imposing $|y_i| \leq r_d$ (Figure 3.4) leads to

$$r_o \frac{d}{f_1} \leq r_d. \tag{3.12}$$

Eqs.(3.11)-(3.12) above are the field-lens design equations with d and f_2 as solving parameters. A further benefit of the inclusion of a field lens is that the image spot onto the detector/fiber is larger than without a field-lens, thus averaging out uneven spatial responsivity effects over the detector area [*Simeonov et al.*, 1999]. This is illustrated in Figure 3.4 by parallel incident rays 1, 2, 3 spreading over the detector as rays $1'$, $2'$, $3'$.

Following [*Comerón et al.*, 2011], when a field lens and detector combination is used, the OVF can be computed following [*Halldórsson and Langerholc*, 1978] and by taking the field-lens edge as the field stop. This is because photodetectors usually have a NA equal to 1, hence not limiting the angle of arrival of the rays emerging from the field lens. In contrast, when a fiber optics is placed at (or close to) the field lens focal plane (F_2 in Figure 3.4) instead of a detector, the NA of the fiber is responsible for an additional limitation on the maximum angle of arrival of rays. The mathematical treatment of this case is given by Eq.(13) in the same reference.

3.3 RAY TRACING MODEL FOR OVF COMPUTATION

The target cross-section $\overline{O_1O_2}$ at the target range R from the lidar (Figure 3.1) is modelled as a bi-dimensional source of rays following a normalised Gaussian distribution,

$$p(x,y) = \frac{1}{2\pi} e^{\frac{-(x^2+y^2)}{2}}, \quad x, y \in (-\infty, \infty), \tag{3.13}$$

where (x,y) are local cartesian co-ordinates in the disk. In what follows this source of rays will simply be addressed as the "test disk" (Figure 3.5). When a population of N rays is considered, p(x,y) represents the percentage of rays emitted from a point Q(x, y) on the disk. Following Figure 3.5 the rays associated to the point Q(x, y) are emitted following a uniform angular distribution over a hemisphere. In the simulation it is not necessary to simulate rays for each point Q(x, y) over a hemisphere just over the solid angle, $\Delta\Omega$, under which the telescope is seen from the range R. The intensity distribution on the telescope aperture contributed by each radiating point of the disk continues to be uniform. However, the superposition of all emitted rays from the test disk gives rise to a Gaussian distribution on the aperture because of the weighting function, p(x, y). The R. Knoop polar version [*Press et al.*, 2007] of the Box-Muller transformation [*Box and Muller*, 1958] is used to generate the bi-dimensional Gaussian deviates according to Eq.(3.13) above from two independent uniform random distributions.
As mentioned in Section 3.2, the OVF at each range R can be interpreted as the ratio

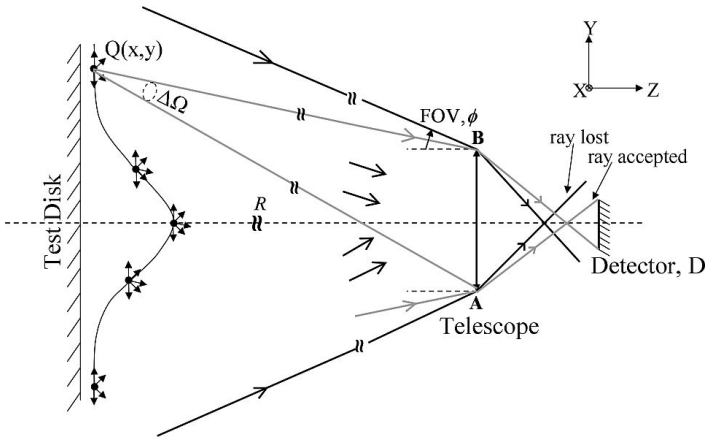

Figure 3.5: Determination of the OVF using a Gaussian test disk. The test disk is located at the target range R. $\overline{\mathrm{AB}}$ represents the telescope aperture lens, ϕ is the field of view and D is the detector.

of energy transferred to the detector/fiber, E_{det}, to the energy incident on the telescope aperture, E_{in}. Equivalently, as the ratio of the number of rays reaching the detector area to the number of rays reaching the telescope aperture (entrance pupil),

$$OVF(R) = \frac{E_{\mathrm{det}}(R)}{E_{in}(R)}. \tag{3.14}$$

In the case of fiber-coupled systems, E_{det} represents the number of rays being accepted by the NA of fiber.
Complete f/10 and f/11 Schmidt-Cassegrain models have been simulated in Zemax$^{\mathrm{TM}}$ [$ZEMAX$] so as to model the key optical parts of the telescope (Table 3.1). In the simulation, Zemax$^{\mathrm{TM}}$ ray tracing software is used so that each ray is monitored from the starting random point on the test disk to the last receiving surface (detector/fiber) and passing through the different telescope optical parts (the citation of software trademarks or manufacturers does not constitute any endorsement or preferential treatment by the authors or by the project funding entities).

3.4 CASE STUDIES

3.4.1 OVF enhancement: f/10- vs. f/11- telescope, detector-coupled lidar systems

The following case studies illustrate a migration example from a low-aperture (f/10, 200-mm telescope) detector-coupled elastic lidar to a medium-aperture (f/11, 356-mm telescope) fiber-coupled multi-spectral elastic/Raman lidar at the RSLab (Table 3.1). While in an elastic lidar the return radiation is not wavelength shifted from the emission one so is in a Raman system. Typical Raman return levels are 3 to 4 orders of magnitude lower than elastic ones, which motivates large reception apertures.

3.4.1.1 Insertion of a field lens

Discussion results are presented next for a simulation wavelength of 532 nm using the ray-tracing model described in Section 3.3. The f/10 lidar system is always detector coupled

while for the f/11 system both detector- and fiber-coupled options are examined.

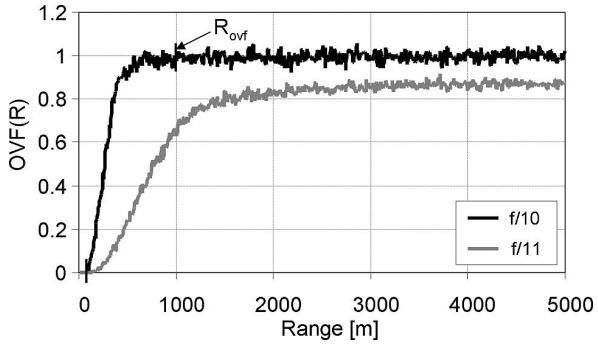

Figure 3.6: Simulated OVF for f/10 and f/11 telescopes (Table 3.1). R_{ovf} corresponds to the starting range of full overlap (Figure 3.3). For the f/11 case, R_{ovf} is beyond the simulation range ($R_{ovf} > 5$km).

Figure 3.6 compares the OVF of f/10 and f/11 detector-coupled lidar systems. Because the FOV of the f/11 telescope is approximately half as much that of the f/10 telescope this results in an *unbearable* large increase of starting range of full overlap, R_{ovf}. Two possible solutions to overcome this problem are: (i) usage of a larger detector or (ii) inclusion of a *field lens* imaging the telescope input aperture onto the detector surface (Section 3.2.2). When these solutions are simulated in Figure 3.7 it emerges that even when the detector size is doubled, solution (i) is poorer than that using a field-lens with the same detector size (solution (ii)). The latter being a more efficient and economic solution.

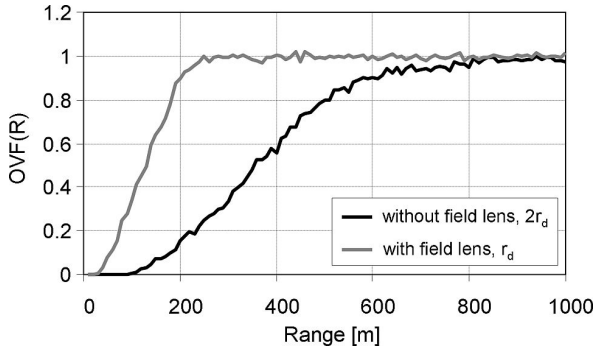

Figure 3.7: OVFs for the f/11 telescope for the cases (i) doubling the detector size (without field lens) and (ii) inserting a field-lens. See Table 3.1 for simulation parameters.

3.4.1.2 Sensitivity analysis (f/11 telescope)

Sensitivity to laser divergence.- For a well-aligned lidar system (Eq.(3.8) in the oversimplified case of Section 3.2.1), the starting range of full overlap, R_{ovf} increases as so does the laser divergence (Figure 3.3b). Figure 3.8 shows a sensitivity analysis as a function of the laser divergence carried out for the f/11 telescope lidar system. It is seen that insertion of the field lens not only lowers the range of full overlap but also makes the system almost *insensitive* to the simulated ranges of laser divergence (0.1 to $\sim$ 1 mrad). The reduction in the starting range of full overlap in presence of the field lens is $\sim$ 80% for θ=0.1 mrad and $\sim$ 90% for θ=0.5 mrad. In absence of the field lens, R_{ovf} is beyond the maximum simulation range when θ is in the 0.5-0.9-mrad interval.

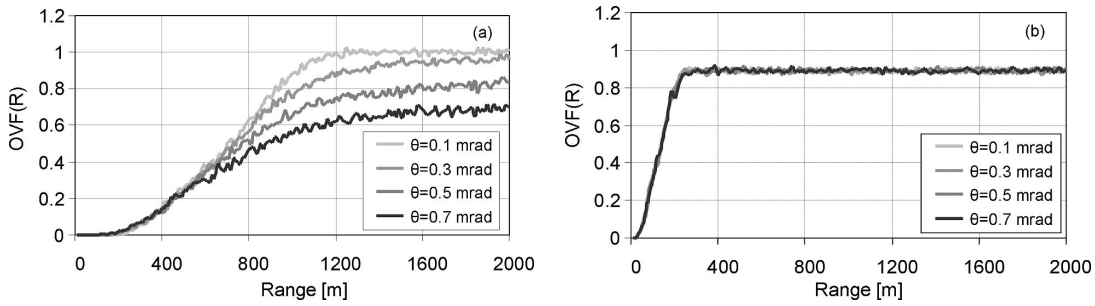

Figure 3.8: OVF sensitivity to laser divergence. (a) Without field lens. (b) With field lens.

Sensitivity to field-lens and detector positions.- Figure 3.9 shows the OVF when slightly varying the field-lens and detector nominal positions in the optical axis ($d_1 = f_1$, $d_2 = f_2$, Figure 3.4), that is, field-lens at the telescope focal plane and detector at the field-lens focal plane. It is seen that when the field lens position varies ($\Delta d_1 \approx \pm 1.5 \times 10^{-2} f_1$, approximately ± 60 mm, note that $f_1 >> f_2$) with respect to the telescope focal plane and the detector is kept fixed at the lens focal plane ($d_2 = f_2$) the OVF is virtually unaffected (R_{ovf} varies less than 1%, Figure 3.9a). In contrast, the OVF changes significantly when the lens-to-detector distance varies (Δd_2) while keeping the lens position fixed at the telescope focal plane ($d_1 = f_1$, $d_2 = d$, Figure 3.9b). This gives rise to the possibility of optimising the detector position to enhance the OVF in the near range (i.e., to lower the R_{ovf}). It is seen that the lowest R_{ovf} is achieved by placing the detector slightly off-focus and closer to the field-lens ($\Delta d_2 \simeq -8, -12\%$). For closer positions the starting range of full overlap increases again and hence moves out of the minimum achieved.

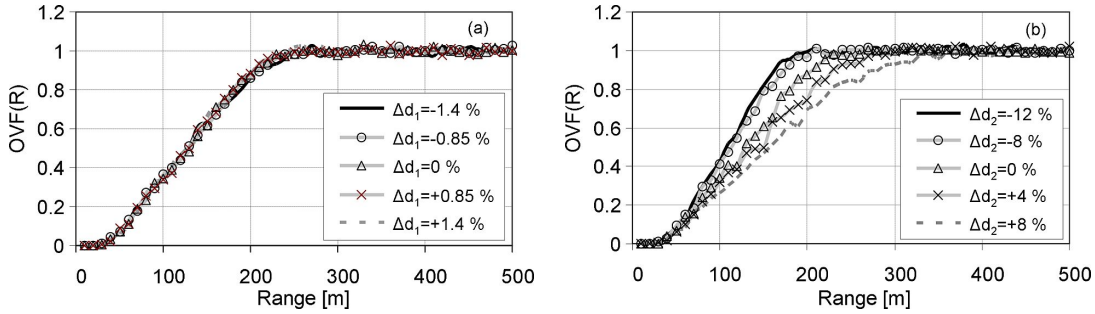

Figure 3.9: OVF sensitivity to field-lens and detector positions (refer to Figure 3.4). (a) Parameterisation as a function of the percent deviation from the nominal field-lens position (percentages shown are times the telescope focal length, f_1). (b) As a function of the nominal lens-to-detector distance (percentages shown are times the field-lens focal length, f_2).

3.4.2 Fiber-coupled lidar system (f/11-telescope)

The presence of a fiber optics instead of a detector at the field-lens focal plane (F_2 in Figure 3.4) imposes an additional and more stringent angular acceptance constraint due to the NA of the fiber, which causes the overlap factor to significantly change in the near-range. For optimum capture of the backscattered radiation the NA of the fiber should be compatible with the field-lens aperture ratio or f-number ($(f\#)_2 = f_2/D_2$, where f_2 is the field-lens diameter and D_2 the focal length). The optimum match of the fiber's NA to the field-lens

f-number requires [*Jenness et al.*, 1997]

$$NA = \left\{ 4\left[(f\#)_2\right]^2 + 1 \right\}^{-\frac{1}{2}}. \tag{3.15}$$

This assumes that the field-lends edge acts as the field stop receiving optical system, as is the practical case.
Figure 3.10 shows the simulated OVF for such a fiber-coupled lidar system. In the detector plane, a 3-mm core-diameter fiber is used. The R_{ovf} *increases* significantly when *reducing* the NA (Figure 3.10b) while it is *insensitive* to the NA of the fiber in absence of the field lens (Figure 3.10a). The latter case becomes evident because the NA of the fiber is much greater than that of the telescope.

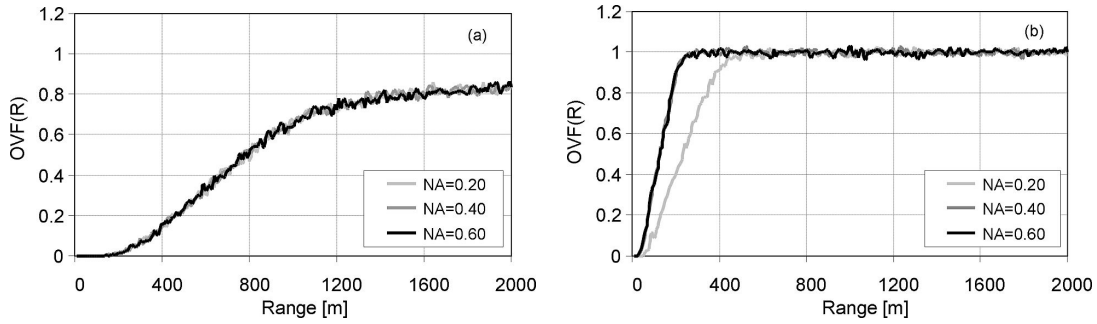

Figure 3.10: OVF sensitivity to fiber's numerical aperture (NA). (a) Without field lens. (b) With field lens.

When the simulations of Figure 3.9 are repeated here for the fiber-coupled case, similar results are reencountered. Thus, the OVF is virtually insensitive to small variations in the field-lens position when maintaining the fiber at the field-lens focal plane (counterpart of Figure 3.9a, figure not shown). The sensitivity of the OVF as a function of the field-lens-to-fiber distance (counterpart of Figure 3.9b) is shown in Figure 3.11 for two different fiber NAs. For $NA \geq 0.45$ (0.45 corresponding to the lowest NA according to Eq.(3.15)) the OVF starts to become sensitive to the field-lens-to-fiber distance as in the detector-coupled case of Figure 3.9b. As expected, for larger NAs (NA=0.60 in Figure 3.11b) the NA fiber is not limiting the angle of arrival of the rays coming from the field lens (Section 3.2.2) and hence the fiber behaves as the "detector-coupled" case of Figure 3.9b.

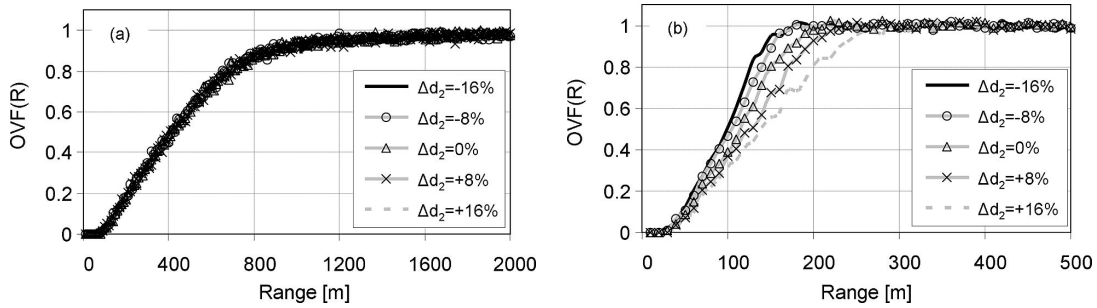

Figure 3.11: OVF sensitivity to fiber's position (refer to Figure 3.4). Parameterisation as a function of the percent deviation from the nominal field-lens-to-fiber distance (percentages shown are times the field-lens focal length, f_2). (a) NA=0.12. (b) NA=0.60.

3.4.3 Comparison with analytical models

In this Section the ray-tracing approach of Section 3.3 for an f/11 telescope is compared to the previously published analytical results of [*Halldórsson and Langerholc*, 1978] (detector at the telescope focal plane) and [*Comerón et al.*, 2011] (fiber at the field-lens focal plane). Figure 3.12 shows that both these analytical models and the ray-tracing model of Section 3.3 assess the same OVF profiles up to $\theta = 0.5$ mrad laser divergence. Because the telescope FOV with the detector at its focal plane is FOV=r_d/f_1=0.38 mrad (Table 3.1) for laser divergences $\theta >>$ FOV ($\theta = 1.0$ mrad and above) ray-tracing results start to largely deviate from the analytical ones. This is justified because the size of the test disk at $\pm 3\sigma$ (equivalently, the illuminated atmospheric cross section) is much bigger than the cross section seen by the telescope and, therefore, the simulation starts to be largely influenced by the number of simulated rays (a much larger population of rays is required). Letting apart this comment, the agreement between the proposed ray-tracing models and the analytical models so far published becomes evident.

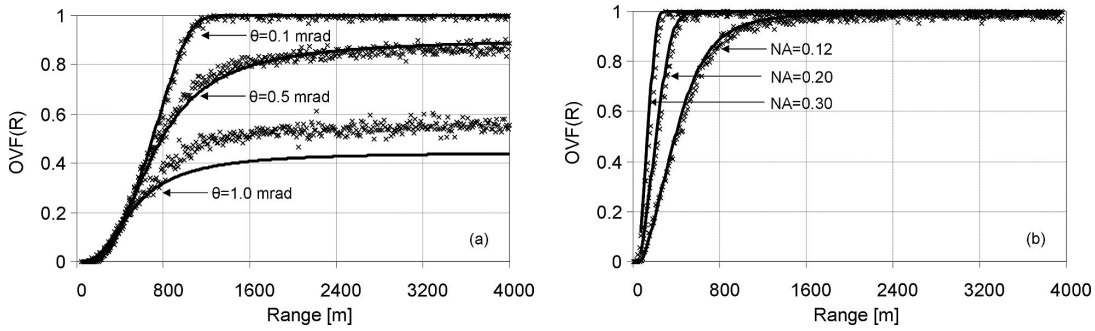

Figure 3.12: Comparison between the OVF assessed by previously published analytical methods and the ray-tracing model of Section 3.3, f/11 lidar system. (a) Analytical method [*Halldórsson and Langerholc*, 1978]. Detector in the telescope focal plane (absence of field lens). θ stands for the laser divergence. (b) Analytical method [*Comerón et al.*, 2011]. Fiber in the field-lens focal plane (θ=0.5 mrad). Solid lines represent the analytical model and crosses the ray-tracing model.

3.5 CONCLUSIONS

A ray-tracing model and sensitivity study for OVF assessment in medium-size aperture (f/10, f/11) bi-axial lidar systems under Gaussian illumination has been presented and validated. Ray-tracing simulations have been presented for detector and fiber-coupled alternatives.
Ray-tracing foundations under the oversimplified case of uniform illumination along with field-lens design equations have been reviewed in Section 3.2. The proposed Gaussian ray-tracing model for OVF computation (Section 3.3) is based on (i) a test disk emitting a Gaussian population of rays with uniform angular distribution over the solid angle under which the telescope is seen from the disk at a range R and (ii) definition of the OVF as the ratio of the number of rays reaching the detector/fiber-core area to the number of rays reaching the telescope aperture (input pupil of the lidar system), Eq.(3.14).
The simulation case studies presented in Section 3.4 have shown that inclusion of a field lens is a necessary requirement for medium-size telescopes (f/11 in the case examples presented), which otherwise require unbearable detector sizes at the telescope focal plane (Figs. 3.6-3.7). The field lens provides a shorter starting range of full overlap (R_{ovf}) and a faster rise of the OVF, thus, widening the near sounding range of the lidar. Besides, because the field lens

images the telescope input aperture onto the detector area, the incident rays on the telescope do not focus on a point on this area but spread over it instead, hence, averaging uneven spatial detector responsivity effects (Figure 3.4). Besides, the system is more insensitive to laser divergence (Figure 3.8). For fiber-coupled systems the NA of the fiber puts an additional constraint to the angle of arrival of rays and design-equation Eq.(3.15) provides the NA lower limit ensuring that incoming rays from the previous optical stage of the fiber (usually the field lens) are accepted by the fiber (Figure 3.10).
The OVF remains virtually unaffected for small variations of the field-lens position while keeping the detector/fiber at the field-lens focal plane (Figure 3.9a, analogous result for the fiber-coupled case). In contrast, the OVF is sensitive to variations in the field-lens-to detector distance while the field lens is kept at the telescope focal plane (Figure 3.9b). This behaviour is analogous for fiber-coupled systems compliant with the design-equation above. As a result, the OVF can be optimised in the near range. For example, for the f/11-telescope detector-coupled lidar system, the lowest R_{ovf} has been achieved by placing the detector off focus and closer to the field lens ($\Delta d_2 \approx -10\% f_2$, Figure 3.9b) and similarly for the fiber-coupled case ($\Delta d_2 = -16\% f_2$, Figure 3.11b).
Finally, the Gaussian ray-tracing model for OVF assessment has successfully been validated against previously published analytical integral methods (Section 3.4.3) and proved to be a straightforward alternative.

Telescope parameters	**f/10**	**f/11**
Primary aperture diameter, $2r_0$	200 mm	355.6 mm
Secondary obstruction diameter, $2r_s$	54 mm	114 mm
Focal length, f_1	2000 mm	3910 mm
Field of view, ϕ (half angle)	0.75 mrad	0.385 mrad
f-number, $(f\#)_1$	10	11
Laser-to-telescope axial distance, d_0	180 mm	247.5 mm
Common parameters		
Laser divergence, $\theta = 0.5$ mrad		
Laser tilt angle, $\delta = 0$		
Detector/fiber-core radius, r_d=1.5 mm		
Field-lens focal length, f_2=25.4 mm. f-number, $(f\#)_2 = 1$.		

Table 3.1: Simulation parameters for the f/10- and f/11-telescope based lidar systems presented.

Chapter 4

POLYCHROMATOR DESIGN AND IMPLEMENTATION

This chapter focuses on the design and implementation of the 6-channel dichroic-based polychromator of the new RSLAB multispectral elastic/Raman lidar. Light emission is made at 355-nm (ultraviolet, UV), 532-nm (visible, VIS) and 1064-nm (near infrared, NIR) wavelengths. In reception, the polychromator is the spectral separation unit that splits the laser backscattered composite return into 3 elastic (355, 532, 1064-nm wavelengths) and 3 Raman channels (386.7, 607.4 and 407.5-nm (water-vapor) wavelengths). The polychromator houses photo-multiplier tubes (PMT) for all channels except the NIR one, which is avalanche photodiode (APD) based.
Main polychromator optical design parameters, that is, light collimation trade-offs, end-to-end transmissivity, net channel responsivity, light distribution and spot size onto the active area of the photodetectors are addressed. The polychromator along with the rest of the RSLAB lidar system has successfully been tested in a recent lidar system intercomparison campaign (SPALI10) carried out in Madrid (Spain), Oct. 2010. This chapter is organized as follows: Section 4.1 provides an overview of the polychromator optical and mechanical design, and Section 4.2 focuses on the key design considerations and trade-offs.
The following contents are an adaptation of two proceedings from the author [*Kumar et al.*, 2006] and [*Kumar et al.*, 2011].

4.1 POLYCHROMATOR DESIGN OVERVIEW

The polychromator is the spectrally selective unit which separates the backscattered composite light return into the various wavelengths of interest. The RSLAB polychromator is dichroic based, features 1-inch optics and has been designed for 3 elastic (355, 532, 1064nm) and 3 Raman (386.7, 607.4 and 407.5nm (water-vapour) channels. The receiving optics front-end is formed by five photomultiplier tubes (PMT) and one avalanche photodiode (APD) based receivers. Three PMTs are used for the three Raman channels (386.7 and 607.4nm atmospheric N2-Raman shifts, and 407.5nm water-vapour Raman shift). The other two PMTs are for the 354.7 and 532.1nm elastic channels. All PMT and APD (1064nm)-based channels are simultaneously recorded in analog and photon-counting modes by means of an array of 6 mixed analog/photon counting Licel® transient recorders (Table 2.1). A fiber bundle is used to convey the composite lidar return from the telescope focal plane to the input of the polychromator.

4.1.1 Optical Design Layout

The polychromator optical layout (Table 4.1) has been simulated using ZEMAX® ray tracing software [*ZEMAX*] (Figure 4.1). The main polychromator optical components are dichroic filters (D1-D4), lenses (L2-L4(1,2)), beam splitter (BS1), mirrors (M11, M12) as well as interference filters (I1-I6) [*Kumar et al.*, 2006] and corresponding detector eye-piece lenses (E1-E2). D1 is a long-wave pass filter that separates the UV wavelengths from the rest of the composite lidar return spectrum. D2, D3 and D4 respectively separate the 1064-nm wavelength from the composite 1064/607.4/532.1-nm wavelength at the D2 input, the 607.4-nm wavelength from the composite 607.4/532.1-nm wavelengths at the D3 input, and finally, the 354.7-nm from the UV composite 354.7/ 386.7/407.5-nm wavelengths at the D4 input.

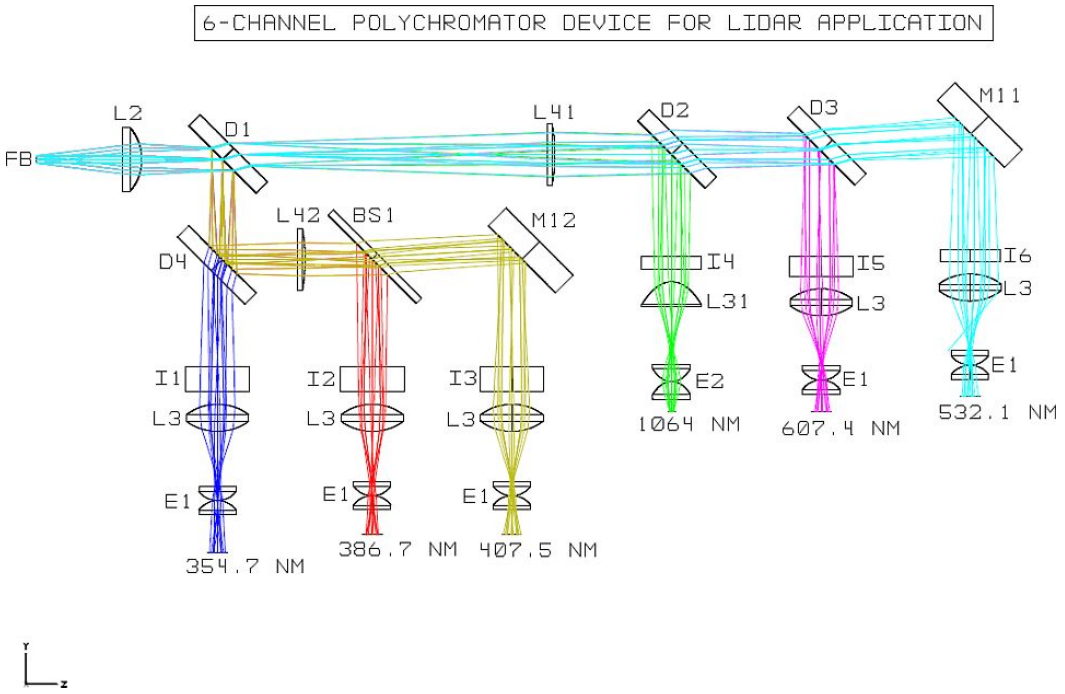

Figure 4.1: 3+3 Polychromator optical layout and related ZEMAX® ray tracing at 354.7 nm, 532.1 nm, and 1064 nm (elastic channels), 386.7 nm and 607.4 nm (N2-Raman channels), and 407.5 nm (water-vapour Raman channel). (FB) fiber-bundle, (L2) collimating lens, (L41, L42) correcting lenses, (D1-D4) dichroic filters, (BS1) beam splitter, (M11, M12) mirrors, (I1-I6) interference filters, (L3, L31) collecting or focusing lenses, (E1, E2) eye-piece lenses.

At the end of the two main optical paths (D1-M11 for the VIS-NIR subband and D4-M12 for the UV subband), the mirror M1(1,2) is used to reflect the signal onto the last detector of each branch (532.1 and 407.5nm detectors, respectively). Given the impossibility to find a dichroic filter selective enough to separate the two closest UV wavelengths of 407.5 and 386.7nm, a UV beamsplitter (BS1) is used, instead. The functionality of the lenses is as follows: L2 tends to collimate the incoming light beam from the fiber bundle (an extended light source), L4(1,2) corrects for the divergence of the VIS/NIR beam (D1-M11 optical path) and UV beam (D4-M12 optical path), and lenses L3 focus the already separated light beams onto each respective photodetector. The distance between L3 and the active area of each respective photodetector can be slightly adjusted for each channel. In the mechanical construction of each receiver, the focusing lenses L3 and their respective interference filters are assembled into aluminium cylinders screwed to the opto-electronic receiver bodies

(Figure 4.2a). Different antireflection coatings have been used in all polychromator's lenses depending on the operational spectrum band. That way, the transmissivity of the lenses can be assumed nearly ideal (better than 93%). Motorised neutral density filters and motorised shutter diaphragms are included in front of interference filters I1-I6 (Figure 4.2a).
In order to assist the optical design layout three pairs of rays have been simulated in ZEMAX® CAD ray-tracing software, one pair coming out from the center and the other two pairs coming out from the diametral ends of the fiber bundle at the entrance of the polychromator (FB in Figure 4.1). This corresponds to a distance of -1.5, 0 and +1.5 mm (3-mm fiber size) from the optical axis. The angles of incidence of these rays were calculated from the numerical aperture of the fiber bundle. To reduce position sensitivity problems, the distance between the lenses L3 and their respective photodetectors was chosen so that the simulated spot sizes onto the detector active areas are approximately one half of their effective active areas. Uneven spatial responsivity effects over the detector active area are arranged out by means of the eye-piece pairs (E1 or E2) in all the channels. The optical set formed by the neutral density filter and the diaphragm has been placed between the focusing lens (L3) and the eye-piece (E1 or E2).

Lenses	L2	L3	L4(1,2)
Type	Plano-convex	Bi-convex	Plano-convex
Effective focal length (mm)	38.0	25.4	150
Φ(mm)	**25.4**	**25.4**	**25.4**

Dichroics	D1	D2	D3	D4
Reflectivity	≥99% at 407, 386, 355nm	≥99% at 1064nm	≥98% at 607nm	≥98% at 407nm
Transmissivity	≥85% at 1064, 607, 532nm	≥80% at 607, 532nm	≥60% at 532nm	≥60% at 355nm

Mirror	M1(1,2)	**Beamsplitter**	BS
Diameter	38.00mm	Diameter	50mm
Wavelengths	400-800nm	Wavelengths	350-450nm

Interference filters	I1	I2	I3	I4	I5	I6
CWL (nm)	354.7±0.45	386.7±0.45	407.5±0.45	1064±2	607.4±0.45	532.1±2
FWHM (nm)	1	1	1	1	1	1
ξ_{IF} (%)	>50	>50	>50	>45	>60	>50
n*	2.16	2.16	2.10	1.87	1.91	1.97
Eye-pieces	f=18mm, d=15mm	f=18mm, d=15mm	f=18mm, d=15mm	f=11.25mm, d=15mm	f=18mm, d=15mm	f=18mm, d=15mm

Table 4.1: Optical components specifications

4.1.2 Mechanical Design Layout

The design goal at this stage has been to fit the polychromator unit into a light-sealed mechanical box following EURORACK dimension standards. The external mechanical box dimensions are 600 mm x 460 mm x 150 mm (160 mm with its cover). The polychromator unit inside has an "L" shape with maximum dimensions 580 mm x 180 mm x 95 mm. The complete mechanical drawing of the polychromator using computer aided design (AutoCAD®) is shown in Figure 4.3. Because of its comparatively small active area, the APD-based receiver uses a XY-axis translation/elevation micro-positioning stage (Figure 4.2b). The optical axes of the polychromator are kept at 35 mm from the basis.
Figure 4.4 shows different individual components used during the opto-mechanical design and later integrated in the polychromator. Figure 4.5 shows an internal view of the polychromator. Figure 4.5a shows the mounting of different optical components as described in

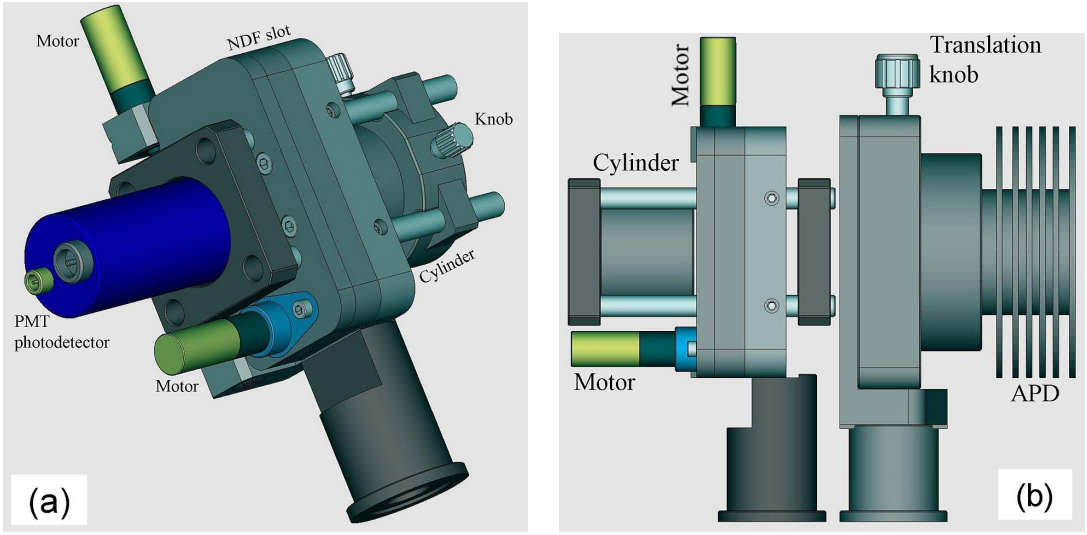

Figure 4.2: Mechanical layout (AutoCAD®) of the motorised detector assemblies. One micro-motor controls the neutral-density-filter (NDF) attenuation and the other the diaphragm. The "cylinder" houses interference filter (I(1-6)) and focusing lens (L(3,31)) in Figure 4.1. (a) PMT module. (b) APD module.

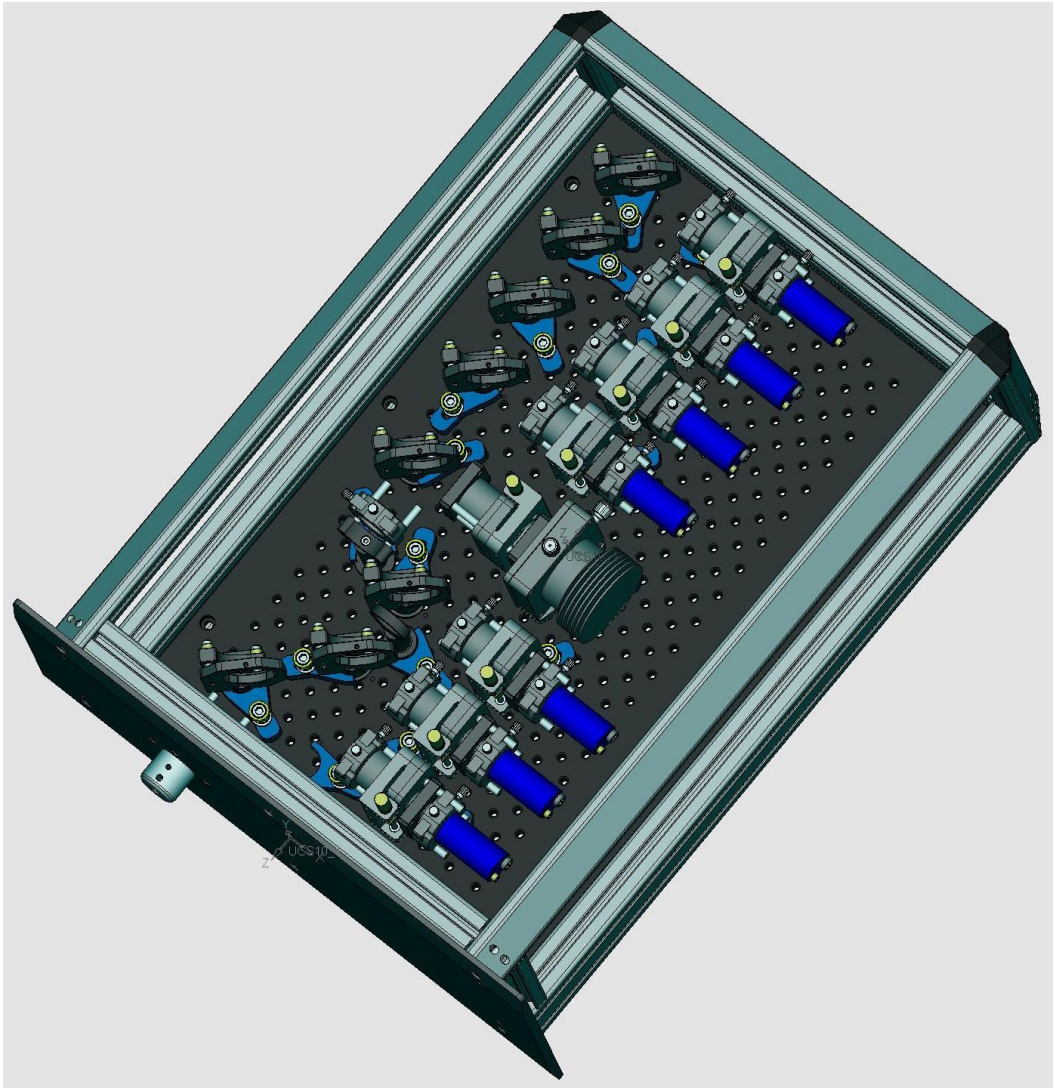

Figure 4.3: Opto-mechanical implementation of the 3+3 Polychromator (also showing two future extra channels added (7 PMT-based and 1 APD-based channels)) (AutoCAD®).

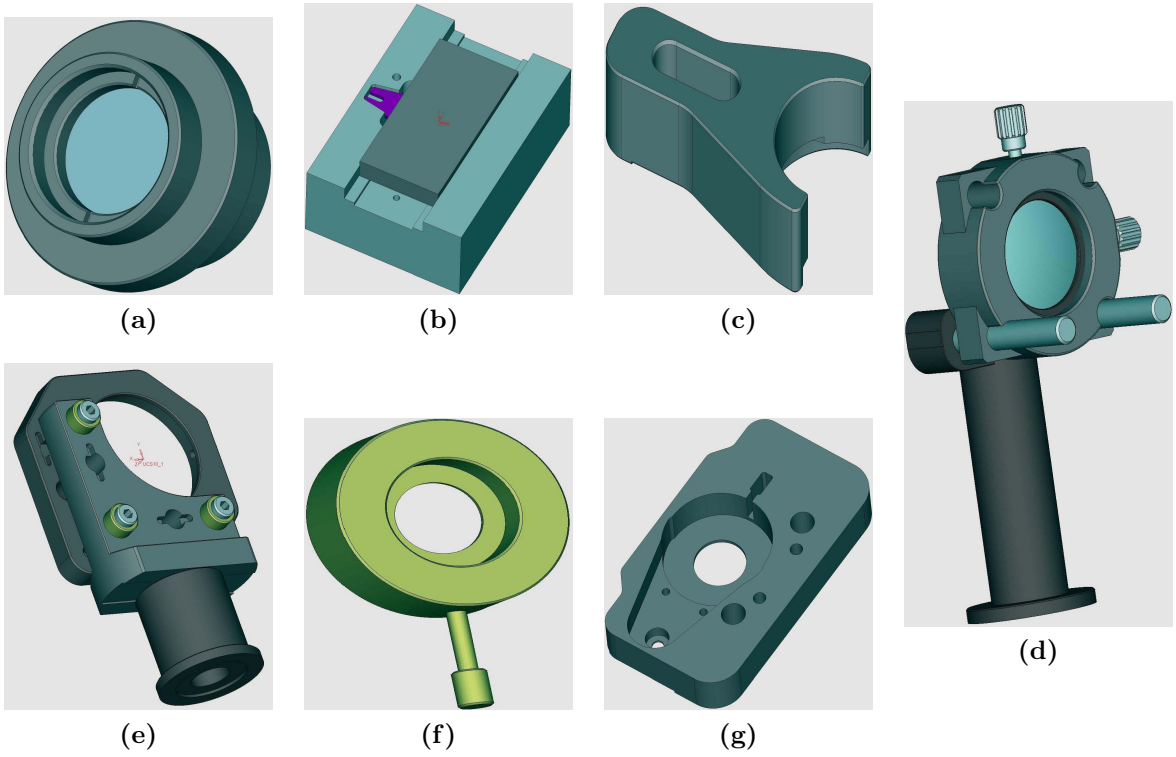

Figure 4.4: Polychromator opto-mechanical parts. (a) Collimator ((L2) in Figure 4.5a). (b) Optical attenuator housing (N in Figure 4.5b). (c) Clamp holder (B in Figure 4.5a). (d) Focusing-lens holder (L41 in Figure 4.5a). (e) Dichroic/Mirror holder ((D1-D4)/M12 in Figure 4.5a). (f) Diaphragm mount (D in Figure 4.5b). (g) Diaphragm housing (D in Figure 4.5b).

Section 4.1.1. The diaphragm ("D" in Figure 4.5b) and the neutral density filters ("N" in Figure 4.5b) are automatically controlled by means of stepping motors ("S1" and "S2" in Figure 4.5c) via a pulley "P" (Figure 4.5c).

4.2 DESIGN CONSIDERATIONS

Light Collimation.- In the multichannel polychromator designed (Figure 4.1), lens L2 is used as a nearly-collimating lens. Since the input light source to the polychromator (a fiber bundle, composed of 400 fibers, (FB) in Figure 4.1 and see bundle specs in Table 2.1) is not a point source but an extended light source, perfect collimation (i.e., obtaining parallel light rays at the output of L2) is not possible. In contrast, L2 is moved slightly off focus with respect to the fiber bundle in order to minimize the beam divergence at its output (L2-L4(1,2) optical path). Based on (ZEMAX®) simulation the FB-L2 distance was determined to be $d = 34$ mm, which corresponds to $d = 0.90f$ with f the focal-length of L2. Therefore, L2 was located off-focus and closer to the fiber bundle.

Light divergence at the output of the collimating lens system.- In Figure 4.1 the collimation lens system output is formed by either one single lens (L2) in the case of the 355-nm channel or by a pair of lenses (L2, L4(1,2)), which are separated a travelling-path distance d, in the case of all other channels. This collimation lens system is noted L2' in Figure 4.6. In order to calculate the maximum beam divergence at the equivalent collimating lens output (L2'), we apply Abbe's invariant [*Möller*, 2007a] to both rays a and b (Figure 4.6),

$$\theta_{1a}y_{1b} - \theta_{1b}y_{1a} = \theta_{2a}y_{2b} - \theta_{2b}y_{2a}, \tag{4.1}$$

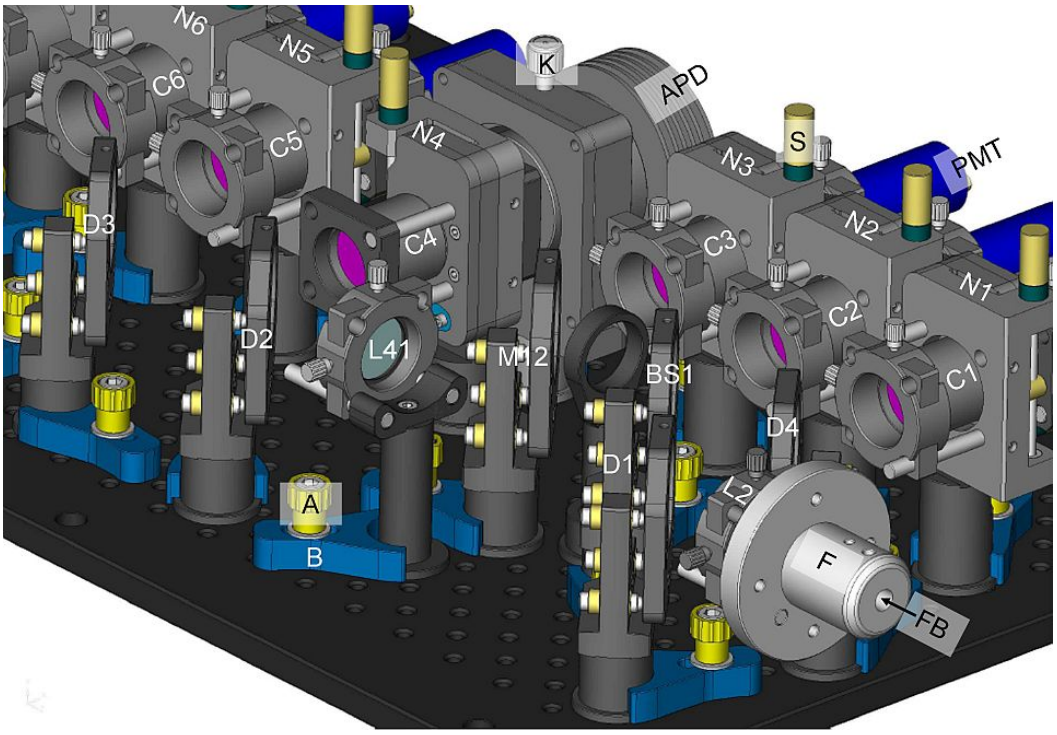

(a)

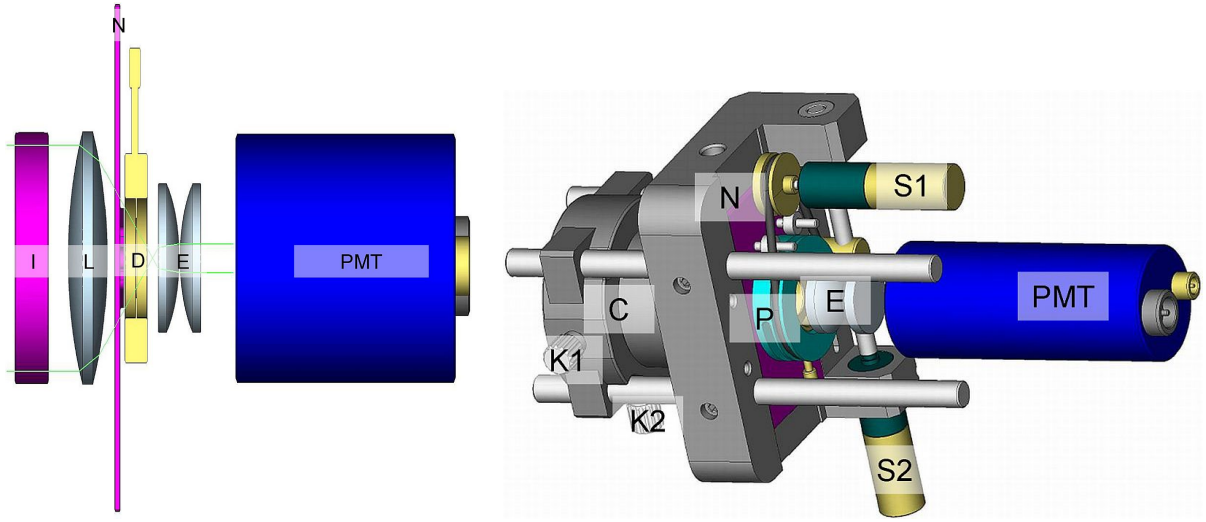

(b) **(c)**

Figure 4.5: Polychromator (internal view). (a) Mounting of components. ((FB), (L2), (D1-D4), (BS1), (M12) and (L41) are the same as in Figure 4.1), (F) fiber ferrule, (S) stepping motor, (K) translation knob, (A) Screw, (B) clamp holder, (C1-C6) cylinders (Inside these cylinders there are: Interference filters (I1-I6 in Figure 4.1) and focusing lenses (L3, L31 in Figure 4.1)), (N1-N6) slots for NDFs and diaphragms, (PMT) PMT detector, (APD) APD detector. (b) Ray trajectory and optical parts details. (I) interference filter (I1-I6 in Figure 4.1), (L) focusing lens (L3, L31 in Figure 4.1), (N) same as (N1-N6) in subfigure (a), (D) diaphragm, (E) eye-piece lens pair (E1, E2 in Figure 4.1). (c) Internal view of photo-detector module. (K1-K2) same as (K) in subfigure (a), (P) pulley, (C) same as (C1-C6) in subfigure (a), (S1-S2) same as (S) in subfigure (a), rest of items same as in subfigure (b).

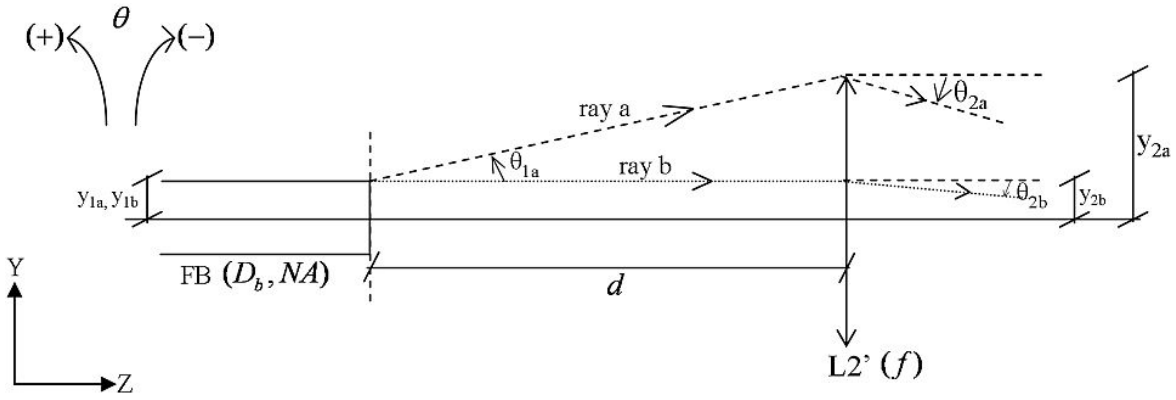

Figure 4.6: Calculation of light divergence inside the polychromator

where the pairs (θ_{1a}, y_{1a}), (θ_{1b}, y_{1b}) and (θ_{2a}, y_{2a}), (θ_{2b}, y_{2b}) describe the corresponding angles and heights for the rays a and b at the fiber (FB) and the collimating lens (L2') outputs respectively. NA denotes the numerical aperture of the fiber, D_b the fiber diameter and f the equivalent focal-length of the collimating system (L2'). Using that ($\theta_{1a} = \theta_{NA}$, $y_{1a} = D_b/2$, $\theta_{1b} = 0$, $y_{1b} = D_b/2$, $\theta_{2b} = -\frac{D_b/2}{f}$, $y_{2b} = D_b/2$, $y_{2a} = D_b/2 + \theta_{NA} \cdot d$), the light divergence at the output of the collimating lens system (L2') is given by

$$\theta_{2a} = \theta_{NA} - \frac{1}{f} \cdot \left(\frac{D_b}{2} + \theta_{NA} \cdot d \right), \tag{4.2}$$

where θ_{NA} is defined as $\theta_{NA} = \sin^{-1}(NA)$.
Following Eq.(4.2), light divergence at the output of the collimating lens system (single lens L2 in the case of 355nm channel, L2-L4(1,2) lens pair for all other channels, Figure 4.1) is calculated to be $\sim 28\, mrad$, which is *less than one fourth the angle associated to the numerical aperture of the bundle*. Assessing the maximum light divergence of the "collimated" beam is important for two reasons: (i) in order to estimate the centre wavelength (CWL) de-tuning of the interference filters and, consequently, their *minimum required bandwidth* and (ii) in order to specify the *required eye-pieces* to be placed in front of the photo-detectors (i.e. at the end of the each optical receiving path). Detector's eye-pieces fulfil the important mission of averaging spatial responsivity inhomogeneties over the detector's active area.

Filter's *center wavelength* de-tuning.- Optical filters such as the interference filters listed in Table 4.1 always specify their center wavelength (CWL) for normal incidence of rays at their input. When the input light beam has some divergence (Eq.(4.2)) or includes rays with oblique incidence ($[-\theta_{2a}, \theta_{2a}]$), the CWL of the filter becomes shifted. The CWL shift can be computed as [*Omegafilters*]

$$\lambda_\theta = \lambda_0 \left[1 - \left(\frac{n_e}{n^*} \right)^2 \sin^2 \theta \right]^{\frac{1}{2}}, \tag{4.3}$$

where λ_θ is the CWL wavelength for oblique incidence, λ_0 is the CWL wavelength at normal incidence, n_e is the refractive index of external medium ($n_e = 1$, air), n^* is the effective refractive index of the filter and θ is the angle of incidence. Table 4.2 shows the CWL shift for the polychromator's channels in response to a maximum angle of incidence ($\theta = \theta_{2a} \cong 28\, mrad$, Eq.(4.3)) From Table 4.2 the maximum CWL shift for a $28 - \text{mrad}$ input

λ_0(nm)	n^*	λ_θ(nm)	$\Delta\lambda$=$\lvert\lambda_\theta - \lambda_0\rvert$
386.7	2.16	386.67	0.03
407.5	2.10	407.46	0.04
607.4	1.91	607.33	0.07
354.7	2.16	354.67	0.03
532	1.97	531.95	0.05
1064	1.87	1063.88	***0.12***

Table 4.2: Estimated CWL shift for various channels ($\theta_{2a} \cong 28mrad$)

divergence is about 0.12 nm (1064 nm, the worst channel) and the minimum bandwidth required is $\approx$ 0.24 nm (2×0.12 nm). In those conditions and given a 15%-error bound for the CWL specified by the manufacturer, *a minimum bandwidth of 0.3 nm is needed* to guarantee reception. In the practical implementation a more conservative figure of 1nm has been used, instead.

Uneven spatial detector responsivity.- The image of the backscattered lidar return in the telescope focal plane always has 'comma' like shape with its head due to the near range signal and its tail due to the far-range signal. The use of a PMT detector with a non-uniform spatial responsivity to detect lidar signals can cause artifacts when transducing the lidar signal into an electrical signal. Previous studies [*Simeonov et al.*, 1999] show that the normalized spatial uniformity on the active area of an $8-$mm PMT diameter can vary from 0.2 to 2.8 times the average value defined for the central part of the detector. Practically, the useful diameter of the Hamamatsu 7400 PMT (nominally 8 mm) is only about 5 mm including mounting and adjustment tolerances. The eyepiece (E1 or E2) not only makes the detector rather insensitive to several misalignments (axial/radial shifts) but also averages out spatial responsivity inhomogeneities. Axial misalignments are the the most critical as it is difficult to determine the exact location of the PMT cathode with respect to the PMT housing [*Freudenthaler*, 2004].
Determination of the photo-detectors' eye-piece.- Figure 4.7 shows the equivalent optical layout of a polychromator channel. The fiber bundle (FB) conveys the backscattered light to the photodetector (D3) by combining the collimating lens (L1) [note that L1 in Figure 4.7 stands for L2 (355-nm channel) or the L2-L4(1,2) pair (all other channels) in Figure 4.1], the collecting lens (L2), and the eye-piece lens (L3). In order to specify the eye-piece lens in terms of size and focal-length, let us consider two rays leaving the fiber bundle at heights $+D_b/2$ and $-D_b/2$ and forming respective angles with the optical axis equal to NA of the bundle. In order to average uneven spatial responsivity effects it is necessary that the lens L3 ensures a beam diameter equal to the detector area (8 mm for PMTs, 3 mm for the APD) at the detector plane. This can be achieved when lenses L2 and L3 form an afocal system (F2'=F3), which means that parallel beams entering L2 leave L3 parallel. Therefore, the distance between the lenses L2 and L3 is $d = f_2 + f_3$. With such a system, the beam diameters D_2 and D_3 are connected by the paraxial approximation,

$$\frac{D_2}{D_3} = \frac{f_2}{f_3}. \tag{4.4}$$

Using standard 1-inch optics, assuming a maximum beam diameter $D_2 \approx 20$ mm (in any case < 25.4 mm, the standard optics diameter), $f_2 = 25.4$ mm (L3 in Table 4.1), $D_3 =$ 8 mm (PMT) or 3 mm (APD), Eq.(4.4) yields $f_3 = 10.16$ mm (PMT) and $f_3 = 3.81$ mm (APD). The Zemax® simulation of Figure 4.8 illustrates the benefits of including the eye-piece regarding the imaged spot onto the detector active area. As can be seen in the simulated spot diagrams the eye-piece is very effective in spreading the incoming rays onto the entire

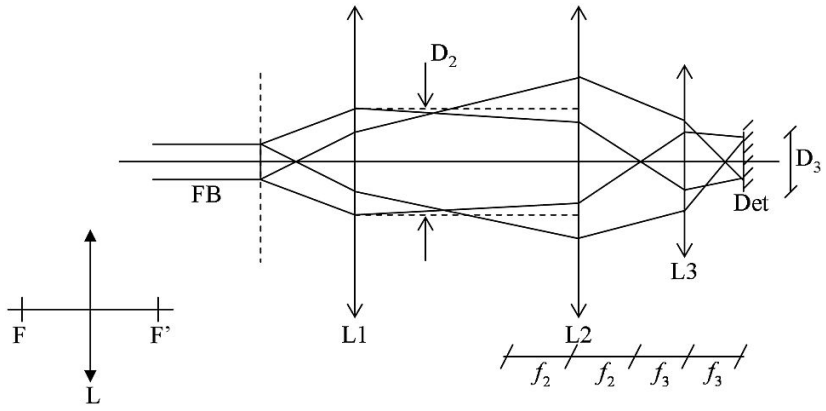

Figure 4.7: Equivalent optical layout of a polychromator channel. D_2 stands for the maximum allowable diameter of the light beam in the L1-L2 path. D_3 stands for the detector's active area diameter.

surface of the detectors.

End-to-end transmissivity.- Finally, In order to achieve the highest net channel responsivity, it is necessary to minimize optics transmission losses in the polychromator reception chain. At this point, selection of the best antireflection coatings in all optical components (dichroics and lenses) is essential. The end-to-end channel transmissivity is given in Eq.(2.19) and listed in Table 2.1 for each receiving channel.

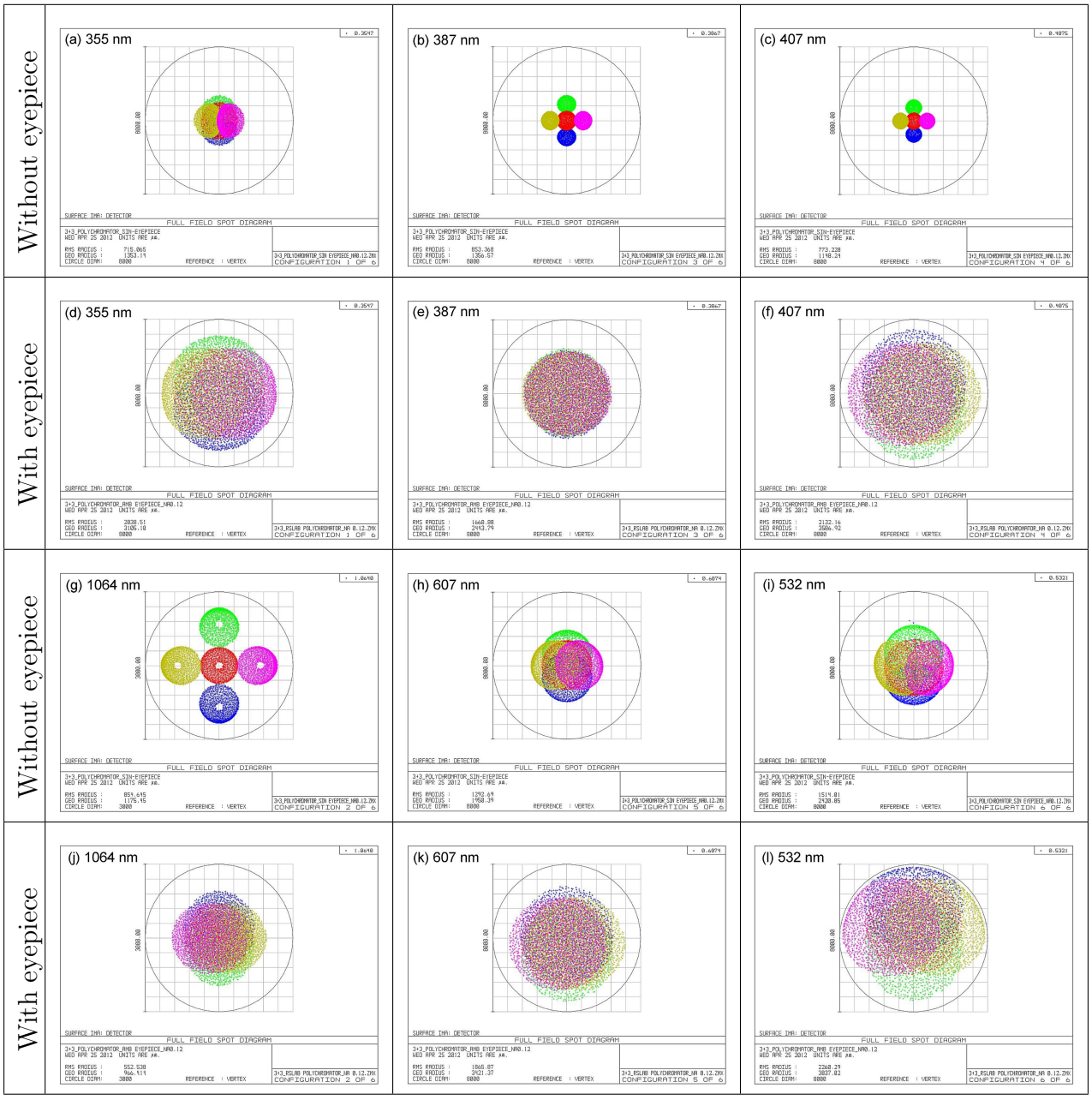

Figure 4.8: Effect of the eye-piece (L3 in Figure 4.7) on the light distribution over the detector's active area. (Without eye-piece) (a)-(c) and (g)-(i). (With eye-piece) (d-f) and (j-l). (Different colours correspond to rays emerging from different diametral positions along the bundle aperture, see FB in Figure 4.1).

Chapter 5

PRACTICAL ANALYTICAL BACKSCATTER-COEFFICIENT ERROR ESTIMATES FOR THE TWO-COMPONENT ELASTIC-LIDAR INVERSION ALGORITHM

Total-backscatter inversion error bounds for the two-component lidar inversion algorithm (the so-called Fernald's or Klett-Fernald-Sasano's method) are derived in analytical form in response to three error sources: (i) the observation noise (i.e., signal-to-noise ratio in reception), (ii) the user uncertainty in the backscatter-coefficient calibration, and (iii) in the aerosol extinction-to-backscatter lidar ratio.
First-order error-propagated error bounds are presented. Error bounds are formulated in explicit analytical form, which is of advantage for practical physical sensitivity analysis and computational implementation. A Monte Carlo approach is used to validate the error bounds at 532-nm wavelength.
This Chapter is an adaptation of [*Rocadenbosch et al.*, 2012] with focus on first-order error-propagated approximate error bounds and joint contributions from D. Kumar and D. Lange. In contrast to the final version of the paper, here we study the algorithm under fast raising slopes in the aerosol profile by simulating a trapezium-shaped aerosol profile.

5.1 INTRODUCTION

Elastic-backscatter lidars are relatively low-cost laser remote-sensing instruments widely used as range-resolved ground-based, air- and space-borne atmospheric probes [*Reagan et al.*, 1989]. Examples are found in ground-based aerosol-observation networks such as the EARLINET (European Aerosol Research Lidar Network) and the MPLNET (Micro-Pulse Lidar Network) among others [*Rocadenbosch et al.*, 2008], and in space missions such as the LITE (Lidar In-space Technology Experiment, 1994) [*Winker et al.*, 1996], which used a backscatter lidar onboard the Discovery shuttle (NASA) to measure cloud structure and atmospheric aerosols at global scale and, more recently, onboard the CALIPSO satellite (NASA-CNES, 2006) [*Winker and Pelon*, 2003].

Because the lidar equation is inherently underdetermined for it contains two unknowns (the atmospheric extinction and the backscatter coefficient) and one single observable (the optical power returned as a function of time) backscatter lidars are only capable to provide range-resolved attenuated backscatter profiles (i.e., the product of the "total" backscatter coefficient (aerosol plus molecular atmospheric components) times the two-way transmission through the atmosphere) [*Collis and Russell*, 1976; *Bösenberg and Hoff*, 2007]. This underdetermination is in contrast to (single-pointing) elastic-Raman systems, HSRL (High Spectral Resolution Lidars), and variational multi-angle backscatter-lidar retrievals [*Sicard et al.*, 2002], all of which enable independent inversion of both aerosol extinction and backscatter parameters [*Ansmann et al.*, 1992].

Historically, in 1981 and thanks to the previous works from Hitschfeld and Bordan (1951) [*Hitschfeld and Bordan*, 1954], Barret and Ben-Dov [*Barret and Ben-Dov*, 1967], Viezee et al. [*Viezee et al.*, 1969], Davis [*Davis*, 1969], Fernald [*Fernald et al.*, 1972], Collis and Russell [*Collis and Russell*, 1976], and Kohl [*Kohl*, 1978], among others, Klett presented a stable inversion algorithm to invert the elastic single-scattering lidar equation assuming a *one-component* atmosphere [*Klett*, 1981] (i.e., no separation between aerosol and molecular components just "total" components). In 1984, Fernald presented the *two-component* version of the algorithm [*Fernald*, 1984] (separated components), which, later on, Klett reformulated in a unified approach [*Klett*, 1985]. Both the one-component (Klett's method, KLT for short) and the two-component inversion algorithm (Fernald's method, also known as Klett-Fernald-Sasano's method, KFS for short) require additional user inputs to solve the under determination of the lidar equation, that is, provision of 1) a boundary calibration and 2) a *range-dependent* extinction-to-backscatter ratio. Methods to assess the boundary condition for the Klett's one-component inversion algorithm were proposed by Klett himself [*Klett*, 1983, 1986] and for the two-component algorithm by Sasano and Nakane [*Sasano and Nakane*, 1987]. Besides, several authors carried out extinction-retrieval error-sensitivity studies concerning uncertainties in the extinction-to-backscatter ratio [*Sasano and Nakane*, 1984] (KFS method) and the impact of assuming a range-independent ratio [*Sasano et al.*, 1985] (KFS), uncertainties in the input boundary value [*Bissonnette*, 1986; *Matsumoto and Takeuchi*, 1994] (KLT and KFS), and the forward/backward stability of the (KLT) method as function of the optical depth [*Qiu*, 1988].

Though historically this was not the case, today both one- and two-component inversion methods are usually formulated in *backscatter form.* The backscatter coefficient is always the preferred magnitude to be inverted for the extinction coefficient must be estimated by multiplying the backscatter-coefficient profile with the extinction-to-backscatter profile used before as input in the backscatter-coefficient retrieval, thus largely amplifying errors [*Bösenberg and Hoff*, 2007], especially in scenes with a complex layering of aerosols [*Ansmann*, 2006]. Kunz [*Kunz*, 1996] and Kovalev [*Kovalev*, 1993, 2003] have proposed alternative variants (not the object of this paper) allowing trustworthy extinction retrievals, where the single-point far-end boundary calibration is replaced by information on the transmission losses over the sounding path or by a near-end calibration and a nephelometer measurement, respectively. The synergetic combination of a backscatter lidar with a sun photometer is also intensively used [*Reba et al.*, 2010; *Reba*, 2010]. Furthermore, optimal estimation [*Stephens and Engelen*, 2001] and adaptive filtering [*Rocadenbosch et al.*, 1999] methods offer the possibility to incorporate different relevant information (such as optical thickness or spectral radiance measurements [*Huneeus and Boucher*, 2007]) into the lidar inversion problem and provide full inversion error indicators. These advanced methods, which usually find applications in the context of global space-borne measurements and are, however, more complex.

Though from a purely mathematical analysis both the one- and the two-component algorithms give equivalent solutions, the two-component algorithm is always the preferred one.

This is because the KFS algorithm enables to input an *aerosol* extinction-to-backscatter ratio – the so-called "lidar ratio"- (a major environmental parameter from which microphysical aerosol information can be derived [*Böckmann et al.*, 2008]) instead of a *total* extinction-to-backscatter ratio (one-component, KLT method). From a physical point of view, the assumption of a constant "total" lidar ratio (i.e., folding the molecular ratio ($8\pi/3$) and the range-dependent aerosol lidar ratio into a constant total lidar ratio) cannot be justified under relatively clear atmospheres. In contrast, for optically thick atmospheres (where the aerosol component becomes dominant), the "total" lidar ratio reduces to the "aerosol" lidar ratio, which gave rise to the first applications of the one-component algorithm in the 1980's.

This paper concentrates on the *two-component backscatter-coefficient inversion algorithm* and is the fifth in a series [*Rocadenbosch and Comerón*, 1999; *Comerón et al.*, 2004; *Sicard et al.*, 2009a; *Rocadenbosch et al.*, 2010a; *Reba*, 2010](1999-today) from the RSLAB (Remote Sensing Lab.) related to study the behaviour and error sensitivity of the one- and two-component algorithms. The work presented here first contributes to the lidar community a comprehensive analytical approach *in explicit mathematical form* merging into a single body all the main error sources involved in the KFS aerosol-backscatter inversion: 1) errors due to user uncertainties in the backscatter-coefficient calibration, 2) errors due to a (range-dependent) aerosol extinction-to-backscatter ratio (i.e., the lidar ratio), and 3) errors due to the observation noise (i.e., finite signal-to-noise ratio (SNR) in the reception channel) in all range cells except at the calibration cell, and 4) errors due to the observation noise at the calibration cell.

The progression followed in this publication series has forcibly begun by analyzing the KLT numerical kernel for the KFS kernel is too complex to be tackled at once. Thus, in the first paper of the series [*Rocadenbosch and Comerón*, 1999] the multi-branch response of the KLT algorithm was studied and extinction error envelopes were derived in response to a constraint placed on two user-input error bounds in the original formulation of Klett's algorithm: the boundary extinction calibration and the power-law exponent modeling the total extinction-to-backscatter relationship (Eq.(6) in [*Klett*, 1981]). The "historical" extinction- rather than the backscatter-inversion form was still considered there.

The second paper of the series [*Comerón et al.*, 2004] addresses the KLT kernel reformulated in backscatter-coefficient form (i.e., in terms of the reliable optical quantity to be inverted) and derives a mathematical expression describing the behavior of the inverted backscatter-coefficient profile in the presence of noise (error sources (3-4) above). It is shown that the calibration-range signal noise (error source 4) is the dominant error source in front of the shot noise from all other cells in the inversion path (error source 3), which explains the subdivision between error sources (3-4) above.

The third paper [*Sicard et al.*, 2009a] (in what follows the "implicit error-bound paper") provides a first statistical treatment quantifying the noise-induced error bounds (error sources (3-4)) for both KLT and KFS inversion methods (a partial correspondence between KLT and KFS numerical kernels is derived) in terms of constant confidence-level error envelopes. In spite of the fact that exact analytical expressions are formulated, its main limitations are: i) the mathematical complexity of the solution equations, which are given in *implicit* -integral form and which must be solved for each cell along the inversion range, ii) the ill-conditioned behaviour of the numerical solutions for dense atmospheres, and iii) the fact that only one error source (the noise) is studied.

The need for an *explicit* –rather than implicit – error-bound formulation is accomplished in the fourth paper of the series [*Rocadenbosch et al.*, 2010a] (in what follows this reference will be addressed as the "KLT-counterpart paper") which again retraces steps back to the KLT numerical kernel –as a previous step towards the KFS algorithm-. First-order derivative KLT-backscatter-coefficient error bounds are derived in response to the error sources (1-4)

above. The mean backscatter-coefficient relative error between the analytically estimated error bounds and the "true" Monte Carlo (MC) error bounds (obtained via simulation) is below than 10% for practical SNRs ($SNR \geq 10$), optical depths, $\tau \leq 5$, and typical user uncertainties.

From this background, the present paper provides the sought-after backscatter-coefficient error bounds for the KFS algorithm as follows: (i) in *explicit* -rather than in implicit- straightforward practical form, and (ii) including all four error sources above. First-order derivative error bounds (i.e., approximated ones corresponding to the KFS counterpart of KLT kernel sensitivity in [*Rocadenbosch et al.*, 2010a]) for the dominant error sources (1, 2 and 4 above) are presented. The error bounds presented are MC *multi-wavelength* validated at the Nd:YAG wavelength of 532 nm (visible, VIS).

The approach followed here is self-contained so that the paper can be read on its own. Notation is consistent with the KLT-counterpart paper and Sections 5.2-5.5 here parallel a similar structure. This chapter is organised as follows: In Section 5.2 the KFS inversion kernel is reviewed and reformulated in both backward and forward form. In Section 5.3, first-order analytical error bounds and a stochastic approach (error variance propagation) are presented. In Section 5.4, the error bounds derived are validated using a MC method. Finally, conclusion remarks are given in Section 5.5.

5.2 REVIEW OF THE KFS TWO-COMPONENT METHOD

5.2.1 Review of KFS method

Klett-Fernald-Sasano's inversion algorithm is formulated in backward backscatter-coefficient form as

$$[\beta^{aer}(R) = \frac{\left[R^2 P(R)\right] \exp\left\{2\int_R^{R_m}\left[S^{aer}(u) - S^{mol}\right]\beta^{mol}(u)\,du\right\}}{\frac{[R_m^2 P(R_m)]}{\beta^{aer}(R_m)+\beta^{mol}(R_m)} + 2\int_R^{R_m} S^{aer}(u)\left[u^2 P(u)\right]\exp\left\{2\int_u^{R_m}\left[S^{aer}(v) - S^{mol}\right]\beta^{mol}(v)\,dv\right\}du} - \beta^{mol}(R)], \tag{5.1}$$

where $P(R)$ is the single-scattering optical-return lidar power, R is the range along sight, $S^{aer}(R)$ and $S^{mol} = 8\pi/3$ are the aerosol and the molecular (Rayleigh) lidar ratios, respectively, $\beta^{aer}(R)$ and $\beta^{mol}(R)$ are the aerosol and molecular backscatter components, and R_m ($R \leq R_m$) is the boundary calibration range. In Eq. 5.1 note that in spite of the two-component separation, the term $\beta(R_m) = \beta^{aer}(R_m) + \beta^{mol}(R_m)$ represents the total backscatter coefficient. In practical tropospheric applications, the calibration range is usually chosen in an atmospheric molecular reference range aloft where the aerosol backscatter component becomes negligible ($\beta^{aer}(R_m) \ll \beta^{mol}(R_m)$), consequently, $\beta(R_m) \approx \beta^{mol}(R_m)$.

5.2.2 Modified backward KFS form

In what follows the aerosol and the molecular backscatter terms, $\beta^{aer}(R)$ and $\beta^{mol}(R)$, are assimilated into the total backscatter-coefficient term, $\beta^{tot}(R) = \beta^{aer}(R) + \beta^{mol}(R)$, and errors on the molecular backscatter term are disregarded so that

$$d\beta^{aer}(R) = d\beta^{tot}(R)\,. \tag{5.2}$$

This is justified on account of the error superposition principle, which is to say that the molecular component is assumed to be perfectly known (i.e., no error contribution) so that

molecular backscatter systematic errors are studied elsewhere. In practice, the atmospheric molecular component is estimated from local temperature/pressure radio-sounding measurements or a US-standard atmosphere model given ground-level temperature and pressure data [*Bodhaine et al.*, 1999].

By introducing the discrete range, $R_j = R_{\min} + (j-1)\,\Delta R, \quad j = 1..N$, with ΔR the spatial resolution of the lidar data to be inverted and N the number of samples (or inversion cells), Eq.(5.1) can be rewritten in discrete form as

$$\beta_j^{tot}\left(\beta_N^{tot}, \vec{S}, \vec{U}\right) = \frac{\beta_N^{tot}\, U_j F_j\left(\vec{S}\right)}{U_N + 2\beta_N^{tot}\, H_j\left(\vec{S}, \vec{U}\right)}, \tag{5.3}$$

where U_j, F_j and H_j stand, respectively, for $U(R_j)$, $F(R_j)$ and $H(R_j)$ and $\vec{S}$ stands for the range-dependent *aerosol* lidar ratio, $S^{aer}(R_j)$, in vector form. Auxiliary functions U_j, F_j and H_j are defined as

$$U_j = R_j^2 P(R_j), \tag{5.4}$$

$$F_j\left(\vec{S}\right) = \exp\left[2G_j\left(\vec{S}\right)\right], \tag{5.5}$$

where

$$G_j\left(\vec{S}\right) = \begin{cases} \sum_{i=j}^{N} w_i \left(S_i^{aer} - S_i^{mol}\right)\, \beta_i^{mol} & j < N \\ 0 & j = N \end{cases}, \tag{5.6}$$

and

$$H_j\left(\vec{S}, \vec{U}\right) = \sum_{i=j}^{N} w_i S_i^{aer} U_i F_i\left(\vec{S}\right). \tag{5.7}$$

In Eqs.(5.6)-(5.7) above $w_i, \quad i = 1..N$ stand for generic discrete integration weights (e.g., $w_i = h, \quad i = 1..N-1; \quad w_N = 0$ in the case of rectangle integration, which requires $N \geq 2$ points). Notation $\beta_j^{tot}\left(\beta_N^{tot}, \vec{S}, \vec{U}\right)$ is a reminder that the total inverted backscatter coefficient at the range cell, $R = R_j$, depends on the total backscatter coefficient at the far-range calibration point, β_N^{tot}, the user-input range-dependent aerosol lidar ratio, $\vec{S}$ (i.e., the function $S(R)$), and the range-corrected power, $\vec{U}$ (i.e., the function $U(R)$). We also note that when calibrating in a molecular atmospheric layer,

$$\beta_N^{tot} = \beta^{tot}(R_N) = \beta^{aer}(R_N) + \beta^{mol}(R_N) \approx \beta^{mol}(R_N). \tag{5.8}$$

In what follows *notation is simplified as follows:* 1) Superscript "tot" for the *total* backscatter coefficient is skipped so that β stands for β^{tot}, and 2) superscript "aer" for the *aerosol* extinction-to-backscatter lidar ratio is also skipped so that $\vec{S}$ refers to $\vec{S}^{aer}$.

5.2.3 Comparison with Klett's one-component method

When comparing KLT versus KFS kernel equations (Eqs.(5)-(6) in the "KLT-counterpart paper" with Eqs.(5.3), (5.5) and (5.7) above) the KLT-to-KFS kernel transformation table arises (Table 5.1). The U_j into $U_j F_j\left(\vec{S}\right)$ relationship agrees with previous published results (Table 1 in [*Sicard et al.*, 2009a]) and the $G_j\left(\vec{S}, \vec{U}\right)$ into $H_j\left(\vec{S}, \vec{U}, \vec{F}\right)$ is a new relationship completing the kernel transformation.

KLETT	KFS
$\beta_j\left(\beta_N,\vec{S},\vec{U}\right)=\frac{\beta_N U_j}{U_N+2\beta_N G_j\left(\vec{S},\vec{U}\right)}$	$\beta_j\left(\beta_N,\vec{S},\vec{U}\right)=\frac{\beta_N\ U_j F_j\left(\vec{S}\right)}{U_N+2\beta_N\ H_j\left(\vec{S},\vec{U}\right)}$
$\vec{S}$ stands for the total lidar ratio, $\vec{S}^{tot}$	$\vec{S}$ stands for the aerosol lidar ratio, $\vec{S}^{aer}$
U_j	$U_j F_j\left(\vec{S}\right)$
$G_j\left(\vec{S},\vec{U}\right)$	$H_j\left(\vec{S},\vec{U},\vec{F}\right)$

Table 5.1: KLT-KFS kernel transformation relationships. Notation: In both methods, β_j stands for *total* (aerosol plus molecular) backscatter-coefficient at the range cell R_j.

5.2.4 Forward case

In the forward-integration form of the KFS method (i.e., calibration point located at the near end of the inversion range) the following changes must be considered:

1. Replace the far-end calibration at $R=R_N$ by the near-end calibration $R=R_1$, (i.e., $\beta_N\rightarrow\beta_1$) in Eq.(5.3).

2. Replace $\sum_{i=j}^{N}(.)$ by $-\sum_{i=1}^{j}(.)$ in all subsequent formulas here.

Eq.(5.3) for the forward case is written as

$$\beta_j\left(\beta_1,\vec{S},\vec{U}\right)=\frac{\beta_1\ U_j F_j^F\left(\vec{S}\right)}{U_1+2\beta_1\ H_j^F\left(\vec{S},\vec{U}\right)}, \tag{5.9}$$

where $F_j^F\left(\vec{S}\right)=\exp\left(2G_j^F\right)$ after Eq.(5.5) and G_j^F and H_j^F are defined following Eqs.(5.6)-(5.7) above but replacing $\sum_{i=j}^{N}(.)$ by $-\sum_{i=1}^{j}(.)$, as mentioned. This leads to well know classic forward form including a minus sign in front of the factor "2" in the denominator and in the exponential arguments of Eq.(5.1). Note also that the minus sign arising from the change no. 2 above is algebraically equivalent to substituting $S^{aer}\rightarrow -S^{aer}$ and $S^{mol}\rightarrow -S^{mol}$ into the KFS backward form of Eq.(5.3).

5.3 FIRST-ORDER ANALYTICAL BACKSCATTER-COEFFICIENT ERROR BOUNDS

5.3.1 Overview: The error-propagation approach

This section parallels Section 5.3 of the KLT-counterpart paper, where the backscatter-coefficient error bounds are computed from the superposition of error sources 1-4 (Section 5.1) using a first-order derivative approach. Following Eq.(5.7) there,

$$\begin{cases} |d\beta_j|=\left|\frac{\partial\beta_j}{\partial\beta_N}d\beta_N\right|+\sum_{k=1}^{N}\left|\frac{\partial\beta_j}{\partial S_k}dS_k\right|+\sum_{k=1}^{N-1}\left|\frac{\partial\beta_j}{\partial P_k}dP_k\right|+\left|\frac{\partial\beta_j}{\partial P_N}dP_N\right|; & j<N \\ |d\beta_j|=|d\beta_N|; & j=N \end{cases}, \tag{5.10}$$

where $d\beta_N$, dS_k, dP_k, and dP_N, respectively stand for error sources (1)-(4).

For the case $j<N$ the terms $\frac{\partial\beta_j}{\partial\beta_N}$, $\frac{\partial\beta_j}{\partial P_k}$ and $\frac{\partial\beta_j}{\partial P_N}$ can be computed from Eqs.(5.8), (5.10)-(5.18) there and the function substitutions indicated in the KLT-to-KFS kernel transformation Table 5.1. Yet, this procedure cannot be followed when computing the errors due

to the lidar ratio, $\frac{\partial\beta_j}{\partial S_k}$, for the KFS-kernel functions F_j and H_j (Eqs.(5.5), (5.7)) also depend on the lidar ratio. This case is revisited in the Annex A of [*Rocadenbosch et al.*, 2012]. The case $j = N$ in Eq.(5.10) expresses the user's assumed error on the backscatter-coefficient calibration input. Finally, the error-propagated expressions, $\varepsilon_{j,1-4}$ are given in Table 5.2.

CONCEPT	EQUATION
Total backscatter-coefficient error (case $j < N$) where	$\|d\beta_j\| = \left\|\frac{\partial\beta_j}{\partial\beta_N}d\beta_N\right\| + \sum_{k=1}^{N}\left\|\frac{\partial\beta_j}{\partial S_k}dS_k\right\| + \sum_{k=1}^{N-1}\left\|\frac{\partial\beta_j}{\partial P_k}dP_k\right\| + \left\|\frac{\partial\beta_j}{\partial P_N}dP_N\right\|;\ j < N$ (5.10)
1. Error due to the backscatter-coefficient calibration	$\varepsilon_{j,1} = \frac{\partial\beta_j}{\partial\beta_N}d\beta_N = \left(\frac{\beta_j}{\beta_N}\right)^2\frac{U_N}{U_jF_j}d\beta_N$ (5.11)
2. Error due to the (range-dependent) lidar ratio	$\varepsilon_{j,2} = \sum_{k=1}^{N}\frac{\partial\beta_j}{\partial S_k}dS_k = 2\beta_j dI_{j,1} - \frac{2\beta_j^2}{U_jF_j}dI_{j,2} - \frac{4\beta_j^2}{U_jF_j}dI_{j,3}$ (5.12)
where	$dI_{j,1} = \sum_{k=j}^{N} w_k\beta_k^{mol}dS_k$ (5.13)
	$dI_{j,2} = \sum_{k=j}^{N} w_kU_kF_kdS_k$ (5.14)
	$dI_{j,3} = \sum_{k=j}^{N} w_kS_kU_kF_kdI_{k,1}$ (5.15)
3. Error due to the observation noise (range cells 1..N-1)	$\varepsilon_{j,3} = \sum_{k=1}^{N-1}\frac{\partial\beta_j}{\partial P_k}dP_k = \frac{\beta_j}{U_j}dU_j - \frac{2\beta_j^2}{U_jF_j}\sum_{k=j}^{N} w_kS_kF_kdU_k$ (5.16)
4. Error due to the observation noise at the calibration cell (range cell N)	$\varepsilon_{j,4} = \frac{\partial\beta_j}{\partial P_N}dP_N = -\frac{\beta_j^2}{\beta_NU_jF_j}dU_N - \frac{2\beta_j^2}{U_jF_j}w_NS_NdU_N$ (5.17)
Total backscatter-coefficient error (case $j = N$, calibration point)	$\|d\beta_j\| = \|d\beta_N\|;\qquad j = N$

Table 5.2: Total backscatter-coefficient error-propagated terms for the KFS backward inversion method in response to error sources Eqs.(5.1)-(5.4) (see Section 5.3.1). For the case $j = N$, the total backscatter-coefficient error is directly the calibration error. For the KFS forward method consider Section 5.2.4 changes.

5.3.2 Computation: The stochastic approach

Though systematic errors (backscatter-coefficient calibration and lidar ratio) and random errors (noise) are fundamentally different, a common treatment using error propagation and error variances is possible. Details can be found in Eq.(4.20), [*Barlow*, 1989a].

Since no a priori knowledge of either the magnitude or the sign of the calibration and lidar-ratio errors is assumed, they are treated as drawn from independent probability distribution functions (pdf), usually Gaussian or uniform. While the assumption of a uniform pdf assumes no a priori knowledge of the calibration (just that the systematic deviation has constant probability over the width of the pdf) the Gaussian distribution assumes the well-known

bell-shaped probability distribution, i.e., a higher likelihood towards the mean value of the distribution or "most likely" assumed calibration. In the case of noise its pdf is associated to the normal distribution of noise, a physical property of the noise itself, not to a user's uncertainty.

The stochastic approach assumes that error sources $d\beta_N$ (calibration error), dS_k (lidar-ratio error) and dU_k (range-corrected noise perturbation, $dU_k = R_k^2 dP_k$, Eq.(5.4), dU_k and dP_k are formally equivalent) are independent Gaussian random variables with standard deviations, σ_{β_N}, σ_{S_k}, and σ_{U_k}, respectively. Thus, the backscatter-coefficient total-error standard deviation is computed by adding them in mean square form (Eq.(5.26), Table 5.3). Computation of the error standard deviations $\sigma_{\varepsilon_{j,1}}$ (error due to the backscatter-coefficient calibration) and $\sigma_{\varepsilon_{j,3-4}}$ (observation noise) from Table 5.2 is straightforward once Table 5.1 and the calculus tips used in the KLT kernel (Section 3B and Table 1, p.3386 in the KLT-counterpart paper) are followed. At this point, note that $G_N = 0$ and $F_N = 1$ (Eqs.(5.5)-(5.6)) and that, when considering error sources (3) and (4), $d\left(U_k F_k\right) = F_k dU_k,\ k = 1..N$, because the only "fluctuating" variable due to noise is the range-corrected power, U_k. As previously mentioned, computation of the $\sigma_{\varepsilon_{j,2}}$ (lidar ratio) requires a specific analysis for the KFS kernel. Detailed comments follow:

5.3.2.1 Comments on error sources 1, 3 and 4 ($\sigma_{\varepsilon_{j,1}}$ and $\sigma_{\varepsilon_{j,3-4}}$)

i. Errors due to the backscatter-coefficient calibration ($\sigma_{\varepsilon_{j,1}}$) / observation noise at the calibration cell ($\sigma_{\varepsilon_{j,4}}$).
From Eq. (5.27) and Eq.(5.38), Table 5.3 both error sources can be related to one another as

$$\frac{\sigma_{\varepsilon_{j,1}}}{\sigma_{\varepsilon_{j,4}}} \approx \left|\frac{U_N}{\beta_N}\right| \frac{\sigma_{\beta_N}}{\sigma_{U_N}} = \mathrm{SNR_N} \varepsilon_r^{\beta_N} \ , \tag{5.18}$$

where $\varepsilon_r^{\beta_N} = \sigma_{\beta_N}/\beta_N$ is the relative error in the backscatter-coefficient calibration and SNR_N is the SNR at the boundary calibration range, $R = R_N$. Eq.(5.18) reencounters Eq.(28) in the KLT-counterpart paper and, therefore, the effects of these two error sources on the inverted backscatter coefficient are qualitatively the same on both KLT and KFS kernels.
ii. Errors due to the observation noise ($\sigma_{\varepsilon_{j,3}}$ and $\sigma_{\varepsilon_{j,4}}$). When analysing $\sigma_{\varepsilon_{j,3}}$ (Eqs. (5.36)-(5.37), Table 5.3) it arises that the backscatter-coefficient error on the j-th range cell is inversely proportional to: (a) the range-dependent SNR at the cell of interest (j-th cell), $SNR_j = U_j \big/ \sigma_{U_j}$, and (b) to the cross-cell SNR defined as $SNR_{j,k} = U_j/\sigma_{U_k}$ (see cumulative term $\sigma_{HU,j}^2 \big/ U_j^2$). (a) and (b) are analogous to the "instantaneous noise effect" (i.e., arising from the same j-th cell) and to the "memory noise effect" (i.e., $\sigma_{HU,j}^2$ here) outlined in [*Comerón et al.*, 2004], Section 4.A.3, p.3389 of the KLT-counterpart paper, and earlier by Knauss [*Knauss*, 1982], who predicted an inverse SNR sensitivity.

Concerning $\sigma_{\varepsilon_{j,4}}$, Eq.(5.38) can be rewritten as $\sigma_{\varepsilon_{j,4}} \approx \left|\frac{\beta_j^2 U_N}{\beta_N U_j F_j}\right| \frac{1}{SNR_N}$ (see similar justification steps in p.3383). It emerges that a finite SNR at the calibration range propagates noise errors down to all the inversion range.

5.3.2.2 Error source 2: Error due to a (range-dependent) lidar ratio, $\sigma_{\varepsilon_{j,2}}$.

Correlated lidar-ratio errors with range.- A widely used assumption in practice is to define a lidar-ratio relative error, p (or systematic error) relating the range-dependent lidar-ratio

error and the true atmospheric lidar ratio as

$$dS(R) = pS(R) \Leftrightarrow dS_k = pS_k. \tag{5.19}$$

Equivalently, the atmospheric lidar ratio is assumed to lie within $S(R)(1 \pm p)$ at 1-σ confidence level from the user's side.

Error bound computation uses first-order series expansion of Eq.(5.3) around p. Towards this end Eq.(5.3) is rewritten as a function of lidar-ratio perturbation p as

$$\beta_j(p) = \frac{\beta_N U_j F_j(p)}{U_N + 2\beta_N H_j(p)}, \tag{5.20}$$

where the incremental auxiliary function $F_j(p)$ is related to $G_j(p)$ via Eq.(5.5), and $G_j(p)$ and $H_j(p)$ (Eqs.(5.6)-(5.7)) become

$$G_j(p) = \begin{cases} (1+p)\, g_{j,1} - g_{j,2}; & j < N \\ 0 & j = N \end{cases}, \tag{5.21}$$

where

$$g_{j,1} = \sum_{i=j}^{N} w_i S_i^{aer} \beta_i^{mol}, \quad g_{j,2} = \sum_{i=j}^{N} w_i S_i^{mol} \beta_i^{mol}, \tag{5.22}$$

and

$$H_j(p) = (1+p) \sum_{i=j}^{N} w_i S_i^{aer} U_i F_i(p). \tag{5.23}$$

From Eqs.(5.21)-(5.22) above and Eq.(5.5), $F_j(p)$ takes the form

$$F_j(p) = \exp[2G_j(p)] = F_j(0) \exp(2pg_{j,1}). \tag{5.24}$$

Finally, the backscatter-coefficient error is obtained after first-order series expansion as

$$\sigma^C_{\varepsilon_{j,2}} = |d\beta_j^S| \approx \left| \left. \frac{\partial \beta_j}{\partial p} \right|_{p=0} p \right|, \tag{5.25}$$

where superscript "C" is a reminder of "correlated" and subscript "S" of "due to the lidar ratio". Eq.(5.25) is computed by substituting the correlation condition of Eq.(5.19) into the general expression of the propagated lidar-ratio error, $\varepsilon_{j,2}$ (Eqs.(5.12)-(5.15)). The result is summarised in Table 5.3 and gives symmetrical error bounds ($\pm$ sign of p). The integral term $g_{j,1}$ in Eq.(5.21) has been renamed to $I_{j,1}$ for notation unification reasons.

Uncorrelated lidar-ratio errors with range.- As discussed in the KLT-counterpart paper this hypothesis is less realistic for it assumes that lidar ratio errors between any two different range cells (and, in particular, from adjacent range cells) are completely different *random realizations* (i.e., uncorrelated ones, $E[dS_i dS_j] = 0; \quad i \neq j$) that can average out during KFS integration. As a result, a lower backscatter-coefficient error bound, $\sigma_{\varepsilon_{j,2}}$ is obtained (Table 5.3). Its calculus departs from Eqs.(5.12)-(5.15), and interprets lidar-ratio errors, dS_k, as uncorrelated random variables with variances $\sigma^2_{S_k}$ ($k = 1..N$).

WHAT MODELS	FORMULA
Total backscatter-coefficient error bound (case $j < N$) where	$\sigma_{\beta_j} = \left(\sigma^2_{\varepsilon_{j,1}} + \sigma^2_{\varepsilon_{j,2}} + \sigma^2_{\varepsilon_{j,3}} + \sigma^2_{\varepsilon_{j,4}}\right)^{\frac{1}{2}}$ (5.26)
1. Error due to the backscatter-coefficient calibration	$\sigma_{\varepsilon_{j,1}} = \left\lvert \left(\frac{\beta_j}{\beta_N}\right)^2 \frac{U_N}{U_j F_j} \right\rvert \sigma_{\beta_N}$ (5.27)
2. Error due to the (range-dependent) lidar ratio (correlated case)	$\sigma^C_{\varepsilon_{j,2}} = \lvert p \rvert \left\lvert 2\beta_j I_{j,1} - \frac{2\beta_j^2}{U_j F_j} I_{j,2} - \frac{4\beta_j^2}{U_j F_j} I_{j,3} \right\rvert$ (5.28)
where	$I_{j,1} = \sum_{k=j}^{N} w_k \beta_k^{mol} S_k$ (5.29)
	$I_{j,2} = \sum_{k=j}^{N} w_k U_k F_k S_k$ (5.30)
	$I_{j,3} = \sum_{k=j}^{N} w_k S_k U_k F_k I_{k,1}$ (5.31)
(uncorrelated case)	$\sigma_{\varepsilon_{j,2}} = \left[(2\beta_j)^2 \sigma^2_{I_{1,j}} + \left(\frac{2\beta_j^2}{U_j F_j}\right)^2 \sigma^2_{I_{2,j}} + \left(\frac{4\beta_j^2}{U_j F_j}\right)^2 \sigma^2_{I_{3,j}} \right]^{\frac{1}{2}}$ (5.32)
where	$\sigma^2_{I_{1,j}} = \sum_{k=j}^{N} \left(w_k \beta_k^{mol}\right)^2 \sigma^2_{S_k}$ (5.33)
	$\sigma^2_{I_{2,j}} = \sum_{k=j}^{N} \left(w_k U_k F_k\right)^2 \sigma^2_{S_k}$ (5.34)
	$\sigma^2_{I_{3,j}} = \sum_{k=j}^{N} \left(w_k S_k U_k F_k\right)^2 \sigma^2_{I_{1,k}}$ (5.35)
3. Error due to the observation noise (range cells 1..N-1)	$\sigma_{\varepsilon_{j,3}} = \left[\left(\frac{\beta_j}{U_j}\right)^2 \sigma^2_{U_j} + \left(\frac{2\beta_j^2}{U_j F_j}\right)^2 \sigma^2_{HU,j} \right]^{\frac{1}{2}}$ (5.36)
where	$\sigma^2_{HU,j} = \sum_{k=j}^{N} \left(w_k S_k F_k\right)^2 \sigma^2_{U_k}$ (5.37)
4. Error due to the observation noise at the calibration cell (range cell N)	$\sigma_{\varepsilon_{j,4}} = \left(\left\lvert \frac{\beta_j^2}{\beta_N U_j F_j} \right\rvert + \left\lvert \frac{2\beta_j^2}{U_j F_j} w_N S_N \right\rvert \right) \sigma_{U_N} \approx \left\lvert \frac{\beta_j^2}{\beta_N U_j F_j} \right\rvert \sigma_{U_N}$ (5.38)
Total backscatter-coefficient error bound (case $j = N$, *calibration point)*	$\sigma_{\beta_j} = \sigma_{\beta_N}$

Table 5.3: *First-order* analytical (explicit) error bounds for the KFS backward inversion method in response to error sources Eq.(5.1)-(5.4) (see Section 5.3). For the case $j = N$, the backscatter-coefficient error bound is directly the calibration error bound. For the KFS forward method consider Section 5.2.4 changes.

5.4 DISCUSSION

First-order error bounds (Table 5.3) are validated here (in altered order for contextual reasons) using a multi-wavelength Monte Carlo (MC) approach at 532-nm (VIS) wavelength. In the MC simulation, for each wavelength, a set of 100 aerosol backscatter-coefficient profiles has been inverted in response to 100 noise-corrupted power lidar returns generated from a synthetic backscatter atmospheric profile (simulation input) and a range-dependent SNR profile (Figure 5.1).

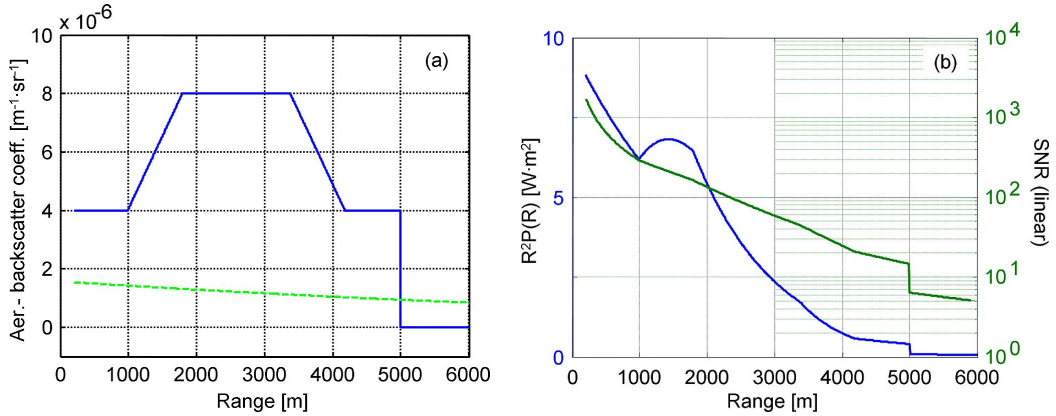

Figure 5.1: Simulated lidar signals. (a) Aerosol backscatter-coefficient atmospheric profiles (blue trace) and related molecular (Rayleigh) levels (green). (b) Noisy range-corrected power returns (blue) and related signal-to-noise ratio (SNR, green) profiles.

The two-component atmospheric model combines a trapezium-shaped aerosol-backscatter component at 532 nm along with a U.S. standard atmosphere molecular model [*Bodhaine et al.*, 1999] (15°C and 1013.15 hPa ground-level boundary conditions). The aerosol backscatter profile simulates fast slopes in an aerosol layer aloft measured with the RSLAB lidar (slant path, 54-deg elevation angle). An approximate mean total atmospheric extinction, $\bar{\alpha} \approx 3 \times 10^{-4} m^{-1}$, which corresponds to a trapezium bottom base, $\alpha_{bottom} \approx 2 \times 10^{-4} m^{-1}$ (equivalently, 20 km visibility) and top base, $\alpha_{top} = 2\alpha_{bottom}$, is simulated. The total optical depth is $\tau \approx 1.5$. Aerosol and molecular components are assumed λ^{-1} and λ^{-4} spectral dependencies, respectively. For comparison, a wavelength-independent aerosol lidar ratio, $S^{aer} = 50sr$ is used and all the three lidar channels are normalised to a SNR of 5 at the maximum range, $SNR(R_{\max}) = 5$ (a relatively modest figure in practice). The inversion interval ranges from $R_{\min} = 0.2km$ to a maximum range, $R_{\max} = 6km$. The calibration range is chosen at $R_{cal} = R_{\max} = 6km$ coinciding with a molecular reference range in the 5-6 km interval (see Section 5.2.1).

Lidar system parameters are based on the new MRL (Multispectral elastic-Raman Lidar) of the RSLAB (40/130/130-mJ energy at 355/532/1064-nm wavelength, respectively, 3.6-ns pulse width, Nd:YAG laser source; 35.5-cm aperture, 3.9-m focal-length telescope). As described in Chapter 2 the VIS channel is PMT (Photo-Multiplier Tube) based with an approximate reception channel NEP (Noise Equivalent Power), $NEP_s^{532} = 7.7 \times 10^{-15} \left[W \cdot Hz^{-1/2}\right]$. The SNR model used is described in [*Rocadenbosch et al.*, 1998], Annex A, and assimilates signal-shot photo-induced, dark-shot, and thermal noise components into a single range-dependent noise-equivalent variance.

5.4.1 Error sources 3-4: Errors due to the observation noise (Section 5.3.2.1).

Error source 3: Observation noise corrupting all range cells except the calibration cell ($\sigma_{\varepsilon_{j,3}}$ in Table 5.3, refer to Figure 5.2). According to the superposition principle the simulation runs with $SNR(R)$ *for* $R \neq R_{cal}$, Figure 5.1b, and all other error sources inactive, that is, $SNR(R_{cal}) \to \infty$ (noiseless return power at the calibration cell, error source (4)), perfect backscatter-coefficient calibration (error source (1)), and "true" atmospheric aerosol lidar ratio (error source (2)).

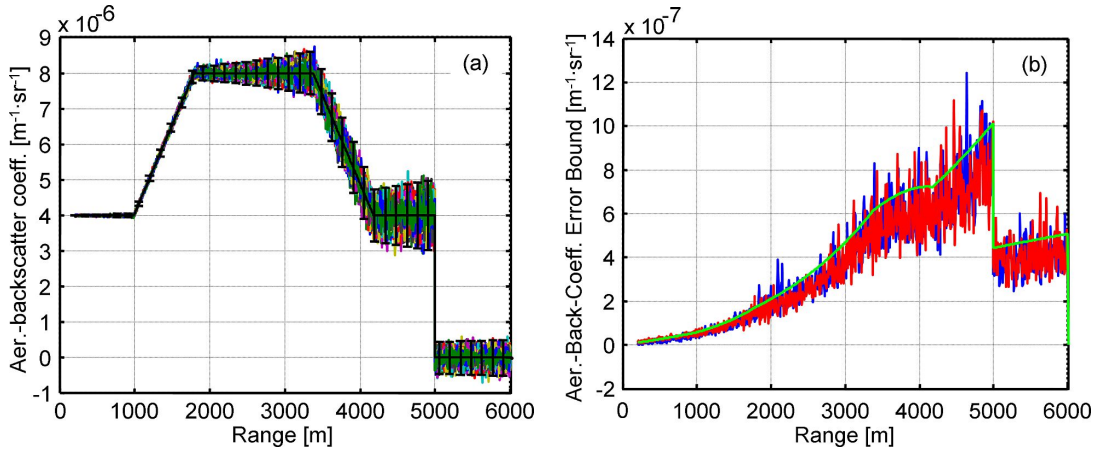

Figure 5.2: Analysis of error source Eq.(5.3) ($\sigma_{\varepsilon_{j,3}}$ in Table 5.3, see Section 5.3.2.1.ii): Noise in the return power corrupting all range cells except the calibration cell (SNR profile in Figure 5.1b). (a) Aerosol backscatter-coefficient realizations from Monte Carlo (MC) inversion (100 signal realizations) with superimposed *first-order* analytical error bounds (vertical error bars) at 3σ. (b) Amplitude of the backscatter-coefficient error bounds as a function of range: Comparison between MC error bounds (noisy traces) and first-order analytical error bounds (green trace).

Figure 5.2a plots the envelopes of the family of the MC aerosol-backscatter inverted profiles along with *first-order* analytical error bounds (Eq.(5.36), Table 5.3) computed at 3σ (analytical error bounds are plotted as vertical error bars centered in the input "true" atmospheric backscatter-coefficient profile) while Figure 5.2b compares their error amplitudes. The error amplitudes represent the difference between the upper and lower backscatter-coefficient error bounds and the true atmospheric backscatter-coefficient profile. In Figure 5.2b, upper and lower MC error bounds superimpose and appear as two noisy traces. Because of the first-order series expansion, first-order analytical error bounds are always symmetric. Besides, Figure 5.2b shows perfect agreement between both MC and first-order analytical error bounds.

Figure 5.2 shows that errors increase with range in response to a progressively decreasing range-dependent SNR (Figure 5.1b). An explanation for that is that the $\sigma_{\varepsilon_{j,3}}$ term $(\beta_j/U_j)\,\sigma_{U_j} = \beta_j/SNR_j$ in Eq.(5.36), Table 5.3 is inversely proportional to the SNR and directly proportional to the backscatter coefficient. Besides, the term $\sigma_{HU,j}$ (Eq.(5.37)) becomes numerically much lower because noise averages out when integrating.

Error source 4: Observation noise corrupting the calibration cell ($\sigma_{\varepsilon_{j,4}}$ in Table 5.3, refer to Figure 5.3). Simulation conditions are analogous to those used for the error source Eq.(5.3) above except that now $SNR(R_{cal}) = SNR_N = 5$ and $SNR(R) \to \infty$, $R \neq R_{cal}$.

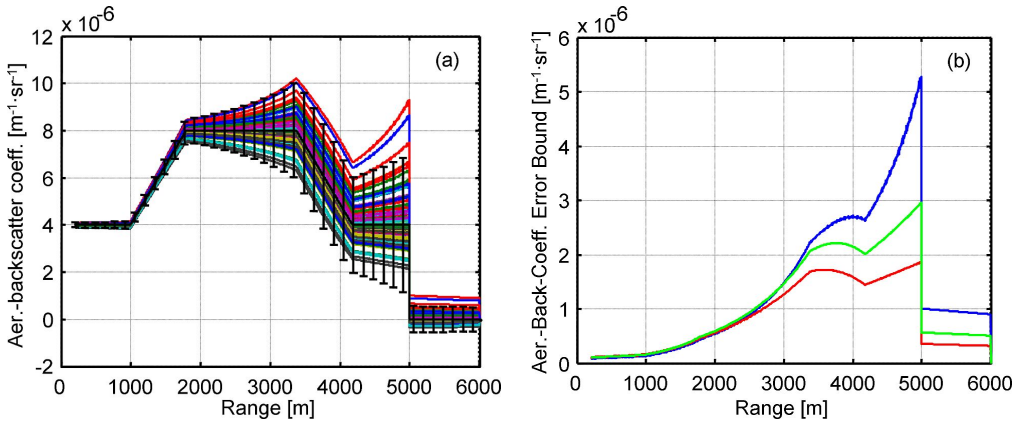

Figure 5.3: Analysis of error source Eq.(5.4) ($\sigma_{\varepsilon_{j,4}}$ in Table 5.3, see Section 5.3.2.1.ii): Noise in the return power at the calibration range ($SNR(R_{cal}) = 5$, $SNR(R) \to \infty$, $R \neq R_{cal}$). (a) Same description as in Figure 5.2a. (b) (Green trace) *First-order* analytical error-bound amplitudes at 3σ. (Blue/red traces) MC error-bound amplitudes (blue/red traces correspond to upper/lower MC error bounds, respectively). Note that MC error bounds cease to be symmetrically distributed for large errors.

Figure 5.3a shows that the effects of the observation noise at the calibration cell propagate down to all the inversion cells in accordance with [*Comerón et al.*, 2004]. Additionally, it has been found that the amplitude of the error-propagated errors is largely influenced by the boundary-layer transition at 5 km and the simulation wavelength. Figure 5.3b shows fairly good agreement between *first-order* analytical error bounds ($\sigma_{\varepsilon_{j,4}}$ in Table 5.3) and MC error bounds, evidenced by first-order error bounds falling in between upper and lower MC error bounds. In contrast to what happened when studying the error source Eq.(5.3), MC error bounds are no longer symmetric. An explanation for that is that noise at the calibration range tends to be the dominant error source ($\sigma_{\varepsilon_{j,4}} \geq \sigma_{\varepsilon_{j,3}}$ over the whole inversion range), hence causing that larger backscatter-coefficient errors cease to be Gaussian distributed.

Superposition of error sources 3-4: Observation noise corrupting all cells ($\sigma_{\varepsilon_{j,3-4}}$ in Table 5.3, refer to Figure 5.4). *First-order* analytical (explicit) error bounds ($\sigma_{\varepsilon_{j,3-4}}$) are compared with the *implicit integral* ones. Both error bounds are computed at 3σ ($p = 99.73\%$ probability that an inverted backscatter-coefficient realization falls within the error bounds). To compute first-order error bounds $3\sigma_{\varepsilon_{j,3-4}}$ (Table 5.3) is used.

Because upper and lower integral error bounds must be solved for each range cell and the solutions become numerically ill-conditioned for dense atmospheres ($\tau > 2$, approximately), they have only been computed for a discrete set of six ranges, from 1 to 6 km, equi-spaced 1 km. In nearly all simulation runs the upper and lower MC error bounds computed with 100 lidar signal realizations coincided with the integral error bounds (i.e., the exact theoretical reference) so that the MC error bounds can be considered reliable bounds of the 3-σ inverted backscatter-coefficient population and, therefore, equivalent trustworthy extrapolations of the integral "exact" error bounds over all the inversion range cells.

Figure 5.4a shows fairly good performance of the first-order analytical error bounds, which give error bound amplitudes in between those of the MC error bounds or slightly closer to the MC lower error-bound. Figure 5.4b evidences that for these practical levels of SNR (Figure 5.1b) *first-order* error bounds give fairly acceptable estimates as compared with the MC and *implicit-integral* error bounds with the advantage of being formulated in explicit form, being simpler to compute, and providing range-resolved information.

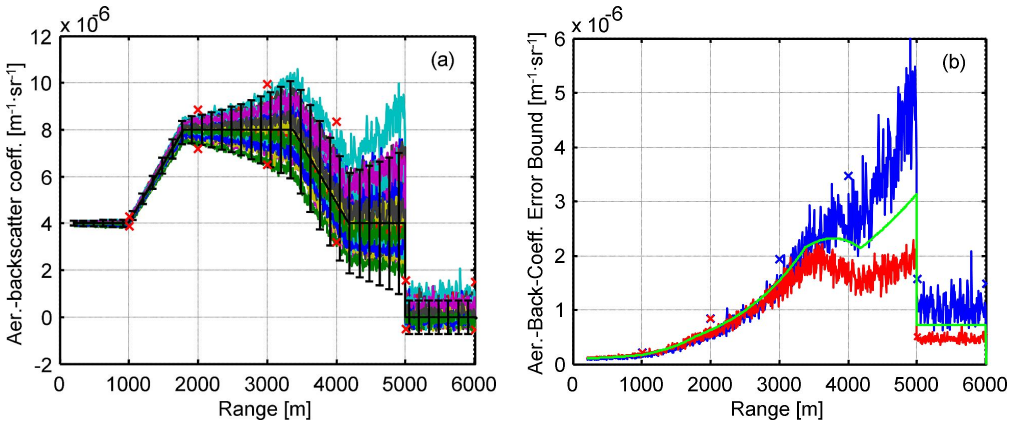

Figure 5.4: Superposition of error sources Eqs.(5.3) and (5.4) ($\sigma_{\varepsilon_{j,3-4}}$ in Table 5.3, see Section 5.3.2.1.ii): Noise corrupting all range cells. Comparison among first-order, MC, and the implicit-integral error bounds of [*Comerón et al.*, 2004]. **(a)** Aerosol backscatter-coefficient realizations: (Upper/lower crosses) *Implicit-integral* upper and lower error-bound amplitudes at 3σ, respectively. (Noisy traces) Family of MC inverted backscatter-coefficient profiles. (Vertical error bars) First-order error-bound amplitudes at 3σ. **(b)** Amplitude of the backscatter-coefficient error bounds as a function of range: (Green trace) *First-order* analytical error-bound amplitudes at 3σ. (Blue/red noisy traces) Upper/lower MC error-bound amplitudes, respectively. (Blue/red crosses) *Implicit-integral* upper and lower error-bound amplitudes at 3σ, respectively.

5.4.2 Error source 1: Errors due to the backscatter-coefficient calibration ($\sigma_{\varepsilon_{j.1}}$ in Table 5.3, refer to Figure 5.5).

Though being of systematic nature, the sensitivity behaviour of this error source is qualitatively identical to that of the noise at the calibration range (error source (4), Figure 5.3). Hence, analogous plots are retrieved (figure not shown) because according to Eq.(5.18) the error standard deviation of these two error sources on the inverted backscatter coefficient ($\sigma_{\varepsilon_{j.1}}$ and $\sigma_{\varepsilon_{j.4}}$, respectively) can be related to one anoher by a scaling factor $C = \mathrm{SNR_N}\varepsilon_r^{\beta_N}$. That is, the error-bound amplitude plots for this error source Eq.(5.1) become Figure 5.3b scaled by $C = 0.5$ when a relative backscatter-coefficient calibration error $\varepsilon_r^{\beta_N} = \sigma_{\beta_N}/\beta_N = 0.1$ is simulated ($SNR_N = 5$ in Figure 5.3a). For example, when in Figure 5.3b the first-order error-bound amplitude at 5 km is $3{\times}10^{-6}$ it is half this value ($3{\times}10^{-6}{\times}$C) in Figure 5.5. Therefore, identical conclusions apply. This is best corroborated in Figure 5.5 , which uses an error strength, $\varepsilon_r^{\beta_N} = 0.1$.

5.4.3 Error source 2: Errors due to the lidar ratio ($\sigma^C_{\varepsilon_{j,2}}$ in Table 5.3, refer Figure 5.6).

Simulation conditions for this case assume noiseless power lidar returns ($SNR(R) \to \infty$ in all range cells), perfect backscatter-coefficient calibration, and correlated lidar-ratio errors defined by a relative error figure, p (Eq.(5.19)). p is simulated both as Gaussian random variable with standard deviation $p = 10\%$ and $p = 30\%$ (3-σ deviation equal to 30% and 90%, respectively) and as uniform random variable with standard deviation $p' = 3p$ so as to ensure similar error spans in both probability distributions.

When the simulation is carried out for low-error intensities (p=10%, which corresponds to a *uniform* error span of ±30%, figure not shown) the error bounds tend to distribute more symmetrically around the "true" optical atmospheric backscatter-coefficient profile. This is

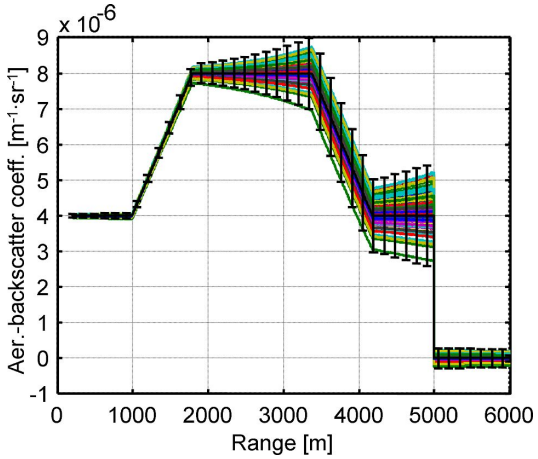

Figure 5.5: Analysis of error source Eq.(5.1) (aerosol backscatter-coefficient calibration, $\sigma_{\varepsilon_{j,1}}$ in Table 5.3, see Section 5.3.2.1.i). Same description as in Figure 5.2a. Error strength: ±10% Gaussian fluctuation over the nominal backscatter Rayleigh level at the calibration range ($R_{cal} = R_{\max} = 6km$).

no longer the case for higher error intensities. Thus, in Figure 5.6 first-order analytical error bounds are intercompared assuming Gaussian distribution of the lidar-ratio user uncertainty (p=30%). It is shown that first-order error bounds at 3-σ encompass most of the inverted backscatter-coefficient population though they are slightly down biased.

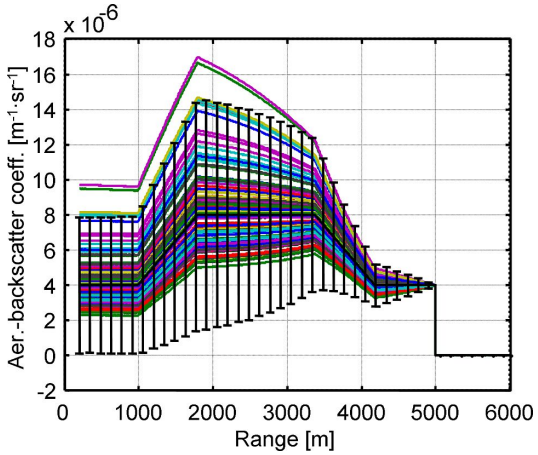

Figure 5.6: Analysis of error source Eq.(5.2) ($\sigma^{C}_{\varepsilon_{j,2}}$ in Table 5.3, see Section 5.3.2.2): Performance of first-order error bounds in the assessment of correlated lidar-ratio errors. Error strength, $p = 30\%$. Gaussian fluctuation over the nominal aerosol lidar ratio. Same description as in Figure 5.2a.

5.5 CONCLUSIONS

First-order analytical error bounds (Section 5.3) have been formulated in *explicit* analytical form for the two-component KFS lidar inversion algorithm in response to error sources 1-4 ($\sigma_{\varepsilon_{j,1-4}}$ in Table 5.3). Error bounds have been validated using a Monte Carlo's (MC) method.

Such error bounds provide the classic error-propagation approach and give fairly approximate symmetric error bounds lying in between upper and lower MC error bounds, their

amplitudes being representative of a large part of the inverted backscatter-coefficient profile population in practical situations ($SNR \geq 5$, lidar-ratio relative error strength, $p \leq 30\%$, Section 5.4). Yet, strictly speaking, first-order error bounds only yield approximate error bounds. Thus, with higher error intensities (lower SNRs and/or higher user error uncertainties), upper and lower MC error bounds become progressively asymmetric, property that first-order error bounds fail to estimate.

It has been shown that when the error source is assumed to follow a Gaussian distribution (case of the random noise or case of the user's uncertainty for systematic errors), first-order error bounds computed at 3σ are in acceptable agreement with 3-σ statistical confidence limits in inversion situations with SNRs at the maximum range above approximately 5 and user's systematic-error uncertainties below 10%.

As in the KLT kernel, the effects of noise at the calibration cell (error source 4) are dominant (particularly towards the NIR) in front of the noise from all other range cells (error source 3). Though fundamentally different in their physical nature, the contribution of error sources (1) and (4) to the backscatter-coefficient error can be accounted via sensitivity Eq.(5.18), all of which leaves error sources (4) and (2) as the key ones.

The explicit analytical error bound formulation summarised in Table 5.3 is -to the best of our knowledge- new in the state of the art of lidar inversion algorithms.

Chapter 6

SYSTEM INTEGRATION AND PRELIMINARY VALIDATION

In this chapter the new 6-channel multi-spectral lidar system of the RSLAB and a preliminary system validation including a first intercomparison campaign is presented. In addition to the 3+2 aerosol channels ranging from the UV to the NIR, the lidar instrument includes a water-vapour channel. This multi-spectral capabilities enable aerosol studies on a wider scale such as inversion of extinction and backscatter-coefficient profiles, aerosol lidar ratio, Ångström coefficients and color ratios (i.e., spectral dependence), identification of aerosol layers and, when combined with appropriate inversion algorithms, retrieval of microphysical properties (e.g., volumetric and surface concentrations, distribution of size parameters, index of refraction) and type of aerosols (urban pollution, dust, maritime, etc.). The system has recently started regular operation as part of the European Aerosol Research Lidar Network (EARLINET).
This chapter is divided into two parts: In Section 6.1 system integration is presented focusing on the main hardware and control software units involved (Spanish NSF, projects TEC2006-07850 and TEC2009-09106). At the end of this part a specification scheme concerning full automation of the system is presented as part of the infrastructure project UNPC10-4E-442. Section 6.2 illustrates validation of the RSLAB lidar system by means of SPALI-10 intercomparison campaign, which is part of EARLINET quality assurance actions. At the end a summary list of the field campaigns carried out in this Ph.D. is presented. Section 6.2 is based on coauthored conference papers [*Molero et al.*, 2011, 2012].

6.1 SYSTEM INTEGRATION

The RSLAB multi-spectral lidar system uses a 20-Hz pulsed Nd:YAG laser source emitting simultaneously 130-mJ energy at 1064 nm, 130 mJ at 532 nm and 40 mJ at 355 nm, and a 355.6-mm aperture diameter, f/11 Schmidt-Cassegrain telescope in reception (see Table 2.1 for details). Both emission and reception systems are mounted on a tri-dimensional scanning platform. The fiber-coupled polychromator (Chapter 4) is responsible for splitting the composite light return into the six wavelengths of interest (elastic channels at the emission wavelengths above, nitrogen-Raman channels at 387 and 607-nm wavelengths and water-vapour channel at 407 nm). A control rack holds the optical polychromator subrack, the detector control subrack, the 6-channel acquisition unit subrack, Ethernet switch for remote control over the Internet, and a LabView^{TM}-based industrial control computer. While description of the optical system is presented in Section 6.1.1, system control is presented at hardware level (control rack) and software level in Section 6.1.2.

6.1.1 HARDWARE LEVEL

6.1.1.1 Optical transmission-reception subsystem

Telescope.- Raman channels require large telescope apertures to deal with the faint Raman returns (with typical Raman returns 3-4 orders lower than elastic ones, Figure 2.4a). Ideally, moderate f-numbers (the ratio of the focal-length of a lens or a lens-system to the effective diameter of its aperture) are needed to ensure reduced tube lengths and hence, weight with a view to ease telescope assembly in the lidar scanning mechanical structure (Figure 6.1).

The choice of a Cassegrain telescope in reception (more precisely, a Schmidt-Cassegrain type) is justified because its optical architecture enables a short tube length while usually having a long focal length. Cassegrain design provides moderate-to-high f-numbers (f/11 for the RSLAB lidar, $f\# = 11$, $D = 355.6 - mm$ aperture, $f = 3910mm$) and allows achieving FOV figures as low as a few hundred rad ($\sim$380 μrad for the simplest case of a 3-mm diameter detector placed at the telescope focal plane, i.e., without field lens, see Section 3.2.1). Technologically, this has lead to telescope lengths that are half of the length of a comparable Newtonian one [*Kovalev*, 2004]. Configuration of such narrow FOV also gives the benefit of efficient background light reduction with as low levels as 1.24×10^{-14} [W] at 386.7 nm, 607.4 nm and 407.5 nm (night-time operation, Eq.(2.21)). The larger aperture of the f/11 telescope provides a SNR enhancement of almost 10 times in comparison to the old $f/10$ telescope ($D = 203.2 - mm$ aperture).

In the RSLAB lidar system a laser-telescope biaxial configuration is used. Because the starting range of full overlap (R_{ovf}) (equivalently, the near-range sounding capability of the lidar) is inversely proportional to the receiving optics FOV, the very narrow FOV of the f/11 telescope yields $R_{ovf} \simeq$1000 m, Figure 3.12b. As discussed in Chapter 3 there is a way out to lower the R_{ovf} by including a $\sim$25.4-mm focal-length field lens at the telescope focal plane. The biaxial geometry, inclusion of a field-lens, and the detection sensitivity determine the dynamic range in reception.

Fiber coupling.- The simplest mechanical solution to couple the composite light return collected by the telescope to the polychromator is the use of an optical fiber coupled to the telescope focal plane. Its impact on the OVF of the system has been studied in Section 3.4.2. For optimum capture of the backscattered radiation the numerical aperture of the fiber (NA) should be compatible with the receiver's aperture ratio or f-number (f/D), where D is the diameter of the telescope primary mirror (entrance pupil). The optimum match of the fiber NA to the telescope f-number ($f\#$) requires [*Jenness et al.*, 1997]

$$f\# = 0.5 \left[\left(\frac{1}{NA} \right)^2 - 1 \right]^{1/2} . \tag{6.1}$$

For the f/11 Schmidt-Cassegrain telescope used a quite low fiber's NA is obtained (NA$\approx$0.045). The RSLAB lidar system uses a fiber bundle (without field-lens) with NA=0.12 (Table 2.1).

Polychromator unit.- The polychromator sub-rack (Figure 6.2, subrack E in Figure 6.4) is a 19-inch 4EH-height Eurorack (580 mm x 180 mm x 95 mm) housing the 1-inch optics polychromator unit described in Chapter 4. The detector array is composed of five

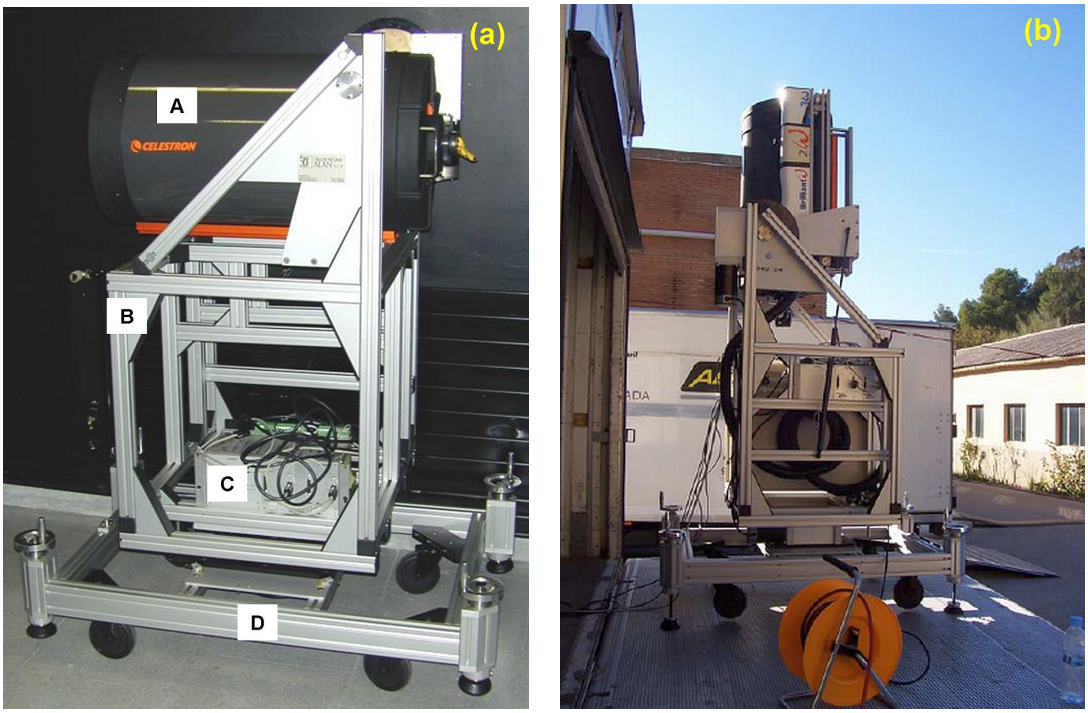

Figure 6.1: Mechanical integration of the RSLAB multispectral lidar system. (a) The f/11 Schmidt-Cassegrain telescope assembled in the tri-dimensional (elevation and azimuth) scanning platform. (b) Laser-telescope subsystem assembled into the scanning platform and pointing vertically to the atmosphere during SPALI10 campaign (Madrid, Oct. 18 - Nov. 5, 2010). The laser power supply is located in the inner part at the bottom of the aluminium structure. Labels: (A) Telescope (Celestron^{TM} CGE1400). (B) Scanning platform. (C) Electronic driver box of the scanning elevation/azimuth motors. (D) Base frame of the scanning platform (houses wheels for easy transportation).

Figure 6.2: The 6-channel polychromator built at the RSLAB. Labels: (L2) condensing lens, (D1-D4) dichroics, (BS1) beam splitter, (M11-M12) mirrors, (L41-L42) correcting lenses, (S) stepping motor, (C) cylinder including interference filter and focusing lens, (N) slot for the neutral density filter and diaphragm, (E) eye-piece lens pair, (PMT) PMT photodetectors, (APD) APD photodetector, and (EXTRA) extra future channel.

photomultiplier tubes (PMTs) and one avalanche photodiode (APD). Two of the five PMTs are used for the aerosol Raman channels at 386.7- and 607.4-nm wavelength (N_2-Raman shifts), one for the water-vapour Raman channel at 407.5-nm wavelength, and two others for the elastic channels at 354.7- and 532.1-nm wavelength. The APD is used for the 1064-nm elastic channel.

Figure 6.2 shows the different components integrating the polychromator. The condensing lens (L2, Figure 4.1) is placed in a holder attached to the polychromator input (L2 in Figure 6.2). D1 in Figure 6.2 shows the dichroic used for splitting the composite light return into two sets of wavelengths, 1) 354.7, 386.7 and 407.5 nm and 2) 1064, 607.4 and 532.1 nm (D1, Figure 4.1). D2-D4 in Figure 6.2 show the respective dichroics D2-D4 in Figure 4.1. BS1 in Figure 6.2 shows the beamsplitter mounted for splitting 386.7 and 407.5 nm wavelengths (BS1, Figure 4.1). M11 and M12 in Figure 6.2 show the mirrors mounted for diverting 532.1 and 407.5 nm wavelengths onto the respective photodetectors (M11-M12, Figure 4.1). L41 and L42 in Figure 6.2 show the correction lenses (L41-L42, Figure 4.1) used for reducing the beam divergence of (i) 1064, 607.4 and 532.1 nm channels and (ii) 386.7 and 407.5 nm channels, respectively.

The focusing lenses (L3, L31) and the respective interference filters (I1-I6), Figure 4.1, are assembled into Thorlab^{TM} aluminium cylinders (C in Figure 6.2) screwed to the optoelectronic receiver body, which consists of a slot (N in Figure 6.2) having inside the neutral density filter and the diaphragm. S in Figure 6.2 shows the micro-stepping motor mounted to automatically move the diaphragm and the neutral density filter. The eye-piece lens pair (E1 and E2, Figure 4.1) to overcome uneven spatial responsivity effects over the detector active area is assembled into a separate holder attached to the optoelectronic receiver body (E in Figure 6.2).

The APD detector used for the infrared channel (1064 nm) is housed into a XY-translation stage (Figure 4.2b) so as to ease precise positioning due to its small diameter (Table 2.1). The APD detector module (APD in Figure 6.2) includes a cooling stage to reduce thermal noise (Figure 2.6c). PMT detectors used for the remaining channels are labelled "PMT" in Figure 6.2. An extra channel for future integration is labelled "EXTRA" in Figure 6.2.

6.1.1.2 Control rack: Signal detection and acquisition

APD-based channel.- The new multispectral RSLAB lidar system uses Licel^{TM} Si-APD Module based on Perkin Elmer^{TM} C30956E detector for the 1064-nm channel. The detector module consists of a high-speed low-noise preamplifier, HV supply, and a thermoelectrically-cooled detector [*Licel*, 2007b, 2009a]. Thermo-electric (TE) cooling is necessary on account of the high level of thermal noise (Figure 2.6c).

PMT-based channels.- PMT-based detectors (Hamamatsu R-7400U/P model, [*Licel*, 2009b]) are used in all 5 other channels. This provides quite low dark current and hence dark noise levels (Table 2.1) and high photocurrent linearity (Figure 2.4b).

Data acquisition unit.- Simultaneous recording of near and far-range lidar signals [*Lange et al.*, 2012] requires dynamic ranges five orders of magnitude. The RSLAB lidar uses Licel^{TM} TR40-80 transient recorders and a common NI-DAQ data interface for data recording in mixed analog/photon counting mode, which after data gluing provides the required acquisition dynamic range. Figure 6.3 shows the architecture block diagram of such data recorders.

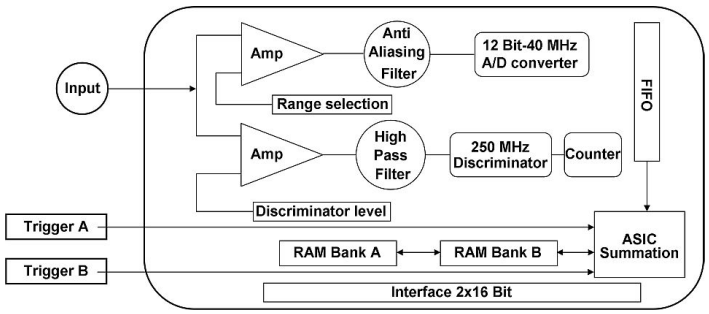

Figure 6.3: Block diagram of Licel^{TM} transient recorder (TR40-80). Source: [*Licel*, 2009c]

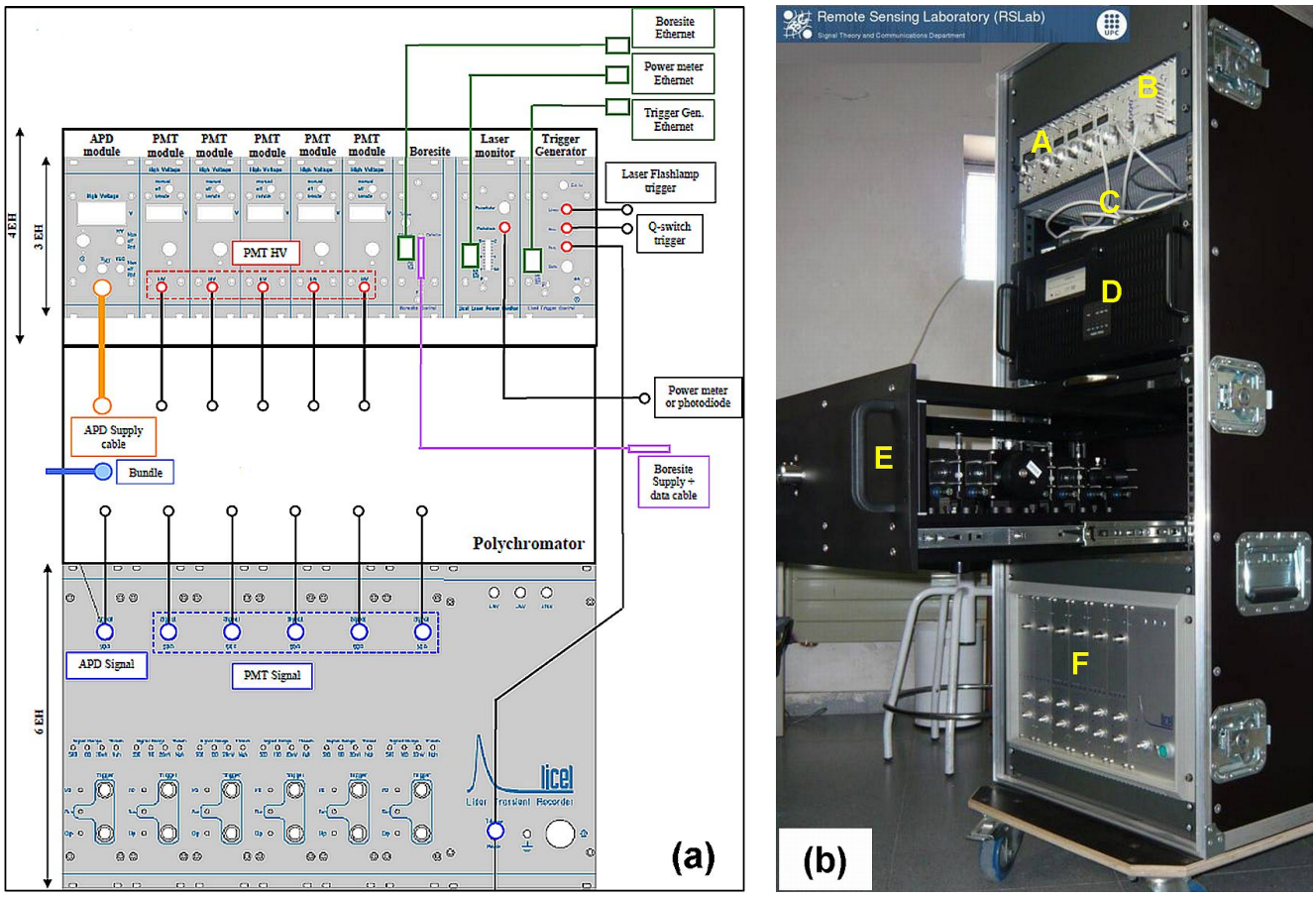

Figure 6.4: The RSLAB multispectral lidar control rack. (a) Schematic of the hardware connections. (b) Integrated control rack. Labels: (A) Photo-detectors power supply-and-control subrack. (B) Trigger, power-meter and boresite control subrack. (C) Ethernet switch. (D) Industrial-computer (host PC) subrack. (E) Polychromator subrack (open). (F) Transient recorders' subrack.

The recorder combines a 12-bit A/D converter (at 40 Msps) with a 250-MHz fast photon counting system. Signal averaging is performed by means of specially designed ASIC's. A high speed data interface to the host computer allows readout of the acquired signal. The recorder is comprised of a fast transient digitizer with an on-board signal averaging, a discriminator for single photon detection, and a multichannel scaler combined with preamplifiers for both analog/photon-counting systems [*Licel*, 2007b, 2009c].

For analog detection a hardware adder is used to write the the summed signal into a 24-bit wide RAM. Depending on whether trigger A or B is used, the signal is added to RAM A or B, which allows acquisitions of two repetitive lidar channels if these signals can be measured sequentially. The photon counting acquisition system includes a fast three-stage preamplifier and a discriminator with 64 threshold levels, controlled by the host computer. A time resolution of 50 ns without any dead time or overlap between two memory bins is achieved. The photon counting signal is written to a 16-bit wide summation RAM which allows averaging of up to 4094 acquisition cycles.
Since a high speed and high gain amplification is needed for photon counting, whereas a strictly linear amplification below the Nyquist frequency of the A/D converter is necessary for analog measurement, the integration of two complete acquisition chains from the preamplifier to the summation memory therefore enables to combine both techniques for increased linear dynamic range [*Licel*, 2009c].

Finally, Figure 6.4 shows the RSLAB multispectral lidar system control rack. The Ethernet switch enables intercommunication of the different Ethernet-based subracks as an instrumentation LAN (Local Area Network) and full remote control of the lidar system over the Internet.

6.1.2 SOFTWARE LEVEL

The software modules used to control the different hardware units of the RSLAB lidar system are fully based on Ethernet control and described in Labview^{TM} (Figure 6.4). Each software module is addressed at its respective Ethernet address to transfer data and communicate with the host computer.

The Transient Recorder Control Module.- Licel^{TM} transient recorder control module (Barcelona Acquis_2.vi, Figure 6.5) used in the RSLAB lidar system has been customized to control 6 transient recorders (Subrack F in Figure 6.4). The module is addressed at the Ethernet address 192.168.1.11 set as the hardware parameter. The typical data transfer rate is 200 kb/sec.

The transient recorder Ethernet control module works in the so called "push mode" as data transfer mode. In the push mode the transient recorders get their start, stop, and readout commands from the Ethernet controller without any direct interaction with the PC. The Ethernet controller then pushes the data to the PC. At the PC level, a periodic task reads the data when it becomes available from the TCP/IP buffer. This frees the PC from controlling the transient recorders by itself and reduces the communication load [*Licel*, 2007b]. LabView^{TM} data acquisition software (Barcelona Acquis_2.vi) is based on 'acquis.vi' software module of Licel^{TM} [*Licel*, 2007b] and consists of following configuration parameters (Figure 6.5):

1. Global information

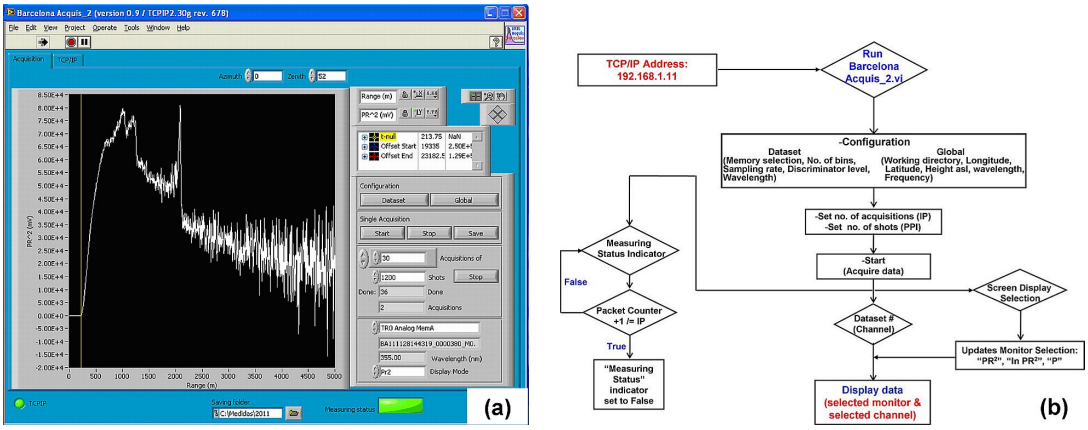

Figure 6.5: RSLAB lidar data acquisition program (Barcelona Acquis_2.vi). (a) User interface. (b) Flow chart. (Source: Chapter 6 in [*Licel*, 2007b]).

2. Dataset information.

The global information (Figure 6.6a) allows the user to set values that are stored in the header data file which tells later about what sort of conditions were existent at the time the data was acquired. These are global values which usually do not vary from measurement to measurement. The dataset information contains all the information needed to configure the transient recorders. One can set the configuration of the transient recorder information according to their own dataset configuration which is saved in the dataset configuration file (Acquis.ini). Figure 6.6b shows the various fields to be configured for each dataset such as

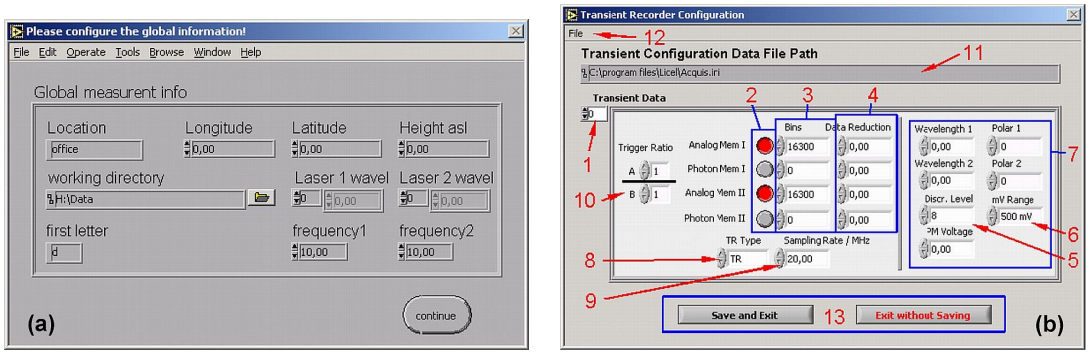

Figure 6.6: Configuration parameters of the RSLAB lidar data acquisition program (Barcelona Acquis_2.vi) shown in Figure 6.5. (a) Global configuration block. (b) Dataset configuration block. Source: Section 6.3 in [*Licel*, 2007b].

(follow labels in Figure 6.6b): The rack ID number of the transient recorder (label "1"); the four memory banks available, Analog Memory A, Photon Memory A, Analog Memory B, and Photon Memory B (label "2"); the number of bins to be read out ("label 3"); the data reduction allowed for binning (label "4"); the discriminator level set ($0 \leq$level≤ 63, which corresponds to a range of 0-24 mV) (label "5"); the input range values of the transient recorder (label "6"); comment parameters (label "7") including the laser wavelengths, polarisation and photodetector voltages used; transient recorder model (label "8", TR40-80 in our case); sampling rate (label "9", 40MHz in our case); trigger ratio (label "10", to be used only if acquisitions are enabled for both memories, A and B); file path for the dataset information

(label "11"); menu item "file" (label "12" to load/save data files); and options to exit the configuration program (label "13").

After configuring the global and dataset information according to the configuration of the RSLAB lidar system, one is required to input the no. of total acquisitions (e.g., typically 30 signal acquisitions with 1-min time averaging in case of EARLINET regular measurements and 150 signal acquisitions with 1-min time averaging in case of CALIPSO measurements) and the no. of laser shots (typically 1200 laser shots so that each "total" acquisition corresponds to a time average of 1 min. with a laser PRF of 20Hz, Table 2.1). Further additional parameters are 'azimuth' and 'zenith' angles whose information is recorded in the header file but have no effect on the recorded data. The acquired data can be seen as either raw data or range-corrected data or logarithmic range-corrected data depending upon the display selection.
Once the measurement is finished, the complete information is recorded in two separate sets of files, one header file and data files (one file recorded for analog and another for the photon counting dataset for each channel in operation). A customized ASCII data format was specified by the RSLAB and customised by Licel^{TM} to interface MATLAB^{TM} existing lidar routines within the research group.

Integrated PMT-APD High Voltage Control Module.- The integrated PMT-APD power supply Licel control module (Control APD-PMT.vi, Section 7.1 in [*Licel*, 2007b]) can control up to 8 PMT modules and 4 APD modules (subrack A in Figure 6.4). The module can be activated by means of fixed Ethernet address 192.168.1.12 when selected in automatic mode. Figure 6.7 shows the power supply control software programme customized for RSLAB lidar system which includes 6 photodetectors (5 PMTs + 1 APD). The control voltage range for PMTs is between 0 and 1V and for the APD it is between 0 and 1.8V (the latter translates into 0-450V for the APD High Voltage input). PMTs and APD with an active high voltage are indicated by a LED. Usual voltage supply used for PMT (Figure 6.7a) and APD (Figure 6.7b) detectors is ∼800V and ∼300V, respectively. The thermoelectric cooler used for APD can also be remotely activated.

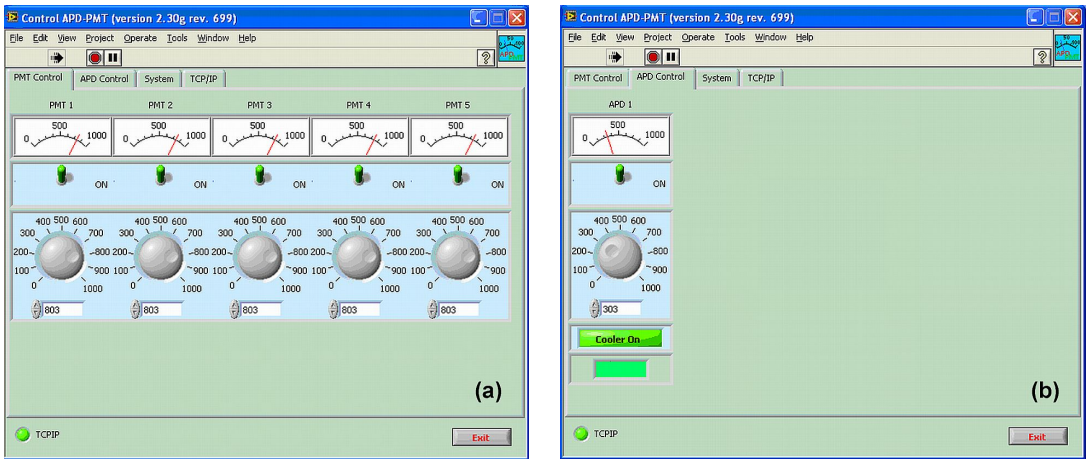

Figure 6.7: RSLAB Lidar photo-detectors' control program. (a) PMTs control. (b) APD control. Source: Section 7.1 in [*Licel*, 2007b].

The Licel Trigger Module.- Figure 6.8 shows the Licel^{TM} trigger module (subrack B in Figure 6.4, (Control Timing.vi in Section 7.2 [*Licel*, 2007b]) which incorporates one trigger input and 4 different outputs to build up compact detection systems. The trigger input can be used to synchronize the system to an external laser flash lamp or Q-switch trigger. The module can run either internally or externally triggered. The module consists of a timing sub-board which is able to generate (Section 7.2 in [*Licel*, 2007b]):

1. a lamp trigger (*Lamp* in Figure 6.8)
2. a pretrigger for the transient recorder (*Acquisition* in Figure 6.8)
3. a Q-Switch trigger (*Q-switch* in Figure 6.8) and
4. a Gating trigger for gated PMT-Modules (*Gating* in Figure 6.8)

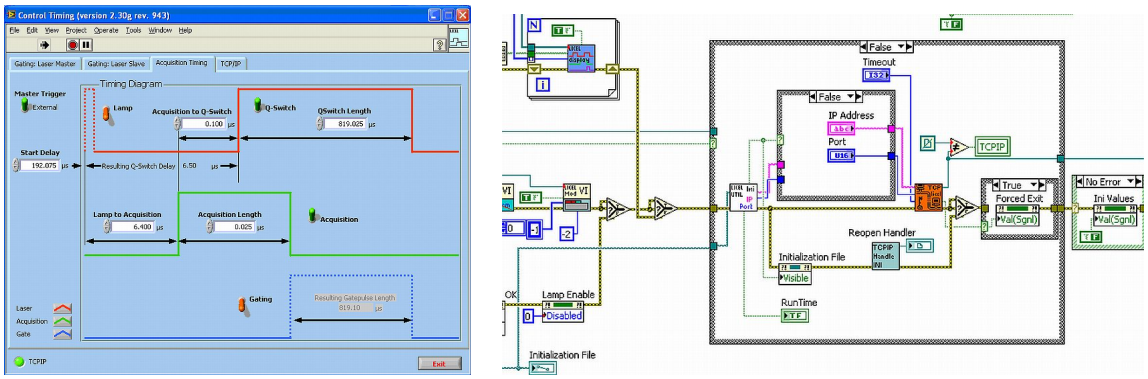

Figure 6.8: Trigger control program. (Left) User interface. (Right) Flow diagram in Labview^{TM}. Source: Section 7.2 in [*Licel*, 2007b].

Trigger-strategy.- The module is activated via Ethernet address 192.168.1.15. In the RSLAB lidar system the external master trigger option has been used because it was not possible to set time delays in fine enough steps. The "Start Delay", "Lamp to Acquisition", and "Acquisition Length" parameters are limited by hardware to too coarse fixed step sizes (See Figure 6.8a).
The "External Master Trigger" option allowed us a convenient timing control. The laser flash-lamp output was used to externally trigger Licel's trigger generator (see "Trigger Generator" in Figure 6.4a) then its "Acquisition output" to trigger the laser Q-switch input. The Q-switch output of trigger generator was used to trigger the transient recorder control rack (see Figure 6.4a and Figure 6.8).

6.1.3 FUTURE PROSPECTS: UNMANNED UNATTENDED OPERATION

This section briefly summarises the full-automation scheme envisaged for the RSLAB lidar system in the framework of UNPC10-4E-442 infrastructure project.
The unmanned unattended approach includes integration, testing and validation of a "container" robot equipped with advanced surveillance systems allowing operation of the RSLAB multispectral LIDAR close to 365/24, remotely over the Internet without people and visually safe for aircraft overflying the lidar station.

The robotized container is an ISO chamber of 6.1 m (20 ft) long and 2.6 m (8.6 ft) high dimensions, reinforced structure, isolated and conditioned ad-hoc, with stability of ±1.5°C within operating temperature range of -15°C to +46°C, to house inside the laser source, optics and electronics. The interior is mechanically, electrically and thermally adapted for mounting the lidar instrument and control racks (lidar system control, single / three-phase power, uninterruptible power system (UPS), wired remote control and Ethernet). The container will be equipped with a hydraulic platform (600 kg) and a sliding roof ("hatch" of 1 m^2) that can take outside the laser-telescope optical head of lidar system, which is equipped as described in Section 6.1.1.1 with 3D scanning capability. To avoid condensation on the optical head (thermal gradient between the exterior and interior of the container), the head will be isolated in a heat cabin. Multiple internal and external sensors such as meteorological (rain, pressure, humidity, and temperature sensors) and radar will be used to monitor and control automatically, or manually remote, the container (e.g., the lidar system automatically shuts down if it starts raining, system off / reset over the internet etc.).
The "surveillance system" will be composed by a fishing radar (Furuno^{TM}, Mod. 141944 CC) and a CCD camera and will integrate the information of possible "hot" targets detected (e.g., an aircraft within the lidar field of view), to disable the system. The fundamentals of operation of the surveillance radar system for a vertically pointing lidar are based on [*Duck*, 2005].

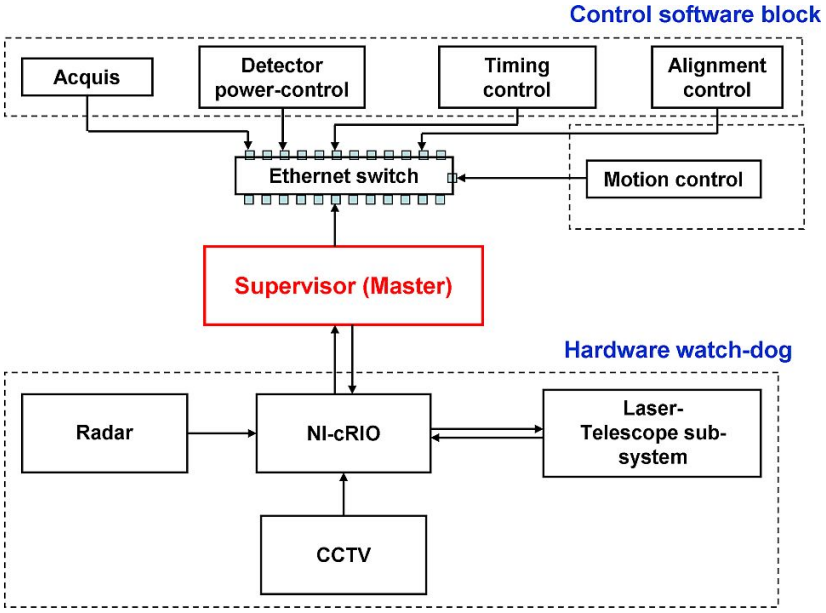

Figure 6.9: Schematic diagram of RSLAB lidar software control for unmanned unattended operation.

Figure 6.9 shows the block diagram of the fully-automated lidar system. The diagram is divided into two blocks: 1) the hardware watch-dog, and 2) the software control block. The hardware watch dog consists of an NI-cRIO control processor that keeps a watch over the laser-telescope subsystem (i.e., laser temperature and laser power output), the surveillance radar and the CCD camera. The NI-cRIO has bi-directional communication with both the laser/telescope subsystem and the master supervisor. Thus, the NI-cRIO periodically polls the supervisor to issue an ACK (acknowledge) signal. If the supervisor sends an alarm or simply if the supervisor does not answer, the NI-cRIO automatically interlocks the laser via hardware. By this means, if the whole software fails the hardware watchdog retains full control to interrupt the laser (system disable or interlock).

6.2 QUALITY ASSURANCE: SPALI-10 INTERCOMPARISON CAMPAIGN

Experimental data were taken during the SPALI10 (SPAin Lidar Intercomparison 2010) field campaign at Madrid (40.45°N, 3.73°W, 663 m asl) from 18 October to 5 November 2010 as part of the quality assurance program of EARLINET (Figure 6.10a) within the framework of the EARLINET-ASOS project (European Aerosol Research LIdar Network - Advanced Sustainable Observation System, [*Molero et al.*, 2011; *Apituley et al.*, 2011; *Freudenthaler et al.*, 2011]). The aim of the campaign was to simultaneously intercompare lidar measurements from four network stations (Madrid, Granada, Barcelona and Évora) with a reference lidar system (MUSA) from CNR-IMAA (Potenza, Italy) in order to assess their performances measuring the same atmosphere during the same time periods. At the same time, an extensive dataset from both ground-level in-situ measurements and remote sensing techniques was collected for characterizing aerosol optical properties. All lidar systems were collocated close

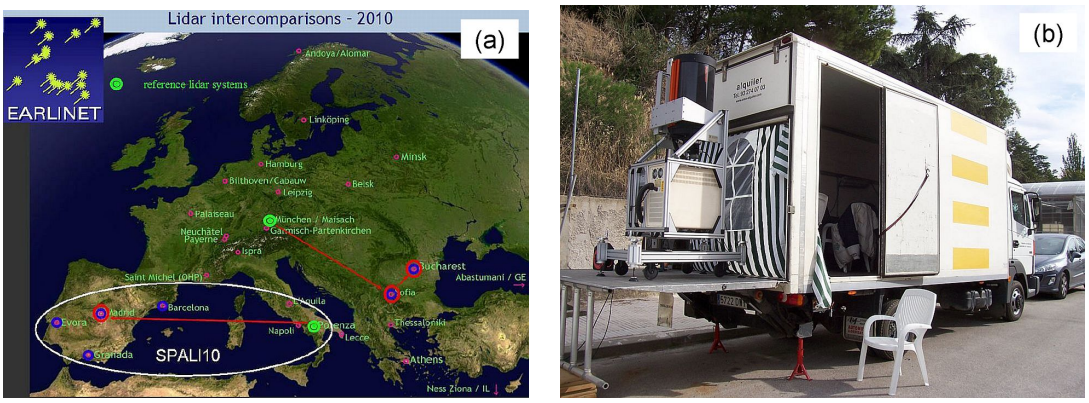

Figure 6.10: SPALI-10 EARLINET intercomparison campaign at hardware level (18^{th} Oct.-5^{th} Nov. 2010). (a) Overview of the participating lidar systems (source photo: Figure 9.1 in [*Freudenthaler et al.*, 2011]). (b) The new RSLAB 6-channel multispectral lidar under operation.

on a flat terrain, with laser pointing close to the zenith. Several sessions each with some hours of measurement time were scheduled for every day of the campaigns, both at day and night, in order to obtain long enough periods with stable atmospheric conditions and with all lidar systems working properly. In order to avoid differences in the raw signal processing by different data analysis, all systems delivered the several-hours datasets of successive one minute averaged signals without any pre-processing to a common data base server, where all signals were then pre-processed by a Single Calculus Chain (SCC) software. The SCC pre-processing calculus module performs:

1. trigger delay shift,
2. dead time correction,
3. atmospheric background and dark measurement subtraction,
4. range correction,
5. vertical smoothing up to a fixed height resolution,
6. cloud screening,

7. handling of signals measured at angle different from zenith, and

8. the time integration of appropriate lidar signals over a selected time window.

The periods for averaging have been determined for each measurement session depending on the stability of the atmospheric conditions, which have been investigated by means of "quicklooks", i.e., colour-coded plots of the range-corrected lidar signals versus time and height (to be shown in Section 6.2.2). The SCC also combines photon counting and analog signals (gluing), and parallel and cross polarized signals into a total profile, if needed.
The first week of the campaign was addressed to the instrument setup and to the verification that the data were correctly submitted to be automatically pre-processed by means of the SCC. During the following two weeks, measurement sessions were regularly scheduled during nighttime and daytime sessions on the base of the weather forecasts. Measurement sessions lasted at least three hours, in order to select the best time intervals where to compare the measurements taking into account the particular vertical atmospheric structures (e.g. clouds, aerosol layers). During a daily meeting, the measurements were discussed and decisions about the corrections on the systems were individuated [*Molero et al.*, 2011].

6.2.1 Lidar systems

All the intercompared lidar systems use pulsed Nd:YAG laser emitting at 1064, 532 and 355 nm, configured in a monostatic biaxial alignment pointing vertically to the zenith, except for the Évora system, which is tilted 5° to improve cirrus studies. The receiving lines consist of Cassegrain or Newtonian telescopes and wavelength separation units with dichroic mirrors, interferential filters and polarization cubes. The collected radiation in terms of the SCC analysis is split into seven channels: elastic signals at 1064, 355 and 532 nm (in parallel and perpendicular components), three Raman channels at 387 and 607 nm, and 407/408 nm water-vapor Raman channel. Not all the systems were equipped with a multi-wavelength Raman lidar system (3+2+1) and depolarization channels (Table 6.1). Potenza and Granada systems were 3+2 lidar systems equipped with channels for cross and parallel polarized radiation at 532 nm; Madrid and Barcelona were 3+2 lidar systems, whereas the Évora system did not measure at 1064 nm.
From the elastic lidar signal, aerosol backscatter coefficient profiles were retrieved using the two-component elastic algorithm discussed in Chapter 5. Radiosounding launches were performed during the whole campaign period, for each measurement session. Temperature and pressure profiles provided by radiosondes data were used to calculate molecular backscatter profiles. As discussed in Section 5.2.1, lidar signals can be fitted to this calculated "Rayleigh" profiles to choose the aerosol-free vertical range for the reference value required by the inversion algorithm.

6.2.2 Discussion and results

Two different intercomparison sessions (27.10.2010, session 01, 20:20-20:50 UTC and 04.11.2010, session 03, 20:00-20:30 UTC) have been selected to illustrate the quality-assurance method followed and resulting statistics (Figure 6.11, Table 6.2 and Figure 6.12, Table 6.3, respectively). The first case example corresponds to a scene with aerosols and clouds all over the sounding range. The second one to a scene with a molecular atmosphere in the far range.
Data intercomparison is carried out by computing vector and scalar statistical indicators from the normalised range-corrected backscattered power profiles of all intervening lidar stations. In what follows the terms "vector" and "function" are assimilated to one another. The RSLAB lidar system is indicated as 'BA' in Table 6.1. The spatial range under analysis

Station	**Évora**	**Madrid**	**Granada**	**Barcelona**	**Potenza**
Country	Portugal	Spain	Spain	Spain	Italy
Abbreviation	**EV**	**MA**	**GR**	**BA**	**PO**
Elastic wavelength [nm]	532, 355	1064, 532, 355	1064, 532, 355	1064, 532, 355	1064, 532, 355
Raman wavelength [nm]	387, 607	387, 607	387, 607, 408	387, 607, 407	387, 607
Depolarization	at 532 nm	No	at 532 nm	No	at 532 nm
Raw resolution [m]	30	7.5	7.5	3.75	3.75
Maximum range [km]	60	30	122	30	61
Full overlap height [m]	500	∼400	300	∼300	
Transportable	Yes	No	Yes	Yes	Yes

Table 6.1: Specifications of the lidar instruments of participants in SPLAI10 intercomparison campaign [*Molero et al.*, 2012, 2011; *Freudenthaler et al.*, 2011].

is divided into two sub-ranges: 615-1515m (near range) and 2025-5025m (far range). The starting range of analysis (615 m) can be considered well above the apparent height of full overlap between the emitted laser beam and the receiving telescope's field of view.
The signal processing validation methodology is based on comparing the range-corrected signals of each of the lidar systems in the test session to an approximate maximum-likelihood (ML) "reference" signal (or "mean" range-corrected signal). This "mean" reference signal has been created by piece-wise weighting, as a function of range, the range-corrected signals of all the stations involved in the test session (Eq.(A.6) in Appendix A). The mean reference signal is estimated by taking the best part of the different lidar signals, which should be close to the unknown true signal. For this purpose the data range under analysis (10 km in Figure 6.11-Figure 6.12) is partitioned in sub-ranges of 500 m length each. Next, in each sub-range, the measured signal from each lidar station is given a weight '1' if the signal is trustworthy and a weight '0' if it is not. Though weights are subjective from an expert user's side there are two clear instances in which a weight '1' is given: a) the measured signal lies in an aerosol layer and this signal corresponds to the "reference" station (Potenza, "PO" in Table 6.1) and b) the measured signal lies in an aerosol-free layer and follows the Rayleigh level. Once weights are assigned to all station signals ("PO", "MA", "GR", "EV", and "BA", see abbreviations in Table 6.1) in all sub-ranges, the weighted mean of these signals is computed to obtain the reference "mean" signal. Weights used to compute 27.10.2010 and 04.11.2010 reference signals are given in Figure A.1. Validation has been carried out by computing for all the reception channels of each lidar station:

1. the range-dependent relative deviation between the measured range-corrected signal and the reference signal. A relative-error vector is obtained, $\overrightarrow{\Delta U}_{a,rel} = \overrightarrow{\Delta U}_a \Big/ \overrightarrow{U}_{ref}$ with $\overrightarrow{\Delta U}_a = \overrightarrow{U}_a - \overrightarrow{U}_{ref}$, $\overrightarrow{U}_a$ and $\overrightarrow{U}_{ref}$ the RSLAB and the reference signals, respectively [see Appendix A, Figure 6.11(c1-c6), Figure 6.12(c1-c5)], and

2. scalar indicators derived from this relative-error vector, namely, its mean and standard deviation (Eqs.(A.3) and (A.4) in Appendix A, see $\overline{\Delta U}_{a,rel}$ and $\sigma_{a,rel}$, respectively, in Tables 6.2-6.3), and the correlation coefficient (Eq.(A.5) in Appendix A, $\rho_{a,ref}$ in Tables 6.2-6.3) between the normalised range-corrected signal of the station under study and the reference signal.

STATION ID	DATE and TIME	WAVE-LENGTH λ [nm]	NORMALISED CROSS-CORRELATION COEF., $\rho_{a,ref}$	MEAN of the relative-deviation vector, $\overline{\Delta U}_{a,rel}$ (%)	STANDARD DEV. of the relative-deviation vector, $\sigma_{a,rel}$ (%)	HEIGHT INTERVAL (near / far range) [m]
PO	27.10.2010, 20:20-20:50 (UTC)	355	1	0	0	near
PO			0.999	0.03	0.57	far
MA			0.995	*13.13	3.05	near
MA			0.995	1.89	2.35	far
GR			0.995	*12.99	3.60	near
GR			0.996	1.34	1.66	far
EV			*0.299	3.92	6.43	near
EV			0.990	2.13	2.79	far
BA			0.980	0.44	2.11	near
BA			0.998	1.21	1.46	far
PO	27.10.2010, 20:20-20:50 (UTC)	532	0.977	-2.30	1.00	near
PO			0.991	-0.10	0.95	far
MA			0.910	4.14	3.18	near
MA			0.997	-0.21	0.62	far
GR			*-0.079	*97.81	38.92	near
GR			0.993	8.84	10.84	far
EV			*0.610	-6.40	11.48	near
EV			0.992	0.60	1.19	far
BA			*0.840	-1.84	2.28	near
BA			0.998	-0.28	0.56	far
PO	27.10.2010, 20:20-20:50 (UTC)	1064	0.999	-5.41	1.30	near
PO			0.982	-0.469	1.69	far
MA			0.983	-0.67	5.26	near
MA			0.932	-0.453	3.27	far
GR			*0.657	*26.23	*27.95	near
GR			*0.470	1.61	*21.34	far
BA			0.986	6.08	5.26	near
BA			0.970	0.92	2.52	far
PO	27.10.2010, 20:20-20:50 (UTC)	387	0.997	0.50	0.79	near
PO			0.997	-0.13	0.87	far
MA			0.958	*-16.87	4.24	near
MA			0.888	-5.00	6.38	far
GR			0.994	9.92	1.82	near
GR			0.976	1.13	2.95	far
EV			*0.248	1.41	5.78	near
EV			0.993	0.51	1.51	far
BA			0.996	-0.50	0.79	near
BA			0.994	0.13	1.29	far
PO	27.10.2010, 20:20-20:50 (UTC)	607	0.979	0.976	1.20	near
PO			0.975	0.05	1.72	far
MA			0.966	-4.93	4.38	near
MA			0.882	-2.22	3.80	far
GR			0.989	*78.62	19.16	near
GR			0.968	7.51	9.57	far
EV			*-0.721	-8.70	11.05	near
EV			0.984	-0.04	1.38	far
BA			0.924	-2.44	2.54	near
BA			0.914	0.01	3.21	far
GR-BA	27.10.2010, 20:20-20:50 (UTC)	407	0.854			near
			*0.474			far

Table 6.2: Statistics for SPALI-10 intercomparison case example I (27.10.2010, session 01, 20:20-20:50 UTC). In the "height interval" column "near" corresponds to 615-1515 m in height and "far" to 2025-5025 m in height. Normalisation range: 3-4 km. See Appendix A for detailed formulation of $\rho_{a,ref}$, $\overline{\Delta U}_{a,rel}$, and $\sigma_{a,rel}$. (*) See text for discussion of these large-deviation cases.

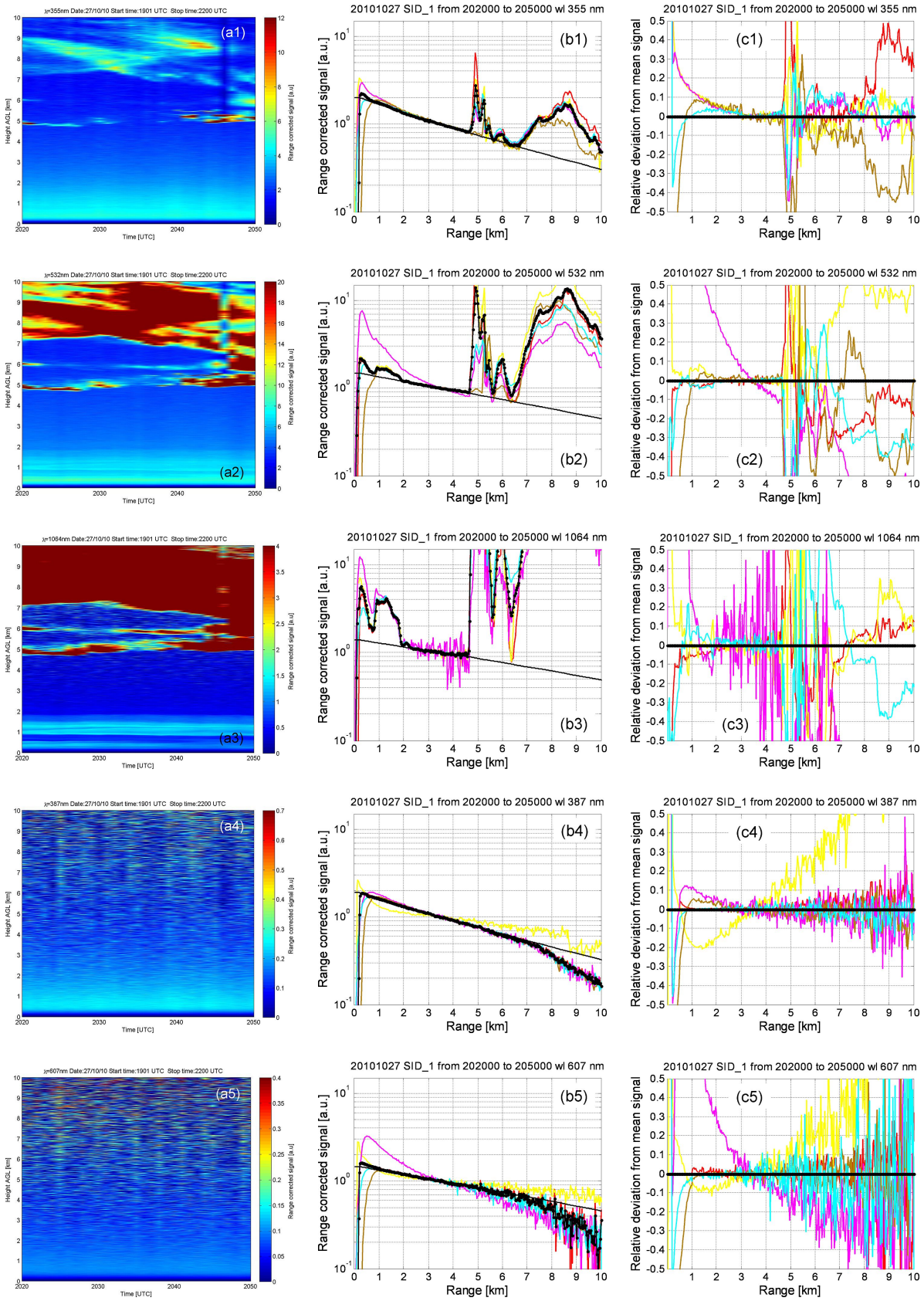

Figure 6.11: SPALI-10 intercomparison case example I (27.10.2010, session 01, 20:20-20:50 UTC). (a1)-(a5) Quicklooks for BA system (height-time colour-coded plots). (b1)-(b5) Range-corrected power signals (all stations). (c1)-(c5) Range-dependent relative deviation between the measured range-corrected signal and the reference signal, $\overrightarrow{\Delta U}_{a,rel}$ (%). (Red) Potenza (PO), (yellow) Madrid (MA), (magenta) Granada (GR), (brown) Évora (EV), (cyan) Barcelona (BA), (dashed black) Rayleigh signal, and (dotted black) mean "reference" signal, $\overrightarrow{U}_{ref}$. (Top to bottom) 355-nm, 532-nm, 1064-nm, 387-nm, and 607-nm channels.

STATION ID	DATE and TIME	WAVE-LENGTH λ [nm]	NORMALISED CROSS-CORRELATION COEF., $\rho_{a,ref}$	MEAN of the relative-deviation vector, $\overline{\Delta U}_{a,rel}$ (%)	STANDARD DEV. of the relative-deviation vector, $\sigma_{a,rel}$ (%)	HEIGHT INTERVAL (near / far range) [m]
PO	04/11/2010, 20:00-20:30 (UTC)	355	0.999	-2.06	0.76	near
PO			0.999	0.05	0.93	far
GR			0.999	2.06	0.76	near
GR			0.999	-0.03	0.81	far
EV			-0.903	*-19.95	*14.79	near
EV			0.995	0.58	1.79	far
BA			-0.904	*-32.41	7.59	near
BA			0.990	-8.53	3.49	far
PO	04/11/2010, 20:00-20:30 (UTC)	532	0.999	0.73	0.34	near
PO			0.998	0.05	0.77	far
MA			0.997	-0.01	0.97	near
MA			0.996	0.89	1.13	far
GR			0.999	-0.73	0.34	near
GR			0.998	0.08	0.73	far
EV			-0.936	*-35.09	*15.4	near
EV			0.989	-3.89	2.57	far
BA			-0.978	*-36.41	7.20	near
BA			0.979	-7.60	4.96	far
PO	04/11/2010, 20:00-20:30 (UTC)	1064	0.998	21.10	1.97	near
PO			0.996	0.47	1.35	far
MA			0.994	8.70	4.50	near
MA			*0.570	*-13.74	*12.90	far
GR			0.977	-29.80	3.84	near
GR			*0.129	*-36.96	*60.87	far
BA			*-0.769	*-30.70	*15.88	near
BA			0.854	-7.15	6.88	far
PO	04/11/2010, 20:00-20:30 (UTC)	387	0.998	-1.96	0.32	near
PO			0.996	-0.12	1.76	far
GR			0998	1.96	0.32	near
GR			0.991	0.68	2.69	far
EV			*-0.878	*-21.95	*13.69	near
EV			0.994	-1.95	2.19	far
BA			-0.965	*-33.35	7.27	near
BA			0.976	-6.53	5.56	far
PO	04/11/2010, 20:00-20:30 (UTC)	607	0.981	1.24	1.26	near
PO			0.957	0.73	3.36	far
MA			-0.895	*-29.50	4.85	near
MA			0.902	-10.10	5.79	far
GR			0.953	-3.85	2.06	near
GR			0.946	-0.38	3.73	far
EV			-0.951	*-31.98	*16.96	near
EV			0.950	-2.08	3.60	far
BA			-0.979	*-34.06	9.15	near
BA			*0.708	-4.53	7.35	far
	04/11/2010, 20:00-20:30 (UTC)	407	Data not available			

Table 6.3: Statistics for SPALI-10 intercomparison case example II (04.11.2010, session 03, 20:00-20:30 UTC). In the "height interval" column "near" corresponds to 615-1515 m and "far" to 2025-5025 m. Normalisation range: 6-8 km for 355nm and 5-6 km for rest wavelengths. See Appendix A for detailed formulation of $\rho_{a,ref}$, $\overline{\Delta U}_{a,rel}$, and $\sigma_{a,rel}$. (*) See text for discussion of these large-deviation cases.

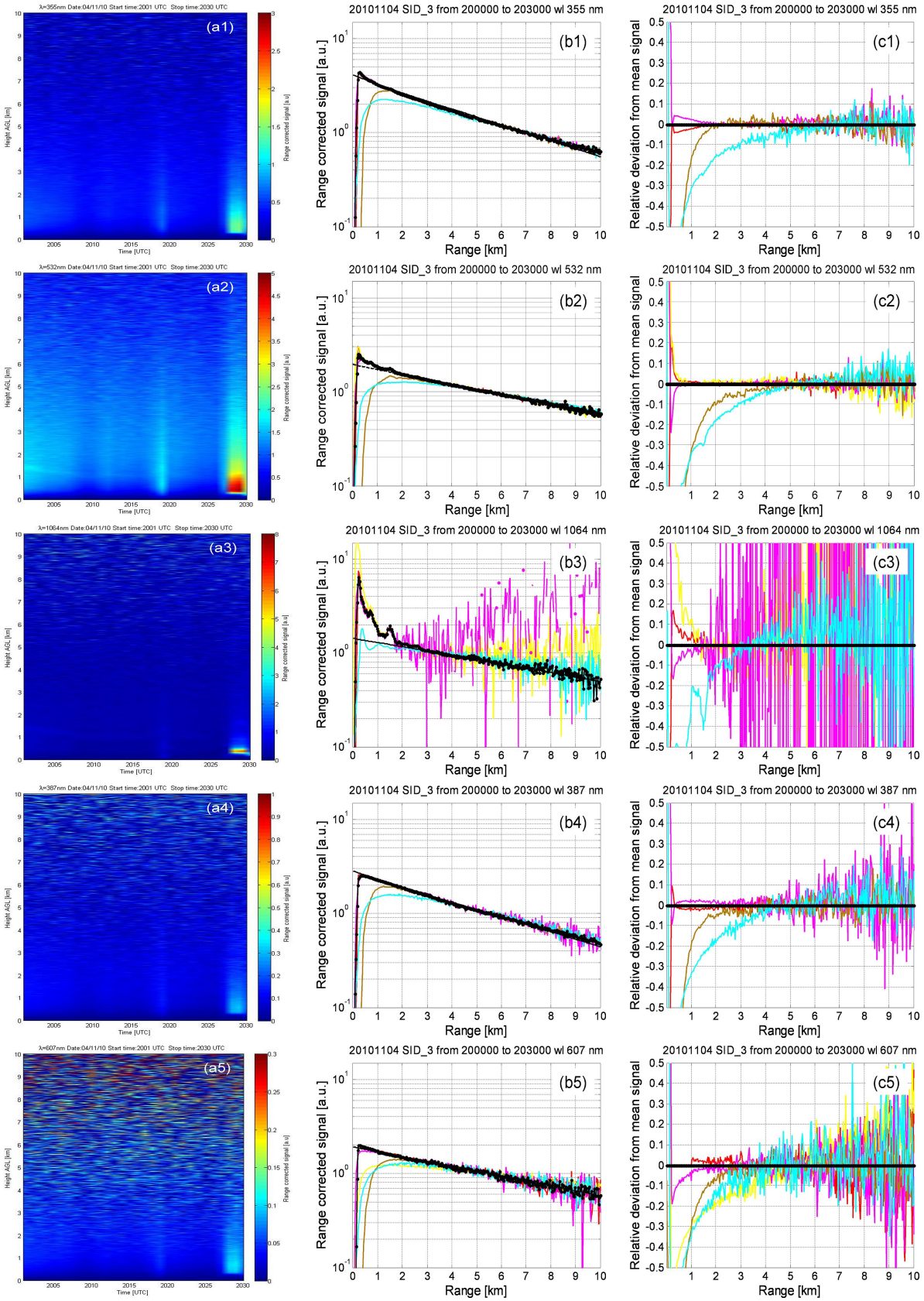

Figure 6.12: SPALI-10 intercomparison case example II (04.11.2010, session 03, 20:00-20:30 UTC). Quicklooks for BA system (height-time colour-coded plots). (b1)-(b5) Range-corrected power signals (all stations). (c1)-(c5) Range-dependent relative deviation between the measured range-corrected signal and the reference signal, $\overrightarrow{\Delta U}_{a,rel}$ (%). (Red) Potenza (PO), (yellow) Madrid (MA), (magenta) Granada (GR), (brown) Évora (EV), (cyan) Barcelona (BA), (dashed black) Rayleigh signal, and (dotted black) mean "reference" signal, $\overrightarrow{U}_{ref}$. (Top-to-Bottom) 355-nm, 532-nm, 1064-nm, 387-nm, and 607-nm channels.

The signal processing strategy is analogous to Section 9 of [*Freudenthaler et al.*, 2011]. A detailed statistical formulation of these parameters can found in Appendix A. Discussion on system performance at the different reception wavelengths follows:

355-, 532-, and 1064-nm elastic channels.

355-nm channel.- On 27.10.2010 session (Figure 6.11 and Table 6.2), the high value of the correlation coefficient ($\rho_{a,ref}$>95%, Table 6.2) for all lidar systems except in the near range of EV system evidences fairly good results with similar shapes in the measured range-corrected signals. In the case of EV, the near range is problematic because this system is optimised for cirrus clouds studies and, therefore, the starting range of full overlap occurs at higher heights. The comparatively high value of the mean relative-deviation indicator, $\overline{\Delta U}_{a,rel}$>10% for MA and GR systems in the near range evidences scaled versions of the range-corrected signals (Figure 6.11) as compared to the reference signal. At this point, recall that the correlation coefficient is insensitive to scaled versions of a signal, i.e., the correlation coefficient between a signal and a scaled version of it is unity (Appendix A). The low standard deviations obtained ($\sigma_{a,rel}$<10%) support the discussion above.
On 04.11.2010 session (Figure 6.12 and Table 6.3), EV and BA systems have problems in the near range (Table 6.3). Letting apart EV, which as explained is due to its specific design for cloud studies, in the case of BA the high starting range of full overlap was due to a misalignment problem (Figure 6.12). MA system was not available for intercomparison in this session.

532-nm channel.- On 27.10.2010 session (Figure 6.11 and Table 6.2), GR, EV and BA systems have problems in the near range. Apart from EV, which will no longer be discussed, the problem with GR was not identified during the test but a posteriori. In the case of BA, the problem was due to mispositioning the pinhole used to avoid detector saturation. On 04.11.2010 session, the starting range of full overlap, R_{ovf} for BA system is as high as 5 km. This problem occurs at the near range for all wavelengths, which is a clear indicator of a laser-telescope misalignment.

1064-nm channel.- On 27.10.2010 session, the BA system shows quite good behaviour in both near and far ranges, which is corroborated by $\rho_{a,ref}$>95% and quite low mean and standard deviations (<6%). Problems are only identified for GR system, which had a noisier reception channel. On 04.11.2010, as already explained for the 532-nm channel, the BA system had misalignment problems affecting the near range of all its channels. GR and MA systems also suffered from high noise levels in their detection systems particularly evident in the far range of Figure 6.12(b3) and from the mean and standard-deviation statistical indicators of Table 6.3. EV channel was not available for intercomparison in any of these sessions.

387- and 607-nm nitrogen Raman channels.

Behaviour of N_2-Raman channels is substantially different from that of their elastic counterparts. For example, comparing 355- and 387-nm, and 532- and 607-nm quicklooks in Figure 6.11, 387- and 607-nm quicklooks are basically void because only nitrogen molecules contribute to the backscatter coefficient, not aerosols. N_2-Raman channels are also called "aerosol" Raman channels because as a consequence of the Raman lidar inversion algorithm [*Ansmann et al.*, 1992] the minus slope of the logarithm of the range-corrected Raman signal is proportional to the aerosol extinction coefficient [*Rocadenbosch et al.*, 2007]. With reference to [Figure 6.11(a1)(a2)] this motivates that when from 7 km up the extinction increases, Eq.(2.18), the Raman signal is further attenuated and the slope of the Raman range-corrected signal in Figure 6.11(b4)(b5) falls below the Rayleigh level ("zero aerosol load" reference).

387-nm channel.- On 27.10.2010 session all stations except MA and EV performed satisfactorily (the near-range particularities of EV system have already been discussed). In the case of MA station the far-range of the N_2-Raman range-corrected signal is above the Rayleigh level indicating that signal distortions become too strong. On 04.11.2010 session, BA was misaligned and MA data was not available.

607-nm channel.- Comments for the 607-nm Raman channel are analogous to the 387-nm Raman channel. GR system exhibits similar behaviour to MA system but too far from the mean reference signal. This is identified by a mean deviation $\overline{\Delta U}_{a,rel} \approx 79\%$ (near range) and 8% (far range) in Table 6.2, a problem solved on 04.11.2010 session. BA system shows quite satisfactory performance with mean deviations below 3%. On 04.11.2010 session, BA system was misaligned as evidenced by a starting range of full overlap, R_{ovf}≈5 km.

407-nm water-vapour (WV) Raman channel.

SPALI-10 intercomparison campaign did not include any reference station with a WV channel. Besides, the Single-Calculus-Chain (SCC) pre-processor did not process data for the WV channel. Since only BA and GR lidar systems were equipped with a WV Raman channel at 407/408 nm, respectively, Table 6.2 computes the correlation coefficient between these two systems. No other statistical parameters are listed since a reference is lacking. The correlation coefficient obtained is $\rho_{BA,GR}$=85% in the near range and $\rho_{BA,GR}$=47% in the far range. The near-range correlation coefficient indicates similar shapes in the measured WV profiles. The far-range coefficient is largely influenced by noise [Figure 6.13] as expected from the assessed maximum system range in Figure 2.8 ($R_{\max}$≈1.4 km with 30 min observation time).

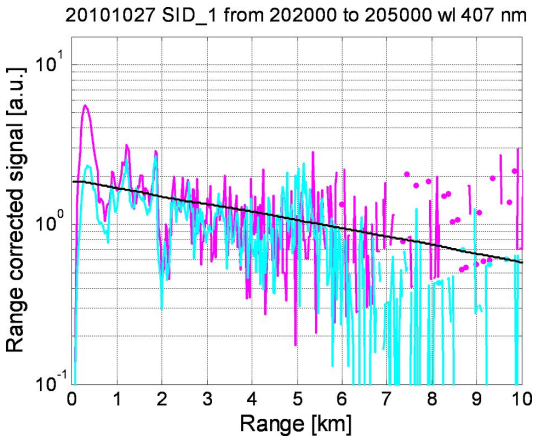

Figure 6.13: SPALI-10 intercomparison case example I (27.10.2010, session 01, 20:20-20:50 UTC). Water-vapour range-corrected signal at 407 nm (Granada and Barcelona). (Magenta) Granada (GR), and (cyan) Barcelona (BA).

"Summing up, the results of the campaign can be considered satisfactory". The campaign allowed checking the performances of the systems and when they were not fully satisfactory, the reasons of the failure were understood and the way to solve them were identified. A major output of the intercomparison campaign was an estimate of the starting range of full overlap (R_{ovf}) for BA system, which was around 1000 m under well-aligned conditions. In order to lower R_{ovf} towards the 300 m goal specified in Table 6.1 the 3-mm fiber (NA=0.12) used in the campaign to couple the telescope to the polychromator was changed by another one with NA>0.45 in combination with a field-lens (Figure 3.10).

6.2.3 Internal system quality check: Rayleigh fit

The Rayleigh fit test shows the accuracy of agreement between a lidar signal and a calculated molecular (Rayleigh) signal in a lidar range presumably without aerosols. Figure 6.14 shows the Rayleigh test carried out for RSLAB lidar system on 03.08.2011 when an aerosol free range is assumed between 13 km and 14 km. Although there are several aerosol signatures, the deviation plot at right indicates that the lidar signal can be used up to about 14 km, above which the presence of a cloud appears [*ACTRIS*].

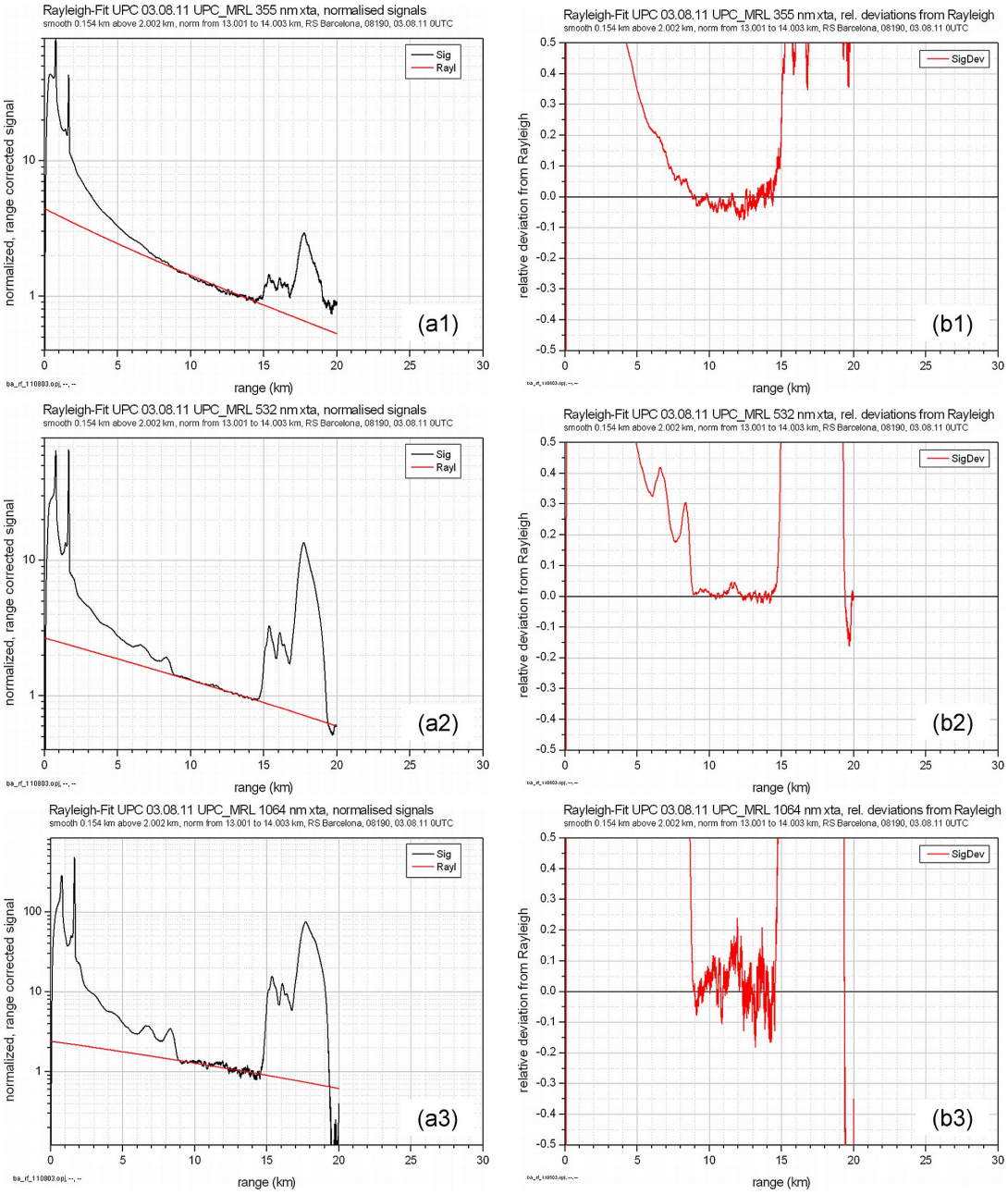

Figure 6.14: Rayleigh fit internal quality test for the new RSLAB multispectral lidar system. (a1)-(a3) Measured normalized range-corrected signal (black) and calculated Rayleigh signal (red). (b1)-(b3) Relative deviation from Rayleigh signal. Normalization range between 13 and 14 km. (Top-to-Bottom) 355, 532 and 1064 nm. Source: Section 3 in [*ACTRIS*].

6.2.4 Participation in field campaigns

Finally, Table 6.4 summarizes the main intensive field campaigns made since 2006 contributed as part of this Ph.D. and using both the old 2+1-channel and the new 3+2+1-channel RSLAB lidar systems.

Campaign	**Location and date**	**System**	**Objectives**
El Arenosillo 2006 [*Sicard et al.*, 2007]	El Arenosillo (Huelva, Spain) 28 June–2 July, 2007	Lidar 2+1	Intercomparison of four lidar stations at hardware and software levels (elastic backscatter coefficient inversions at two wavelenghts). Nucleus of the Spanish Lidar Network (SPALINET).
Canarias 2007 [*Sicard et al.*, 2008] [*Sicard et al.*, 2010]	Teide Observatory (Tenerife island, Spain) 30 June-4 July, 2007 Roque de los Muchachos Observatory (La Palma island, Spain) 5 July-11 July, 2007	Lidar 2+1	Characterization of the nocturnal boundary layer (NBL) of astronomical sites in terms of height development and optical thickness. Preliminary retrieval of wind fields using elastic lidar systems and correlation techniques. Campaign held in the frame of the ELT (Extremely Large Telescope) project.
La Palma 2008 [*Sicard et al.*, 2009b] [*Sicard et al.*, 2010]	Roque de los Muchachos Observatory (La Palma island, Spain) 26 May-14 June, 2008	Lidar 2+1	NBL characterization in terms of height development and aerosol stratification versus synoptic conditions. Campaign led by the IAC (Instituto de Astrofsica de Canarias).
Banyoles 2008	Banyoles (Girona, Spain) 15 July 2008	Lidar 2+1	Collaboration with the Institut Cartogràfic de Catalunya (ICC) for radiometric performance of digital cameras. Backscatter and extinction coefficient profiles at two wavelengths were obtained.
SPALI10 [*Molero et al.*, 2011]	Madrid (Spain) 18 Oct.–5 Nov., 2010	**Lidar 3+3**	EARLINET Quality-assurance intercomparison campaign. (See Section 6.2)

Table 6.4: Summary of the RSLAB lidar field campaigns

Chapter 7

CASE EXAMPLE: LIDAR FOR CHERENKOV-TELESCOPE ASTROPHYSICAL STUDIES

Ground-based Cherenkov telescopes of the Imaging Atmospheric Cherenkov Telescope (IACT) class detect cosmic gamma-rays above few tens of Giga-electron-Volts, by observing the Cherenkov light produced in Extensive Atmospheric Showers (EAS) initiated by the interaction of the primary cosmic gamma-ray with the atmospheric constituents. The current generation of IACTs, and specially HESS, MAGIC and VERITAS, has most of their systematic errors in the energy reconstruction and absolute scale of the gamma-ray measured fluxes due to uncertainties in the determination of the opto-atmospheric parameters.
This chapter is an application case of the methodology and link-budget assessment tools developed in Chapter 2 and describes the current design of a tropospheric elastic/Raman lidar (355/387-nm wavelength) system to be used for atmospheric characterisation (optical extinction and backscatter). Concept-design of the IFAE/UAB lidar system including system architecture and specs, opto-atmospheric parameter modelling, formulation of the power link-budget, and assessment of the system performance (signal-to-noise ratio (SNR), and maximum system range as a function of observation time) is presented. The lidar will be installed and operated at the Cherenkov Telescope Array (CTA) observatory which is the future generation of IACTs.
This chapter is organized as follows: Section 7.2 presents an overview of the IFAE/UAB elastic/Raman lidar system, Section 7.3 focuses on the atmospheric modelling of the optical parameters and assessment of the system performance (return power levels, range-dependent SNR, and maximum system range). Finally, Section 7.4 gives conclusion remarks.

7.1 INTRODUCTION

Ground-based Cherenkov telescopes of the Imaging Atmospheric Cherenkov Telescope (IACT) [*Angelis*, 2009] class observe cosmic gamma-rays in the GeV–TeV regime[1] by collecting the Cherenkov light [*Boley*, 1964] produced by electrons and positrons in electromagnetic showers initiated by primary cosmic gamma-rays when interacting in the top Earth atmosphere. When a primary gamma-ray reaches the atmosphere a pair electron-positron is produced. These charged particles re-emit secondary gamma-rays via Bremmstrahlung. The secondary gamma-rays, in turn, pair-produce electrons and positrons, and so on. Therefore, a shower

[1] $1GeV = 10^9 eV, 1TeV = 10^{12} eV (eV = electronvolt)$

of hundreds of particles is developed along several tens or hundreds of meters. The energy of the electrons in each step of the shower is roughly half of that of the previous step until it reaches the ionization yield and the shower dies [*Rossi and Greisen*, 1941].

In the first stages of the showers, the electrons travel at a speed greater than the speed of light in the atmosphere and, therefore, produce Cherenkov light. This light is a ultraviolet (UV)-optical flash of the duration of few nanoseconds, in the shape of a cone aligned with the primary gamma-ray direction, which illuminate the ground in a circle of roughly 120 m radius after having crossed the atmosphere. Whenever an IACT is placed inside the Cherenkov light pool and given that enough Cherenkov photons hit the mirror, the shower is recorded and through an image reconstruction, the energy, direction, and arrival time of the primary gamma-ray are obtained [*Hillas*, 1985].

The current generation of IACTs, and specially HESS, MAGIC and VERITAS (Figure 7.1) has most of the systematic errors in the energy reconstruction and absolute scale of the gamma-ray measured fluxes due to systematic errors in the determination of atmospheric parameters. Of particular concern is the poorly known 'total extinction' that Cherenkov photons undergo in their travel from the emission region, typically located between 20 and 10 km a.s.l., to the ground. Despite the fact that some instruments are currently used to measure the atmospheric transparency, their data are only used to retain good-quality observation time slots, and currently only a minor effort is done to correct data with atmospheric information [*Nolan et al.*, 2007; *Dorner et al.*, 2009].

Figure 7.1: The MAGIC array of two 17-m diameter Cherenkov telescopes, located in the City La Palma (Canary Island, Spain).

On the other hand, the entire IACT community is now focussed on the design of a new generation of Cherenkov telescopes with improved performance. The leading project is the Cherenkov Telescope Array (CTA) observatory [*Doro*, 2011] (see (Figure 7.2)), which is a worldwide effort for the construction of several tens of IACTs to be operated simultaneously, compared to the current generation of installations which comprises 2-4 telescopes. CTA will be operated by a wide international community of scientists and based on a high-quality level of data dissemination, which is typical for the larger astronomical installations. To reach this goal, the atmosphere should be monitored continuously and precisely, so that the data could be corrected offline before dissemination. The characterization of atmosphere can be successfully done at night using an elastic/Raman lidar system [*Behrendt et al.*, 2002; *Ansmann et al.*, 1992; *Inaba*, 1976] which could be a good technique for data calibration in the energy reconstruction and absolute scale of the gamma-ray measured fluxes due to systematic errors in the determination of atmospheric parameters in the area of Astronomy [*Zimmer and McGraw*, 2010].

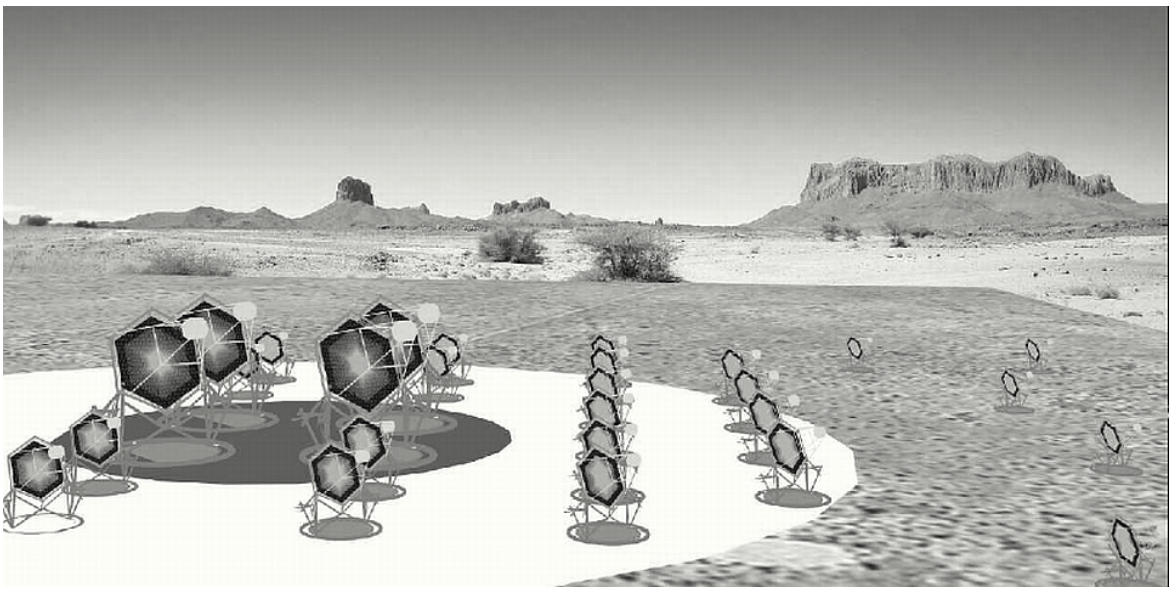

Figure 7.2: The Cherenkov Telescope Array (CTA). Artistic view showing the different telescope sizes and the planned arrangement of the array. The area coverage will be between 1 and 10 km^2.

With this aim, the Institut de Física d'Altes Energies (IFAE) and the Universitat Autónoma de Barcelona (UAB), in the context of the Atmospheric Calibration (ATAC) working group of CTA, and both being members of the MAGIC collaboration, are currently designing a non-scanning pulsed elastic/Raman lidar system to be used for systematic data error correction due to poorly known molecular and particle extinction coefficients. The lidar will be installed and operated at the CTA site, currently under definition, with the goal of reducing the systematic uncertainties of the imaging atmospheric Cherenkov technique of the telescope and increasing the duty cycle thanks to a better knowledge of the atmosphere. Two other groups are also developing Raman lidars for CTA: the LUPM (Laboratoire Univers et Particules de Montpellier) in Montpellier (France) and the CEILAP (Centro de Investigaciones Láser y sus Aplicaciones) group in Villa Martelli (country-Argentina).
The elastic/Raman lidar solution for atmospheric characterization is a mature solution within, for example, the European Aerosol Research LIdar Network (EARLINET) [*Rocadenbosch et al.*, 2008] - of which the Remote Sensing Lab (RSLab) of the UPC is member- and the GAW (Global Atmospheric Watch) Aerosol LIdar Observation Network (GALION) worldwide [Chapter 1].

7.2 OVERVIEW OF THE IFAE/UAB ELASTIC-RAMAN LIDAR SYSTEM

The 1+1 configuration is the basis of the IFAE/UAB elastic-Raman lidar. A sketch of the system architecture is illustrated in Figure 7.3a. System specs are given in Table 7.1. The elastic channel operates at 355-nm wavelength (ultraviolet, UV) and the Raman channel at 387-nm wavelength (nitrogen Raman shift for a 355-nm excitation wavelength). In addition to the fact that Cherenkov radiation occurs mainly in the UV, a UV wavelength is chosen because of the higher atmospheric scattering towards this band (λ^{-4} molecular spectral dependence due to Rayleigh scattering and typical λ^{-1} dependence for aerosol particles/water droplets) [*Collis and Russell*, 1976]. The emission sub-system is based on a 20-Hz repetition-

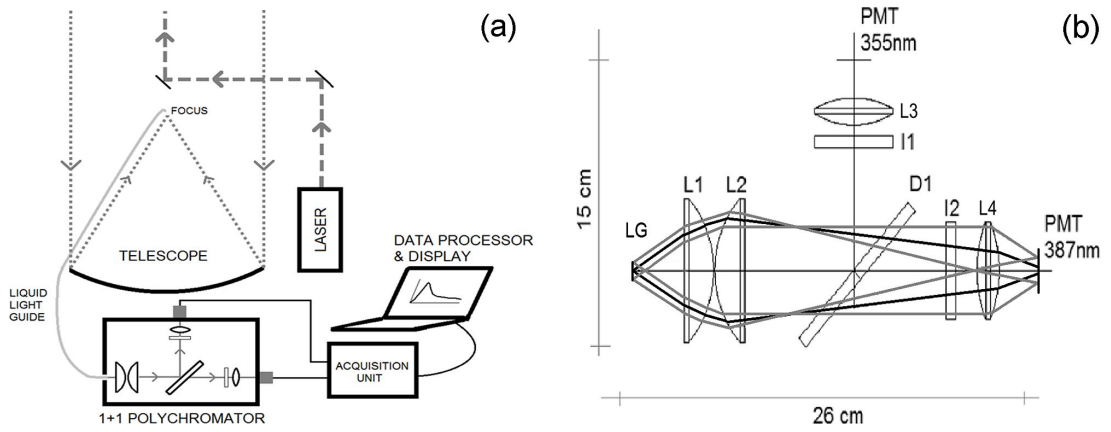

Figure 7.3: Architecture of the IFAE/UAB 1+1 channel elastic/Raman lidar system. (a) Sketch of the system architecture. (b) Polychromator design layout and related ZEMAX® ray tracing at 355 nm (elastic channel) and 387 nm (nitrogen Raman channel). (LG) Liquid guide. (D1) Dichroic mirror. (L1 to L4) Lenses. (I1, I2) Interference Filters. See Table 7.2 for specs.

rate, Q-switched, Nd:YAG solid-state pulsed laser providing light emission at 1064, 532 and 355-nm wavelengths by means of second- and third-harmonic generators (SHG and THG, respectively) from a fundamental wavelength of 1064 nm. 355 nm is, however, the wavelength of interest for characterisation of the optical atmospheric parameters.
The reception sub-system, which is coaxially arranged with the emission optical axis (see Figure 7.3a), is based on a 1.8-m diameter, 1.8-m focal-length parabolic mirror (adapted from a Cassegrainian telescope) for collecting the returned light signal. In its focus, a liquid light guide is used to convey the composite atmospheric return radiation (elastic plus Raman) from the telescope focal plane to the polychromator unit (i.e., the spectrally selective unit in reception). The guide collection efficiency is, approximately, $\xi_{PSF} = 90\%$ (this figure being computed from the light spot overspill on the guide aperture due to the point-spread function (PSF) of the telescope). The polychromator (Table 7.2 and Figure 7.3b) is formed by two collimating lenses (L1-L2), one dichroic mirror (D1), two interference filters (I1, I2), and two focusing lenses (L3, L4). The condenser lenses (L1-L2) *nearly* collimates the composite light beam emerging from the liquid guide at the polychromator's input. The dichroic mirror (D1) separates the composite light return into two optical paths, one for the 355-nm wavelength (elastic-channel) and another for the 387-nm wavelength (Raman-channel), at the end of which pertinent PMT (Photo-Multiplier Tube)-based detectors are located. Lenses (L3, L4) are used to focus light on the active area of the detectors. In front of the PMTs, the interference filters select the desired wavelength range. A ZEMAX® ray-tracing computer-aided design (CAD) software has been used to ensure that the reception field of view is the same for both channels, as it is shown in Figure 7.3b.

Signal acquisition is carried out by means of Licel® transient recorders, which combine a 20 Msps, 12-bit, analog-to-digital converter (ADC) with a 250-MHz count-rate, 50-ns bin time, photon counter architecture, thus, enabling simultaneous analog and photon-counting acquisition modes in each lidar channel with a spatial resolution of 7.5 m. The elastic channel is acquired in analog mode, which is the usual one when dealing with high light level signals (see Section 7.3), while the Raman channel is acquired in mixed analog/photon-counting mode. In the near-range of the Raman channel, where the return signal is more intense, the analog mode is used; in the far-range, where the signal is much weaker, the photon-counting mode is used, instead [*Hamamatsu*, 1998]. The opto-electronic receivers can be controlled

EMITTER		
Laser	Type	Nd:YAG
	Model	Quantel Brilliant
	Emitted wavelength, λ	355 nm
	Energy per pulse, E	60 mJ
	Pulse Repetition Frequency, PRF	20 Hz
	Beam waist (diameter)	6 mm
	Beam divergence, θ	0.5 mrad
	Pulse duration, τ_p	5 ns
RECEIVER		
Telescope	Geometry	Cassegrain
	Diameter, d	1.8 m
	Shadow diameter, d_{sh}	0.08 m
	Focal length, f	1.8 m
	Transmissivity, ξ_T	0.55
Liquid-guide-to-telescope coupling efficiency, ξ_{PSF}	0.9	
Liquid Guide	Manufacturer	Lumatec, Model Series 300
	Active area diameter, d_b	8 mm
	Numerical Aperture, NA	0.59 (36° half-angle)
	Transmissivity, ξ_{LG}	>0.7 (in the UV)
Polychromator	*Ad hoc* design, see Table 7.2	
Photodetectors	Type	PMT
	PMT model	Hamamatsu R1924A
	Active area diameter (all PMTs), d_d	22 mm
Acquisition unit (transient recorder)	Type	Mixed analog-to-digital converter (ADC) / Photon counter (PC)
	Model	ADC 20 Msps 12bit / 250-MHz PC Licel TR20-160
CHANNEL SPECIFICATIONS		
Wavelength	355 nm	387 nm (N_2)
Type	Elastic	Raman
Spatial Resolution, $c\tau_d/2$	7.5 m (B_N=10 MHz, analog mode; τ_d=50 ns/bin, photon-counting mode)	
Polychromator TX, ξ_{poly} (Eq.(7.2))	$0.90\times0.90^3\times0.60 = 0.39$	$0.90\times0.90^3\times0.65 = 0.43$
Channel transmissivity, ξ_{net} (Eq.(7.1))	0.15	0.16
Spectral Bandwidth, $\Delta\lambda$ [nm]	10	10
Type of Detector	PMT	PMT
Model	R1924A (Hamamatsu)	R1924A (Hamamatsu)
Internal Gain, M	2×10^6	2×10^6
Noise Factor, F	1.8	1.8
Dark current, I_d [nA]	3	3
Current responsivity, R_i[AW^{-1}]	1.1×10^5	1.1×10^5
Transimpedance gain (input impedance of the transient recorder) [Ω]	50	50
Channel responsivity, R'_v [VW^{-1}] (Eq.(2.20))	8.0×10^5	8.7×10^5
Channel NEP, NEP_s [fW·Hz$^{-1/2}$]	3.8	3.5

Table 7.1: 1+1-channel elastic/Raman lidar system specs.

thanks to a specific CPU-distributed design by means of a user-friendly LabView® interface. Remote control of the lidar instrument will be interfaced with the high-level control system of CTA (not defined yet).

7.3 ASSESSMENT OF SYSTEM PERFORMANCE

The two-component (aerosol plus moelcular) atmospheric model is completely analogous to the one presented in Chapter 2, Section 2.1 (visibility margin, $V_m = 39.12\ km$; lidar ratio,

Dichroic mirror (D1)			
Size	1.5" DIA x 0.25"THIC		
$^*\rho$, ξ	$\rho \geq 90\%$ @ 355nm $\tau \geq 90\%$ @ 387 nm		
Lenses			
	Diameter (mm)	Effective Focal Length (mm)	Model (THORLABS)
Plano-Convex Set (L1-L2)	75	38.0	LA1238
Bi-convex Lens (L3, L4)	50.8	60	LB1723
Interference Filters (I1, I2)			
CWL [nm]	355±1.5	387±1.5	
FWHM [nm]	10±2.0	10±2.0	
Transmissivity, ξ [%]	Peak>60%	Peak>65%	

$^*\rho$ and ξ respectively represent reflectivity and transmissivity. Also, DIA and THIC respectively stand for diameter and thickness. All lenses transmission is 90%.

Table 7.2: Specs of the 1+1-channel elastic/Raman polychromator

$S_{355}^{aer} = 25\ sr$). A wavelength-dependent aerosol component is modelled as a homogenous load of aerosols up to 3 km in height (Atmospheric Boundary Layer, ABL). Beyond the ABL a purely molecular atmosphere is considered.

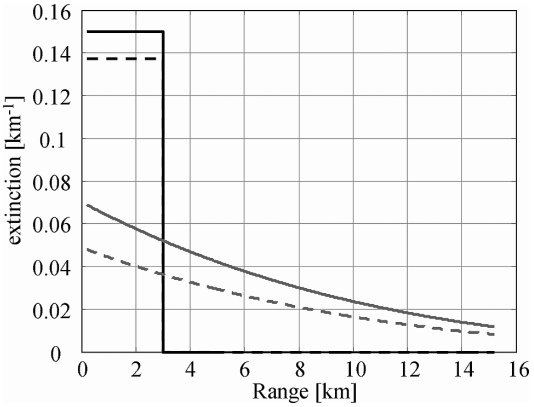

Figure 7.4: Simulated opto-atmospheric parameters. (Step profiles) Aerosol (Mie) extinction profile. (Exponential-like profiles) Molecular (Rayleigh) extinction. In (solid trace) the elastic channels, in (dashed trace) the Raman ones.

Figure 7.4 plots the molecular and aerosol extinction components as a function of height.

7.3.1 Return Power Levels

Figure 7.5a simulates the range-corrected power return signals incident on the telescope at the elastic and Raman wavelengths according to Eq.(2.14) and Eq.(2.18), respectively. The simulation range is 200 m to 15 km. Because of the large dynamic range of the lidar signals spanning some 4 orders of magnitude in both channels, simultaneous analog and photon-counting recorded data will be glued according to the procedure described in [*Licel*, 2007a; *Donovan et al.*, 1993]. Besides, a gated PMT solution (i.e., including an electronic enable/disable feature) will be used to disable reception during the first 200 m of the lidar signal where, due to the laser-telescope coaxial arrangement, the detectors become blind. For the elastic channel, it also is envisaged inclusion of neutral density filters to accommodate the return power levels of Figure 7.5a to levels comparable to those of the Raman channel, since with such a large-aperture telescope, the input light levels can drive the PMT detector into

deep saturation, from Figure 7.5a and the PMT current responsivity, $R_i = 1.1 \times 10^5 \mathrm{AW}^{-1}$ in Table 7.1, the photo-induced current at 6 km is 10 mA, a figure well reported above experimental maximum pulsed-current saturation ratings, 1.6 mA for 0.1% detector linearity in the case of PMT 7400U [*Licel*, 2007a; *Bristow*, 1998].

Channel transmissivity: The channel transmissivity ($0 \leq \xi_{net}(\lambda) \leq 1$) is defined as the product of the individual subsystem transmission factors (i.e., the inverse of the optical losses) along the optical receiving chain. Formally,

$$\xi_{net}(\lambda) = \xi_T(\lambda)\,\xi_{PSF}(\lambda)\,\xi_{LG}(\lambda)\,\xi_{poly}(\lambda), \tag{7.1}$$

where $\lambda = \lambda_0$, λ_R is the elastic/Raman reception wavelength, $\xi_T(\lambda)$ is the telescope transmission, $\xi_{LG}(\lambda)$ is the liquid-guide transmission, $\xi_{PSF}(\lambda)$ is the guide-to-telescope coupling efficiency due to the PSF of the telescope (Section 7.2), and $\xi_{poly}(\lambda)$ is the total polychromator transmission (Figure 7.3b) defined as

$$\xi_{poly}(\lambda) = \xi_{dichr}(\lambda)\,\xi_{lens}^{n}(\lambda)\,\xi_{IF}(\lambda), \tag{7.2}$$

where $\xi_{dichr}(\lambda)$, $\xi_{lens}(\lambda)$, and $\xi_{IF}(\lambda)$ are the dichroic mirror (D1), lenses (L1-L2 and L3 for the 355-nm optical path; L1-L2 and L4 for the 387-nm path), and interference-filter (I1 for the 355-nm optical path, I2 for the 387-nm path) transmission factors (Table 7.2). In Eq.(7.2), $n = 3$ is used, which stands for the three lenses in each optical path of the polychromator with nearly identical transmissivities. The elastic/Raman channel transmissivities according to Eq.(7.1) are listed in Table 7.1 along with the channel voltage responsivity (or net voltage responsivity, Eq.(2.20)).

7.3.2 Signal-to-Noise Ratio

Figure 7.5b plots the assessed SNR versus range for both the elastic channel (Eq.(2.22), analog mode) and the Raman channel (Eq.(2.22), analog mode; Eq.(2.27), photon-counting mode). At this point, it is important to notice that SNRs have been computed under night-time operation (background radiance, L=2.7×10^{-13} $\mathrm{Wcm^{-2}nm^{-1}sr^{-1}}$ [*Mirzoyan*, 1998]) which will be the operational mode of the lidar.

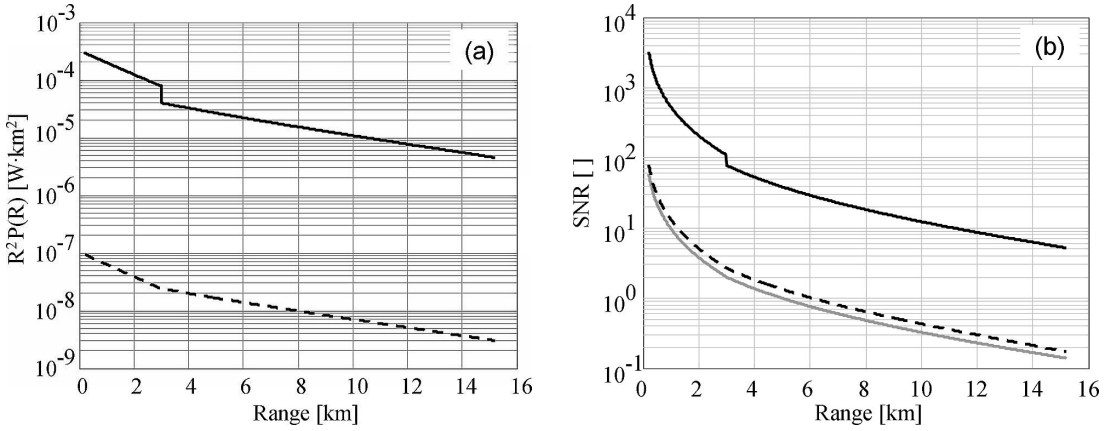

Figure 7.5: Elastic/Raman channel performance under night-time operation. (a) Simulated range-corrected power levels. (b) Simulated signal-to-noise ratios (SNR). (Solid black) Elastic channel. (Dashed black) Raman channel (photon-counting detection mode). (Solid grey) Raman channel (analog detection mode). The step at 3 km in the elastic channel corresponds to the end of the atmospheric boundary layer.

Figure 7.6 provides a more insightful analysis on the different noise variance components contributing to the system SNR (variances are computed in analog mode for the elastic channel and in photon-counting mode for the Raman channel, the latter is the most significant mode of operation for the Raman channel in terms of noise performance). It is seen that both channels operate in signal-induced shot-dominant regime, which ensures a slow $\sqrt{P(R)}$ decay in the SNR (i.e., nearly proportional to a $1/R$ decay for clear atmospheres) in front of a faster $1/R^2$ decay, characteristic of all other noise-dominant regimes (Section 2.2.2)[*Measures*, 1992b]. When comparing the background with the dark-noise variance, the latter is always below the background variance, which evidences quiet PMT detectors and a sufficient selection of the interference filter bandwidth (10nm for both channels, Table 7.2). With the

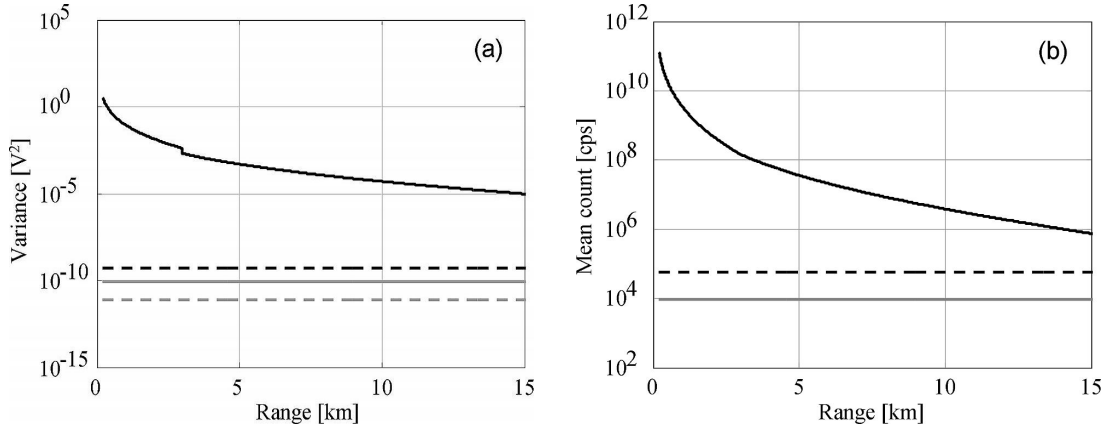

Figure 7.6: Noise variances. (a) Elastic channel (analog mode). (b) Raman channel (photon-counting mode). (Solid black) Signal-induced shot noise. (Dashed black) Background-induced shot noise (night-time operation). (Solid grey) Dark shot noise. (Dashed grey) Thermal noise.

elastic- and Raman-channel specifications of Table 7.1, the NEP_s (Eq.(2.33)) figure obtained is 3.5 and 3.8 $fW \cdot Hz^{-1/2}$, respectively, which corresponds to a detection sensitivity of about 1200 photons/s.

7.3.3 Observation Time versus Maximum System Range

The assessed $R_{\max}$ vs. observation time for both system channels is plotted in Figure 7.7 for the "very clear" atmospheric condition defined in Section 2.2.3 and a vertically pointing lidar (so that "range" corresponds to "height"). The Raman-channel simulation shows that for a 0 m a.s.l. ground-based lidar, an observation time of about 0.4 s is enough to surpass the boundary layer ($R_{\max} = R_{PBL} \approx 3km$). For 10-s observation time, the maximum range becomes $R_{\max} \approx 10km$, thus, reaching the top of the troposphere. In the case of the elastic channel (which is comparatively 3 orders of magnitude more intense than the Raman channel, see Figure 7.5a) even operating on a single-pulse basis ($n_i = 1$), $R_{\max} \approx 10$km is easily reached. The discrete "step-ladder" shape of the curves for very small observation times is consequence of the reduced number of light pulses emitted to the atmosphere.

7.4 CONCLUSIONS

A 1+1 elastic/Raman channel configuration operating night-time at 355/387-nm wavelengths has been proposed as the co-operative atmospheric-extinction calibration sensor for the

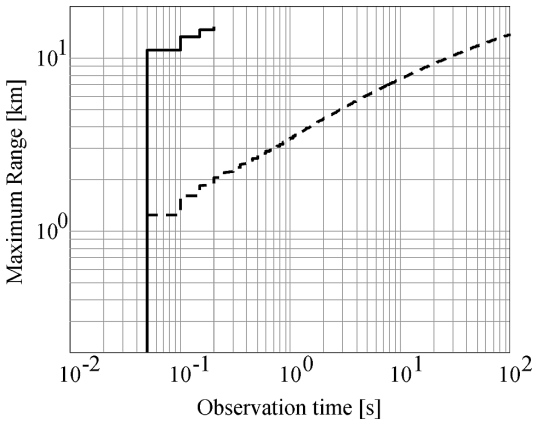

Figure 7.7: Estimated maximum system range vs. observation time (night-time operation, vertical pointing of the lidar). Maximum system range condition, $SNR_{goal} = 10$. (Solid) Elastic channel. (Dashed) Raman channel.

Cherenkov Telescope Array (CTA) under construction. Concept design of the IFAE/UAB lidar system has been presented in terms of an engineering overview of the main subsystems involved (Section 7.2), system specs (Table 7.1) and estimated system performance (Section 7.3). The simplified atmospheric model along with an ad-hoc methodological link-budget formulation used here to estimate return-power signal levels, SNR, and maximum system range has been presented in Chapter 2. Major assessment data products of this study are Figures 7.5–7.7.

The lidar system is based on a 60-mJ energy, 20-Hz rep. rate, 355-nm tripled Nd:YAG source coaxially arranged with a 1.8-m aperture, 1.8-m focal-length parabolic mirror conveying light by means of a liquid-guide to a polychromator equipped with 22-mm diameter PMT detectors. The Raman channel exhibits return power levels some 3 orders of magnitude below the elastic channel and reaches the top of troposphere (10 km in height) with a $SNR_{goal} = 10$ (photon-counting detection) with just 10-s observation time (Figure 7.7). Because of the large dynamic range of the lidar signal spanning some 4 orders of magnitude mixed Licel® analog/photon-counting transient recorders are planned to be used along with a software data-gluing procedure.

Future work comprises construction of the lidar prototype, its co-location on the final CTA site, and development of an inversion toolbox for Cherenkov data calibration taking into account the opto-atmospheric parameters measured by the lidar. Neutral density filters are foreseen to be included in the elastic channel of the polychromator along with an electronic gating feature for the PMT detectors (both channels disabled below approx. 200 m) in order to avoid detector saturation.

All in all, the IFAE/UAB Raman lidar holds promise of reducing the systematic uncertainties and increasing the observation duty cycle thanks to a better knowledge of the atmosphere.

Chapter 8

CONCLUSIONS

This Ph.D. thesis has dealt with the design, integration and analysis of the new RSLAB 3+2+1 multispectral elastic/Raman lidar system. The motivation and objectives of this study in the international context and, specifically, in order to fulfil the needs for quality-assured advanced lidar stations with sufficient channels for aerosol microphysical inversion and satellite cal/val within the European Lidar Network (EARLINET) have been given in Chapter 1. Chapter 2 has presented the power link-budget and opto-atmospheric model used for concept design and performance assessment of this new lidar system. Overlap factor (OVF) assessment and related sensitivity to different system parameters has been presented in Chapter 3, and optical design and opto-mechanical construction of the 6-channel polychromator in Chapter 4. First-order error-propagated backscatter-coefficient inversion error bounds for the two-component lidar inversion algorithm have been formulated in Chapter 5. In Chapter 6 integration of the new 3+2+1 lidar and a preliminary validation in terms of range-corrected signals in the framework of EARLINET SPALI-10 intercomparsion campaign has been presented. Finally, and subsidiary to Chapter 2, Chapter 7 has illustrated a case example concerning the design of the UAB-IFAE elastic/Raman lidar to be used for reducing the systematic uncertainties in astrophysical data in Cherenkov-Telescope Astrophysical (CTA) studies. An outlook of the main conclusion remarks follows.

8.1 ON THE THESIS WORK PRESENTED

(PART 1) On concept design of the RSLAB multi-spectral lidar system:

Chapters 2 and 3 have provided an essential methodology for concept design of elastic and Raman lidar systems.
Link-budget.-The link-budget methodology of Chapter 2 is completely valid for small-to-large aperture lidar systems. The RSLAB is a clear exponent of a medium-size aperture elastic/Raman case example (Chapter 2 itself) and the UAB-IFAE lidar that of a large aperture system (Chapter 7). A main output of the link-budget methodology is its capability to assess three key system performance parameters:

1. signal levels in reception,
2. signal-to-noise (SNR) ratio in reception, and
3. maximum system range at the different sounding wavelengths.

Point (1) above is of concern to photo-detector output current linearity and dynamic range in reception [*Bristow*, 1998; *Licel*, 2007a] (Figure 2.4). The former motivates the incorporation of neutral density filters to attenuate the return power levels of 355- and 532-nm elastic channels to levels comparable to those of the Raman channels. The latter motivates data gluing between analog and photon-counting (PC) acquisition units (analog recorders are not sensitive enough to deal with the weak signal levels at the far range of the lidar signal while PC units saturate in the near range) [*Kumar et al.*, 2012b].

Point (2) above has enabled to assess the SNR as a function of range under day-/night-time operating conditions (Figure 2.5). For the RSLAB lidar it has been shown (Section 2.2.2) that elastic channels at 355-, 532-, and 1064-nm wavelengths (day-time operation) operate in signal-induced shot-limited regime ($SNR \propto 1/R$, [*Measures*, 1992a]) from the starting sounding range until 12, 14, and 3 km, respectively, and under clear-air atmospheres (Figure 2.3). From these threshold ranges onwards the 1064-nm channel is in thermal-limited regime, and 355- and 532-nm channels are in background-limited mode ($SNR \propto 1/R^2$). When analyzing Raman channels (night-time operation), 387- and 607-nm channels are signal-shot limited over the whole simulation range and up to 2.4 km the 407-nm channel where from it becomes dark-shot limited.

Concerning point (3), Figure 2.7 has shown that the maximum system range (SNR_{goal}=10, [*Rocadenbosch et al.*, 1998]) does not virtually degrade from night-time to day-time operation for the elastic channels. This is not the case for Raman channels. Thus, under night-time operation a maximum sounding range of 10 km is reached with approximately 5 s observation time for the elastic channels at 355 and 532 nm (PMT based) and about 280 s (4.7 min) for the elastic channel at 1064 nm (APD based). 387- and 607-nm aerosol Raman channels take 2400 s (40 min) and 580 s (9.7 min), respectively, to reach that height. The water-vapour Raman channel (407 nm), requires 30-min to 1-h observation time to reach 1-2 km for the simulated mixing-ratio decay profile of Figure 2.2.

For the case example of the 1+1 elastic/Raman UAB-IFAE lidar [*Eizmendi*, 2011] the specs of the main subsystems involved have been summarised in Table 7.1 and the estimated system performance in Chapter 7, Section 7.3 and Figure 7.5-Figure 7.7. The Raman channel, which is of crucial importance to assess the atmospheric optical extinction, reaches the top of troposphere (10 km in height) with only 10-s observation time (SNR_{goal}=10, photon-counting detection). Because of the laser-telescope coaxial arrangement and the large telescope aperture (1.8 m) inclusion of neutral density filters in the elastic channels along with an electronic gating feature for the PMT detectors is a must in order to avoid saturation in the near range (below roughly 200 m).

Overlap factor assessment.- The OVF analysis of Chapter 3 has yield three main outputs:

- A ray-tracing model for OVF assessment in medium-size aperture (f/10-f/11), bi-axial lidar systems under Gaussian illumination (Section 3.3) [*Kumar et al.*, 2012c].

- The fact that inclusion of a field lens is a necessary requirement for medium-size telescopes (f/11 for the RSLAB lidar), which otherwise require unbearable detector sizes at the telescope focal plane (Figures 3.6-3.7).

- A sensitivity study on the OVF variations to field-lens and detector/fiber positions, and fiber's numerical (NA).

The ray-tracing model has been validated against previously published analytical-integral methods in the literature [*Halldórsson and Langerholc*, 1978; *Comerón et al.*, 2011] and proved to be a straightforward and simpler alternative.

Simulations have shown that the main advantages of including a field lens are mainly that (i) the incident rays on the telescope spread over the whole detector active area, hence, averaging out spatial inhomogeneities in the detector responsivity [*Simeonov et al.*, 1999; *Freudenthaler*, 2004], and (ii) a larger OVF insensitivity to laser divergence and variations in the field-lens position while keeping the detector/fiber at the field-lens focal plane. The latter has enabled to optimise the OVF (i.e., to lower the starting range of full overlap) by moving the detector position off-focus and closer to the field lens (Figure 3.9 and Figure 3.11). For fiber-coupled lidar systems the results are similar provided that the minimum NA is chosen according to Jenness. et al. [*Jenness et al.*, 1997], Eq.(3.15).

(PART 2) On polychromator design and implementation:

Though Chapter 4 has been written "a posteriori" and the design has been presented in linear text flow, its practical design is much more involved and requires to retrace steps back to the link-budget simulation tool, particularly, for the impact optical losses have on the estimated SNR and maximum system range at the different channel wavelengths. On an iterative design basis, Figure 4.1 and Table 4.1 summarise the final design achieved. The polychromator optical design is based on 1-inch optics (including dichroic filters) and a 3-mm fiber with NA=0.12.

Because the fiber optics at the polychromator input is not a point source (recall that the fiber is responsible for conveying the return lidar radiation from the telescope focal plane to the polychromator), light can not perfectly be collimated [*Möller*, 2007a] and the polychromator optical design has been more involved. As a result of large population of rays with oblique incidence, center wavelength and bandwidth of optical filters shift in wavelength (Eq.(4.3), [*Omegafilters*]). The filters' bandwidth has been chosen to cope with the "worst case" oblique incidence angle, which occurs for the 1064-nm channel. A 1-nm interference filter bandwidth has been used in all the channels. Eye-piece lens pairs have been placed in front of the detectors to average out uneven spatial responsivity effects (Figure 4.8).

At mechanical level, construction of the opto-mechanical and micro-mechanical parts has been outsourced. The optical parts of the polychromator fit an "L" shape structure with maximum dimensions 580 mm x 180 mm x 95 mm. The mechanical subrack enclosing the polychromator measures 600 mm x 460 mm x 160 mm.

(PART 3) On system integration and preliminary validation:

First-order backscatter-coefficient error bounds.-First-order analytical error bounds for the total atmospheric backscatter coefficient inverted from the two-component KFS lidar inversion algorithm have been formulated in Chapter 5 [*Rocadenbosch et al.*, 2012]. These error bounds are in explicit analytical form and in response to the four error sources ($\sigma_{\varepsilon_{j,1-4}}$) shown in Table 5.3. The error bounds obtained for the measurement noise (error sources (3) and (4)) are a function of the inverse of the SNR and hence, a SNR link-budget design specification from Chapter 2 and can be evaluated in terms of the estimated error on the inverted backscatter.

It has been shown that first-order error bounds are only approximate (classic error-propagation solution). However, their amplitudes usually lie between upper and lower Monte Carlo (MC) error bounds and are representative of a large part of the inverted population of backscatter-coefficient profiles under random noise / systematic uncertainties in practical situations. First-order error bounds computed at 3σ are in acceptable agreement with 3-σ statistical confidence limits in inversion situations with $SNR \geq 5$ at the maximum range above approximately 5 and systematic-error uncertainties below 10%. Though fundamentally different in their physical nature, the contribution of error sources (1) and (4) to the backscatter-coefficient error can be accounted via sensitivity Eq.(5.18), all of which leaves error sources (4) and (2) as the key ones.

RSLAB lidar system validation.- Chapter 6 has presented final integration both at hardware and software level of the 3+2+1 multi-spectral RSLAB lidar, today in routine operation. SPALI-2010 intercomparison campaign held in Madrid (18 Oct.-5 Nov. 2010) as part of EARLINET quality-assurance network activity has enabled to successfully validate operation of RSLAB lidar with exception of the water-vapour channel. The latter is due to the fact that only another station (Granada), which was also undergoing the intercomparison, was equipped with a water-vapour channel.
The signal processing validation methodology (Section 6.2) has been based on intercomparing the different lidar systems in terms of their range-corrected powers with respect to an approximate maximum-likelihood reference signal (or "mean" range-corrected signal) composed from the records of all the stations involved in each specific test session.

8.2 FUTURE LINES

The increasing demand for larger observation times and availability periods in a coordinated manner within the EARLINET makes essential the need of fully automated unmanned unattended lidar stations with service times close to 365/24. A definition scheme on the full automation of the new RSLAB multispectral lidar system has been introduced in Chapter 6. It includes integration, testing and validation of a robotic lidar "container" equipped with advanced surveillance systems and allowing operation in 365/24 mode, remotely controlled over the Internet, and visually safe for both overflying aircrafts and surrounding persons.

The multispectral capabilities of the RSLAB lidar here presented should pave the way to microphysical inversion and classification of aerosol characteristics (level-2 data products). This has recently been proposed in the Spanish National Science Foundation (Spanish Ministry of Economy and Competitivity, MEC) project "Multi-spectral atmospheric lidar observation, signal processing, and retrieval of data products: European Network and satellite cal/val (EUMULIDAR)" (submitted 2012). Such level-2 products will be of application to Earth's radiative-budget computations and provide good synergies with AERONET sunphotometer data.

From the point of view of signal processing, error bound estimation (in Chapter 5 preliminarily limited to backscatter-coefficient retrieval from the KFS elastic algorithm) must be extended to the derivation of error bounds for the extinction coefficient and to Raman channels as well. More important, the link-budget methodology presented in Chapter 2 should be linked with the error estimates in order to come up with an end-to-end performance simulator relating lidar design to performance estimates on the retrieved lidar products.

Appendix A

STATISTICAL FORMULAE

The mean value (a scalar), $\overline{U}_a$, of an observed range-dependent signal (e.g., the range-corrected power record of a given station "a") in Section 6.2, $\overrightarrow{U}_a = U_a(R_i)$, $i = 1, 2, ..., N$, is defined as [*Barlow*, 1989c]

$$\overline{U}_a = \frac{1}{N}\sum_{i=1}^{N} U_a(R_i). \tag{A.1}$$

In what follows functions and vectors are indistinctly treated. If the difference between two signals, $\overrightarrow{U}_a$ and $\overrightarrow{U}_{ref}$ with $\overrightarrow{U}_{ref}$ the reference profile is $\overrightarrow{\Delta U_a} = \overrightarrow{U}_a - \overrightarrow{U}_{ref}$ then the relative deviation of the signal $\overrightarrow{U}_a$ with respect to $\overrightarrow{U}_{ref}$ is

$$\overrightarrow{\Delta U}_{a,rel} = \frac{\overrightarrow{\Delta U_a}}{\overrightarrow{U}_{ref}}. \tag{A.2}$$

In Eq.(A.2) above, the relative deviation vector, $\overrightarrow{\Delta U}_{a,rel}$, is a *vector* performance indicator associated to the lidar stations "a" under analysis. The division sign stands for component-by-component division [i.e., $\overrightarrow{\Delta U}_{a,rel}(R) = \overrightarrow{\Delta U_a}(R)/U_{ref}(R)$]. Next, we compare two well-known scalar statistical indicators for $\overrightarrow{\Delta U}_{a,rel}(R)$, that is, the mean and the standard deviation.
The mean *of the relative deviation vector* $\overrightarrow{\Delta U}_{a,rel}$ is the scalar

$$\overline{\Delta U}_{a,rel} = \frac{1}{N}\sum_{i=1}^{N} \Delta U_{a,rel}(R_i), \tag{A.3}$$

where $\overline{\Delta U}_{a,rel}$ formerly stands for $(\overrightarrow{\Delta U}_{a,rel})$.

Likewise, the standard deviation (of the relative deviation vector $\overrightarrow{\Delta U}_{a,rel}$) is the scalar quantity [*Barlow*, 1989c]

$$\sigma_{a,rel} = \sqrt{\frac{1}{N-1}\sum_{i=1}^{N} (\Delta U_{a,rel}(R_i) - \overline{\Delta U}_{a,rel})^2}, \tag{A.4}$$

where $\sigma_{a,rel}$ stands for the standard deviation of vector $\overrightarrow{\Delta U}_{a,rel}$, std$(\overrightarrow{\Delta U}_{a,rel})$.

When comparing two data signals, be them from two different stations, $\overrightarrow{U}_a$ and $\overrightarrow{U}_b$, as from one station under test and the reference data, $\overrightarrow{U}_a$ and $\overrightarrow{U}_{ref}$, the normalized cross-correlation coefficient yields a very convenient scalar indicator because it is "shape" sensitive. In other words, the correlation coefficient between $\overrightarrow{U}_a$ and $\overrightarrow{U}_{ref}$ remains unaffected when $\overrightarrow{U}_a$ is scaled upto $k\overrightarrow{U}_a$, $k > 0$. The normalised cross-correlation coefficient between two signals, $\overrightarrow{U}_a$ and $\overrightarrow{U}_{ref}$ is defined as [*Barlow*, 1989c]

$$\rho_{a,ref} = \frac{\sum_{i=1}^{N}[U_a(R_i) - \overline{U_a}][U_{ref}(R_i) - \overline{U}_{ref}]}{\sqrt{\sum_{i=1}^{N}[U_a(R_i) - \overline{U_a}]^2}\sqrt{\sum_{i=1}^{N}[U_{ref}(R_i) - \overline{U}_{ref}]^2}}. \tag{A.5}$$

In the context of Section 6.2, $\overrightarrow{U}_a$ and $\overrightarrow{U}_{ref}$, stand for the range-corrected signals $U_a(R) = R^2P_a(R)$ and $U_{ref}(R) = R^2P_{ref}(R)$ in the data range $R \in R_i$, i=1,2,...,N. If, instead the statistics are to be computed in a certain subrange R_i, $i = N_1, ..., N_2$ then Eqs.(A.1-A.5) continue to hold with $\sum_{i=1}^{N}$ replaced by $\sum_{i=N1}^{N2}$ and N by $M = N_2 - N_1 + 1$. Finally note that if vector $\overrightarrow{\Delta U}_{a,rel}$ is computed in units of percentage % in Eq.(A.2), percentage units are also propagated to Eqs.(A.3) and (A.4).

Estimation of the reference signal.- A mean signal has to be constructed from the best parts of all signals as a common reference, which should be close to the unknown true signal. For this purpose each signal gets range dependent weights by an expert's guess reflecting its assumed accuracy, from which a first-guess, weighted mean signal is calculated. Formally,

$$U_{ref}(R) = \sum_{j=1}^{K} w_j(R)U_j(R), \tag{A.6}$$

where $\overrightarrow{U}_{ref}$ is the reference signal, $\overrightarrow{U}_j$, $j = 1, ..., K$ is the signal from the j-th station, K is the total number of stations in the intercomparison, and $w_j(R_i)$ is the range-dependent weight assigned to station "j" at the range R_i. Figure A.1 represents the range-dependent weights corresponding to the intercomparison case examples presented in Figure 6.11 and Figure 6.12 in Section 6.2.

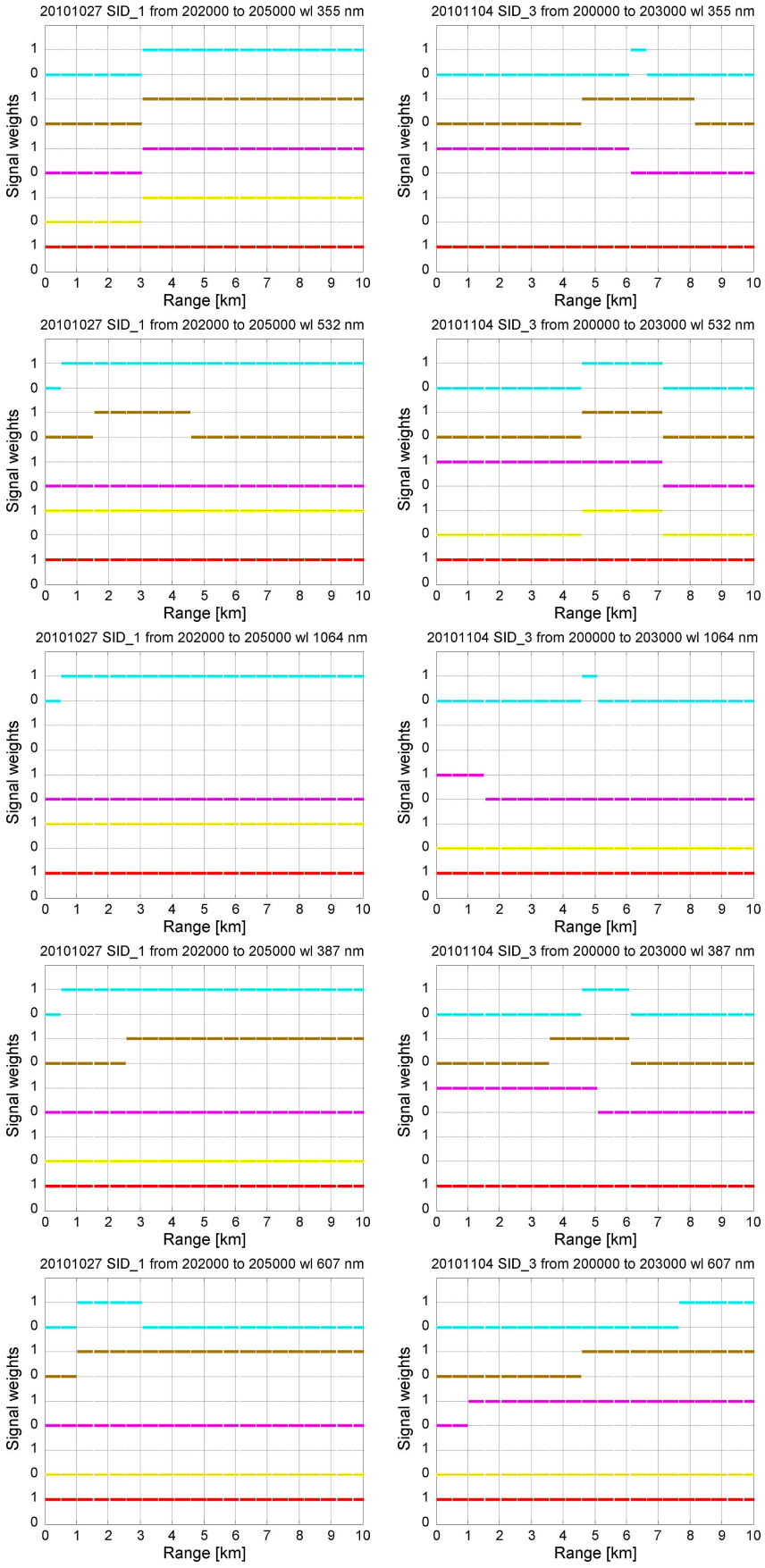

Figure A.1: Signal weights used for the calculation of the mean "reference" signal in the case examples shown in Figure 6.11, Table 6.2 and Figure 6.12, Table 6.3, respectively (SPALI-10 intercomparison). (Left) Weights for case example I (27.10.2010, session 01, 20:20-20:50 UTC). (Right) Weights for case example II (04.11.2010, session 03, 20:00-20:30 UTC). (Red) Potenza (PO), (yellow) Madrid (MA), (magenta) Granada (GR), (brown) Évora (EV), and (cyan) Barcelona (BA).

Appendix B

LIST OF PUBLICATIONS

Journals

1. Rocadenbosch, F., S. Frasier, D. Kumar, D. Lange, E. Gregorio, and M. Sicard, Backsactter error bounds for the elastic lidar two-component inversion algorithm, *IEEE Trans. Geosci. Remote Sens.*, in press (accepted on March 17, 2012), 2012.

2. Comerón, A., M. Sicard, D. Kumar, and F. Rocadenbosch, Use of a field lens for improving the overlap function of a lidar system employing an optical fiber in the receiver assembly, *Appl. Opt.*, *50*(28), 5538–5544, 2011.

3. Sicard, M., F. Rocadenbosch, M. N. M. Reba, A. Comerón, S. Tomás, D. García-Vízcaino, O. Batet, R. Barrios, D. Kumar, and J. M. Baldasano, Seasonal variability of aerosol optical properties observed by means of a Raman lidar at an EARLINET site over Northeastern Spain, *Atmos. Chem. Phys.*, *11*, 175190, doi:10.5194/acp-11-175-2011, 2011.

International Conferences

1. Comerón, A., M. Sicard, D. Kumar, F. Rocadenbosch, and D. Lange, Utilization of a field lens to improve the overlap function in lidar systems using optical fibers, *Proc. 20th ILRC*, submitted, 2012.

2. Kumar, D., D. Lange, and F. Rocadenbosch, Backscattered signal level and SNR validation methodology for tropospheric elastic lidars, *IEEE International Geoscience and Remote Sensing Symposium*, Munich (Germany), accepted, 2012a.

3. Kumar, D., D. Lange, F. Rocadenbosch, S. Tomás, M. Sicard, C. Muñoz, and A. Comerón, Power budget and performance assessment for the RSLAB multispectral elastic/Raman lidar system, *IEEE International Geoscience and Remote Sensing Symposium*, Munich (Germany), accepted, 2012b.

4. Lange, D., D. Kumar, F. Rocadenbosch, M. Sicard, and A. Comerón, Optimized data-gluing method for mixed analog/photon-counting lidar signals, *Óptica Pura y Aplicada*, accepted, 2012.

5. Molero, F., A. J. Fernandez, M. Pujadas, M. Sicard, S. Tomás, A. Comerón, D. Lange, D. Kumar, J. Giner, C. Muñoz, F. Rocadenbosch, F. Navas-Guzmán, M. J. Granados, L. Alados-Arboledas, J. A. Bravo, J. Preißler, F. Wagner, and J. L. Guerrero-Rascado,

Study on aerosol properties over Madrid (Spain) by multiple instrumentation during EARLINET lidar intercomparison campaign: SPALI10, *Óptica Pura y Aplicada*, accepted, 2012.

6. Kumar, D., F. Rocadenbosch, M. Sicard, A. Comerón, C. Muñoz, D. Lange, S. Tomás, and E. Gregorio, Six channel polychromator design and implementation for the U.P.C. elastic/Raman LIDAR, 8182, pp. 81,820W/1–81,820W/10, *Proc. SPIE*, doi: 10.1117/12.896305, 2011.

7. Rocadenbosch, F., M. N. M. Reba, M. Sicard, S. Tomás, and D. Kumar, Lidar ratio estimation using a two-point calibration in an turbid layer aloft, pp. 59–62, *Proc. 25th International Laser Radar Conference*, ISBN: 978-5-94458-109-9, 2010b.

8. Reba, M. N. M., F. Rocadenbosch, M. Sicard, D. Kumar, and S. Tomás, On the lidar ratio estimation from the synergy between aeronet sun-photometer data and elastic lidar inversion, pp. 883–886, *Proc. 25th International Laser Radar Conference*, St. Petersburg (Russia), ISBN: 978-5-94458-109-9, 2010.

9. Hiebsch, A., U. Wandinger, I. Mattis, A. Ansmann, G. Pappalardo, L. Mona, F. Madonna, G. D'Amico, A. Giunta, H. Linné, I. Serikov, A. Apituley, K. Wilson, L. Alados-Arboledas, F. N. Guzmán, D. Balis, E. Giannakaki, A. Chaikovsky, F. D. Tomasi, M. R. Perrone, V. Freudenthaler, M. Wiegner, F. Schnell, I. Grigorov, D. Stoyanov, M. Iarlori, V. Rizi, R. E. Mamouri, A. Papayanis, F. Molero, M. Pujadas, A. Pietruczuk, F. Rocadenbosch, S. Tomás, D. Kumar, N. Spinelli, and X. Wang, Long-term aerosol and cloud database from correlative EARLINET-CALIPSO observations, pp. 1241–1244, *Proc. 25th International Laser Radar Conference*, St. Petersburg (Russia), ISBN: 978-5-94458-109-9, 2010.

10. Sicard, M., M. N. M. Reba, F. Rocadenbosch, E. Gregorio, D. Kumar, S. Tomás, A. Comeron, F. Molero, M. Pujadas, J. L. Guerrero-Rascado, L. Alados-Arboledas, R. Pedrós, and J. A. Martínez, Intercomparison of spanish advanced lidars in the framework of EARLINET, pp. 2763–2766, *Proc. IEEE International Geoscience and Remote Sensing Symposium*, 2007.

11. Kumar, D., M. Sicard, S. Tomás, C. Muñoz, F. Rocadenbosch, and A. Comerón, Engineering of a water vapour, raman, elastic-backscatter lidar at the technical university of catalonia (spain), 6367, pp. 63,670U/1–63,670U/12, *Proc. SPIE*, doi:10.1117/12.690701, 2006.

National Conferences

1. Molero, F., A. Amodeo, M. Sicard, J. Preißler, F. Navas-Guzmn, V. Freudenthaler, A. J. Fernandez, A. Giunta, S. Tomás, F. Wagner, M. Granados, I. Mattis, M. Pujadas, G. D'Amico, A. Comerón, J. Guerrero-Rascado, L. Alados-Arboledas, D. Lange, J. Bravo, D. Kumar, G. Pappalardo, J. Giner, C. Muñoz, and F. Rocadenbosch, Study on aerosol properties over Madrid (Spain) by multiple instrumentation during SPALI10 lidar campaign, *V Reunión Española de Ciencia y Tecnologa de Aerosoles (RECTA)*, pp. B4/1–B4/6, 2011.

2. Guerrero-Rascado, J. L., M. Sicard, F. Molero, F. Navas-Guzmán, J. Preißler, D. Kumar, J. A. Bravo-Aranda, S. Tomás, M. N. M. Reba, L. Alados-Arboledas, A. Comerón, M. Pujadas, F. Rocadenbosch, F. Wagner, and A. M. Silva, Monitoring of the Eyjafjalla Volcanic Plume at Four Lidar Stations over the Iberian Peninsula: 6 to 8 May 2010, *IV*

Reunión Española de Ciencia y Tecnología del aerosol (RECTA), pp. C15/1–C15/6, 2010.

3. Kumar, D., Design and Implementation of Multi-spectral Remote Sensing Capabilities in the U.P.C. Lidar System, pp. 39–40, *Proc. Barcelona Forum on Ph.D. Research in Communications, Electronics and Signal Processing*, Universitat Politècnica de Catalunya, Barcelona (Spain), 2010.

Appendix C

LIST OF SYMBOLS

Latin Symbols

A_r	Telescope effective area [m^2]
aer	Sub/super-index term for aerosol [ ]
B_N	Noise-equivalent bandwidth [Hz]
c	Speed of light in vacuum (2.998×10^8 [ms^{-1}])
E	Transmitted laser energy [J]
$e(R)$	(Range-dependent) Water-vapour pressure [hPa]
$e_s(R)$	Saturated water-vapour pressure [hPa]
F	Excess-noise factor [ ]
G_T	Transimpedance gain [Ω]
h	Planck's constant (6.625×10^{-34} [J·s])
I_{ds}, I_{db}	(Photo-detector) Surface-dark current, Dark-bulk current [A]
K	Lidar system constant [W·m^3]
k	Boltzmann's constant (1.38×10^{-23} [JK^{-1}])
L_{back}	Background spectral radiance [$Wcm^{-2}nm^{-1}sr^{-1}$]
M	Photo-detector internal gain [ ]
mol	Sub/super-index term for molecular [ ]
MW	Molecular weight [g·mol^{-1}]
N	Number of samples [samples]
NEP	Noise Equivalent Power [W·$Hz^{-1/2}$]
n_i	Number of integrated pulses
$N_{sh,s}, N_{sh,b}, N_{sh,d}, N_{th}$	Signal-induced shot-noise power [V^2], Background-induced shot-noise power [V^2], Dark shot-noise power [V^2], Thermal noise power [V^2]
N_X	Molecule number density for gas species 'X' [molecules·m^{-3}]
N'_s, N'_b, N'_d	Mean number of counts per second due to the lidar return signal, to the background light, and to the dark current, respectively
OVF_λ	Overlap factor at wavelength λ [ ]
$P(R)$	(Range-dependent) power signal [W]
$p(R)$	(Range-dependent) Air pressure [hPa]
$P_{back}(\lambda)$	Background-radiation power [W]
$P_{DryAir}(R)$	(Range-dependent) Dry-Air pressure [hPa]
PRF	Pulse Repetition Frequency [Hz]
q	Electron charge (1.602×10^{-19} [C])

R	Observation range [km]
RH	Relative humidity [ ]
R_{in}	Input impedance [Ω]
R_i, R_{io}	(Photo-detector) Current responsivity [AW^{-1}], Intrinsic current responsivity [AW^{-1}]
R_v, R'_v	(Photo-detector) Voltage responsivity [VW^{-1}], Net voltage responsivity [VW^{-1}]
$SNR(R)$	(Range-dependent) Signal-to-noise ratio [ ]
S_{aer}, S_{mol}	Aerosol extinction-to-backscatter ratio (lidar ratio) [sr], Molecular lidar ratio [sr]
$T(R)$	(Range-dependent) Atmospheric transmissivity [ ]
t_{obs}	Observation time [s]
$U(R)$	(Range-corrected) signal [W· km^2]
V_m	Visibility margin [km]
w	Water-vapour mixing ratio [g·kg^{-1}]
z	Height [km]

Greek Symbols

α	Extinction coefficient [km^{-1}]
β	Backscatter coefficient [$km^{-1}sr^{-1}$]
$\Delta\lambda$	Full-Width Half-Maximum (FWHM) of the interference filter [nm]
$\Delta\Omega$	Solid angle [sr]
$d\sigma_x/d\Omega$	Differential molecular backscatter cross-section at λ_x per solid angle unit [m^2sr^{-1}]
κ	Wavelength-dependence power law exponent (Ångström coefficient) [ ]
λ	Wavelength [nm]
$\sigma^2_{sh,s}, \sigma^2_{sh,d}, \sigma^2_{th}$	Photo-induced signal-shot spectral density [V^2Hz^{-1}], Dark-shot spectral density [V^2Hz^{-1}], Thermal-noise spectral density [V^2Hz^{-1}]
$\sigma_{\varepsilon_{j,1}}, \sigma_{\varepsilon_{j,2}}, \sigma_{\varepsilon_{j,3-4}}$	Error standard deviation due to the backscatter-coefficient calibration [$km^{-1}sr^{-1}$], to the lidar ratio [$km^{-1}sr^{-1}$], and to the observation noise [$km^{-1}sr^{-1}$], respectively
τ	Optical depth [ ]
θ	Laser half-divergence angle [°]
$\varepsilon_r^{\beta_N}$	Relative backscatter-coefficient calibration error [ ]
$\xi_{net}(\lambda), \xi_t(\lambda), \xi_b(\lambda), \xi_{poly}(\lambda)$	Receiving channel transmissivity [ ], Telescope transmission [ ], Fiber-bundle transmission [ ], Polychromator transmission [ ]

Appendix D

LIST OF ACRONYMS AND ABBREVIATIONS

ABL	Atmospheric Boundary Layer
ACTRIS	Aerosol, Clouds and Trace gases Research Infrastructure Network
ADC	Analog-to-digital conversion
AD-NET	Asian Dust-NETwork
AOT	Aerosol Optical thickness
APD	Avalanche Photo-Diode
asl	Above Sea Level
CALIOP	Cloud-Aerosol Lidar with Orthogonal Polarization
CALIPSO	Cloud-Aerosol Lidar and Infrared Pathfinder Satellite
cal/val	Calibration/Validation
EARLINET	European Aerosol Research LIdar Network
EARLINET-ASOS	EARLINET-Advanced Sustainable Observation System
ELT	Extremely Large Telescope
ESA	European Space Agency
EU	European Union
FOV	Field of View
FP	Framework Programme
GALION	GAW LIdar Observation Network
GAW	Global Atmosphere Watch
HSRL	High Spectral Resolution Lidar
KFS	Klett-Fernald-Sasano (two-component elastic lidar inversion)
KLT	Klett (one-component elastic lidar inversion)
LIDAR	LIght Detection and Ranging
LITE	Lidar In-space Technology Experiment
MC	Monte Carlo
MPLNET	Micro Pulse Lidar NETwork
NASA	National Aeronautics and Space Administration
NDF	Neutral density filter
Nd:YAG	Neodymium-doped Yttrium Aluminium Garnet
NEP	Noise Equivalent Power
NIR	Near infrared
O/E	Opto-electronic
OVF	Overlap factor
pdf	Probability Density Function
PMT	Photo-Multiplier Tube
RSLAB	Remote Sensing LABoratory
SPALINET	Spanish and Portuguese Aerosol LIdar NETwork
UPC	Universitat Politècnica de Catalunya
UV	Ultra-violet
VIS	Visible

REFERENCES

ACTRIS, Report on first internal quality checks for hardware: Deliverable WP2/D2.2, *Tech. rep.*, `http://www.actris.net/` (accessed on March 2012). xxiii, 90

Angelis, A. D., Very-high-energy gamma astrophysics, *Nuovo Cimento*, *C-32*(N5-6), 19, 2009. 93

Ansmann, A., Ground-truth aerosol lidar observations: Can the Klett solutions obtained from ground and space be equal for the same aerosol scenario?, *Appl. Opt.*, *45*, 3367–3371, 2006. 56

Ansmann, A., M. Riebesell, and C. Weitkamp, Measurement of atmospheric aerosol extinction profiles with a raman lidar, *Opt. Lett.*, *15*(13), 746–748, 1990. 4

Ansmann, A., U. Wandinger, M. Riebesell, C. Weitkamp, and W. Michaelis, Independent measurement of extinction and backscatter profiles in cirrus clouds by using a combined raman elastic-backscatter lidar, *Appl. Opt.*, *31*(33), 7113–7131, 1992. 6, 56, 88, 94

Ansmann, A., J. Bösenberg, A. P. Chaikovsky, A. Comerón, R. Eixmann, V. Freudenthaler, P. Ginoux, L. Konguem, H. Linné, M. Á. L. Márquez, S. Manoj, V. Matthias, I. Mattis, V. Mitev, D. Müller, S. Nickovic, J. Pelon, L. Sauvage, P. Sobolewsky, A. Stohl, O. Torres, G. Vaughan, U. Wandinger, and M. Wiegner, Long-range transport of Saharan dust to northern Europe: The 11-16 October 2001 outbreak with EARLINET, *Journal of Geophysical Research*, *108*(D24), 4783, doi:10.1029/2003JD00375, 2003. 2

Ansmann, A., U. Wandinger, O. L. Rille, D. Lajas, and A. G. Straume, Particle backscatter and extinction profiling with the spaceborne high-spectral-resolution Doppler lidar ALADIN: methodology and simulations, *Appl. Opt.*, *46*, 6606–6622, 2007. 4

Apituley, A., V. Freudenthaler, and F. Rocadenbosch, EARLINET approach to optimisation of individual network instruments with the aim of homogenisation of aerosol data products and increased data coverage, pp. (II–414)–(II–417), *Proc. IEEE International Geoscience and Remote Sensing Symposium*, 2008. 10

Apituley, A., V. Freudenthaler, and A. Comeron, Report on the Implementation of Optimised Standard Solutions and Improvement of Performance, *Tech. rep.*, EARLINET-ASOS, Deliverable D4.6, 2011. xvii, 5, 81

Barlow, R., Errors, in *Statistics: A Guide To The Use of Statistical Methods In The Physical Sciences*, edited by F. Mandl, R. Ellison, and D. Sandiford, chap. 4, pp. 48–67, Wiley, Chichester, England, 1989a. 61

Barlow, R., Estimation, in *Statistics: A Guide To The Use of Statistical Methods In The Physical Sciences*, edited by F. Mandl, R. Ellison, and D. Sandiford, chap. 5, pp. 68–96, Wiley, Chichester, England, 1989b. 25

Barlow, R. J., Describing the data, in *Statistics. A Guide to the Use of Statistical Methods in Physical Sciences*, edited by F. Mandl, R. Ellison, and D. Sandiford, chap. 2, pp. 3–19, Wiley, Chichester, England, 1989c. 107, 108

Barret, E. W., and O. Ben-Dov, Application of the lidar to air pollution measurements, *J. Appl. Meteor.*, *6*, 500–515, 1967. 56

Behrendt, A., T. Nakamura, M. Onishi, R. Baumgart, and T. Tsuda, Combined raman lidar for the measurement of atmospheric temperature, water vapor, particle extinction coefficient, and particle backscatter coefficient, *Appl. Opt.*, *41*(36), 7657–7666, 2002. 94

Berezhnyy, I., A combined diffraction and geometrical optics approach for lidar overlap function computation, *Optics and Lasers in Engineering*, *47*, 855–859, 2009. 32

Bissonnette, L. R., Sensitivity Analysis of Lidar Inversion Algorithms, *Appl. Opt.*, *25*(13), 2122–2125, 1986. 56

Böckmann, C., D. Müller, L. Osterloh, P. Pornsawad, and A. Papayannis, From EARLINE-TASOS raman-lidar signals to microphysical aerosol properties via advances regularizing software, pp. (II–422)–(II–425), *IEEE International Geoscience and Remote Sensing Symposium*, 2008. 4, 57

Bodhaine, B. A., N. B. Wood, E. G. Dutton, and J. R. Slusser, On rayleigh optical depth calculations, *Atmos. and Ocean. Technol.*, *16*(11), 1854–1861, 1999. 13, 14, 59, 65

Boley, F., Atmospheric Cherenkov Radiation from Cosmic-Ray Air Showers, *Reviews of Modern Physics*, *36*, 792–808, 1964. 93

Bösenberg, J., and R. Hoff, Plan for the implementation of the GAW Aerosol Lidar Observation Network (GALION), *Tech. rep.*, Hamburg, Germany, GAW Report no. 178, WMO/TD-No. 1443, 2007. 1, 56

Bösenberg, J., and V. Matthias, EARLINET: A European Aerosol Research Lidar Network to Establish an Aerosol Climatology, *Final report (2000-2003) 191*, Max-Planck Institut für Meteorologie, Hamburg (Germany), 2003. 32

Box, G. E. P., and M. E. Muller, A note on the generation of random normal deviates, *The Annals of Mathematical Statistics*, *29*(2), 610–611, 1958. 37

Bristow, M. P., Lidar-signal compression by photomultiplier gain modulation: influence of detector nonlinearity, *Appl. Opt.*, *37*(27), 6468–6479, 1998. 20, 99, 104

Buck, A. L., New equations for computing vapor pressure and enhancement factor, *Appl. Meteorol.*, *20*, 1527–1532, 1981. 16

Buck, A. L., *Buck Research Manual*, updated equation from Buck A. L., New equations for computing vapor pressure and enhancement factor, 1996. 16

CALIPSO, `http://www-calipso.larc.nasa.gov/` (accessed on January 2009). 1, 4

Chourdakis, G., A. Papayannis, and J. Porteneuve, Analysis of the receiver response for a noncoaxial lidar system with fiber-optic output, *Appl. Opt.*, *41*, 2715–2723, 2002. 31, 32

Collis, R., and P. Russell, Lidar measurements of Particles and Gases by Elastic Backscattering and Differential Absorption, in *Laser Monitoring of the atmosphere*, edited by E. Hinkley, chap. 4, pp. 71–102, Springer-Verlag, New York, 1976. xviii, 14, 17, 18, 56, 95

Comerón, A., F. Rocadenbosch, M. A. López, A. Rodríguez, C. Muñoz, D. García-Vizcaíno, and M. Sicard, Effects of noise on lidar data inversion with the backward algorithm, *Appl. Opt.*, *43*(12), 2572–2577, 2004. xxi, 57, 62, 67, 68

Comerón, A., M. Sicard, D. Kumar, and F. Rocadenbosch, Use of a field lens for improving the overlap function of a lidar system employing an optical fiber in the receiver assembly, *Appl. Opt.*, *50*(28), 5538–5544, 2011. xx, 31, 32, 36, 37, 42, 105

Comerón, A., M. Sicard, D. Kumar, F. Rocadenbosch, and D. Lange, Utilization of a field lens to improve the overlap function in lidar systems using optical fibers, *Proc. 20th ILRC*, submitted, 2012.

Davis, P. A., The analysis of lidar signatures of cirrus clouds, *Appl. Opt.*, *8*(10), 2099–2102, 1969. 56

Donovan, D. P., J. A. Whiteway, and A. I. Carswell, Correction for nonlinear photon-counting effects in lidar systems, *Appl. Opt.*, *32*, 6742–6753, 1993. 19, 98

Dorner, D., K. Nilsson, and T. Bretz, A method to correct IACT data for atmospheric absorption due to the Saharan Air Layer, 1085, pp. 677–680, *Proc. American Institute of Physics (AIP) Conference*, 2009. 94

Doro, M., CTA - A Project for a New Generation of Cherenkov Telescopes, *Nucl. Instrum. Meth.*, *A 630*, 285, 2011. 94

Duck, J., Aircraft-protection radar for use with atmospheric lidars, *Appl. Opt.*, *44*(23), 4937–4945, 2005. 80

EARLINET, NA 4, Handbook of Instruments, `www.earlinet.org` (accessed on Jun. 2011). 32

Eizmendi, M. I., Development and characterisation of a Raman LIDAR at the Universitat Autònoma de Barcelona (UAB), Masters' thesis, Escola Tècnica Superior d'Enginyeria de Telecomunicació de Barcelona (ETSETB), Dept. of TSC, Universitat Politècnica de Catalunya (UPC), Advisors: Dr. M. Doro (UAB), Dr. F. Rocadenbosch, 2011. 104

ESA, Clouds, Aerosols, and Radiation Explorer, *Tech. Rep. ESA SP-1279(1)*, ESTEC, Noordwijk, The Netherlands, 2004. 1, 4

ESA, ESA's Wind Mission ADM-AEOLUS, *Tech. Rep. BR-236*, ESTEC, Noordwijk, The Netherlands, 2005. 1, 4

Fernald, F. G., Analysis of Atmospheric Lidar Observations: Some Comments, *Appl. Opt.*, *23*(5), 652–653, 1984. 56

Fernald, F. G., B. M. Herman, and J. A. Reagan, Determination of aerosol height distribution by lidar, *J. Appl. Meteor.*, *11*, 482–489, 1972. 56

Fiocco, G., and L. Smullin, Detection of Scattering Layers in the Upper Atmosphere (60-140 km) by Optical Radar, *Nature*, *199*, 1275–1276, 1963. 1

Freudenthaler, V., Effects of spatially inhomogeneous photomultiplier sensitivity on lidar signals and remedies, pp. 37–40, *Proc. 22nd International Laser Radar Conference* , 2004. 52, 105

Freudenthaler, V., The Telecover Test: A quality assurance tool for the optical part of a lidar system, pp. 145–146, *Proc. 23rd International Laser Radar Conference*, 2006. 32

Freudenthaler, V., A. Amodeo, and I. Serikov, Report on IC-campaign, part 1+2: Deliverable D3.6, *Tech. rep.*, EARLINET report, `www.earlinet.org` (accessed on March 2012), 2011. xxii, xxv, 81, 83, 88

Guerrero-Rascado, J. L., M. Sicard, F. Molero, F. Navas-Guzmán, J. Preißler, D. Kumar, J. A. Bravo-Aranda, S. Tomás, M. N. M. Reba, L. Alados-Arboledas, A. Comerón, M. Pujadas, F. Rocadenbosch, F. Wagner, and A. M. Silva, Monitoring of the Eyjafjalla Volcanic Plume at Four Lidar Stations over the Iberian Peninsula: 6 to 8 May 2010, *IV Reunión Española de Ciencia y Tecnología del aerosol (RECTA)*, pp. C15/1–C15/6, 2010.

Halldórsson, T., and J. Langerholc, Geometrical form factors for the lidar function, *Appl. Opt.*, *17*, 240–244, 1978. xx, 31, 32, 37, 42, 105

Hamamatsu, P., Photon Counting Using Photomultiplier Tubes, in *Application notes TPHO9001E02*, Japan, 1998. 21, 23, 96

Harms, J., Lidar return signals for coaxial and noncoaxial systems with central obstruction, *Appl. Opt.*, *18*, 1559–1566, 1979. 31, 32

Hiebsch, A., U. Wandinger, I. Mattis, A. Ansmann, G. Pappalardo, L. Mona, F. Madonna, G. D'Amico, A. Giunta, H. Linné, I. Serikov, A. Apituley, K. Wilson, L. Alados-Arboledas, F. N. Guzmán, D. Balis, E. Giannakaki, A. Chaikovsky, F. D. Tomasi, M. R. Perrone, V. Freudenthaler, M. Wiegner, F. Schnell, I. Grigorov, D. Stoyanov, M. Iarlori, V. Rizi, R. E. Mamouri, A. Papayanis, F. Molero, M. Pujadas, A. Pietruczuk, F. Rocadenbosch, S. Tomás, D. Kumar, N. Spinelli, and X. Wang, Long-term aerosol and cloud database from correlative EARLINET-CALIPSO observations, pp. 1241–1244, *Proc. 25th International Laser Radar Conference*, St. Petersburg (Russia), ISBN: 978-5-94458-109-9, 2010.

Hillas, A. M., Cherenkov Images of EAS produced by primary gamma rays and by nuclei, 3, p. 445, *Proc. of the 19th International Cosmic Ray Conference (ICRC)*, La Jolla, USA, 1985. 94

Hitschfeld, W., and J. Bordan, Errors inherent in the radar measurement of rainfall at attenuating wavelengths, *J. Appl. Meteor.*, *11*, 58–67, 1954. 56

Hoff, R. M., J. Bösenberg, and G. Pappalardo, The GAW Aerosol Lidar Observation Network (GALION), *IEEE International Geoscience and Remote Sensing Symposium*, Boston (MA, USA, 2008. 4

Hu, S., X. Wang, Y. Wu, C. Li, and H. Hu, Geometrical form factor determination with raman backscattering signals, *Opt. Lett.*, *30*, 1879–1881, 2005. 31

Huneeus, N., and O. Boucher, One dimensional variational retrieval of aerosol extinction coefficient from synthetic LIDAR and radiometric measurements, *J. Geophys. Rsch.*, *112*(D14303), doi: 10.1029/2006JD007625, 2007. 56

Inaba, H., Detection of Atoms and Molecules by Raman Scattering and Fluorescence, in *Laser Monitoring of the Atmosphere*, edited by E. D. Hinkley, chap. 5, pp. 143–206, Springer-Verlag, New York, 1976. 15, 19, 94

Jenness, J. R., D. B. Lysak (Jr)., and C. R. Philbrick, Design of a lidar receiver with fiber-optic output, *Appl. Opt.*, *36*(18), 4278–4284, 1997. 31, 32, 41, 72, 105

Klett, J. D., Stable Analytical Inversion Solution for Processing Lidar Returns, *Appl. Opt.*, *20*(2), 211–220, 1981. 56, 57

Klett, J. D., Lidar Calibration and Extinction Coefficients, *Appl. Opt.*, *20*, 514–515, 1983. 56

Klett, J. D., Lidar Inversion with Variable Backscatter/Extinction Ratios, *Appl. Opt.*, *24*, 1638–1643, 1985. 10, 56

Klett, J. D., Extinction boundary value algorithms for lidar inversion, *Appl. Opt.*, *25*(15), 2462–2464, 1986. 56

Knauss, D., Significance of the boundary value term in the Klett lidar inversion formula, *Appl. Opt.*, *21*(23), 4194, 1982. 62

Kohl, R. H., Discussion of the interpretation problem encountered in single-wavelength lidar transmissometers, *J. Appl. Meteor.*, *17*, 1034–1038, 1978. 56

Kokhanenko, G. P., I. E. Penner, and V. S. Shamanaev, Expanding the dynamic range of a lidar receiver by the method of dynode-signal collection, *Appl. Opt.*, *41*(24), 5073–5077, 2002. 20

Koshmieder, H., Theorie der horizontalen sichtweite, *Beitr. Phys. Freien Atmos.*, *12*, 33–53, 1924. 14, 18

Kovalev, V. A., Lidar measurement of the vertical aerosol extinction profiles with rangede-pendent backscatter-to-extinction ratios, *Appl. Opt.*, *32*(30), 6053–6065, 1993. 56

Kovalev, V. A., Stable near-end solution of the lidar equation for clear atmospheres, *Appl. Opt.*, *42*(3), 585–591, 2003. 56

Kovalev, V. A., Detectors, Digitizers, Electronics, in *Elastic Lidar: Theory, Practice, and Analysis Methods*, edited by V. A. Kovalev and W. E. Eichinger, chap. 4, pp. 105–142, John Wiley & Sons, Inc., USA, 2004. 72

Kruse, P. W., L. D. McGlauchlin, and R. B. McQuistan, *Elements of Infrared Technology*, Wiley, New York, 1963. 18

Kumar, D., Design and Implementation of Multi-spectral Remote Sensing Capabilities in the U.P.C. Lidar System, pp. 39–40, *Proc. Barcelona Forum on Ph.D. Research in Communications, Electronics and Signal Processing*, Universitat Politècnica de Catalunya, Barcelona (Spain), 2010.

Kumar, D., M. Sicard, S. Tomás, C. Muñoz, F. Rocadenbosch, and A. Comerón, Engineering of a water vapour, raman, elastic-backscatter lidar at the technical university of catalonia (spain), 6367, pp. 63,670U/1–63,670U/12, *Proc. SPIE*, doi:10.1117/12.690701, 2006. 9, 25, 45, 46

Kumar, D., F. Rocadenbosch, M. Sicard, A. Comerón, C. Muñoz, D. Lange, S. Tomás, and E. Gregorio, Six channel polychromator design and implementation for the U.P.C. elastic/Raman LIDAR, 8182, pp. 81,820W/1–81,820W/10, *Proc. SPIE*, doi: 10.1117/12.896305, 2011. 9, 45

Kumar, D., D. Lange, and F. Rocadenbosch, Backscattered signal level and SNR validation methodology for tropospheric elastic lidars, *IEEE International Geoscience and Remote Sensing Symposium*, Munich (Germany), accepted, 2012a. 13

Kumar, D., D. Lange, F. Rocadenbosch, S. Tomás, M. Sicard, C. Muñoz, and A. Comerón, Power budget and performance assessment for the RSLAB multispectral elastic/Raman lidar system, *IEEE International Geoscience and Remote Sensing Symposium*, Munich (Germany), accepted, 2012b. 9, 13, 104

Kumar, D., F. Rocadenbosch, and A. Comerón, Determination of the overlap factor and its enhancement for medium-size tropospheric lidar systems: a ray-tracing approach, *J. Appl. Rem. Sens.*, submitted, 2012c. 104

Kunz, G. J., Transmission as an input boundary value for an analytical solution of a singlescatter lidar equation, *Appl. Opt.*, *35*(18), 3255–3260, 1996. 56

Lange, D., Adaptive signal processing and inversion techniques for elastic/raman lidar systems, Ph.D. thesis Proposal, Escola Tècnica Superior d'Enginyeria de Telecomunicacio de Barcelona (ETSETB), Universitat Politècnica de Catalunya (UPC), Barcelona (Spain), Thesis advisor: Dr. F. Rocadenbosch, 2012. 4, 10

Lange, D., D. Kumar, F. Rocadenbosch, M. Sicard, and A. Comerón, Optimized data-gluing method for mixed analog/photon-counting lidar signals, *Óptica Pura y Aplicada*, accepted, 2012. 74

Licel, Analysis example: Gluing analog and photon counting data, in *Licel Ethernet Controller-Installation and Reference Manual*, chap. 9.4, Germany, Also, private communication from Bernd Mielke (Licel GmbH), 2007a. 19, 98, 99, 104

Licel, *Licel Ethernet Controller-Installation and Reference Manual*, Licel Gmbh, Germany, 2007b. xxii, 74, 76, 77, 78, 79

Licel, Si-Avalanche Photodiode Module, Licel GbR, Germany, Data sheet, `http://www.licel.com/APD.htm` (accessed on March 2012), 2009a. 74

Licel, Photomultiplier modules, Licel GbR, Germany, Data sheet, `http://www.licel.com/DET-HV.htm` (accessed on March 2012), 2009b. 74

Licel, Licel transient recorder-data sheet, Licel GbR, Germany, Data sheet, `http://www.licel.com/transdat.htm` (accessed on March 2012), 2009c. xxii, 75, 76

Martucci, G., V. Mitev, R. Matthey, and M. Srivastava, Remote-controlled automatic backscatter lidar for PBL and troposphere measurements: description and first results, 5235, pp. 661–672, SPIE, *Proc. of SPIE*, Bellingham, WA, 2003. 5

Matsumoto, M., and N. Takeuchi, Effects of misestimated far-end boundary values on two common lidar inversion solutions, *Appl. Opt.*, *33*(27), 6451–6456, 1994. 56

Matthias, V., V. Freudenthaler, A. Amodeo, I. Balin, D. Balis, J. Bosenberg, A. Chaykovski, G. Chourdakis, A. Comeron, A. Delaval, F. D. Tomasi, R. Eixmann, A. Hagard, L. Komguem, S. Kriepl, R. Matthey, V. Rizi, J. A. Rodrigues, U. Wandinger, and X. Wang, Aerosol lidar intercomparison in the framework of the EARLINET project. 1. Instruments, *Appl. Opt.*, *43*(4), 961–976, 2004. 5

Mattis, I., A. Ansmann, D. Althausen, V. Jaenisch, U. Wandinger, D. Muller, Y. F. Arshinov, S. M. Bobrovnikov, and I. B. Serikov, Relative-humidity profiling in the troposphere with a raman lidar, *Appl. Opt.*, *41*(30), 6451–6462, seminare Maurey-Schwartz (1975-1976), 2002. xviii, 16

Measures, R. M., *Laser Remote Sensing: Fundamentals and Applications*, Wiley, New York, 1984. 31, 36

Measures, R. M., Interaction and Propagation of Radiation, in *Laser Remote Sensing: Fundamentals and Applications*, chap. 4, pp. 138–145, Krieger, Malabar, Fla., 1992a. 14, 17, 22, 104

Measures, R. M., Laser Systems as Remote Sensors, in *Laser Remote Sensing: Fundamentals and Applications*, chap. 4, pp. 226–233, Krieger, Malabar, Fla., 1992b. 1, 23, 100

Mirzoyan, R., Cherenkov light observation with the HEGRA detector at the Roque de los Muchachos Observatory, *New Astronomy Reviews*, *42*, 547–551, 1998. 99

Molero, F., A. Amodeo, M. Sicard, J. Preißler, F. Navas-Guzmn, V. Freudenthaler, A. J. Fernandez, A. Giunta, S. Tomás, F. Wagner, M. Granados, I. Mattis, M. Pujadas, G. D'Amico, A. Comerón, J. Guerrero-Rascado, L. Alados-Arboledas, D. Lange, J. Bravo, D. Kumar, G. Pappalardo, J. Giner, C. Muñoz, and F. Rocadenbosch, Study on aerosol properties over Madrid (Spain) by multiple instrumentation during SPALI10 lidar campaign, *V Reunión Española de Ciencia y Tecnologa de Aerosoles (RECTA)*, pp. B4/1–B4/6, 2011. xxv, 71, 81, 82, 83, 91

Molero, F., A. J. Fernandez, M. Pujadas, M. Sicard, S. Tomás, A. Comerón, D. Lange, D. Kumar, J. Giner, C. Muñoz, F. Rocadenbosch, F. Navas-Guzmán, M. J. Granados, L. Alados-Arboledas, J. A. Bravo, J. Preißler, F. Wagner, and J. L. Guerrero-Rascado, Study on aerosol properties over Madrid (Spain) by multiple instrumentation during EARLINET lidar intercomparison campaign: SPALI10, *Óptica Pura y Aplicada*, accepted, 2012. xxv, 71, 83

Möller, K. D., Geometrical optics, in *Optics: Learning by Computing with example using Mathcad, Matlab, Mathematica and Maple*, pp. 1–73, Springer Science and Business Media, New York, ISBN 13: 978-0-387-26168-3 (print format), ISBN 13: 978-0-387-69492-4 (electronic format), 2007a. 9, 49, 105

Möller, K. D., Matrix Formulation for the Thin lens and Systems of Thin Lenses, in *Optics: Learning by Computing with example using Mathcad, Matlab, Mathematica and Maple*, chap. 1, pp. 38–58, Springer Science and Business Media, New York, ISBN 13: 978-0-387-26168-3 (print format), ISBN 13: 978-0-387-69492-4 (electronic format), 2007b. 32, 33, 36

Müller, D., A. Ansmann, I. Mattis, M. Tesche, U. Wandinger, D. Althausen, and G. Pisani, Aerosol type-dependent lidar ratio observed with Raman lidar, *Journal of Geophysical Research*, *112*, D16,202, doi:10.1029/2006JD008292, 2007. 4

Nolan, S. J., G. Puhlhofer, and P. M. Chadwick, Active atmospheric calibration for H.E.S.S. applied to PKS 2155-304, pp. 532–535, *Proc. 30th International Cosmic Ray Conference (ICRC 2007)*, Mérida, Yucatán, México, HESS Collaboration, 2007. 94

Omegafilters, User's manual, `http://issuu.com/omegaoptical/docs/omega_optical_2012_catalog`, (accessed on April 2012). 51, 105

Press, W. H., S. A. Teukolsky, W. T. Vetterling, and B. P. Flamnery, in *Numerical Receipes: The Art of Scientific Computing*, 3rd ed., chap. 7, pp. 274–328, Cambridge University Press, 2007. 37

Qiu, J., Sensitivity of lidar equation solution to boundary values and determination of the values, *Adv. Atmos. Sci.*, *5*(2), 229–241, 1988. 56

Reagan, J. A., M. P. McCormick, and J. D. Spinhirne, Lidar Sensing of Aerosols and Clouds in the Troposphere and Stratosphere, 77, pp. 433–448, *Proc. IEEE*, 1989. 55

Reba, M. N. M., Data processing and inversion interfacing the UPC elastic-Raman lidar system, Ph.D. thesis, Universitat Politècnica de Catalunya (UPC), Barcelona (Spain), Thesis advisor: Dr. F. Rocadenbosch, 2010. 56, 57

Reba, M. N. M., F. Rocadenbosch, M. Sicard, D. Kumar, and S. Tomás, On the lidar ratio estimation from the synergy between aeronet sun-photometer data and elastic lidar inversion, pp. 883–886, *Proc. 25th International Laser Radar Conference*, St. Petersburg (Russia), ISBN: 978-5-94458-109-9, 2010. 56

Rocadenbosch, F., Lidar Sensing of the Atmosphere: Receiver Design and Inversion Algorithms for an Elastic System, Ph.D. thesis, Universitat Politècnica de Catalunya (UPC), Barcelona (Spain), `http://www.grss-ieee.org/education/phd-theses/`, 1996. 8

Rocadenbosch, F., and A. Comerón, Error Analysis For The Lidar Backward Inversion Algorithm, *Appl. Opt.*, *38*(21), 4461–4474, 1999. 57

Rocadenbosch, F., A. Comerón, and D. Pineda, Assessment of lidar inversion errors for homogeneous atmospheres, *Appl. Opt.*, *37*(12), 2199–2206, 1998. 21, 25, 65, 104

Rocadenbosch, F., C. Soriano, A. Comerón, and J. M. Baldasano, Lidar inversion of atmospheric backscatter and extinction-to-backscatter ratios by use of a Kalman filter, *Appl. Opt.*, *38*(15), 3175–3189, 1999. 56

Rocadenbosch, F., M. Sicard, A. Comerón, and M. N. M. Reba, Statistical considerations on the extinction error variance for the Raman lidar inversion algorithm, pp. 2771–2774, *Proc. IGARSS*, Barcelona(Spain), 2007. 88

Rocadenbosch, F., I. Mattis, C. Böckmann, G. Pappalardo, J. Bösenberg, L. Alados-Arboledas, A. Amodeo, A. Ansmann, A. Apituley, D. Balis, A. Chaikovsky, A. Comerón, V. Freudenthaler, O. Gustafsson, G. Hansen, R. Mamouri, V. Mitev, C. Muñoz, D. Nicolae, A. Papayannis, C. Pérez, M. R. Perrone, A. Pietruczuk, M. Pujadas, J. P. Putaud, F. Ravetta, V. Rizi, M. Sicard, V. Simeonov, N. Spinelli, D. Stoyanov, T. Trickl,

U. Wandinger, and M. Wiegner, The European Aerosol Research Lidar Network (EARLINET): An Overview, pp. (II–410)–(II–413), *IEEE International Geoscience and Remote Sensing Symposium*, Boston, MA, USA, ISBN: 978-1-4244-2808-3, 2008. 10, 55, 95

Rocadenbosch, F., M. N. M. Reba, M. Sicard, and A. Comerón, Practical analytical backscatter error bars for elastic one-component lidar inversion algorithm, *Appl. Opt.*, *49*(17), 3380–3393, 2010a. 57, 58

Rocadenbosch, F., M. N. M. Reba, M. Sicard, S. Tomás, and D. Kumar, Lidar ratio estimation using a two-point calibration in an turbid layer aloft, pp. 59–62, *Proc. 25th International Laser Radar Conference*, ISBN: 978-5-94458-109-9, 2010b.

Rocadenbosch, F., S. Frasier, D. Kumar, D. Lange, E. Gregorio, and M. Sicard, Backsactter error bounds for the elastic lidar two-component inversion algorithm, *IEEE Trans. Geosci. Remote Sens.*, in press (accepted on March 17, 2012), 2012. 55, 61, 105

Rogers, R. R., and M. K. Yau, *A short course in cloud physics*, International series in natural philosophy, Pergamon Press, 1989. 15

Rossi, B., and K. Greisen, Cosmic-ray theory, *Reviews of Modern Physics*, *13*, 240–309, 1941. 94

Sasano, Y., and H. Nakane, Significance of the Extinction/Backscatter Ratio and the Boundary Value Term in the Solution for the Two-Component Lidar Equation, *Appl. Opt.*, *23*(1), 11–13, 1984. 56

Sasano, Y., and H. Nakane, Quantitative Analysis of RHI Lidar Data by an Iterative Adjustment of the Boundary Condition Term in the Lidar Solution, *Appl. Opt.*, *26*(4), 615–616, 1987. 56

Sasano, Y., H. Shimizu, N. Takeuchi, and M. Okuda, Geometrical form factor in the laser radar equation: an experimental determination, *Appl. Opt.*, *18*, 3908–3910, 1979. 31

Sasano, Y., E. V. Browell, and S. Ismail, Error Caused by Using a Constant Extinction/Backscatter ing Ratio in the Lidar Solution, *Appl. Opt.*, *24*(22), 3929–3932, 1985. 56

Sassen, K., and G. Dodd, Lidar crossover function and misalignment effects, *Appl. Opt.*, *21*, 3162–3165, 1982. 31, 32

Sicard, M., P. Chazette, J. Pelon, J. Gwang-Won, and S. C. Yoon, Variational method for the retrieval of the optical thickness and the backscatter coefficient from multiangle lidar profiles, *Appl. Opt.*, *41*(3), 493–502, 2002. 56

Sicard, M., M. N. M. Reba, F. Rocadenbosch, E. Gregorio, D. Kumar, S. Tomás, A. Comeron, F. Molero, M. Pujadas, J. L. Guerrero-Rascado, L. Alados-Arboledas, R. Pedrós, and J. A. Martínez, Intercomparison of spanish advanced lidars in the framework of EARLINET, pp. 2763–2766, *Proc. IEEE International Geoscience and Remote Sensing Symposium*, 2007. 11, 91

Sicard, M., S. Tomás, A. Comerón, F. Rocadenbosch, A. Rodríguez, C. Muñoz, and O. Batet, Planetary boundary layer height and wind field characterization by means of a lidar at the Teide observatory in the Canary Islands, pp. III–915–III–918, *Proc. IEEE International Geoscience and Remote Sensing Symposium*, 2008. 91

Sicard, M., A. Comerón, F. Rocadenbosch, A. Rodríguez, and C. Muñoz, Quasi-analytical determination of noise-induced error limits in lidar retrieval of aerosol backscatter coefficient by the Klett-Fernald-Sasano algorithm, *Appl. Opt.*, *48*(2), 176–182, 2009a. 57, 59

Sicard, M., S. Tomás, M. N. M. Reba, A. Comerón, O. Batet, C. Muñoz, A. Rodríguez, F. Rocadenbosch, C. Muñoz-Tuñón, and J. Fuensalida, Aerosol stratification characterization of an astronomical site by means of a backscatter lidar at the Roque de los Muchachos Observatory, pp. 74,750P–1–74,750P–10, *Proc. SPIE*, 2009b. 91

Sicard, M., M. N. M. Reba, S. Tomás, A. Comerón, O. Batet, C. Muñoz, A. Rodrguez, F. Rocadenbosch, and J. J. Fuensalida, Site-testing results by means of an aerosol backscatter lidar at the Roque de los Muchachos Observatory, *Monthly Notices of the Royal Astronomical Society*, *405*, 129–142, dOI: 10.1111/j.1365-2966.2010.16468.x, 2010. 91

Sicard, M., F. Rocadenbosch, M. N. M. Reba, A. Comerón, S. Tomás, D. García-Vízcaino, O. Batet, R. Barrios, D. Kumar, and J. M. Baldasano, Seasonal variability of aerosol optical properties observed by means of a Raman lidar at an EARLINET site over Northeastern Spain, *Atmos. Chem. Phys.*, *11*, 175190, doi:10.5194/acp-11-175-2011, 2011.

Simeonov, V., G. Larcheveque, P. Quaglia, H. Bergh, and B. Calpini, Influence of the photomultiplier tube spatial uniformity on lidar signals, *Appl. Opt*, *38*(24), 5186–5190, 1999. 37, 52, 105

Spinhirne, J. D., E. J. Welton, S. P. Palm, W. D. Hart, D. Hlavka, A. Mahesh, and R. S. Lancaster, The GLAS Polar Orbiting Lidar Experiment: First Year Results and Available Data, 2, pp. 949–952, *22nd International Laser Radar Conference*, Matera (Italy), 2004. 1

Stelmaszczyk, K., M. Dell'Aglio, S. Chudzyński, T. Stacewic, and L. Wöste, Analytical function for lidar geometrical compression form-factor calculations, *Appl. Opt.*, *44*, 1323–1331, 2005. 31, 32

Stephens, G. L., and R. J. Engelen, Toward retrieving properties of the tenuous atmosphere using space-based lidar measurements, *J. Geophys. Rsch.*, *106*(D22), 28.143–28.157, 2001. 56

Viezee, W., E. E. Uthe, and R. T. H. Collis, Lidar observations of airfield approach conditions: an exploration study, *J. Appl. Meteor.*, *8*, 274–283, 1969. 56

Wandinger, U., and A. Ansmann, Experimental determination of the lidar overlap profile with Raman lidar, *Appl. Opt.*, *41*, 511–514, 2002. 31

Werner, C., Doppler wind lidar, in *Lidar, Range-Resolved Optical Remote Sensing of the Atmosphere*, edited by C. Weitkamp, chap. 12, pp. 325–355, Springer, Singapore, 2005. 1

Whiteman, D. N., Examination of the traditional Raman lidar technique II. Evaluating the ratios for water vapor and aerosols, *Appl. Opt.*, *42*(15), 2593–2608, 2003. 15, 16, 17

Winker, D., J. Pelon, and P. McCormick, Initial Results from CALIPSO, pp. 991–994, *23rd International Laser Radar Conference*, Tokyo Metropolitan Univ., Tokyo, 2006. 4

Winker, D. M., and J. Pelon, The CALIPSO Mission, pp. 1329–1331, *Proc. IEEE International Geoscience and Remote Sensing Symposium*, 2003. 55

Winker, D. M., R. H. Couch, and P. McCormick, An overview of LITE: NASA's Lidar In-Space Technology Experiment, no. 2 in 84, pp. 164–180, *Proc. IEEE*, 1996. 1, 55

ZEMAX, User's manual, `http://www.zemax.com`, (accessed on April 2012). 38, 46

Zimmer, P., and J. McGraw, Measurement Astrophysics (MAP) First Steps: LIDAR Measurements of Atmospheric Extinction, *Bulletin of the American Astronomical Society*, *42*, 401, 2010. 94

INDEX